Title

Structural, Microstructural, and Functional Magnetic Resonance Imaging Measures of the Brain and Spinal Cord are Associated with Neurological Symptoms and Chronic Pain in Patients with Cervical Stenosis

Author

Woodworth, Davis C

Publication Date

2018

Peer reviewed|Thesis/dissertation

UNIVERSITY OF CALIFORNIA

Los Angeles

Structural, Microstructural, and Functional Magnetic Resonance Imaging Measures of the Brain and Spinal Cord are Associated with Neurological Symptoms and Chronic Pain in Patients with Cervical Stenosis

A dissertation submitted in partial satisfaction of the

requirements for the degree Doctor of Philosophy

in Biomedical Physics

by

Davis Christopher Woodworth

2018

ABSTRACT OF THE DISSERTATION

Structural, Microstructural, and Functional Magnetic Resonance Imaging Measures of the Brain and Spinal Cord are Associated with Neurological Symptoms and Chronic Pain in Patients with Cervical Stenosis

by

Davis Christopher Woodworth

Doctor of Philosophy in Biomedical Physics

University of California, Los Angeles, 2018

Professor Benjamin M. Ellingson, Chair

Cervical stenosis (CS), or tightening of the spinal canal, that causes long-term neurological impairment including neck pain and motor weakness, is termed cervical spondylotic myelopathy (CSM). However, substantial compression of the spinal cord does not necessarily entail more severe symptomatology and evaluations of clinical magnetic resonance imaging (MRI) scans are only weakly associated with patient symptom severity and have shown limited value in predicting patient disease progression or response to treatment. Thus, non-invasive imaging biomarkers that better reflect patient symptoms are in great need. While the spinal cord is the primary site of injury

in CSM, the brain can also present with degenerative or compensatory changes in relation to patient symptoms. The purpose of this dissertation was to evaluate, via advanced MRI scans, the associations between structure, function, and microstructure, of the spinal cord and brain, with neurological symptoms and pain severity in patients with CS.

High-resolution structural, resting-state functional, and diffusion MRI scans of the brain and spinal cord were acquired in 26 CS patients and 17 healthy control subjects. Measures of brain and spinal cord structure, functional connectivity, and microstrucutre, were compared to the modified Japanese Orthopedic (mJOA) and the Neck Disability Index (NDI) scores. Similar to previous findings, structural measures of the spinal cord were not associated with symptom severity. However, patients with CS presented decreased brain structure with worsening neurological symptoms in subregions of the primary sensorimotor cortex, the superior frontal gyrus, and precuneus, and in the anterior cingulate and putamen in relation to both neurological and pain symptoms. These regions also demonstrated altered functional connectivity, presenting mostly with increasing connectivity with worsening symptoms. Diffusion MRI revealed altered microstructure consistent with degenerative changes in the spinal cord, both at the site of injury and at uncompressed sites, and further rostrally in the corticospinal tracts in the brain.

This cross-sectional study brings the brain and spinal cord together using advanced MRI to paint a more holistic picture of patients with CSM, and provides a groundwork for future studies to evaluate the brain and spinal cord longitudinally and after surgery to help determine optimal treatment strategies.

The dissertation of Davis Christopher Woodworth is approved.

Daniel B. Ennis

Holden H. Wu

Juan P. Villablanca

Emeran Mayer

Benjamin M. Ellingson, Committee Chair

University of California, Los Angeles

2018

DEDICATION

This compendium of work and knowledge is dedicated to my loving wife, Rebecca Barrera. Love, you done went and got stuck with me…

TABLE OF CONTENTS

ACKNOWLEDGMENTS

I would like to start off by thanking my advisor, Professor Benjamin Ellingson, for his support and mentorship over the years, for challenging me to think like a scientist, for encouraging me to refine my analyses, figures, and writing, and for setting an excellent example of hard work and persistence. I would like to thank my other committee members, Professors Daniel Ennis, Holden Wu, Pablo Villablanca, and Emeran Mayer, for their guidance and direction. As the adage goes "Amateurs think about strategy, but professionals think about logistics," and this being the case I want to thank my committee for helping me to become more professional by guiding me to narrow down on logistically attainable experiments and to focus on testable hypotheses. I would like to thank Professor Langston Holly, whose patients are the crux of this manuscript, and whose clinical expertise and leadership made this study possible. I would like to thank Carrie Bruckner and Lisa Tan from Dr. Holly's office for their help in scheduling patients. I would also like to thank Professor Noriko Salamon for her assistance with radiological aspects of this study and for her help in understanding the results and crafting manuscripts.

I would like to thank various members of the Brain Tumor Imaging Laboratory (BTIL) for their collaboration and friendship. I would like to thank Dr. Kevin Leu and Dr. Robert Harris for blazing the trail ahead of and alongside me as graduate students in the lab. I would also like to thank other members of the BTIL that I worked with throughout the years, including Dr. Anh Tran, Dr. Ruben Nechifor, Edgar Rios Piedra, Catalina Raymond-Guzman, Dr. Todd Tishler, Dr. Ararat Chakhoyan, and Jingwen Yao. I would also like to thank international and visiting scholars who I had the privilege of working with, starting with Dr Hajime Yokota, who assisted with his advice on clinical assessment of spinal cord MRIs, as well as Dr. Akira Yogi, Dr. Iren Orosz, Dr. Henrik Ullman, Dr. Yoko Hirata, and Dr. Emiko Morimoto. I would like to thank Eloisa Rodriguez-Mena

for her help with scheduling meetings and for keeping me in the loop whenever there was free food around the suite.

I would like to thank Professor Emeran Mayer for his support and allowing me to be a part of the Center for the Neurobiology of Stress and Resilience (CNSR) at UCLA. I would like to thank Professors Bruce Naliboff, Jennifer Labus, and Kristen Tillisch, for their wisdom and advice in various projects I assisted with at the CNSR. I would like to thank Cody Ashe-McNalley for his help and friendship, and for the many conversations about programming and life. I would like to thank Cathy Liu for her help in maintaining datasets clean and clear, and I would like to thank Professor Arpana Gupta for her encouragement and comradery in research endeavors.

I am grateful to the UCLA Department of Radiology for providing an excellent environment in which to perform research. I would like to thank the scanner technicians Sergio Godinez, Glen Nyborg, Francine Cobla, Kelly O'Connor, Nick Haid, and Angela Clark, for their help with acquiring the data in patients and advice with scanner-related questions, and I would like to thank the administrative assistants Earline Clausell, Andrea Osuna, Oscar Perez, Brenda Puente-Rios, Yojani Luna, and Reevia McCollins, for their help with scheduling scans. I would also like to thank Gerhard Laub, Yutaka Natsuaki, and Siemens Medical Solutions, for sequences provided through research collaborations and for access to the scanners.

I am grateful to the good people of the Physics and Biology in Medicine graduate program (formerly Biomedical Physics) for their academic and professional investment in my life. I would like to thank Professor Michael McNitt-Gray for his encouragement, availability, and genuine concern with my success as a student and researcher. I would like to thank Reth Im for her help in maintaining my academic progress and for answering program-related questions. I would like to thank the late Terry Moore for helping me in the application and recruitment process, and for

warmly welcoming me into the program. I would like to thank Anthony Hardy for his help in familiarizing me with some of the neuroimaging software that I used in this dissertation. I would like to thank the Biomedical Physics entering class of 2011: guys, we somehow managed to be simultaneously both the best and worst class the program has ever seen. I would like to thank Professors William Grisham and Walter Babiec, for allowing me to help teach the Winter 2018 Neuroscience 101L course as a teaching assistant (TA), and I would like to thank my fellow TA, Elizabeth Cooke, for laboring through the grading alongside me. I would also like to thank the Winter 2018 Neuro 101L students, who were an excellent class and from whom I learned a lot.

I would like to thank my parents, David and Dr. Margot Woodworth, for instilling in me a love for learning and for prioritizing my education. I would like to thank the rest of my immediate and extended family for their love, support, and great sense of humor. I would like to thank my wife, Rebecca Barrera, for putting up with me even when long stretches of time needed to be dedicated to research for this dissertation and other projects. And I would like to thank all the participants who volunteered for this study, especially the patients: without you there would have been no study and no new knowledge that came from it; thank you.

Parts of Chapter II of this dissertation are a version of: Davis C Woodworth, Langston T Holly, Emeran A Mayer, Noriko Salamon, Benjamin M Ellingson; Alterations in Cortical Thickness and Subcortical Volume are Associated With Neurological Symptoms and Neck Pain in Patients With Cervical Spondylosis, *Neurosurgery*, nyy066, https://doi.org/10.1093/neuros/nyy066. Langston T Holly, Noriko Salamon, and Benjamin M Ellingson helped design the study; Benjamin M Ellingson helped perform the data acquisition and analysis; and Langston T Holly, Emeran A Mayer, Noriko Salamon, and Benjamin M Ellingson helped interpret the results and write the manuscript.

BIOGRAPHICAL SKETCH

2011 B.S. in Physics, University of California - Santa Barbara, Santa Barbara, CA

PUBLICATIONS

1. **Woodworth DC**, Holly LT, Mayer EA, Salamon N, Ellingson BM. Alterations in Cortical Thickness and Subcortical Volume are Associated With Neurological Symptoms and Neck Pain in Patients With Cervical Spondylosis. *Neurosurgery*. 2018 Mar 14. doi: 10.1093/neuros/nyy066. [Epub ahead of print]
2. Gupta A†, **Woodworth DC**†, Ellingson BM, Rapkin AJ, Naliboff B, Kilpatrick LA, Stains J, Masghati S, Tillisch K, Mayer EA, Labus JS. Disease-Related Microstructural Differences in the Brain in Females with Provoked Vestibulodynia. *J Pain*. 2018 Jan 29. pii: S1526-5900(18)30027-0. † Denotes both authors contributed equally to the work and share first authorship.
3. **Woodworth D**, Mayer E, Leu K, Ashe-McNalley C, Naliboff BD, Labus JS, Tillisch K, Kutch JJ, Farmer MA, Apkarian AV, Johnson KA, Mackey SC, Ness TJ, Landis JR, Deutsch G, Harris RE, Clauw DJ, Mullins C, Ellingson BM; MAPP Research Network. Unique Microstructural Changes in the Brain Associated with Urological Chronic Pelvic Pain Syndrome (UCPPS) Revealed by Diffusion Tensor MRI, Super-Resolution Track Density Imaging, and Statistical Parameter Mapping: A MAPP Network Neuroimaging Study. *PLoS One*. 2015 Oct 13;10(10):e0140250.
4. **Woodworth DC**, Pope WB, Liau LM, Kim HJ, Lai A, Nghiemphu PL, Cloughesy TF, Ellingson BM. Nonlinear distortion correction of diffusion MR images improves quantitative DTI measurements in glioblastoma. *J Neurooncol*. 2014 Feb;116(3):551-8
5. Ellingson BM, Salamon N, **Woodworth DC**, Yokota H, Holly LT. Reproducibility, temporal stability, and functional correlation of diffusion MR measurements within the spinal cord in patients with asymptomatic cervical stenosis or cervical myelopathy. *J Neurosurg Spine*. 2018 Feb 9:1-9.
6. Young JR, Orosz I, Franke MA, Kim HJ, **Woodworth D**, Ellingson BM, Salamon N, Pope WB. Gadolinium deposition in the paediatric brain: T1-weighted hyperintensity within the dentate nucleus following repeated gadolinium-based contrast agent administration. *Clin Radiol*. 2017 Dec 2.
7. Ellingson BM, Gerstner ER, Smits M, Huang RY, Colen R, Abrey LE, Aftab DT, Schwab GM, Hessel C, Harris RJ, Chakhoyan A, Gahrmann R, Pope WB, Leu K, Raymond C, **Woodworth DC**, de Groot J, Wen PY, Batchelor TT, van den Bent MJ, Cloughesy TF. Diffusion MRI Phenotypes Predict Overall Survival Benefit from Anti-VEGF Monotherapy in Recurrent Glioblastoma: Converging Evidence from Phase II Trials. *Clin Cancer Res*. 2017 Jun 27.
8. Ellingson BM, Harris RJ, **Woodworth DC**, Leu K, Zaw O, Mason WP, Sahebjam S, Abrey LE, Aftab DT, Schwab GM, Hessel C, Lai A, Nghiemphu PL, Pope WB, Wen PY, Cloughesy TF. Baseline pretreatment contrast enhancing tumor volume including central necrosis is a prognostic factor in recurrent glioblastoma: evidence from single and multicenter trials. *Neuro Oncol*. 2017 Jan;19(1):89-98.

9. Akhtari M, Emin D, Ellingson BM, **Woodworth D**, Frew A, Mathern GW. Measuring the local electrical conductivity of human brain tissue. *Journal of Applied Physics*. 2016 Feb 14;119(6):064701.
10. Alger JR, Ellingson BM, Ashe-McNalley C, **Woodworth DC**, Labus JS, Farmer M, Huang L, Apkarian AV, Johnson KA, Mackey SC, Ness TJ. Multisite, multimodal neuroimaging of chronic urological pelvic pain: Methodology of the MAPP research network. *Neuroimage Clin*. 2016 Jan 6;12:65-77.
11. Ellingson BM, Hirata Y, Yogi A, Karavaeva E, Leu K, **Woodworth DC,** Harris RJ, Enzmann DR, Wu JY, Mathern GW, Salamon N. Topographical Distribution of Epileptogenic Tubers in Patients With Tuberous Sclerosis Complex. *J Child Neurol*. 2016 Apr;31(5):636-45.
12. Labus JS, Naliboff B, Kilpatrick L, Liu C, Ashe-McNalley C, Dos Santos IR, Alaverdyan M, **Woodworth D**, Gupta A, Ellingson BM, Tillisch K, Mayer EA. Pain and Interoception Imaging Network (PAIN): A multimodal, multisite, brain-imaging repository for chronic somatic and visceral pain disorders. *Neuroimage*. 2016 Jan 1;124(Pt B):1232-7.
13. Ellingson BM, Salamon N, **Woodworth DC**, Holly LT. Correlation between degree of subvoxel spinal cord compression measured with super-resolution tract density imaging and neurological impairment in cervical spondylotic myelopathy. *J Neurosurg Spine*. 2015 Jun;22(6):631-8. doi: 10.3171/2014.10.SPINE14222.
14. Gupta A, Mayer EA, Sanmiguel CP, Van Horn JD, **Woodworth D**, Ellingson BM, Fling C, Love A, Tillisch K, Labus JS. Patterns of brain structural connectivity differentiate normal weight from overweight subjects. *Neuroimage Clin*. 2015 Jan 13;7:506-17. doi: 10.1016/j.nicl.2015.01.005.
15. Ellingson BM, Kim E, **Woodworth DC**, Marques H, Boxerman JL, Safriel Y, McKinstry RC, Bokstein F, Jain R, Chi TL, Sorensen AG, Gilbert MR, Barboriak DP. Diffusion MRI quality control and functional diffusion map results in ACRIN 6677/RTOG 0625: A multicenter, randomized, phase II trial of bevacizumab and chemotherapy in recurrent glioblastoma. *Int J Oncol*. 2015 May;46(5):1883-92.
16. Leu K, Enzmann DR, **Woodworth DC**, Harris RJ, Tran AN, Lai A, Nghiemphu PL, Pope WB, Cloughesy TF, Ellingson BM. Hypervascular tumor volume estimated by comparison to a large-scale cerebral blood volume radiographic atlas predicts survival in recurrent glioblastoma treated with bevacizumab. *Cancer Imaging*. 2014 Nov 14;14(1):31.
17. Ellingson BM, Kim HJ, **Woodworth DC**, Pope WB, Cloughesy JN, Harris RJ, Lai A, Nghiemphu PL, Cloughesy TF. Recurrent glioblastoma treated with bevacizumab: contrast-enhanced T1-weighted subtraction maps improve tumor delineation and aid prediction of survival in a multicenter clinical trial. Radiology. 2014 Apr;271(1):200-10.
18. Tran AN, Lai A, Li S, Pope WB, Teixeira S, Harris RJ, **Woodworth DC**, Nghiemphu PL, Cloughesy TF, Ellingson BM. Increased sensitivity to radiochemotherapy in IDH1 mutant glioblastoma as demonstrated by serial quantitative MR volumetry. *Neuro Oncol*. 2014 Mar;16(3):414-20.
19. Ellingson BM, Sahebjam S, Kim HJ, Pope WB, Harris RJ, **Woodworth DC**, Lai A, Nghiemphu PL, Mason WP, Cloughesy TF. Pretreatment ADC histogram analysis is a predictive imaging biomarker for bevacizumab treatment but not chemotherapy in recurrent glioblastoma. *AJNR Am J Neuroradiol*. 2014 Apr;35(4):673-9. doi: 10.3174/ajnr.A3748.

Chapter I. Introduction

i. Cervical Spondylotic Myelopathy

Tightening of the spinal canal in the neck due to the degeneration and protuberance of intervertebral discs and vertebra, termed spondylosis, is a common occurrence amongst middle age and elderly populations, with an incidence of around 80% in the total population [1]. When this tightening of the spinal canal impinges on the spinal cord at the cervical level, functional deficits of the spinal cord, or myelopathy, may arise. This condition is termed cervical spondylotic myelopathy (CSM) [2]. CSM can present at various and multiple cervical intervertebral and vertebral levels (**Figure 1.1**), and with a wide variety of symptoms including problems in gait, upper limb weakness, paresthesia and numbness, as well as neck pain and stiffness. In a study at the University of California, Los Angeles, of 58 consecutive patients with CSM who received laminectomy, the symptom distribution at time of surgery was the following: 40 patients had gait abnormalities (69%), 33 patients had loss of hand dexterity (57%), 27 patients had upper extremity sensory disturbance or paresthesia (47%), and 6 patients had lower extremity paresthesia (10%) [3]. Static forces on the spinal cord, along with dynamic forces that may be encountered by the subjects and potential ischemia resulting from chronic impinging of the spinal cord vasculature, can cause changes in the spinal cord of patients with CSM [4].

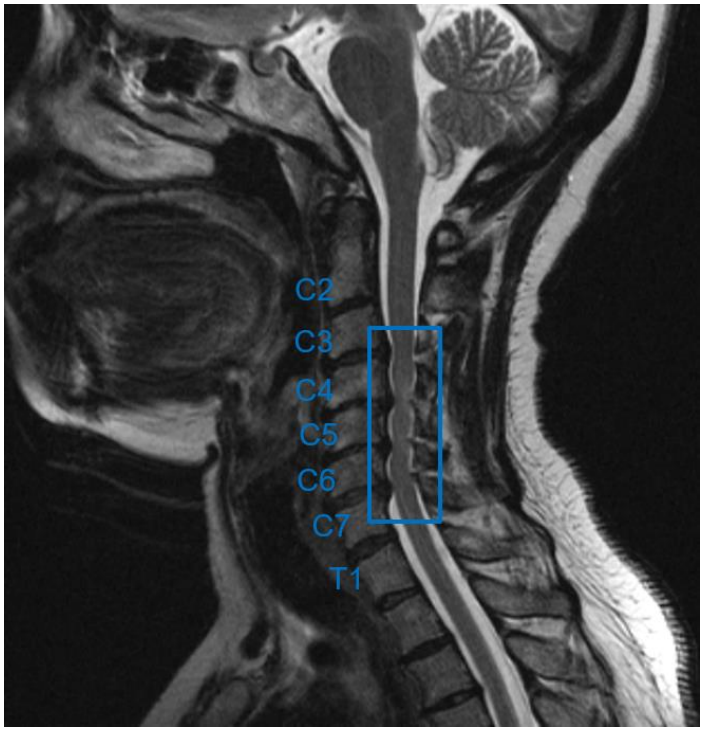

Figure 1.1. Sagittal T2-weighted MRI of patient with CSM. The different cervical levels are labeled, and the box denotes sites of compression from C3-C4 to C6-C7.

Assessing Symptoms in Patients with CSM

Given this wide range of symptomatology, various methods to determine the neurological status of patients exist. One of the most common metrics for judging the neurological symptoms of patients is the modified Japanese Orthopedic Association (mJOA) grade [5-7]. Originally developed as the Japanese Orthopedic Association (JOA) grade [5,8-11], the mJOA scoring system was adapted from the JOA by replacing questions about, for example, the patient's ability to use chopsticks, with questions such as the ability to button a shirt, to enable better assessment of western patient populations. The mJOA grade is an 18-point scale, decreasing in number for worsening neurological symptoms, and assessed using questions about four different components

of neurological status: 1) lower limb motor function, 2) upper limb motor function, 3) upper limb sensory function, and 4) sphincter function (see **Table 1.1**). The mJOA grade can be split into separate categories depending on symptom severity: a score of 18 is classified as asymptomatic, a score of 17 to 15 is classified as mild myelopathy, a score of 14 to 12 is classified as moderate myelopathy, and a score of 11 to 0 is classified as severe myelopathy [12]. Another common score used in CSM is the Nurick grade [13]. Unlike the mJOA grade, the Nurick grade only considers the patient's gait and ability to walk, which is the most common symptom in CSM patients as mentioned above. While mJOA and the Nurick scale are standard and comprehensive clinical measures for disability, other symptom-specific ancillary outcome measures are used as well [14].

In addition to neurological symptoms such as the ones assessed by the mJOA score, many patients with CSM experience neck pain that adversely affects their quality of life [15,16]. In fact, one of the primary means of diagnosing narrowing of the spinal canal, or stenosis, is radiographic evidence on x-rays following a patient's complaints of neck pain and stiffness [15]. Chronic pain is a considerable health and economic burden to society [17,18] affecting around 10% of the US population [17], and 15% of US adults report having neck pain that lasts at least a full day [19]. One measure of neck pain and disability is the Neck Disability Index (NDI) [20,21]. The NDI questionnaire is used to assess patient neck pain and how neck pain affects their ability to complete daily tasks, such as their ability to lift things, their ability to sleep, and their ability to take personal care of themselves (https://www.aaos.org/uploadedFiles/NDI.pdf). The NDI is also often used as an outcome measure for surgical intervention in patients with CSM [22,23].

Table 1.1. Neurological symptom scoring system for the modified Japanese Orthopedic Association (mJOA) grade. Adapted from Benzel *et al* [6].

Score	Definition
Motor dysfunction	
Upper extremities	
0	Unable to move hands
1	Unable to eat with a spoon but able to move hands
2	Unable to button shirt but able to eat with a spoon
3	Able to button shirt with great difficulty
4	Able to button shirt with slight difficulty
5	No dysfunction
Lower extremities	
0	Complete loss of motor & sensory function
1	Sensory preservation without ability to move legs
2	Able to move legs but unable to walk
3	Able to walk on flat floor with a walking aid (cane or crutch)
4	Able to walk up- &/or downstairs w/aid of a handrail
5	Moderate-to-significant lack of stability but able to walk up- &/or downstairs without handrail
6	Mild lack of stability but able to walk unaided with smooth reciprocation
7	No dysfunction
Sensory dysfunction	
Upper extremities	
0	Complete loss of hand sensation
1	Severe sensory loss or pain
2	Mild sensory loss
3	No sensory loss
Sphincter dysfunction	
0	Unable to micturate voluntarily
1	Marked difficulty in micturition
2	Mild-to-moderate difficulty in micturition
3	Normal micturition

Natural History and Treatment of CSM

The natural history of CSM is mixed, with some patients presenting with a stepwise progression, which entails sudden changes in neurological status followed by long segments of stable disease, and some patients presenting with rapid progression of symptoms [24-26]. Somewhere between 20-60% of patients will deteriorate if left without surgical intervention [25]. Given the mixed natural history of CSM, treatment for CSM usually involves one of two approaches: longitudinal follow-up and conservative management, or surgical intervention to decompress the spinal cord. The primary surgical approaches used on CSM patients involve decompression of the cord in the neck through removal of the vertebral body or intervertebral disc (cervical corpectomy and discectomy, respectively), which are anterior to the spinal cord, or through removal or restructuring of the lamina and spinous process (cervical laminectomy and laminoplasty, respectively) which are posterior to the cord [27]. Generally, surgery is recommended for patients presenting with more severe symptomatology, as these are likely to present with neurological improvement after surgery [28,29]. However, for patients with mild symptoms, both surgical intervention and conservative longitudinal observation show mixed results and neither approach seems to present a clear advantage over the other [26,30,31]. In contrast to acute spinal cord injury, where the injury is readily apparent after trauma and rapid treatment is essential for rehabilitation [32], the variation in the natural course of CSM, and the fact that some patients with advanced cervical stenosis and high degrees of spinal cord compression exhibit no symptoms, makes it difficult to assess the length of the disease process and the risk of the patient for worsening of their symptoms [33].

Medical Imaging of CSM

Diagnostically, radiographic X-rays can indicate narrowing of the cervical canal, and computed tomography (CT) can be helpful in assessing disc degeneration and bony anatomy for diagnostic and pre-surgical purposes. For example, based on the bony anatomy visible on radiographic techniques, the Torg-Pavlov Ratio can be computed, which is a measure of spinal canal stenosis that takes the spinal canal diameter and divides it by the vertebral body diameter in order to normalize the measure by vertebral level and across patients [34,35]. **Figure 1.2.A** presents a graphical illustration of an MRI-equivalent version of the Torg-Pavlov Ratio. However, because of its ability to image soft-tissue structures, MRI is the essential diagnostic tool for assessing spinal cord compression in CSM [36]. Broadly, the quantitative and qualitative measures extracted from routine clinical MRI comprise measurement of the cord along anterior-posterior and left-right dimensions, measures of compression that combine measurements of the cord with measurements of the spinal canal or vertebral bodies, evaluation of compression across multiple vertebral segments, and recording the presence and characteristics of T1w and T2w (**Figure 1.2.B**) intensities in the cord [36]. One pattern of T2w hyperintensity that has garnered attention in previous radiological studies is the "Snake Eye" appearance (**SEA, Figure 1.2.C**), in which instead of diffuse T2w hyperintensity, the signal hyperintensity is confined to the ventral horns of the gray matter, appearing as symmetrical round bright spots on the cord [37-39].

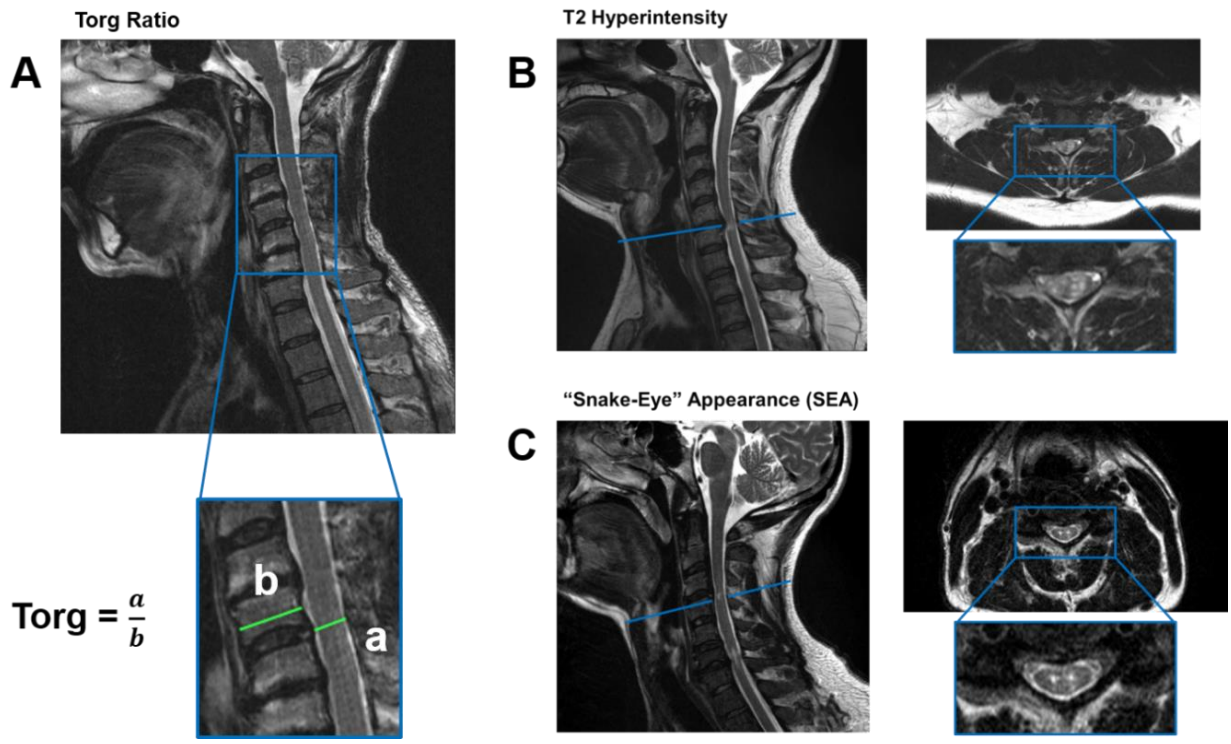

Figure 1.2. Commonly noted measures of spinal cord compression and signal intensity characteristics in CSM patients. A) MRI-equivalent Torg Ratio, a measure of cord compression, which takes the diameter of the spinal canal (a) and divides it by the diameter of the vertebral body (b). B) T2 hyperintesnity in the cord. C) "Snake-Eye" appearance (SEA) T2w hyperintensity.

The Need for New Imaging Biomarkers in CSM

Despite the diagnostic importance of conventional MRI of the spinal cord in CSM, many of the measures of cord compression assessed on these scans have shown at most a modest correlation with neurological symptoms [40-46]. As an illustration, **Figure 1.3** displays two patients with similar degrees of compression, but one is asymptomatic (**Figure 1.3.A**, mJOA of 18) and the other has moderate symptom severity (**Figure 1.3.B**, mJOA of 13), which highlights the sometimes-paradoxical relationship between conventional MRI findings in CSM and the clinical

symptoms experienced by the patient: the severity of compression and signal intensity alterations seen on clinical MRI are not always reflected in the patient's symptomatology. In addition to the paradoxical relationship between imaging findings and symptoms, imaging findings have also proven of limited value for predicting patient response to surgery, where both signal intensity characteristics and measures of compression have thus far provided only low strength of evidence and weak recommendations for using these measures to guide treatment decisions [46,47].

Even though many patients exhibit mild or no symptoms in the presence of spinal cord compression, they may still be at risk for symptom progression or irreversible neurological damage. In patients with cervical stenosis that showed no symptoms, electromyographic findings have been associated with the eventual development of symptoms [24,48]. Additionally, surgical intervention does not always guarantee neurological recovery, and presents varied recovery for different patient populations and different symptom sites. In a study evaluating recovery from surgical decompression in 55 patients, around 70% of patients experienced neurological recovery, but this varied by the site of the symptoms: most of the patients recovered hand function (63%), while fewer presented improved lower limb function (44%), and even fewer presented improved sphincter function (20%) [49]. There is an even starker picture when considering the recovery rate, or the degree to which patients recovered full neurological function after surgery: there was an average of a 37% recovery rate for upper limb function, 23% for lower limb function, and 17% for sphincter function [49].

Given the variable natural history of CSM, the variable success rate of traditional surgical interventions, and the insufficiency of conventional MRI to reflect symptom severity and monitor CSM patients or to predict outcome to surgical intervention, alternative non-invasive biomarkers are of great importance and actively being sought after.

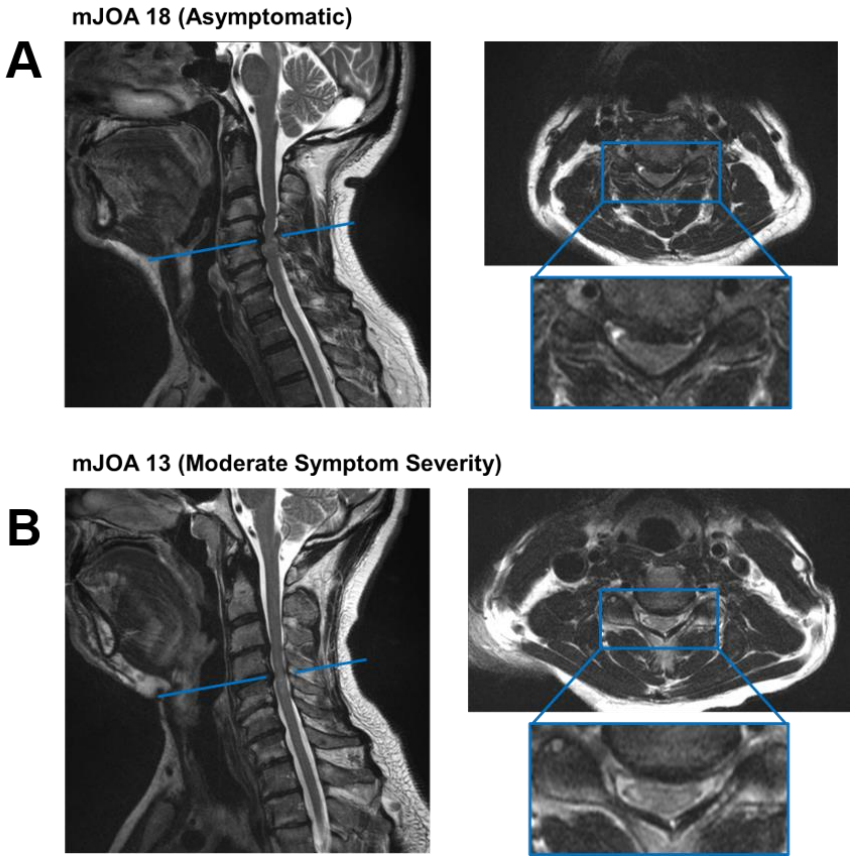

Figure 1.3. Paradoxical relationship between findings on routine clinical MRI scans and neurological symptoms. T2w sagittal (left) and axial (right) scans are shown. A) patient with high degree of cord compression and some T2w signal hyperintensities in the cord, but no neurological symptoms (mJOA 18). B) patient with moderate degree of cord compression and T2w signal hyperintensities, but moderately severe symptoms (mJOA 13).

ii. The Human Neuraxis: Anatomy and Function of the Brain and Spinal Cord

The human central nervous system (CNS) is divided into two major structures: the brain and the spinal cord. Sensation and movement arise from the interaction between the brain and the spinal cord, and both are necessary for a holistic understanding and assessment of injury to the

spinal cord. The chronic compression of the spinal cord that occurs in patients with CSM involves not only the site of compression but also the rostral spinal cord and the brain, which may respond to the localized injury in compensatory or degenerative fashion. What follows is a brief description of the brain and spinal cord and an outlining of relevant brain and spinal cord structures and pathways involved in motor, sensory, and pain processes which are of interest to this dissertation in relation to the symptoms presented by CSM patients.

The Brain

The human brain has a volume of approximately 1365 cm^3, and receives input from the rest of the body, processes information, and sends commands out to the body. The brain is composed of neurons as its basic functional cellular unit, as well as support cells such as glia and oligodendrocytes. Neurons are concentrated in the gray matter of the cortex (approx. 695 cm^3) and in subcortical gray matter structures such as the thalamus (approx. 7 cm^3), and the basal ganglia (approx. 8 cm^3) [50,51]. The cortex of the brain is a thin (approx. 1 - 4.5 mm) sheet-like structure at the surface of the brain which is highly folded into protruding rings (gyri) and in-folded furrows (sulci) [52-54]. Neurons in the CNS communicate with each other and with the rest of the body through axons that carry signals in the form of action potentials. These axons gather together to form large bundles centrally in the brain, the white matter fibers (approx. 670 cm^3) [50]. In addition to these structures in the cerebrum, the brain also contains the cerebellum (approx. 135 cm^3), which is involved in motor coordination, and the brainstem (approx. 135 cm^3), which is the primary means of entrance and exit of white matter fibers to and from the brain and which regulates a host of functions including respiration, circulation, and sleep [50]. The brain is enclosed by the skull and is enveloped in cerebrospinal fluid (CSF, approx. 180 cm^3) [50].

The brain can be divided into various regions based on their cellular architecture [55] or morphology. While complex behavior and actions arise from interaction between many brain regions, the brain possesses a considerable degree of functional modularization, where specific regions engage in specific functional tasks. The primary motor cortex, for example, encodes motor and muscle information for conscious movement, and the primary sensory cortex receives discriminative touch information from the body [50,56,57]. These regions map to the rest of the body: muscle groups across the body are mapped onto the primary motor cortex, and touch sensation for body regions is mapped on the primary sensory cortex. These primary sensorimotor maps were first described after electrical stimulation studies by Penfield and Boldrey [58]. However, the body maps and structure of these regions are not fixed, and can experience plastic rearrangement with learning or after lesioning of cerebral tissue [59-62], or can undergo degenerative changes in disease conditions such as amyotrophic lateral sclerosis (ALS) [63,64]. Thus, evaluation of local structures in the cerebral cortex may help elucidate disease processes or assist in the monitoring of disease progression or response to treatment.

The Spinal Cord

The spinal cord is enclosed by the bony anatomy of the spine and enveloped by CSF, and is involved in motor output, sensory relay, and reflexes [50]. The spinal cord measures around 45 cm in length, and has a common structure oriented along the superior-inferior axis: long myelinated axons form bundles of white matter on the outer regions of the spinal cord and transmit information to and from the brain and peripheral nervous system, and at the center of the spinal cord is gray matter, made up of neuron bodies which are active in processing information for the regional functions at each specific level of the cord. The gray matter and white matter of the spinal

cord are both regionally organized and present with a consistent structure throughout the cord. The gray matter is divided into various lamina defined by cellular architecture [65]. The laminae of the spinal cord gray matter can be broadly divided into two major regions: the dorsal horn, which consists of sensory interneurons and projection neurons, and the ventral horn, which consists of lower motor neurons. The white matter of the spinal cord is also segregated into distinct regions: posteriorly are the dorsal funiculi, the cuneate and gracilis, which carry sensory information from the body to the brain; laterally is the corticospinal tract, which carries motor commands from the brain to the muscles in the body; anterolaterally is the spinothalamic tract, which carries nociceptive information from the body to the brain [50].

The spinal cord is divided into 31 segments with corresponding ventral and dorsal roots that send motor signals to and receive sensory signals from the body. Specific segments of the spinal cord that contain the input and output for the sensory and motor regulation of limbs present with a relative increase in size compared to adjacent segments, and these occur at the cervical enlargement (C3 through T2 vertebral levels, spinal cord cross-sectional area of approximately 70 mm^2, responsible for upper limbs) and the lumbosacral enlargement (L1 through S2 vertebral levels, spinal cord cross-sectional area of approximately 50 mm^2, responsible for lower limbs) [66]. Of importance to CSM, the cervical spinal cord is the uppermost division of the spinal cord, ranging down from the bottom of the brainstem to the 7^{th} cervical level. The cervical spinal cord relays sensory information from the neck, back of the head, shoulders, and arms, and controls motor movements for the neck, shoulders, and, along with the T1 spinal cord level, the arms. The cervical spinal cord from C3 to C7 has an approximate transverse diameter of 12 mm and an approximate sagittal diameter of 7 mm [66], and contains a high proportion of white matter fibers

given that axons from and to both the upper and lower limbs traverse through the cervical cord at these levels.

The spinal cord is an essential bridge that connects the brain and the rest of the body, and contains local neural processing that regulates various functions at each spinal level. Thus, when compromise of this structure occurs it can have devastating effects on the individual, such as in the cases of paraplegia or tetraplegia which can result from traumatic spinal cord injury [67]. Preservation of the spinal cord is essential for the proper functioning of the nervous system, and while the spine and bony anatomy that surrounds the spinal cord is meant to protect it from harm, when these impinge on the spinal cord, either through chronic compressive forces as in CSM or through rapid movement or blunt trauma as in traumatic spinal cord injury, the integrity of the nervous system may be at risk.

While the spinal cord serves as a connection between the brain and the body, it also possesses a high degree of autonomy and internal circuitry that can process information and perform actions independent from the brain. For example, interneurons in the spinal cord are responsible for a large degree of modulation and modification of signals for the ascending somatosensory tracts [68], and even learning of motor commands may take place in the spinal cord via interneuron and reflex mechanisms [69]. Additionally, inhibitory and excitatory descending pathways from the brain can affect the activity of interneurons in the spinal cord [68]. These few examples highlight the complex arrangement and fucntionality of the spinal cord. However, this level of detail is currently difficult to attain using non-invasive imaging techniques, which perform better on gross anatomy and major structures in the spinal cord. Thus, particular large structures and pathways tend to be the focus for neuroimaging studies of the spinal cord.

Primary Motor, Sensory, and Pain Pathways

Figure 1.4 illustrates particular pathways of interest for this dissertation: motor, sensory, and pain. The main connection for motor processing takes place between the precentral gyrus (primary motor cortex, or M1), and the ventral horn of the spinal cord at various levels. The white matter fibers that directly connect these two comprise the corticospinal tract, a large set of axons that run from the pre-central gyrus through the internal capsule, the cerebral peduncle, and mainly cross at the decussation of the pyramids (though around 10% remain ipsilateral forming the anterior corticospinal tract), descend down the lateral portion of the spinal cord white matter, and synapse on the ventral horns in the spinal cord which contain the neurons that control the desired target muscle [50,56].

The primary sensory pathway for fine touch initiates with pseudo-unipolar neurons located in the dorsal root ganglion (DRG), where the signal is transmitted from the peripheral nerve, through the dorsal root, and then ascends the spinal cord through the dorsal column of the spinal cord along the ipsilateral side. These axons synapse in gray matter nuclei (gracile nuclei for lower limbs, and cuneate nuclei for upper limbs) in the medulla, which then cross over to the contralateral side and ascend to synapse in the ventral posterolateral nuclei (VPL) of the thalamus, which then sends the information to the primary sensory cortex (SI, **Figure 1.4**) or secondary sensory cortex (SII) [57]. Discriminative pain information enters the spinal cord through axons in the dorsal root, and these synapses on the dorsal horn of the spinal cord. The neurons in the dorsal horn then relay the information to neurons that cross over to the contralateral side on the same level of the spinal cord, and ascend through the spinothalamic tract to synapse on the VPL nucleus of the thalamus, and from there to SI (**Figure 1.4**) [57,70].

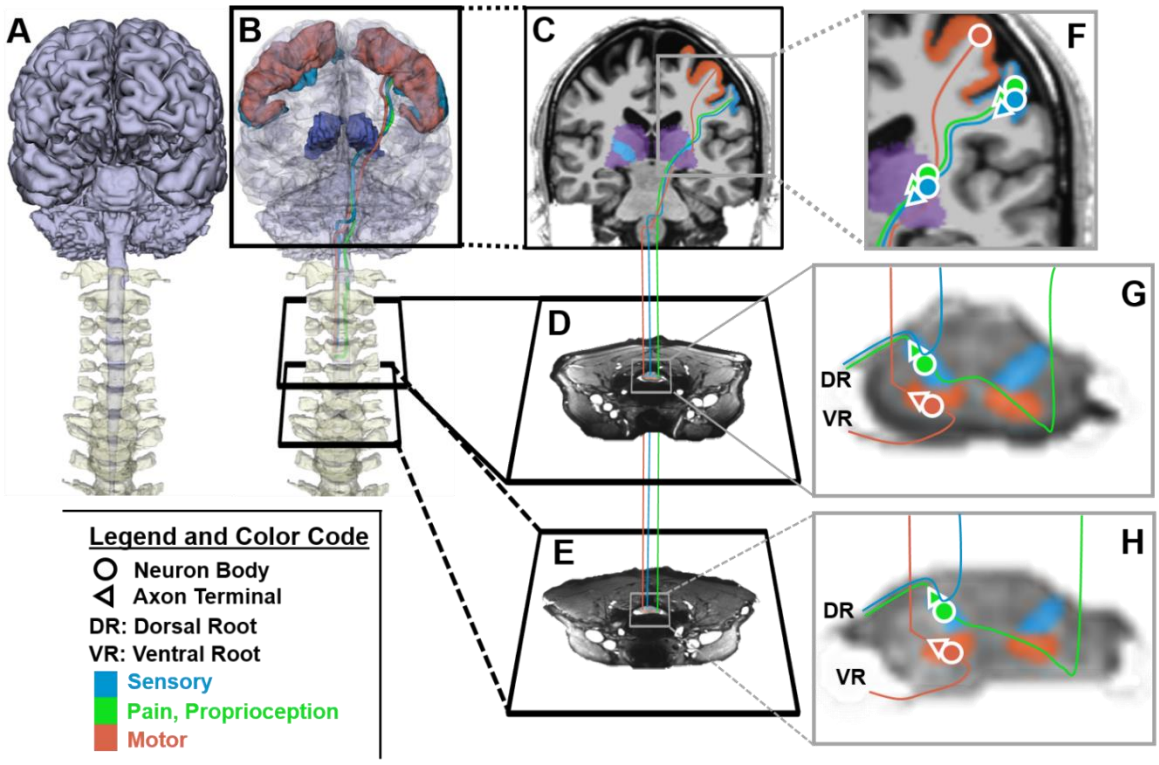

Figure 1.4. Ascending and descending pathways of interest for this dissertation. A) 3D rendering of brain and spinal cord (light purple) with vertebral bodies (transparent beige). B) Glass-brain model with structure for primary motor (red) and primary sensory (blue) cortex, the thalamus (purple) and pathways for voluntary motor (red), discriminative touch (sensory, blue), and pain and conscious proprioception (green). C) 2D MRI slices with highlighted structures previously mentioned, as well as the ventral posterolateral (VPL) nucleus highlighted in blue in the thalamus. D) and E) show a 2D MRI slice with the pathways and the dorsal (sensory, blue) and ventral (motor, red) horns highlighted, for uncompressed and compressed levels in a CS patient, respectively. F), G), and H) display zoomed-in regions of the brain, uncompressed spinal cord, and compressed spinal cord, respectively, highlighting the neuron bodies and axon terminals of interest, dorsal horn is shown in blue (sensory) and ventral horn in red (motor). Not displayed: synapse of discriminative touch pathway in the brainstem (gracile and cuneate nuclei).

In addition to the discriminative pain pathway, there are other pain pathways that relay dull, affective aspects of pain sensation [71], and these pathways synapse in a separate part of the thalamus and relay to brain structures implicated in the affective dimension of pain. One pathway synapses on the medial dorsal nuclei (MDvc) of the thalamus, which then relays the information to the anterior cingulate cortex (ACC) [57,72]. Another pathway synapses on the ventromedial posterior nuclei (VMpo) and relays information to the insula [57,71]. This affective component of pain, mediated by these pathways, is an important aspect of pain, and both the insula and the ACC play an essential role in chronic pain [73-76].

Probing the Structures and Pathways of the CNS using Neuroimaging

Invasive studies, such as tract tracing, cell recordings, staining techniques, are the gold standard to assess the structures and functional characteristics of the CNS. For patient populations, noninvasive imaging techniques to assess the structure and function of key parts of the CNS are preferable and desirable. For CSM subjects, MRI of the spine is already an essential diagnostic tool. However, MRI is a flexible imaging technique that can assess tissue of the CNS via multiple contrast mechanisms. The noninvasive, *in vivo* nature of MRI, and its ability to image both structure and function, has yielded an abundance of research and insight into the human nervous system. The following sections will go over some MRI techniques that can be used to assess the brain and spinal cord structure, function, and microstructure.

iii. Structural MRI and Measures of Atrophy

Three-dimensional T1 Structural MRI Physics and Acquisition

Traditional MRI sequences leverage the differing magnetic properties of various tissues to create contrast between them, distinguishing them on images and enabling visualization of the different tissues, both healthy and pathological. In the brain, differing relaxation times between gray and white matter are used to create images that present each tissue with a different signal intensity. While both T1 and T2 relaxation rates are different between gray matter (T1 ≈ 1350 ms, T2 ≈ 110 ms), white matter (T1 ≈ 830 ms, T2 ≈ 80 ms), and CSF (T1 ≈ 4300 ms, T2 ≈ 2000 ms) at 3T [77,78], for many brain imaging studies T1w scans have been used to define the boundary of gray and white matter (and of gray matter and CSF). T1, or longitudinal, relaxation is a measure of the time it takes for an excited spin population to come back to thermal equilibrium. T1 relaxation is determined by the equation:

Equation 1.1. $$M_Z = M_0 - (M_0 - M_z(0))e^{-t/T_1}$$

where M_Z is the longitudinal component of the magnetization vector, M_0 is the longitudinal component of the magnetization vector at equilibrium, $M_z(0)$ is the initial longitudinal component magnetization after tipping into the transverse plane, and T_1 is the relaxation rate. To maximize the dynamic range between different tissue types an inversion (180°) pulse can be applied so that the initial longitudinal component of the magnetization becomes the inverse of the magnetization vector at equilibrium, $M_z(0) = -M_0$, and the above equation becomes:

Equation 1.2. $$M_Z = M_0(1 - 2e^{-t/T_1})$$

which effectively doubles the dynamic range of the signal compared to a 90° excitation pulse, allowing for generation of greater contrast between the tissue types of interest. The use of 180° in this fashion is termed inversion recovery (IR).

Initially, IR MRI comprised two-dimensional imaging, with high in-plane resolution, thick-slab (>3 mm) slices, which enabled cross-sectional visualization of structures within the slice plane (*e.g.* axial slice), and offered a more limited resolution for perpendicular planes (*i.e.* coronal and sagittal). While informative, these two-dimensional acquisitions were insufficient to capture the actual three-dimensional geometry present in the structures being imaged. To overcome this limitation, rapid three-dimensional T1w IR MR imaging sequences were developed to enable acquisition of the full brain with high-resolution isotropic (~1 mm^3) voxels. One implementation of three-dimensional IR MRI is the magnetization-prepared rapid gradient echo (MPRAGE), which utilizes a small flip angle, additional phase encoding along the slice-selection direction, and three dimensional Fourier transform of the k-space data [79,80]. The high-resolution data acquired using the MPRAGE technique preserves gray-white matter signal intensity differences [81], and can be used for three-dimensional analysis methods.

Measuring the Gray Matter Structure of the Brain using 3D T1 MRI

The data acquired from an MPRAGE scan can be used to segment the cortical and subcortical gray matter across the brain using advanced post-processing techniques (**Figure 1.5.B, C, D**). Utilizing the three-dimensional information of the distribution in signal intensities for gray matter, white matter, and CSF, and taking advantage of the continuous, thin, sheet-like structure of the cortex, these algorithms can segment the gray matter and white matter surfaces in the cortex (**Figure 1.5.D**) with a resolution that surpasses that of the one used to acquire the scan. This is

done via intensity normalization, extraction of the brain tissue, intensity-based tissue classification, and triangular tessellation of the white/gray matter surface and the pial surface [82-85]. The gyral and sulcal anatomy along with atlas-based priors can be further used to parcellate the brain into functionally distinct regions [86,87].

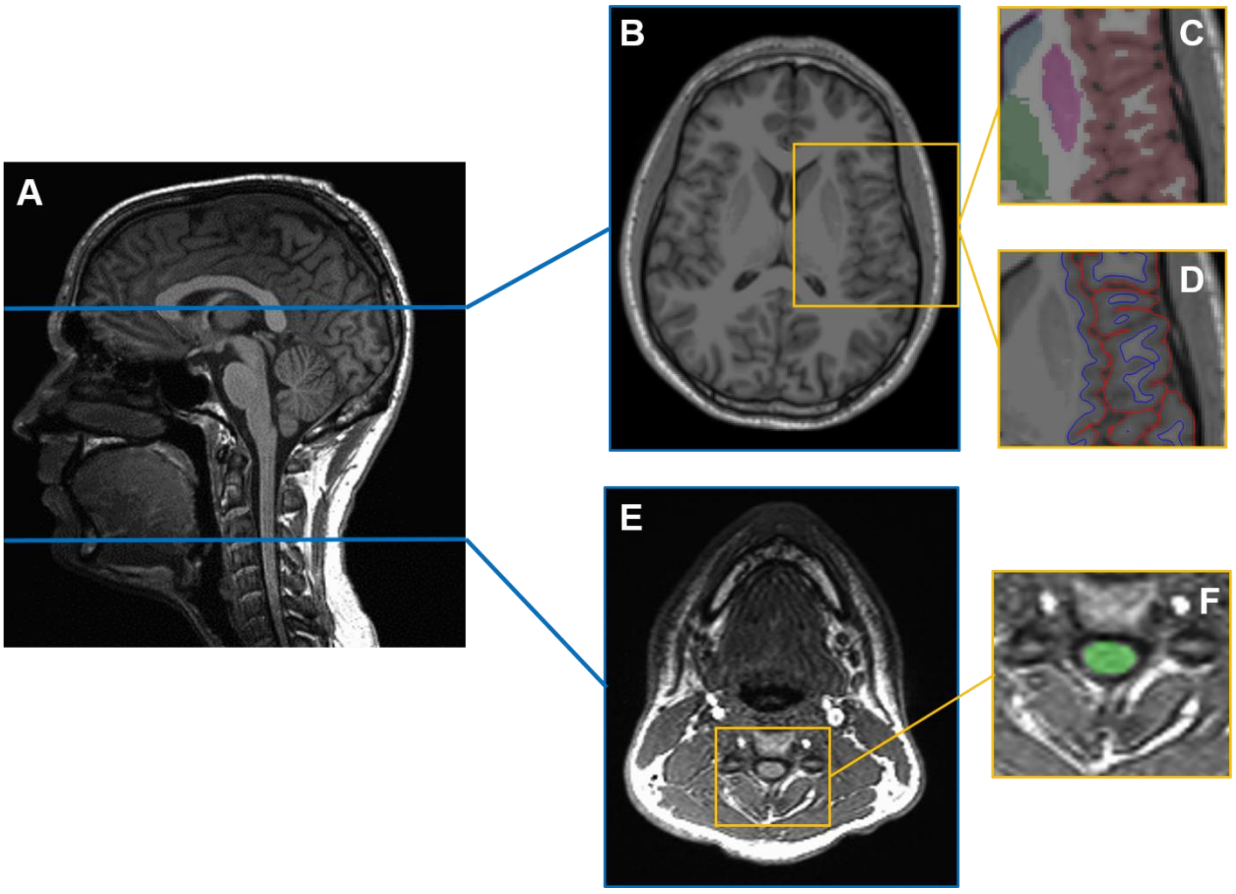

Figure 1.5. Figure illustrating three-dimensional T1 weighted image of the brain and spinal cord, showing different contrast between tissue types that can be exploited for segmentation of specific neuroanatomical structures. A) T1w mid-sagittal slice of brain and spinal cord, with axial slices of brain and spinal cord indicated in blue. B) T1w axial slice of brain. C) Zoomed-in section showing segmentation of cortex (red) and subcortical structures of the caudate (blue), putamen (purple) and thalamus (green). D) Zoomed-in section showing boundary surfaces between white matter and

gray matter (blue), and between the gray matter and CSF (red). E) T1w axial slice of neck and spinal cord. F) Zoomed-in section showing spinal cord and surrounding tissue, with the spinal cord segmentation shown as overlay (green).

These techniques enable evaluation of global as well as local measures of gray matter via metrics such as the thickness of the cortical ribbon of gray matter, termed cortical thickness [54]. Group analyses can reveal differences in cortical thickness between groups of down to 15% with group sizes of 25 subjects in each group [88]. Cortical thickness was first evaluated with respect to aging [89-91] and in Alzheimer's disease [92-94], revealing consistent patterns of atrophy in the cortex associated with both aging and Alzheimer's disease. These differences in signal intensity are also present for subcortical gray matter structures, such as the thalamus, globus pallidus, caudate and putamen, and by using this signal intensity difference and atlas priors, this allows for segmentation and volumetric evaluation of these structures (**Figure 1.4.C**) [95,96].

Because regional differences in gray matter structure may relate to disease processes and symptoms, this dissertation will evaluate the cortical thickness and segmentations of brain regions in their relation to symptom severity in patients with CS.

Measuring Gross Anatomical Structure of the Spinal Cord Using 3D T1 MRI

While the spinal cord has a relatively small cross-sectional area, nevertheless its structure can be probed using MRI. While traditional anatomical sequences have provided high-quality two-dimensional images of the spinal cord (**Figures 1.1, 1.2, 1.3**), fast imaging techniques enable three-dimensional imaging of the spinal cord. This can be done with T2 contrast using a fast spin echo technique [97,98] (*e.g.* Siemens' sampling perfection with application optimized contrasts using

different flip angle evolution, or SPACE technique [99,100]), or three-dimensional IR techniques such as the MPRAGE sequence can also be used. The data obtained from these scans can then be used to segment the spinal cord and obtain relevant measures such as the cross-sectional area or volume of the spinal cord (**Figure 1.5.E, F**) [101]. Automatic spinal cord segmentation takes advantage of the symmetrical, elongated shape of the spinal cord to propagate the segmentation in the inferior and superior directions via deformable meshes [101,102]. Using templates of the spinal cord as priors, the segmentation of the spinal cord can be labeled by vertebral level [103]. For example, spinal cord area has proven an important biomarker in (MS), where patients with specific subtypes of MS, namely primary and secondary progressive, present with a greater decrease in spinal cord cross-sectional area compared to healthy controls and other MS subtypes [104,105]. Spinal cord structure will thus be quantitatively evaluated for levels rostral to the site of injury to see if they are associated with the symptoms of patients with CSM.

iv. Resting State Functional MRI

Resting State fMRI

Functional MRI (fMRI) was first developed by Ogawa *et al*, when they discovered that the magnetic properties of oxygenation in the blood created a difference in the measured MRI signal [106,107], which they termed the blood oxygenation level-dependent (BOLD) contrast or effect. Current fMRI techniques generally consist of an MR sequence that acquires dynamic images at fast intervals (1 scan of the entire brain every 5 seconds or less) with T2* contrast via a gradient recalled echo (GRE) sequence. Because there is a difference in the level of T2* signal produced by hemoglobin and deoxyhemoglobin, an area of the brain with a higher percentage of oxygenated blood will show a larger T2* signal. Neurovascular coupling, where in response to an increase in

metabolic activity of activating neurons there is an accompanying increase in blood flow that increases the amount of blood with a higher percentage of oxygenation, is responsible for this increase in signal in brain regions undergoing activation [108].

These functional activation studies using fMRI usually require a large number of samples of activation (*i.e.* repetitions of the relevant tasks) in order to reach statistical significance, which necessitates longer scan times and greater scanner operator and imaging participant involvement. A more flexible technique to image function in the brain is resting-state fMRI (rs-fMRI), which acquires the T2*-weighted volumes without a task paradigm. Resting-state fMRI was first discovered by Biswal *et al* [109], when they noticed low frequency oscillations (< 0.1 Hz) in the motor cortex that were highly correlated across brain structures and seemed to imitate the regions of functional activation for motor tasks. Since then, consistent patterns of fMRI signal at rest have been observed across functionally related brain regions in healthy control subjects [110,111], and alteration of functional networks of brain regions related to the symptoms of various conditions have been observed. For example, patients with Alzheimer's disease demonstrated disruption in functional connectivity in the hippocampus [112], patients with amyotrophic lateral sclerosis demonstrated altered functional connectivity in the motor network compared to healthy controls [113], and convergence between resting state patterns and results from deep brain stimulation (DBS) in various neurological conditions have further cemented the validity the brain's state activity as probed using fMRI [114].

Resting-State fMRI Functional Connectivity

Resting-state fMRI can be used to calculate functional correlation, or connectivity, between a seed region and other regions or voxels [115-117]. These approaches are graphically illustrated in

Figure 1.6 for correlations between different brain regions and between a brain regions and voxels in the brain. In **Figure 1.6**, the resting-state time-series for three regions, the precentral and postcentral gyri and the supplementary motor area, are shown, and Pearson's correlation coefficient between the time-series is used as the measure of functional connectivity between the regions, and is termed ROI-to-ROI connectivity. This functional connectivity can also be calculated between an ROI and individual voxels, which can then be subjected to p-value and cluster thresholds for significance and is termed an ROI-to-voxel approach. Both the ROI-to-voxel and ROI-to-ROI approaches have demonstrated consistent patterns of functional connectivity across studies [118,119].

In order to obtain functional connectivity related to the low-frequency resting-state activity of the brain, pre-processing of rs-fMRI data is necessary to obtain the functional connectivity. The resting-state signals of interest (low-frequency oscillations around 0.08 Hz) can be obfuscated by different sources of noise, including movement [120,121], physiological artifacts such as breathing and cardiac effects [122-124], and scanner-related drift caused by hardware instabilities over the duration of the scan [125-127]. Once the data has been pre-processed, correlations between regions are calculated using correlation coefficients, such as Pearson's correlation. The Pearson's correlations can then be converted to a normal distribution via Fisher's transformation to a z-score in order to perform general linear model (GLM) analysis [128], and can be used to compare the functional connectivity between groups or the association of functional connectivity with various variables of interest. Because the activity of the brain at rest can relate to underlying processes, rs-fMRI connectivity was evaluated in terms of its relationship to symptoms in patients with CSM.

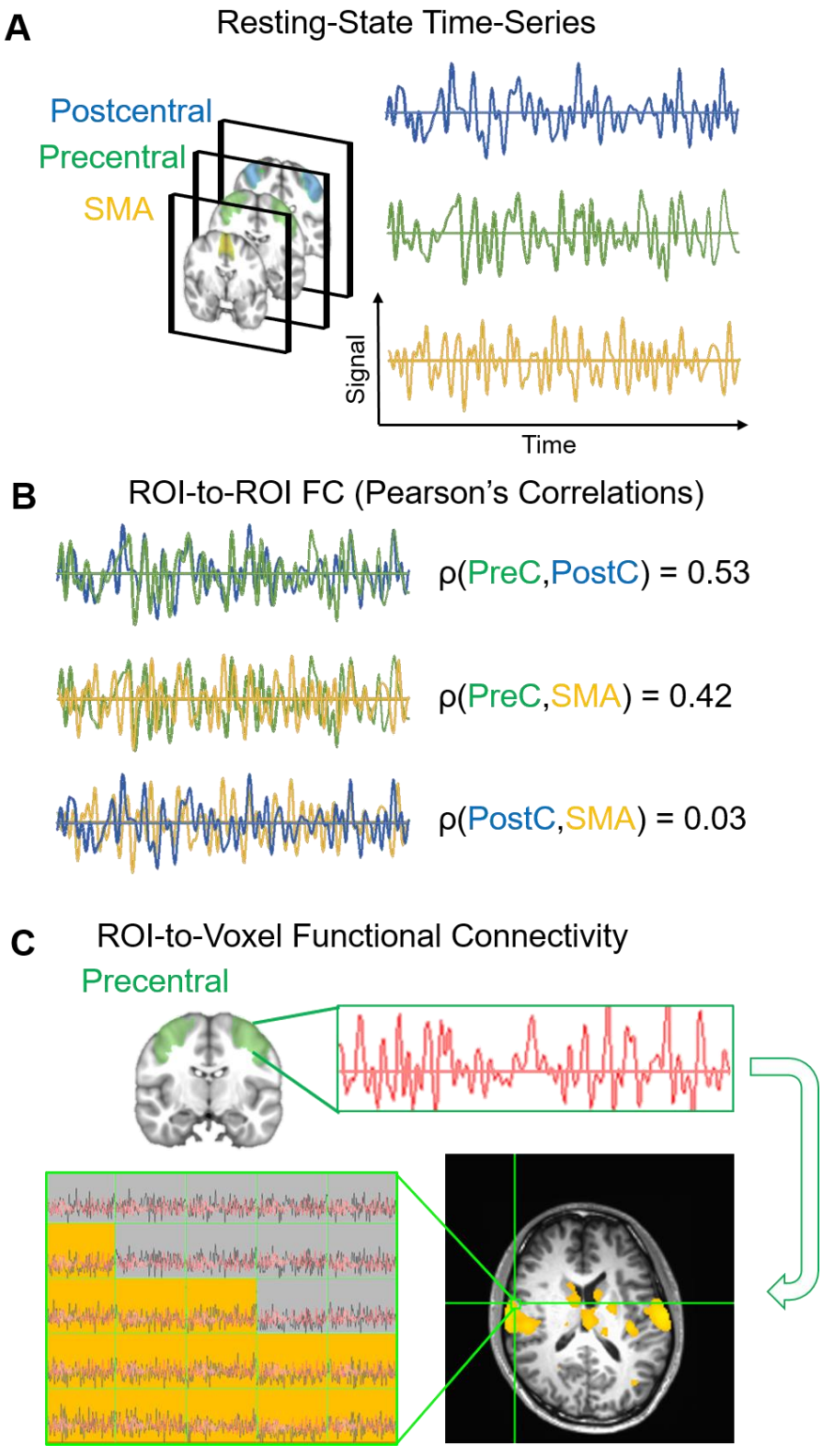

Figure 1.6. Legend presented on next page.

Figure 1.6. Legend: Illustration of functional connectivity from resting state fMRI data. A) The time series from the fMRI data are extracted for each region of interest, here shown for the postcentral gyrus (PostC, blue), the precentral gyrus (PreC, green), and the supplementary motor area (SMA, yellow), each indicated on a representative coronal slice of the brain. B) Computation of ROI-to-ROI functional connectivity: the Pearson's correlation coefficient is calculated for each combination of time-series, time-series are displayed overlayed on each other, with the PreC presenting with high functional connectivity with the SMA and the PostC, while the PostC and SMA present with lower functional connectivity. ROI-to-ROI yields information about the strength of functional connectivity between *a priori* defined regions. C) Computation of ROI-to-voxel functional connectivity, where the mean time-series from a region of interest (ROI, or seed) is used to compute the correlation with individual voxels, and voxels that are significantly correlated are shown (yellow in image and graph box), while other voxels do not pass the threshold (gray in graph box). ROI-to-voxel thus yields information about both the degree of functional connectivity (magnitude of correlation) but also the spatial extent of functional connectivity (location and volume of voxels that show correlation).

Resting State fMRI of the Spinal Cord

While brain rs-fMRI studies have been performed extensively and the methodology for these analyses have been refined by the research community, fMRI of the spinal cord is still in its infancy. The spinal cord contains the bodies of neurons that undergo activity in response to motor cortical input: neuronal bodies in the dorsal horn are involved in nociceptive and course touch and proprioceptive information being relayed up the spinal cord to the brain, and the ventral horn contains the lower motor neurons that receive input from the motor cortex and relay the signal to the respective muscle groups. Thus, the spinal cord is a suitable target for fMRI. The first spinal cord fMRI experiment was performed in 1996 by Yoshizawa *et al* [129]. Early work by Peter Stroman [130-132] overcame some of the initial challenges present in imaging the spinal cord, namely its small area, difficult anatomical environment for imaging with varying bony structures and soft tissue and CSF surrounding the cord, and physiological motion. Studies have been performed looking at neuronal activation in the spinal cord for both motor tasks and for thermal stimulation.

Resting state networks as detected by fMRI were first reported by Wei *et al* in 2010 [133]. A more recent study by Kong *et al* detected spinal cord resting state networks via independent component analysis (ICA) of fMRI data of the spinal cord [7]. Additionally, resting state functional activity has been measured in the spinal cord at 7T [134]. One factor that is of increased importance in the spinal cord compared to the brain is the presence of physiological motion (primarily cardiac and respiratory) affecting the fMRI signal [135]. While multiple strategies exist to compensate for physiological motion and noise, there is still no accepted standard method and optimal strategies vary by protocol and study [135], though recommended physiological noise modeling and regression parameters include cardiac and respiratory monitoring data, CSF signal variation, and motion correction estimations [136].

While the challenges in fMRI of the spinal cord have persisted, two recent studies have implemented a combined brain and spinal cord fMRI protocol for imaging spinal cord function, one of them for a motor learning sequence and one of them for the processing of nociceptive input. Sprenger *et al* used a thermal stimulation at the C6 level (left radial forearm), and they observed activation of the dorsal horn ipsilateral to the stimulation that was functionally correlated with typical regions associated with nociception such as thalamus, sensory cortex, insula, striatum, and the peri-aqueductal gray matter, the last of which's correlation with the C6 dorsal horn was correlated with degree of perceived pain [137]. In another study that instead used a motor learning paradigm, simple and complex motor sequence learning was both detected and differentiated via the spinal cord BOLD signal activation, which was functionally correlated with motor processing cerebral structures such as the primary motor cortex, putamen, and cerebellum [138]. *These studies show that it is feasible to perform simultaneous brain and spinal cord fMRI experiments.* However, in order to image both the spinal cord and brain, these studies had to make sacrifices in terms of TR (3270ms for Sprenger *et al,* and 2500ms for Vahdat *et al*) and in terms of coverage (two sub-volumes with 32 slices for brain and 8 slices for cervical cord centered at C6 for Sprenger *et al,* and 35-37 slices for Vahdat *et al* with 2.5mm in-plane resolution and a slice gap ranging from 80% to 120%).

v. Diffusion MRI

The Diffusion Phenomenon

The random movement of molecules in a liquid caused by the collisions of moving particles, termed Brownian motion, can over time lead to a spread of different populations of

particles when there is a difference in the concentration gradient, which is determined by Fick's first law of diffusion given by the equation:

Equation 1.3. $$J = D\frac{\partial C}{\partial x}$$

where *J* is the flux of particles, *D* is the diffusion coefficient, *C* is the concentration of the diffusing particles, and *x* is the position. The random process of diffusion creates a Gaussian distribution of particles, and the mean displacement of the particles undergoing diffusion is determined by the equation [139]:

Equation 1.4. $$< x(t) > = \sqrt{2Dt}$$

where $<x(t)>$ is the mean expected position of the particles, *D* is the diffusion coefficient, and *t* is time.

While the above equations were developed with the diffusion of a set of distinct particles (solvent) with a set concentration gradient in a medium (solute), particles in homogeneous solutions still undergo this Brownian motion. Thus, these equations govern the self-diffusion of water molecules. In the brain and spinal cord, water is distributed between both intra- and extra-cellular compartments. The constraints presented by cell membranes and other cellular structures change the self-diffusion of water from being isotropic to being directionally-dependent, where the particles are restricted [140] or hindered [141] by cellular membranes. This is especially the case in white matter, where axons form bundled, cohesive structures, and thus limit diffusion along the perpendicular direction, where the water molecules encounter myelin sheaths along their diffusion path, compared to the parallel direction, where there are fewer obstructions for the water molecules to self-diffuse [142].

Diffusion Encoding in MRI

While diffusion is a contrast mechanism that is always present in MR images, traditional anatomic MR images are only affected by diffusion to a small degree and are more strongly determined by the T1, T2, or T2* relaxation characteristics. However, MRI can be used to probe this self-diffusion of water by rendering the signal intensity in MR images more sensitive to the signal loss created by diffusion. Specifically, this is done by applying diffusion sensitizing gradients in specific directions, where the motion of water molecules lose signal by an offset in phase dependent on the amount of diffusion is taking place [143]. **Figure 1.7** illustrates the diffusion MRI technique. Diffusion sensitizing gradients tend to be trapezoidal, due to the fact that this gradient shape helps to lessen eddy current-induced artifacts [144]. The equation for calculating the strength of the diffusion sensitization, or the b-value, for trapezoidal-shaped gradients is given by the equation:

Equation 1.5. $$b = \gamma^2 G^2 (\delta^2 \left(\Delta - \frac{\delta}{3} \right) + \frac{\varepsilon^2}{6} \left(\frac{\varepsilon - 5\delta}{5} \right))$$

where b is the resultant b-value of the diffusion encoding gradient, γ is the gyromagnetic ratio of hydrogen, G is the strength of the diffusion encoding gradient, δ is the length of the diffusion encoding gradient, Δ is the diffusion time, and ε is the rise time of the diffusion encoding gradient. The application of this diffusion sensitizing gradient leads to signal loss determined by the following equation:

Equation 1.6. $$S = S_0 e^{-bD}$$

where S is the signal attenuated by diffusion, S_0 is the original signal without diffusion weighting (i.e. the b0 image), b is the b-value defined above, and D is the diffusion coefficient.

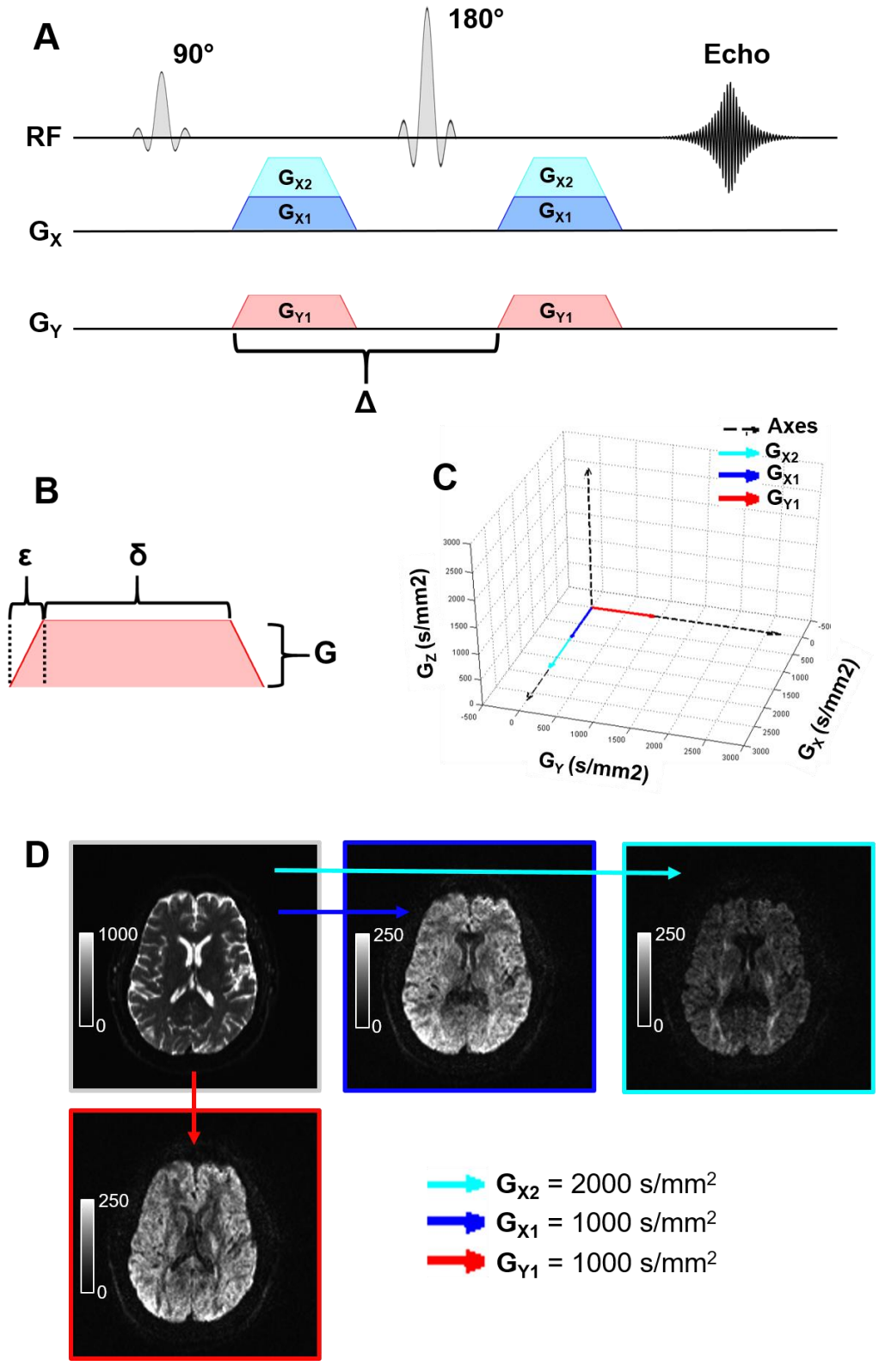

Figure 1.7. Legend presented on next page.

Figure 1.7 Legend: Graphical illustration of diffusion MRI sequence. A) Pulse sequence diagram for spin echo diffusion MRI using trapezoidal diffusion encoding gradients. First line shows 90°- and 180°-degree RF pulses and resultant echo. Second line shows X gradient (G_X), with two different diffusion encodings (G_{X1}, G_{X2}). Third line shows Y gradient (G_Y) with a single diffusion encoding (G_{Y1}). Diffusion time is indicated by Δ. For simplicity, slice encoding, phase encoding, readout, and Z gradients, as well as analog to digital conversion, are not shown. B) Zoomed-in diffusion gradient highlighting measures of interest for computing the b-value of a trapezoidal diffusion encoding gradient: the diffusion encoding gradient strength is G, the rise time is given by ε, and the gradient duration is given by δ. C) Graph of diffusion encoding gradients shown in figure. X-gradients are in same direction, but G_{X2} is twice as strong as G_{X1}. G_{Y1} is the same strength as G_{X1}, but in the Y- versus the X-direction. D) Brain axial non-diffusion weighted (b0, top left) image and diffusion weighted images corresponding to G_{X1} (top center), G_{X2} (top right), and G_{Y1} (bottom left). Signal intensity scale is the same for the diffusion weighted images, but different for the b0 image. G_{X1} image (b-value = 1000 s/mm^2) shows low signal intensity (loss of signal) in corpus callous, in which white matter fibers are oriented along the X-axis, and high signal intensity in the optic tracts in the occipital lobe, which are oriented along the Y-axis, perpendicular to the X-axis; the effect is even more pronounced in the G_{X2} image due to the larger diffusion weighting (b-value = 2000 s/mm^2). GY1 image shows high signal intensity in the corpus callosum and the corticospinal tract (oriented along the Z-axis) and low signal intensity in the optic tracts in the occipital lobe.

Diffusion Tensor Imaging

Diffusivity, *D*, can calculated from **Equation 1.6** by using the signal intensity in the b0 (S_0) and diffusion weighted (*S*) images (DWI). After acquisition of DWIs in a sufficient number of directions (at least 6 non-collinear directions), a tensor fit to the calculated diffusivities in the multiple directions can be performed [145,146]. This tensor fit of the diffusion data takes on the form:

Equation 1.7. $$S = S_0 e^{-b\boldsymbol{D}}$$

where $\boldsymbol{D}$ is a tensor which can be displayed as a 3x3 matrix, which undergo eigenvalue-eigenvector decomposition:

Equation 1.8 $$\boldsymbol{D} = \begin{bmatrix} D_{xx} & D_{xy} & D_{xz} \\ D_{xy} & D_{yy} & D_{yz} \\ D_{zx} & D_{zy} & D_{zz} \end{bmatrix} = \boldsymbol{E} \begin{bmatrix} \lambda_1 & 0 & 0 \\ 0 & \lambda_2 & 0 \\ 0 & 0 & \lambda_3 \end{bmatrix} \boldsymbol{E^T}$$

where $\boldsymbol{E}$ is the orthogonal matrix representing the eigenvectors, and the determinant has the eigenvalues λ_1, λ_2, and λ_3. This model is termed diffusion tensor imaging (DTI). The diffusivities (*D*) can be used for the quantification of the mean amount of diffusion in a voxel via the apparent diffusion coefficient (ADC) or mean diffusivity (MD), which is the average of the three eigenvalues of the diffusion tensor:

Equation 1.9 $$MD = \frac{\lambda_1+\lambda_2+\lambda_3}{3}$$

These measures can reflect tissues microstructure such as the amount of extracellular water. Additional measures can be derived from the diffusion tensor that may be used to infer the degree of directional organization present in the tissue, especially in white matter. These measures include fractional anisotropy (FA):

Equation 1.10 $$FA = \sqrt{\frac{(\lambda_1-\lambda_2)^2-(\lambda_2-\lambda_3)^2-(\lambda_1-\lambda_3)^2}{2(\lambda_1^2+\lambda_2^2+\lambda_3^2)}}$$

which measure the degree to which the diffusion occurring is isotropic (equal in all directions) or anisotropic (preference for diffusion along a particular direction), and the mode of diffusion (MO):

Equation 1.11 $$MO = \frac{\lambda_1\lambda_2\lambda_3}{[((\lambda_1-\lambda_2)^2-(\lambda_2-\lambda_3)^2-(\lambda_1-\lambda_3)^2)/3]^{3/2}}$$

which can be used to examine whether the anisotropy is planar-like (constrained in a single direction while unconstrained in the other two orthogonal directions) or spindle-like (diffusion occurs primarily along the main axis of the tensor) [147].

Diffusion MRI Beyond the Tensor Model

While DTI is widely implemented in the clinical setting, it contains model assumptions that do not hold for all conditions and which may not reflect more complex tissue microstructure. DTI uses a mono-exponential decay fit for the single, clinically-routine, b-values of ~1000 s/mm^2. However, at larger b-values the mono-exponential model can break down as it assesses shorter diffusion distances that are more affected by signal from particles with restricted diffusion [148,149]. While any of the diffusion encoding parameters listed in **Equation 1.6** can be changed to increase the diffusion weighting, usually the diffusion gradient strength, *G*, or the length of the diffusion encoding gradient, *δ,* is changed to achieve these different diffusion weightings [148,149]. The diffusion regimes at which the mono-exponential decay model begins to break down is around b-values of between 1500-2000 s/mm^2 [150]. After this point, additional models of diffusion can be explored, such as multi-exponential or stretched exponential decay models [151], kurtosis models that measure the deviation from Gaussian diffusion [150], and restricted diffusion imaging which

quantifies the density of restricted diffusion relative to free diffusion [152]. While DTI implements a simple ellipsoid model, diffusion in tissue can present with greater complexity in areas with more than one white matter fiber population, such as in regions of crossing fibers [153,154].

Crossing fiber populations can be resolved with more complex models than DTI, such as using multi-tensor instead of a single tensor to model the diffusion in a voxel [155] which operate optimally with b-values of around 2000-3000 s/mm^2 [156]. Other analysis methods of diffusion MRI data that aim to detect crossing fibers involve estimating the orientation distribution function (ODF) of the white matter fibers, which are resolved using higher angular resolution and stronger b-values. These techniques include q-ball imaging [157], in which a single shell of high-angular and high-diffusion weighting is fit using a Funk-Radon transform on the diffusion displacement. These more advanced techniques that model diffusion MRI data may enable a better evaluation of the diffusion characteristics in biological tissue, and as such both DTI and more advanced techniques will be implemented to evaluate possible microstructural alterations associated with symptoms in patients with CSM.

vi. Previous Relevant MRI Research

CSM begins as a degenerative condition of the spine and subsequently develops into chronic spinal cord compression and injury. While only a limited amount of research has been performed in CSM, a much more substantial literature has amassed around traumatic spinal cord injury (SCI), which has a rapid onset caused by blunt force or trauma and requires immediate medical attention. While the disease process is different for acute spinal cord injury and CSM and both conditions present with heterogeneous symptoms and disease courses, nonetheless because of the injury to the spinal cord, acute SCI research is of relevance to CSM. In addition to the

neurological symptoms that are examined with great care in CSM, chronic neck pain is also a crucial issue for the patient's quality of life, and is often overlooked due to being overshadowed by the concern with neurological symptoms. A growing body of research is shedding light on chronic pain conditions, and neuroimaging methods are elucidating important structural and functional alterations in the brains of patients with chronic pain. This research can help in understanding and evaluating chronic pain and related brain changes in patients with CSM. As such, outlined in this section is relevant neuroimaging research in SCI, CSM, and chronic pain. Additionally, advanced imaging of the spinal cord is not yet at the same stage as for the brain, and thus a subsection addressing this discrepancy is also presented.

Neuroimaging of Acute SCI

Traumatic SCI results from blunt trauma to the spinal cord, and can involve serious sequelae and poor prognosis for neurological function [158]. Studies in SCI in both rats and in humans, have shown changes in the spinal cord not only at the site of injury, but also at sites distal from the injury site. In a study comparing patients with SCI to healthy controls, changes in FA and MD were found both at the site of injury, and also in the levels rostral and caudal to the injury [149,159,160], with changes going up to the white matter in the brain [160]. Additionally, in contrast to its role in CSM, measure of spinal cord area have proven useful in evaluating patient, where the primary injury from the blunt force trauma may then lead to secondary injury of continuing damage to neural structures [161]. In this context, the maximal canal compromise (MCC, or measure of greatest tightening of the spinal cord) and maximal spinal cord compromise (MSCC, or the measure of greatest reduced anterior-posterior length in spinal cord) predicted baseline motor scores and MSCC was associated with neurological recovery [162,163]. *The difference in the utility of*

spinal cord compression measures between acute traumatic SCI and CSM points to different pathological states, which are reflected in spinal cord morphological structure in SCI but not in CSM, and highlight a great need to assess chronic spinal cord compression as seen in CSM differently than SCI and the need to find additional biomarkers rostral to the site of injury for patients with CSM.

While resting-state fMRI studies of the spinal cord are still in their infancy and there is a lack of studies evaluating rs-fMRI in clinical populations, there have been some studies that have evaluated rs-fMRI in the spinal cord of primates. One study, conducted by Chen *et al*, evaluated functional connectivity between spinal cord regions in squirrel monkeys and found that there was a significant interhorn connectivity at rest [164]. After unilateral lesioning of the spinal cord at the C5 level, the segments rostral and caudal to the site of injury showed decreased connectivity between spinal cord regions, specifically for the side where the lesion was created, and connectivity was also decreased between the ventral and dorsal portions of the spinal cord at levels away from the site of injury [164]. Based on these very limited results, this dissertation hypothesizes that the intraslice and interslice connectivity of the spinal cord dorsal and ventral horns will be decreased in patients with CSM, and that increasing neurological symptom severity will entail decreasing functional connectivity.

There has also been an increasing interest in the supraspinal alterations that are induced within the sensorimotor network as a response to spinal cord injury, and their influence on disease progression and potential for neurological recovery. These studies have evaluated upstream structural and functional changes within the cerebral cortex and white matter tracts that occur as a result of Wallerian degeneration. Laboratory [165,166] and clinical [167-171] studies have demonstrated that spinal cord injury can induce deleterious cortical alterations ranging from atrophy of

projecting neurons to cell death. Investigations by Freund *et al* [170,171] and Hou *et al* [169] demonstrated that SCI patients had significant cortical atrophy in the primary motor and sensory regions, and that the degree of grey matter loss correlated to functional status. Additionally, Freund *et al* demonstrated altered functional activation in SCI patients, as well as decreased spinal cord area, decreased white matter area in areas of the corticospinal tract, and cortical thinning in the primary sensorimotor areas associated with the controls of the legs [172]. Additionally, functional activation area was increased in SCI subjects for hand-grip task [172]. Grabher *et al* demonstrated degenerative changes in the brain with time after SCI, with both the spinal cord and brain sensory regions showing structural decline [173]. Given these results, permanent structural changes in the brain could serve as a potential barrier to clinical recovery in spite of repair of the local injury site [168].

Resting-state fMRI studies of SCI have yielded varied results in terms of the direction of connectivity, but the relevant brain regions remain similar. For example, a study by Oni-Orisan *et al* showed regions of the sensorimotor cortex as decreased in SCI patients, though connections to the thalamus were significantly increased [174]. In a study by Hou *et al*, the authors observed an increase in functional connectivity between interhemispheric sensorimotor regions such as the primary motor, primary sensory, and supplementary motor areas, as well as the thalamus and cerebellum [175]. Min *et al* also observed an increased functional connectivity between motor areas of the brain such as the primary motor cortex and the supplementary motor cortex, as well as the basal ganglia [176]. In general, functional activation studies have identified multiple regions that showed increased functional activation during motor tasks in SCI subjects. These regions included: the primary motor cortex, the primary sensory cortex, the supplementary motor area, the cingulate motor area, the premotor area, regions of the parietal lobe, cerebellum, and the thalamus and basal

ganglia [177]. *Because of their known role in the sensorimotor network (see* ***Section ii****) and their documented involvement in SCI, these regions constitute the primary brain structures of interest for this study.*

Neuroimaging of Chronic Pain

Chronic pain, in which affected individuals face pain as a constant reality in their lives, is usually defined as pain lasting for longer than 6 months [178], and represents a major burden to the US healthcare system [18]. Chronic pain comes in many different forms. At its most basic level, pain originates from two different sources: constant pain signals originating from painful stimuli at a certain part of the body or pain originating from damaged nerves. These two forms of pain are known as nociceptive and neuropathic, respectively [179]. In addition to these mechanisms involved in acute and chronic pain, the brain and spinal cord play an essential role in the reception, processing, and perception of pain. While chronic pain covers a wide array of conditions, central sensitization, or increased excitation or inhibition of pain pathways in the CNS [180,181], is believed to play a role even in conditions where chronic nociceptive input may be expected, such as in rheumatoid arthritis and osteoarthritis [182]. This is of particular relevance to patients with cervical stenosis, because the neck pain they experience is ostensibly due to arthritic processes in the neck, but in which central sensitization of pain may play a crucial role.

Brain imaging studies in patients with other chronic pain conditions, such as abdominal etiologies, have reported extensive structural and functional changes[183-189]. Taken together, these studies have helped establish a conceptual framework for a common "pain matrix", including regions of the thalamus, insular cortex, cingulate cortex, and the dorsolateral prefrontal cortex (DLPFC)[183,190], consistent with a maladaptive response to recurring pain. Chronic back pain has

been analyzed using various MRI techniques. Resting-state fMRI studies have indicated that the anterior cingulate and precuneus present with altered functional connectivity in chronic back pain patients [191,192]. In addition to the functional changes, consistent patterns of structural changes have been observed in the anterior cingulate and insula [193], the dorsolateral prefrontal cortex and thalamus and anterior cingulate [186], as well as the somatosensory cortex [194]. While less studies have focused white matter changes in chronic pain, emerging results suggest decreasing fiber cohesion with chronic pain as assessed using DTI [195-198]. In addition to the aforementioned studies of neuroimaging in chronic pain conditions where the etiology is either unknown or unclear, studies have also evaluated the relationship between neuroimaging measures of the CNS and pain in patients with SCI. A study by Jutzeler *et al,* SCI patients with chronic pain exhibited decreased cord area and reduced gray matter of the anterior cingulate, insula, and somatosensory cortex, and thalamus, as well as reduced white matter in regions of the corticospinal tract [199].

Neck pain has been largely understudied in CSM patients, and thus a goal of this investigation was to obtain a better understanding of the supraspinal response to neck pain that occurs in patients with cervical spondylosis and myelopathy.

Neuroimaging of CSM

While anatomical measures of spinal cord compression in CSM has shown only weak correlations with symptoms, recent studies of diffusion MRI in the spinal cord have shown great promise by demonstrating a strong relationship between DTI measures in the cord, FA and MD, with patient symptoms. A recent meta-analysis revealed decreases in FA and increased ADC at the site of compression, and a decrease in FA at the site of C2-C3 [200], which indicates that microstructural alterations can occur rostrally along the spinal cord, affecting levels above the site

of compression. Another study showed that DTI metrics were correlated with modified Japanese Orthopedic Association (mJOA) scores and were able to differentiate between asymptomatic, mild, and moderate-to-severe CSM [201]. Studies using region- or tract- specific measures of microstructure in CSM patients have also been performed. Wen *et al* found different microstructural alterations in CSM patients depending on the white matter fiber tract: posterior (sensory) and lateral (motor) white matter regions presented with more drastic drop in FA, while the anterior white matter was relatively spared, suggesting that these regions are differentially affected by compression [202]. *Since changes in spinal cord microstructure in CSM patients have been shown to correlate with symptoms and these changes affect regions proximal and distal to the site of compression, this dissertation hypothesizes this may translate to altered structure, microstructure, and function, rostrally along the corticospinal tract.*

Comparatively less is known about the supraspinal alterations that occur as a result of chronic spinal cord injury associated with cervical disc disease. Unique patterns of functional activation have been observed in CSM patients using task-based functional magnetic resonance imaging (fMRI), with larger areas of activation observed in patients during simple motor tasks, such as dorsiflexion of the ankle and extension of the wrist, when compared to healthy control (HC) subjects. As with acute traumatic SCI patients, it is believed that this recruitment of other cortical areas is a compensatory mechanism designed to maintain neurological function in the face of diminished efferent and afferent connections. After surgery, these same patients displayed a smaller area of activation which correlated with neurological improvement, and was comparable to the area of activation for the same task in HC subjects [203,204]. In another study of brain functional activity in CSM subjects, 12 CSM patients and 10 controls underwent a finger-tapping experiment, and the activation in the precentral gyrus (motor) and postcentral gyrus (sensory) were evaluated,

with an increased activation volume in motor, and a decreased activation volume in sensory cortex for CSM patients; after surgical decompression, volumes of activation increased for both gyri [205]. Other studies of fMRI functional activation in CSM patients found increased activation not only in the primary sensorimotor cortex, but in supplementary brain areas as well, including the supplementary motor area, the anterior cingulate, the thalamus, basal ganglia, and cerebellum [206,207]. This well documented change in task fMRI of motor movements in CSM patients indicates altered motor processing and recruitment of more extensive cortical areas to perform motor tasks, and a change in these areas in some patients after decompression of the spinal cord via surgery. Resting state fMRI studies have shown altered functional connectivity in CSM patients compared to HC subjects, with CSM patients displaying an increased connectivity between premotor and sensory areas [208] and across thalamo-cortical circuits [209].

While many studies of CSM have been more focused on the functional activation alterations associated with this disorder, structural and microstructural changes that may be occurring in CSM are also of interest. Additionally, functional changes may extend beyond the primary motor areas that have been probed in previous fMRI studies in CSM, thus resting-state fMRI connectivity may help pinpoint these regions.

Advanced MRI of the Spinal Cord

While advanced MRI studies of the brain, including high-resolution structural, diffusion, and resting-state functional MRI scans, have become commonplace and been implemented in multicenter clinical trials and studies [210,211], this is not yet the case for the spinal cord, which presents as a more difficult site to image due to its reduced size (approximately 7mm in sagittal diameter and 12mm in transverse diameter) [66], increased motion and physiological noise, and

magnetic field inhomogeneities [212]. However, improvements in MRI scanner and sequence technology, such as tailored functional and diffusion MRI scans [212], and in postprocessing tools, such as the Spinal Cord Toolbox (SCT) [101], are beginning to allow more precise and standardized methods of evaluating structural, diffusion, and functional MRI of the spinal cord. Thus, while more difficult to image than the brain, the role of the spinal cord in neurobiological processes that are related to patient symptoms makes this and future studies an important contribution to our understanding of the disease processes in spinal cord injuries and CSM. As such, this dissertation sought to include the spinal cord in scans of the brain, using a large field of view for the structural scan, and high acceleration factors for diffusion and functional MRI [213], in order to acquire high spatial and temporal resolution data.

vii. Objectives

The main objective of this dissertation was to examine changes in both the spinal cord at the site of injury, as well as changes occurring rostrally in the CNS, with respect to neurological and pain symptoms in CSM patients. The technique used to achieve this objective was to extend a traditional paradigm used in brain imaging, namely the combination of structural T1, resting-state fMRI, and diffusion MRI, to incorporate the spinal cord as well. A sketch and description of the proposed protocol is listed in **Table 1.2**. The protocol was added immediately prior to the clinical scan of the patients with CS, and healthy volunteers were recruited to undergo this protocol as research participants.

Table 1.2. Description of proposed imaging paradigm for use in this dissertation.

Proposed Imaging	**Description and Purpose**	**Time**
3D Structural T1 of Brain and Spinal Cord	High-resolution 3D anatomical image for reference and for segmentation of cortex and spinal cord. Used as a common anatomical space between modalities and will assist in selecting regions of interest for the other modalities.	6:30
Simultaneous Brain and Spinal Cord fMRI	Multiband and parallel imaging accelerated fMRI for high resolution coverage of both brain and spinal cord in each time point. High in-plane resolution to better capture spinal cord fMRI activity	10:00
Brain diffusion MRI	Multiband accelerated diffusion MRI of the brain down to C2-C3 for probabilistic tractography along corticospinal tract and for connectivity between regions.	8:00
	Total time of Protocol	25 min

The acquired neuroimaging MRI data was used to test the specific hypotheses listed below:

1. Subjects with cervical stenosis would present with degenerative brain changes with respect to symptom severity. These would include:
    a. Structural alterations with worsening symptoms. Specifically:
        i. Decreased cortical thickness of the cortical primary motor and sensory areas, and decreased volume of the thalamus and basal ganglia, with worsening neurological symptoms (mJOA score).
        ii. Decreased cortical thickness in the pain-related regions of the anterior cingulate, insula, dorsolateral prefrontal cortex, and decreased volume of the thalamus and basal ganglia, with worsening neck pain (NDI).
    b. Functional alterations with worsening symptoms. Specifically:

i. Increased functional connectivity between sensorimotor regions with worsening neurological symptoms (mJOA).

ii. Increased functional connectivity between pain matrix regions with worsening neck pain (NDI).

c. Microstructural alterations with worsening symptoms. Specifically:

i. Decreased FA and increased MD in the brain in sensorimotor-related tracts along the corticospinal tract with worsening neurological symptoms (mJOA).

ii. Decreased FA and increased MD in the brain in pain-related tracts such as the cingulum bundle and the anterior thalamic radiation with worsening neck pain (NDI).

2. Spinal cord structural (morphological) measures would present with large differences between CS and HC subjects, but would show little or no association with the clinical symptom variables. On the other hand, spinal cord microstructural measures (anisotropy and mean diffusivity) would show associations with clinical symptoms:

a. Spinal cord cross sectional area would be lower in CS patients compared to HC, but would not correlate with neurological or neck pain symptoms.

b. Functional connectivity near the site of injury, both within the same vertebral level and across vertebral levels, would decrease with worsening neurological symptoms.

c. Diffusion metrics at the site of injury and at the C2 level would be associated with worsening symptoms. Specifically:

i. Decreased FA and increased MD with worsening neurological symptoms.

In addition to testing the above hypotheses, this dissertation also explored the relationship between the spinal cord clinical measure, The MRI-equivalent Torg Ratio, and the advanced MRI measures of the brain and spinal cord proposed.

Chapter II. Structural MRI and Atrophy of the Neuraxis in Patients with Cervical Stenosis and Associated Myelopathy

Aging of the spine and intervertebral discs can cause a tightening of the spinal canal, a common occurrence in elderly populations [1]. This chronic tightening of the spinal canal in the neck is called cervical stenosis (CS), and this cervical stenosis can begin to cause chronic compression of the spinal cord which can entail neurological symptoms such as difficulty walking, difficulty with fine manual tasks, and sensory disturbances. CS with resulting neurological symptoms is termed cervical spondylotic myelopathy (CSM) [1,2]. However, not all patients who have compression of the spinal cord have symptoms, and findings on clinical magnetic resonance imaging (MRI) scans have shown only a weak correlation with symptom severity. However, in addition to the injury in the spinal cord, the brain has been associated with the CSM disease process [204].

In this chapter, the structure of the brain and spinal cord was examined in patients with CS and in healthy control (HC) subjects to evaluate whether structural changes were occurring in other portions of the central nervous system, namely the rostral uncompressed spinal cord and the brain, and if these changes were associated with the patient symptom severity, such as neurological status as assessed by the modified Japanese Orthopedic Association (mJOA) score, and neck pain as assessed by the neck disability index (NDI). The main neuroimaging measures of interest for the structure of the brain and spinal cord were: cortical thickness or the mean thickness of the gray matter layer in the cortex, the volume of subcortical structures for the brain, and cross-sectional area of the spinal cord. Clinically-used measures of compression in the spinal cord, such as the MR-equivalent Torg Ratio and the midsagittal diameter of the cord at the site of maximal compression, for the spinal cord, were also examined.

i. Structural MRI Acquisition and Processing

Subject Population

For this chapter, all CS patient and healthy control (HC) data were used, with the demographics for the different groups outlined in **Table A.1** in the **Appendix** section. Briefly, patient data consisted of 26 patients with at least moderate stenosis with or without myelopathy, that underwent a research brain and spinal cord MRI protocol. A set of 17 HC subjects underwent the same protocol, and an additional 28 HC subjects were queried from the Pain and Interoception Imaging Network (PAIN) Repository, (http://uclacns.org/programpain-research-program/pain-repository/) maintained by the UCLA Center for the Neurobiology of Stress and Resilience [214]. These subjects had a similar T1 MRI acquisition, but only brain scans. Demographic information for the subgroups used for analyses are outlined in **Table 2.1**.

Table 2.1. CS patients and HC subjects cohort demographics.

Subject Population	N	Age (mean years +/- SD)	Sex	BMI (mean +/- SD)	mJOA (mean +/- SD)	NDI (mean +/- SD)
CS Patients (Brain + Spine)	26	59 ± 11 years	20M / 6F	27.2 ± 6.7	15.4 ± 2.8	10.6 ± 10
All HC Subjects (Brain)	45	46 ± 10 years	32M / 13F	26.2 ± 4.8	18	
HC Subgroup (Brain + Spine)	17	41 ± 13 years	11M / 6F	26.2 ± 3.0	18	

MRI Acquisition

High-resolution 3D T1-weighted structural magnetic resonance images (MRIs) were acquired on a 3T MR scanner (*Siemens Prisma or Trio; Siemens Healthcare, Erlangen, Germany*) using a 3D magnetization-prepared rapid gradient-echo (MPRAGE) sequence in either the coronal, sagittal, or axial orientation, a repetition time (TR) of 2300-2500ms, an echo time (TE) of 2-3ms, an inversion time (TI) of 900-945ms, a flip angle of 9°, and a field-of-view (FOV) and matrix size chosen for $1mm^3$ isotropic voxel size. For CS patients and the HC that underwent identical T1w structural scanning, the coronal sequence was acquired with a 350mm FOV, and a phase encode matrix size of 178 for 178mm. This protocol provided complete coverage of both brain and spinal cord down to at least the C7 vertebral level (location of C8 spinal cord level, end of cervical spinal levels) for all subjects scanned. Coronal orientation was chosen to enable phase oversampling in the x-direction (left-right), set at 25-50% depending on patient size to avoid aliasing artifacts in the shoulder region. CS patients also underwent routine clinical MRI of the spine, including T2w anatomical axial and sagittal scans. These anatomical spine scans were used to measure the anterior-posterior spinal canal diameter at the site with the largest extent of compression, to measure an MRI version of the Torg-Pavlov ratio [34], and to record the presence of T2 hyperintensity in the cord.

Brain Image Processing and Analysis

Cortical segmentation and computation of cortical thickness was performed using FreeSurfer (https://surfer.nmr.mgh.harvard.edu/fswiki) [82,83,89]. Cortical thickness is defined as the distance between the pial and white matter surfaces, and was calculated from the T1 images. Processed brain surfaces were smoothed with a full-width half-maximum (FWHM) of 10mm then

registered to a standard space. Evaluation of the associations of neuroimaging measures with mJOA scores were performed in the combined group of HC subjects and CS patients. When examining NDI, HC subjects were excluded from the analyses. Age was included as a covariate in all analyses. The vertex-wise level of significance was set at $P<0.05$, with multiple comparisons correction performed by using Monte Carlo permutations [215] with a significance level of $P<0.05$.

Additionally, multiple linear regression analyses were performed in regions identified by FreeSurfer along with pre- and post-central gyrii for the mean cortical thickness in the corresponding region in the Desikan-Killiany-Tourville (DKT) cortical atlas [216], with symptom scores (NDI or mJOA) used as the covariates of interest. Because of the large age range in this study and because of the prominent effect of cortical thinning with age, age was used as a covariate in these analyses. Since cortical thickness has a predominantly linear relation to age [89-91], a linear model is suitable to account for age even with large age ranges in the groups. The relationship between cortical thickness of the anterior cingulate cortex, insular cortex, DLPFC (rostral middle frontal gyrus in the DKT atlas) and NDI scores was examined. The relationship between age, mJOA, and cortical thickness, was also examined within a subset of Brodmann areas (BA) consisting of the primary sensory (BAs 3a, 3b, 1, 2) and primary motor (BAs 4a, 4p) regions [217].

Exploratory analysis was performed to visualize the organization of the motor and sensory strips by quantifying thickness on the unsmoothed brain surfaces in sequential 10mm segments along the primary motor and primary sensory BAs. For the sequential 10mm segments along the motor and sensory strips, the coordinates of the bilateral Brodmann areas 3a, 3b, 1, 2, 4a, and 4p, provided in the FreeSurfer package, were imported into MATLAB (https://www.mathworks.com/). For all BAs areas except BA4a the fully thresholded labels were used; for the left hemisphere BA4a the thresholded label only included a small region on the medial

aspect of the lobe, and thus did not cover the cortical topography necessary along the precentral gyrus. This being the case, a less stringently thresholded version of the data (25%) was used for the mapping of the 10mm segments for both the left (**Figure 2.1.A**) and right hemisphere BA4a regions. Once imported into MATLAB, the points were collapsed onto both the 2D plane of their x- and y-components and onto the 2D plane of their x- and z- components, and locally weighted scatterplot smoothing (LOWESS) regression with a smoothing window of 10 was used to compute a representative line in x-y and x-z planes. Then the y- and z- components were combined with the x- coordinates to form a representative line in 3D space (**Figure 2.1.B**). The line was defined as starting at the most lateral portion along x-, and every 10mm along the length of the line in 3D space a plane perpendicular to the line was computed and the points that were within two consecutive planes were defined as one 10mm segment (**Figure 2.1.C**). Then the 10mm segments for each BA were imported to FreeSurfer (**Figure 2.1.D**) and used to extract mean cortical thickness measures for each subject using their unsmoothed registered cortical surfaces. For the analyses across the 10mm segments of the primary sensorimotor BAs, a two-way analysis of variance (ANOVA) was computed for each BA with group and segment distance as factors, as well as Sidak-Holm [218,219] multiple comparisons corrected tests of the difference between groups in mean cortical thickness at each segment. Additionally, Pearson's correlation coefficients between thickness and mJOA (for combined CS and HC group) and NDI (for subset of CS group with NDI scores) were calculated for the 10mm segments with Sidak-Holm multiple comparisons corrections within each BA.

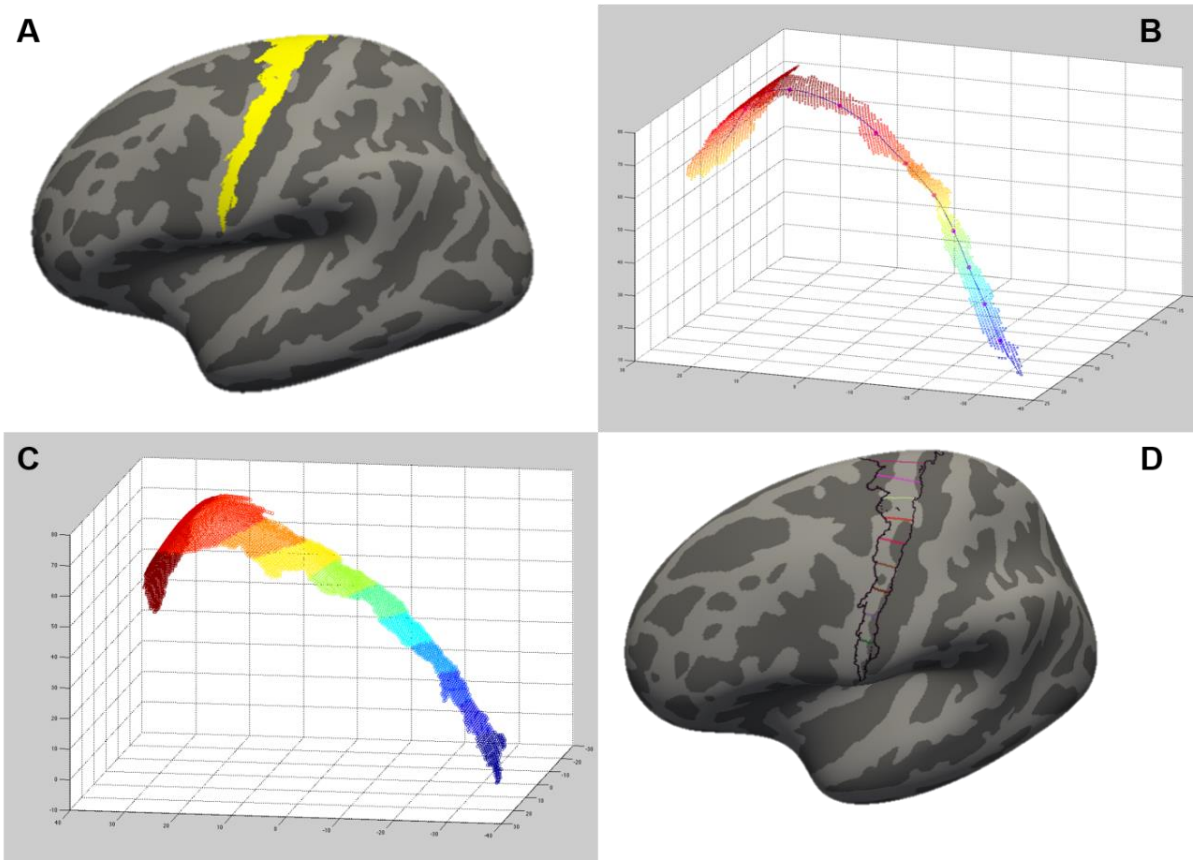

Figure 2.1. Processing of 10mm segments along motor strip. Left hemisphere BA4a is shown in A). In B) the surface coordinates of BA4a are shown along with the representative line traversing through the surface and the points in purple marking the 10mm marks along the line. The color-coded segmented surface coordinates are shown in C), and the resulting divisions of ROIs on the reference cortical surface map are shown in D).

Lastly, the volume of subcortical regions involved in sensory and motor processing, namely the thalamus, caudate, putamen, and pallidum [220] were also evaluated via multiple linear regression, with age and the respective symptom score (NDI or mJOA) as covariates, as these regions are crucial in relaying sensory information (thalamo-cortical loop) as well as in processing sensory and motor commands (cortico-basal ganglia-thalamo-cortical loop). In order to compare

with results of previous studies in a normal sample of the population, linear regression of whole-brain mean cortical thickness with age was also performed in both the CS and HC cohorts, and the resulting slopes of the regression lines were output and contrasted with the results from previous studies that employed a similar methodology [91].

Spinal Cord Image Processing and Analysis

Spinal cord images were processed using the Spinal Cord Toolbox (SCT) software package (https://sourceforge.net/projects/spinalcordtoolbox/) [101], a tool that leverages spinal cord anatomy and symmetry across inferior-superior and left-right axes along with anatomical templates to segment and register spinal cord anatomical images, and perform post-processing for advanced MRI sequences like functional and diffusion MRI of the spinal cord. The structural MRI was processed by isolating the spinal cord section of the images apart from the brain by taking the slice near the superior portion of the C1 vertebra on a midsagittal slice, preserving all the images below that slice as the MRI of the spinal cord. This separation of the spinal cord portion of the MRI scan was done in order to process the scans using the SCT pipelines (which are not designed to handle brain images) and to improve the accuracy of the results by avoiding any potential issues that structures superior to the spinal cord that may cause for the SCT algorithms.

Because patients with CS present with deformations of the spinal canal and spinal cord, in order to increase the robustness of the spinal cord segmentation algorithm the following steps were implemented, and outline in **Figure 2.2**: i) the center of the spinal cord was labeled at every level to provide priors for the segmentation algorithm **(Figure 2.2.B)**; ii) a spinal cord segmentation using the SCT defaults was run to get an initial estimate of location; iii) the spinal cord was smoothed along a regularized inferior-superior axis (an axis that follows the inferior-superior

spinal cord geometry and thus bends at portions where the spine bends) with a Gaussian kernel with FWHM of 5mm **(Figure 2.2.C)**; iv) the spinal cord was segmented on the smoothed image using the labels at the center of the spinal cord (drawn in step i) as priors **(Figure 2.2.D)**. The segmentation was then reviewed visually for accuracy, and if the segmentation was not deemed successful the pipeline was rerun with different smoothing (0mm-10mm) or spinal cord radius length (radius 4 - 5.5mm) initialization parameters. The spinal cord was then labeled by vertebral level using SCT **(Figure 2.2.E)**, either initialized by the z-location of the C2/C3 intervertebral disc, or using another cervical intervertebral disc if the C2/C3 initialization did not correctly label all cervical vertebral levels. Finally, the cervical cross-sectional area (CSA, mm^2) was computed at each slice, and the mean for each vertebral-labeled spinal cord section was output.

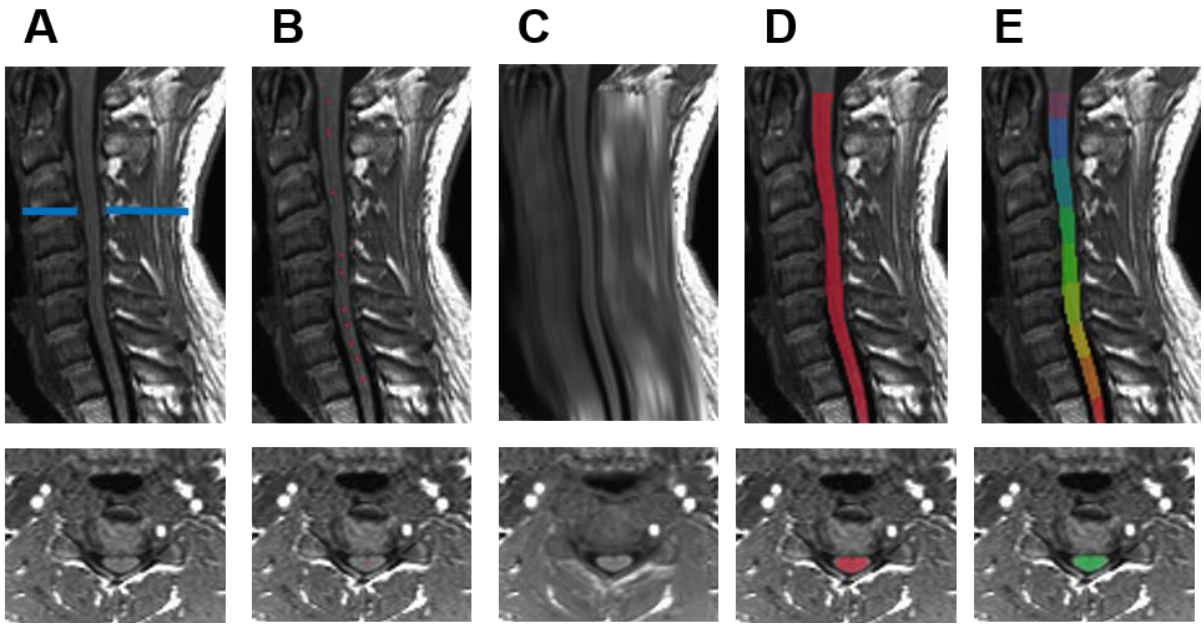

Figure 2.2. Processing steps for spinal cord segmentation and labeling by vertebral level. A) Sagittal slice (top row) showing the spinal cord and surrounding anatomy and indicating the level (blue line) of axial slices (bottom row) shown. B) Manually labeled center of spinal cord, used as priors for spinal cord position. C) Smoothing of spinal cord along regularized z-axis. D) Segmentation of spinal cord. E) Labeling of spinal cord by vertebral levels from C1 (top, purple) to C9 (bottom, red).

The difference between the CSA of the spinal cord of CS patients and HC subjects at each vertebral level was evaluated using a two-way ANOVA with level (cervical levels 2-7, and thoracic level 1) and group (CS vs HC) as factors, and individual T-tests were performed for each level. An overall smaller SC CSA was expected in CS patients, and greater group differences in SC CSA from HC subjects in the cervical levels that presented the most often with stenosis (C3, C4, C5, C6). The linear regression of SC CSA and age between CS and HC groups was also examined, similar to the relevant brain analysis mentioned above. For the SC CSA-age regression

comparison, the C2 and C7 vertebral levels were selected as sites of comparison, because most patients had maximal compression at C3-C4, C4-C5, or C5-C6 intervertebral discs. In addition to this, the spinal cord at the C2 level was more reliably segmented by the SCT pipeline than the spinal cord at the C1 level, and C7 represents the end of the cervical spinal cord levels. The relationships between the spinal cord measures were examined by performing Pearson's correlations across the different spinal cord measures of interest: spinal cord diameter at site of maximal compression, MRI-equivalent Torg Ratio, and CSA at the C2, C7, and maximal compression vertebral levels. For the relationship between symptom variables (mJOA and NDI) and the spinal cord measures, Pearson's correlations with mJOA and multiple linear regression accounting for age with respect to each of the spinal cord measures of interest, were calculated.

Combined Brain and Spinal Cord Analyses

Associations between spinal cord and brain structural measures were also examined. The spinal cord measures of interest and age were used as covariates against cortical thickness in FreeSurfer and followed a similar process as the one outlined for the analyses of symptom variables (mJOA and NDI) with respect to cortical thickness as listed previously. Additional analyses of the various spinal cord measures were also performed of the mean cortical thickness of any regions of the cortex that showed a relationship in the aforementioned analysis, as well as between the volume of subcortical structures, via multiple linear regression accounting for age.

Software and Statistical Analyses

All brain cortical thickness computation, segmentation of subcortical and cortical regions, and general linear models of vertex-wise cortical thickness with symptom variables were

performed using FreeSurfer (Version 5.3.0, https://surfer.nmr.mgh.harvard.edu/fswiki), while MATLAB (MATLAB Version 2014a, https://www.mathworks.com/) was used for segmentation and computation of mean cortical thickness of 10mm segments across the primary sensorimotor BAs. All spinal cord CSA computation and segmentation was performed using Spinal Cord Toolbox (SCT v3.0.3, https://sourceforge.net/projects/spinalcordtoolbox/). Statistical analyses were performed using GraphPad Prism (Version 7.0b, La Jolla California USA, www.graphpad.com), and multiple linear regression was performed in Free Statistics Software (Version 1.1.23-r7, http://www.wessa.net/rwasp_multipleregression.wasp/).

ii. Structural Brain Changes with Neurological and Pain Symptoms

Association Between Cortical Thickness, Subcortical Volume and Neurological Function

Results from the current study demonstrate decreasing cortical thickness in several brain regions with increasing neurological deficits and pain severity while accounting for age and including both CS and HCs. **Figure 2.3** highlights results from vertex-wise correlations with mJOA score, for which there were significantly positively correlated regions (decreasing cortical thickness with decreasing mJOA, *i.e.* worse neurological score) in the left superior frontal lobe (**Figure 2.3;** *Region 2.3.b*) and in a region extending across the right superior frontal lobe and the caudal aspect of the right anterior cingulate (**Figure 2.3;** *Region 2.3.c*). Additionally, increasing cortical thickness with increasing mJOA, bilaterally, within the precuneus was also observed (**Figure 2.3;** *Regions 2.3.a, 2.3.d*). Evaluation of cortical thickness bilaterally within the precuneus, superior frontal lobe, caudal anterior caudate, and pre- and post-central gyrii using multiple linear regression resulted in an observed association with both mJOA and age (**Table 2.3**). In addition to the cortical regions, significant positive association between the volume of the

putamen and both mJOA and age was observed (*Multiple Linear Regression*, R^2=0.45 for the left, and R^2=0.49 for the right putamen). Additionally, for the BA ROIs only the left and right primary motor regions (BA4a and BA4p) mean cortical thicknesses were found to have significant associations with mJOA after accounting for age (**Table 2.2**).

Table 2.2. Multiple Linear Regression of Mean Cortical Thickness and Subcortical Volume with mJOA and Age. LH and RH are left and right hemisphere, Sup. denotes Superior.

Measure	Region	mJOA	mJOA P-Val	Age	Age P-Val	R^2	Adj. R^2	Overall Model P-Val
Cortical Thickness	LH Precuneus	0.019	0.04	-0.0045	0.005	0.2214	0.1988	0.0002
	LH Sup. Frontal	0.020	0.04	-0.0030	0.09	0.1403	0.115	0.006
	RH Precuneus	0.032	0.001	-0.005	0.001	0.3418	0.3224	<0.0001
	RH Sup. Frontal	0.032	0.001	0.0002	0.9	0.164	0.1394	0.002
Subcortical Volume	LH Putamen	145	0.0008	-36	<0.0001	0.4483	0.4321	<0.0001
	RH Putamen	130	0.0005	-35	<0.0001	0.4903	0.4753	<0.0001

Table 2.3. Multiple Linear Regressions of Mean Cortical Thickness with mJOA and Age for primary sensorimotor Brodmann areas (BA). LH and RH are left and right hemisphere.

Region	mJOA	mJOA P-Val	Age	Age P-Val	R^2	Adj. R^2	Overall Model P-Val
LH BA4a	0.034	0.02	-0.0065	0.01	0.2189	0.1959	0.0002
LH BA4p	0.039	0.02	-0.0007	0.8	0.0931	0.0664	0.04
RH BA4a	0.037	0.04	-0.0026	0.4	0.099	0.0725	0.03
RH BA4p	0.041	0.01	0.00037	0.9	0.3202	0.1025	0.03

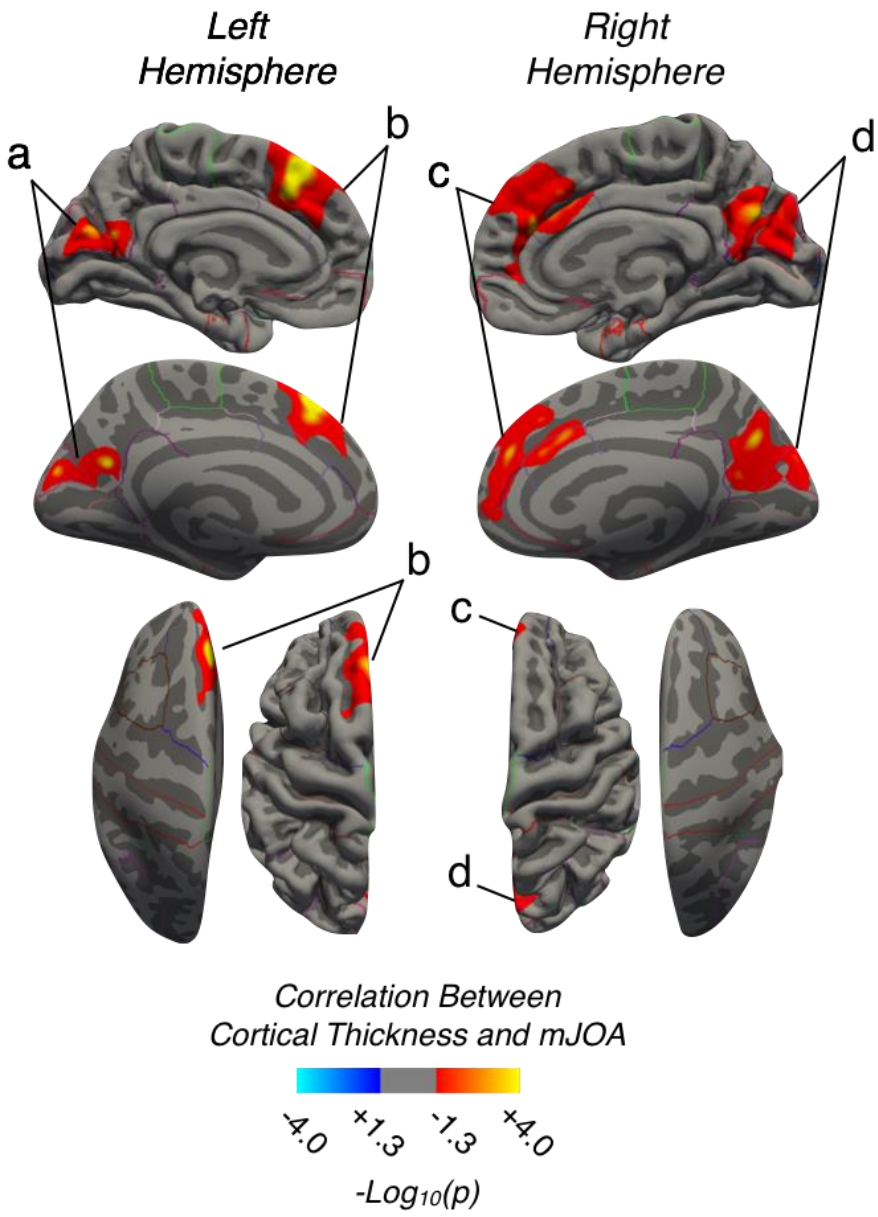

Figure 2.3. Regions demonstrating a strong association between cortical thickness and mJOA in patients with cervical spondylosis (CS) and healthy controls (HC). Red-Yellow denotes increasing cortical thickness with increasing mJOA score (better neurological function). Regions with significant associations were identified in a) left precuneus and cuneus, b) left superior frontal lobe, c) right superior frontal lobe extending into the anterior cingulate, and d) right precuneus and cuneus.

Examination of patients with CS exclusively (N=26; excluding HCs) uncovered similar reductions in cortical thickness within the superior frontal lobe, but thinning within the precuneus was no longer associated with decreased mJOA score (**Figure 2.4**). Multiple linear regression (**Table 2.4**) confirmed the reduction in cortical thickness with decreasing mJOA in right superior frontal lobe (P=0.03) after accounting for clinical variables. The volume of the left and right putamen also remained significant predictors of mJOA.

Table 2.4. Multiple Linear Regression of Cortical Thickness and Subcortical Volume with mJOA and Age, in the CS group only. LH and RH are left and right hemisphere, Sup. is Superior.

Measure	Region	mJOA	mJOA P-val	Age	Age P-val	R^2	Adj. R^2	Overall Model P-Val
Cortical Thickness	LH Precuneus	0.021	0.01	-0.0097	0.008	0.3451	0.2882	0.008
	LH Sup. Frontal	0.016	0.02	-0.0021	0.5	0.0936	0.0148	0.03
	RH Precuneus	0.024	0.06	-0.0088	0.01	0.3474	0.2906	0.007
	RH Sup. Frontal	0.030	0.03	0.00076	0.8	0.1807	0.1095	0.1
Subcortical Volume	LH Putamen	100	0.03	-41	0.003	0.43	0.38	0.001
	RH Putamen	107	0.01	-29	0.01	0.413	0.3619	0.002

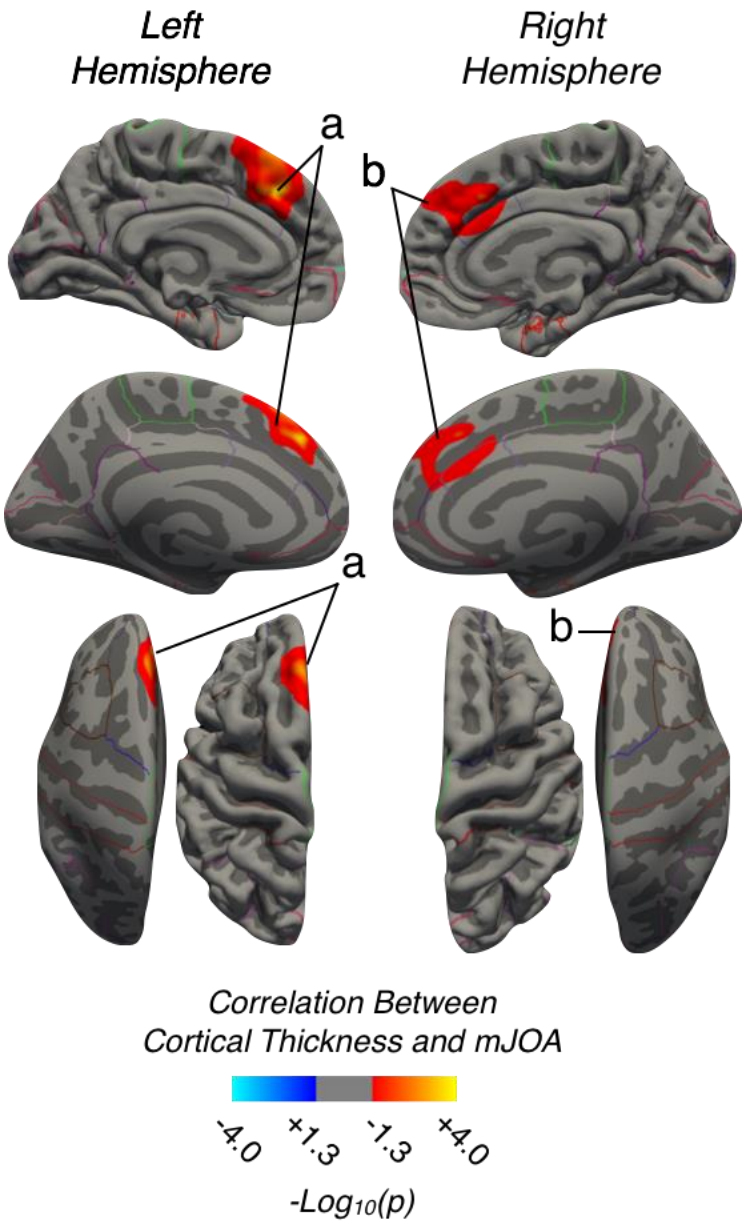

Figure 2.4. Regions demonstrating a strong association between cortical thickness and mJOA within in patients with cervical spondylosis (CS) (excluding healthy controls). First row displays inflated cortical surfaces, second row displays pial cortical surfaces. Red-Yellow denotes increasing cortical thickness with increasing mJOA score (better neurological function) within CS patients. The significant clusters were identified in the a) left and b) right superior frontal lobe extending into the anterior cingulate.

Association Between Cortical Thickness, Subcortical Volume and Neck Pain

Consistent with trends observed in overall neurological status, results also confirmed a significant association between cortical thickness and NDI while accounting for age, as illustrated in **Figure 2.5**. In particular, results indicated a decreasing cortical thickness with increasing NDI (*i.e.* worse neck pain) in the left and right precuneus (**Figure 2.5;** *Regions 2.5.a and 2.5.d*), as well as the left superior frontal lobe (**Figure 2.5;** *Region 2.5.b*), and a region extending across the superior frontal and the caudal and rostral portions of the right anterior cingulate cortex (**Figure 2.5;** *Region 2.5.c*). When accounting for age, bilateral regions of the precuneus, right insula, right superior frontal gyrus, and the rostral and caudal aspects of the right anterior cingulate were all found to be associated with NDI (**Table 2.5**).

Table 2.5. Multiple Linear Regressions of Mean Cortical Thickness and Subcortical Volume with NDI and Age. LH and RH are left and right hemisphere, Sup. denotes Superior, Rost. denotes Rostral, Ant. denotes Anterior.

Measure	Region	NDI	NDI P-Val	Age	Age P-Val	R^2	Adj. R^2	Overall Model P-Val
Cortical Thickness	LH Precuneus	-0.012	0.0008	-0.014	0.0001	0.5934	0.5528	0.0001
	LH Insula	-0.0095	0.01	-0.018	<0.0001	0.6098	0.5708	<0.0001
	RH Caud. Ant. Cingulate	-0.021	0.003	0.0007	0.9	0.3954	0.3349	0.007
	RH Precuneus	-0.012	0.0009	-0.013	0.0002	0.5739	0.5313	0.0002
	RH Rost. Ant. Cingulate	-0.015	0.002	0.0014	0.7	0.4237	0.366	0.004
	RH Sup. Frontal	-0.012	0.004	-0.0041	0.3	0.3524	0.2877	0.01
Subcortical Volume	LH Putamen	-36	0.01	-54	0.0003	0.5122	0.4634	0.0008
	RH Putamen	-38	0.0008	-45	0.001	0.5856	0.5441	0.0001

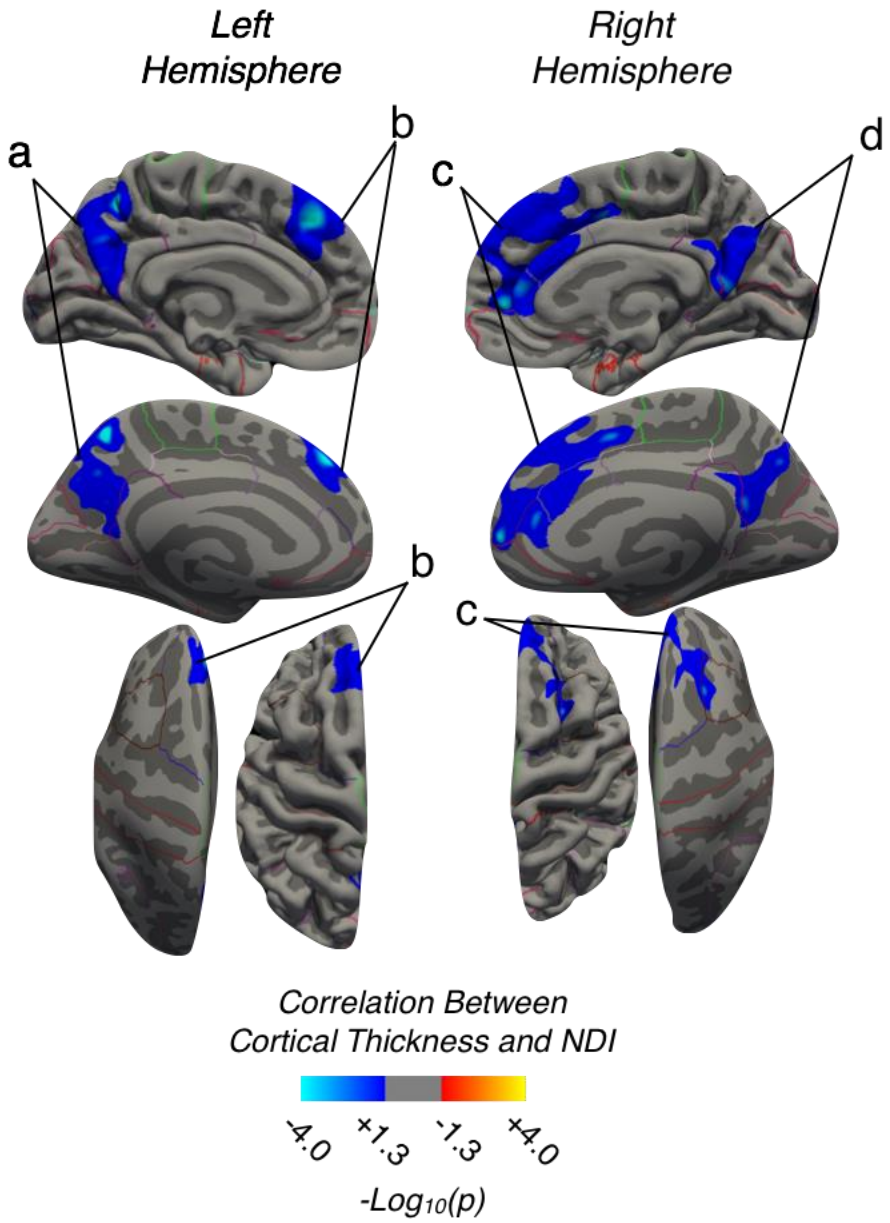

Figure 2.5. Regions demonstrating a strong association between cortical thickness and NDI in patients with cervical spondylosis (CS). Blue-Light Blue denotes decreasing cortical thickness with increasing NDI score (worse neck disability) in CS. Regions with significant associations were identified in a) left precuneus, b) left superior frontal lobe, c) right superior frontal lobe extending into the cingulate, and d) right precuneus.

In order to better assess the location of the changes in the superior frontal lobe, which is a functionally and citoarchitectonically diverse region, a Brodmann area atlas retrieved from the MRIcro software package (http://www.cabiatl.com/mricro/mricro/lesion.html) was superimposed on the standardized brain image. While this is only an approximation of the Brodmann areas, and in reality these regions vary from subject to subject, they assist in estimating the potential Brodmann areas that may be associated with the seen cortical thickness changes with symptoms, as seen in **Figure 2.6**.

Changes in Primary Sensory and Motor Cortical Thickness

Examination of cortical thickness across sensory and motor strips indicated a strong association between thickness in BA3a and mJOA at multiple segments as well as greater mean difference in cortical thickness between CS and HC groups (**Figure** for primary sensory, **2.7** and **Figure 2.8** for primary motor). Both primary motor areas examined (BA4a and BA4p) demonstrated spatially varying and strong relationships between mJOA scores and mean cortical thickness, though generally there was no significant mean cortical thickness differences between CS and HC groups. When looking at the group factor for the two-way ANOVA, most BA showed a significant group effect, meaning that while the differences at each segment were small the general trend for lower thickness across the region in CS patients was still significant. For NDI, none of these analyses reached the threshold for statistical significance, potentially due to lack of statistical power from a slightly smaller cohort of subjects with NDI scores.

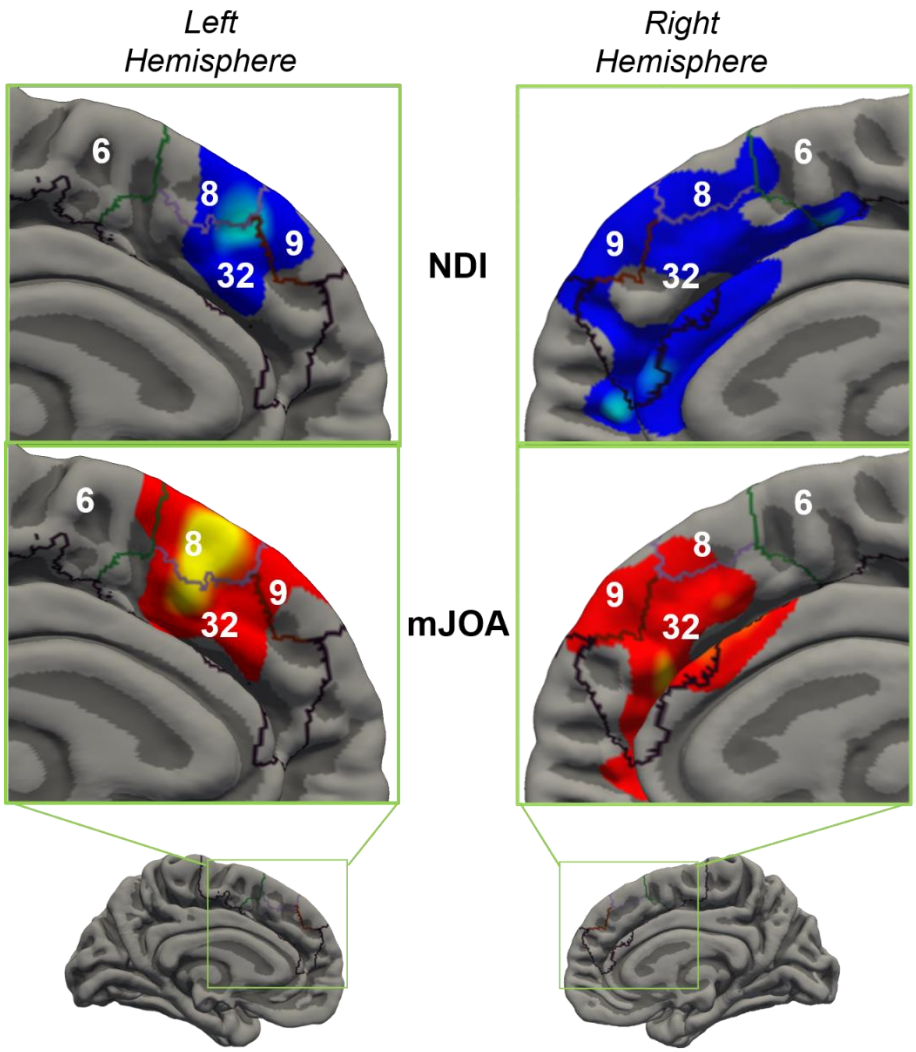

Figure 2.6. Zoomed-in mJOA (from **Figure 2.3**) and NDI (from **Figure 2.5**) cortical thickness correlations in the superior frontal lobe, with Brodmann areas 6, 8, 9, and 32, outlined on the surfaces.

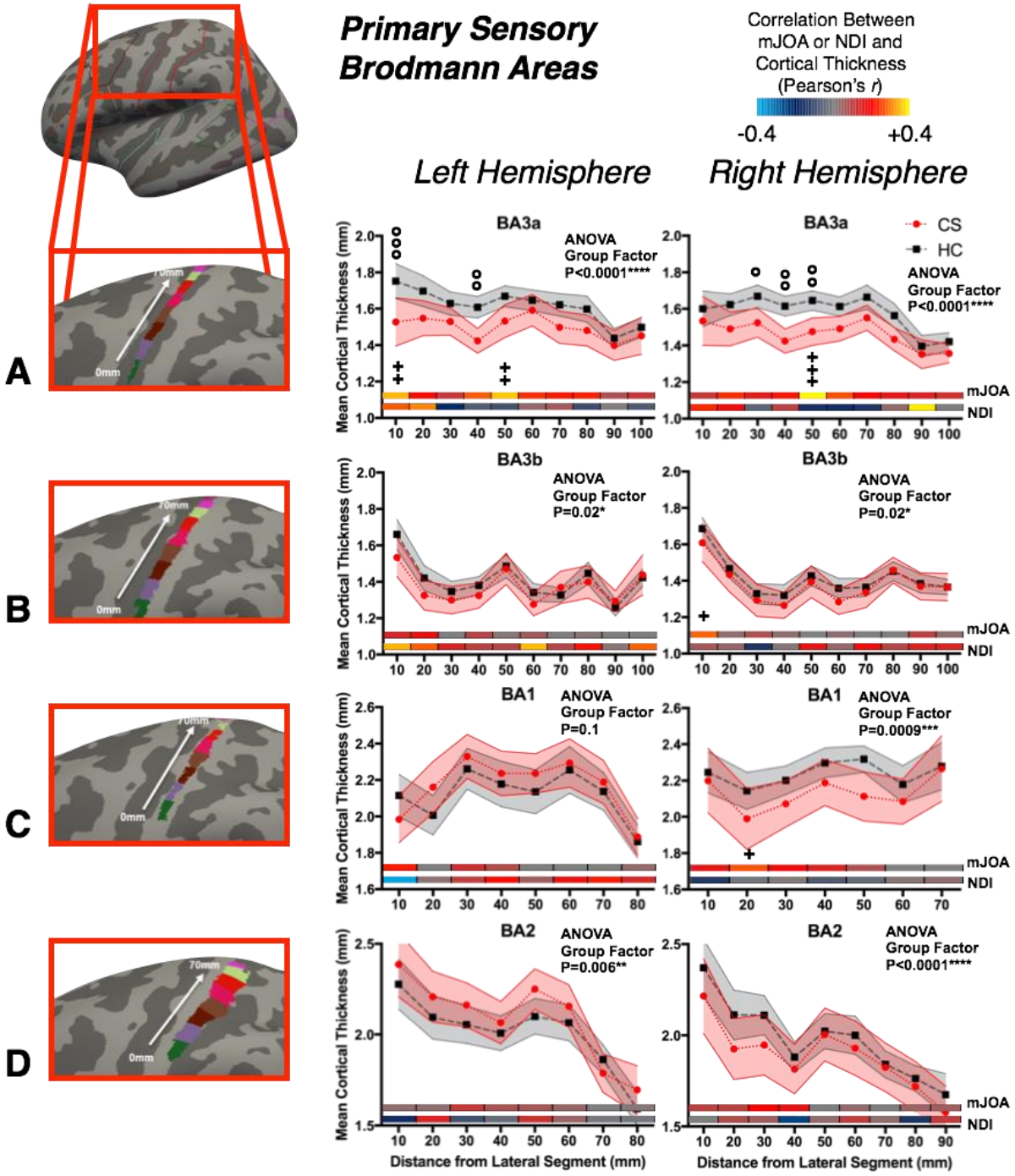

Figure 2.7. Legend presented on next page.

Figure 2.7 Legend: Cortical thickness as a function of distance in 1cm segments across primary sensory Brodmann Areas (BAs), including A) BA3a, B) BA3b, C) BA1, and D) BA2. Values in plot reflect mean and 95% confidence intervals for CS patients and HC subjects. The x-axis is distance from first segment, laterally to medially as illustrated on the figures to the left, the y-axis is cortical thickness, and plotted are the mean values for each group. Displayed within each plot is the color-coded Pearson correlation coefficient for the mJOA and NDI scores with the mean cortical thickness in each segment. For each BA the P-value for the Group Effect in the two-way ANOVA (group and distance) is displayed. Significance after Sidak-Holm correction is shown for group differences (displayed above plotted values for the groups, denoted by the '°' symbol) and Pearson's correlation with mJOA (displayed below the plotted values for the groups and above the color-coded bars, denoted by the '+' symbol); Pearson's correlations with NDI showed no significant results.

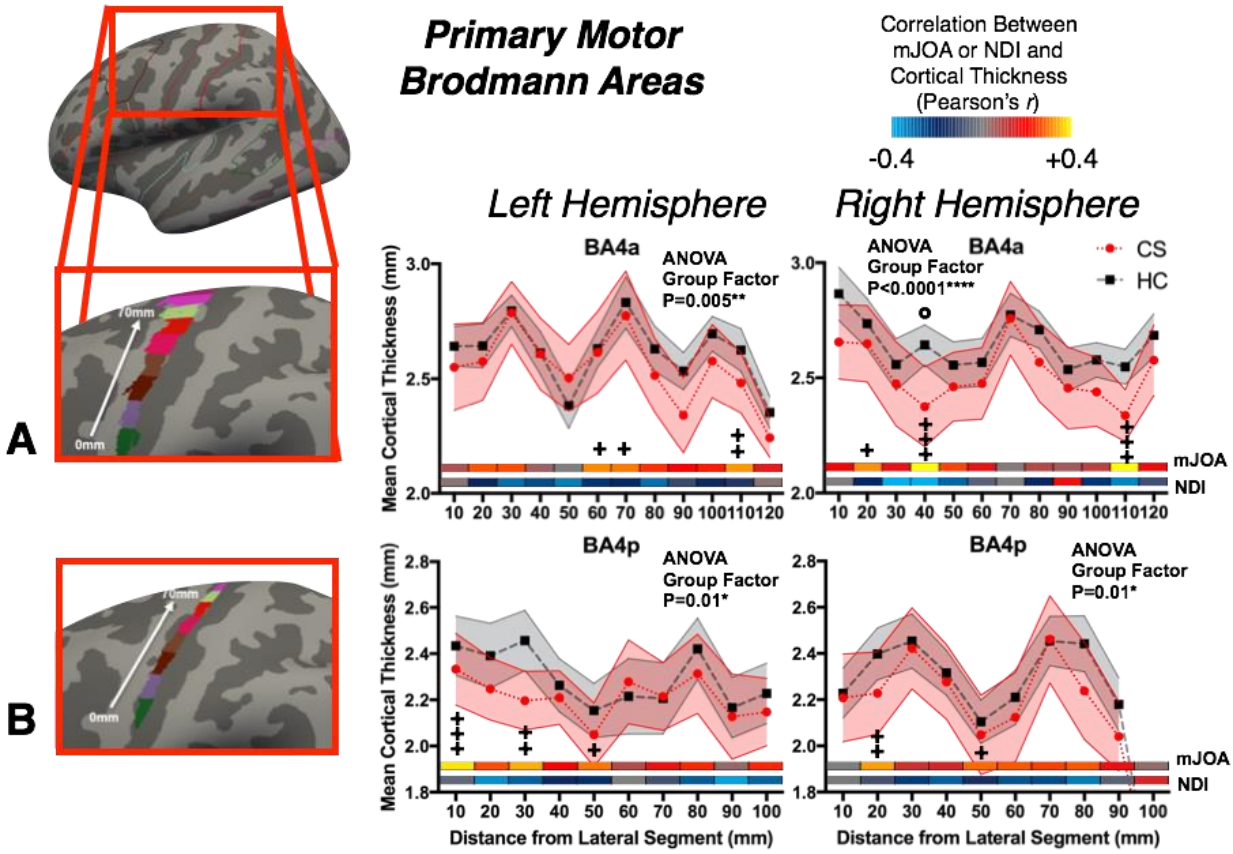

Figure 2.8. Legend presented on next page.

Figure 2.8 Legend: Cortical thickness as a function of distance in 1cm segments across primary motor Brodmann Areas (BA), including A) BA4a and B) BA4p. Values in plot reflect mean and 95% confidence intervals for CS patients and HC subjects. The x-axis is distance from first segment, laterally to medially as illustrated on the figures to the left, the y-axis is cortical thickness, and plotted are the mean values for each group. Displayed within each plot is the color-coded Pearson correlation coefficient for the mJOA and NDI scores with the mean cortical thickness in each segment. For each BA the P-value for the Group Effect in the two-way ANOVA (group and distance) is displayed. Significance after Sidak-Holm correction is shown for group differences (displayed above plotted values for the groups, denoted by the '°' symbol) and Pearson's correlation with mJOA (displayed below the plotted values for the groups and above the color-coded bars, denoted by the '+' symbol); Pearson's correlations with NDI showed no significant results.

Age-Related Changes in Cortical Thickness Between CS and HCs

We explored age-related changes in cortical thickness between CS and HC subjects in the precentral and postcentral gyrii, superior frontal lobe, and the precuneus (**Figure 2.9**). In general, CS patients demonstrated a more rapid decline (larger negative slope) with increasing age in both the left postcentral gryus (P=0.016) and precuneus (P=0.028), potentially implying a faster rate of cortical thinning in patients with CS compared with HCs. Additionally, the left and right putamen (P=0.002 and P=0.008, respectively) and the right precuneus (P=0.009) showed lower mean values in CS patients compared to HC subjects. For whole-brain mean cortical thickness, CS patients had a rate of thinning of a loss of 0.0069 mm/year, and HC presented with a loss of 0.0036 mm/year. Though not statistically significant, the HC rate was more comparable to the loss of 0.004 mm/year reported in a larger study of HC by Lemaitre *et al* [91], while CS patients had a higher rate of thinning.

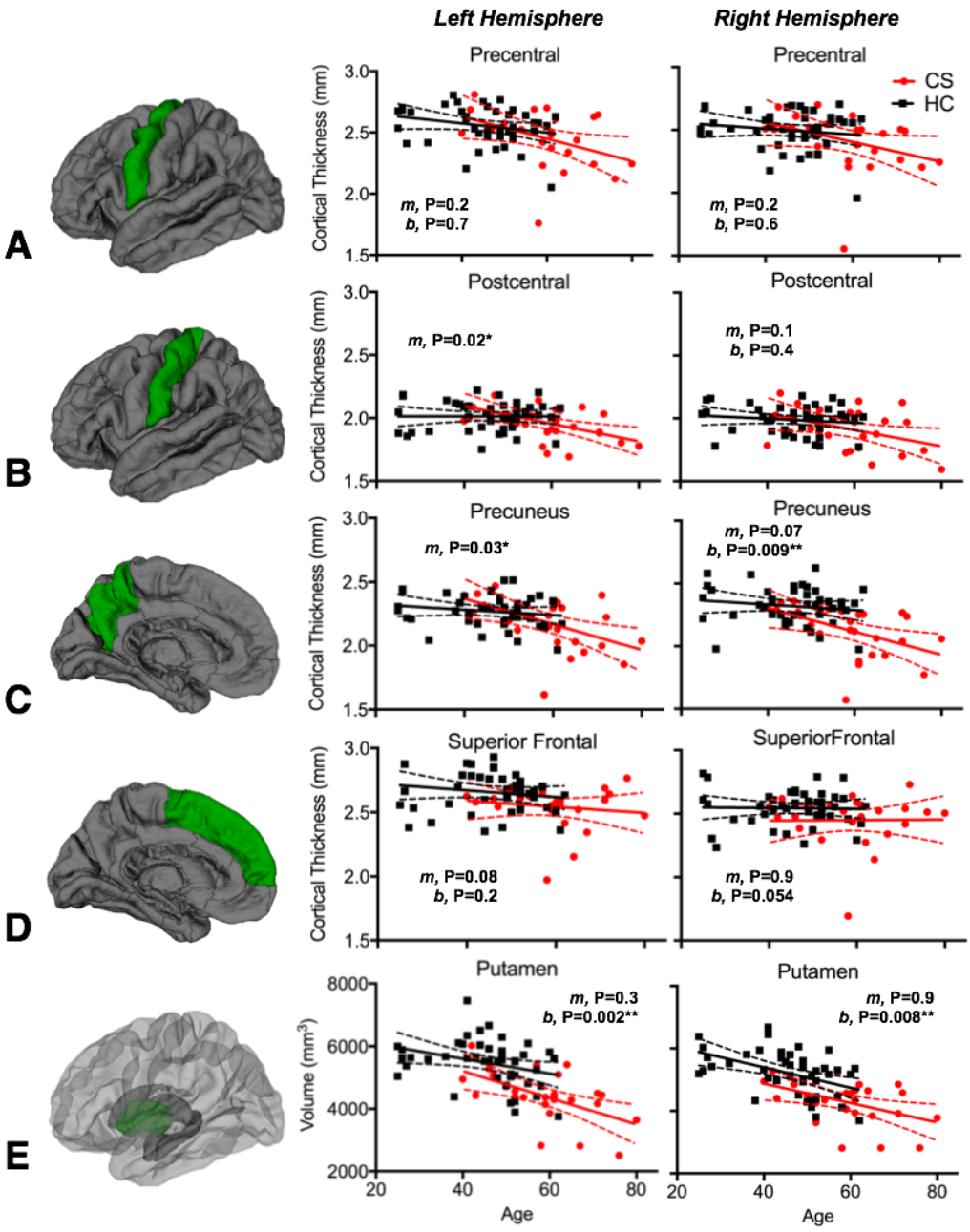

Figure 2.9. Association between cortical thickness in A) the precentral gyrus, B) postcentral gyrus, C) precuneous, D) superior frontal lobe and E) subcortical putamen volume and age for HC and CS patients. Slopes are denoted by "*m*" and intercepts are denoted by "*b*", thus if the "*m*" P-value is significant the slopes differ between the groups, while if the "*b*" p-value is significant the intercepts differ between the groups.

iii. Structural Spinal Cord Changes with Neurological and Pain Symptoms

Spinal Cord Cross-Sectional Area in CS and HC

Figure 2.10 displays the comparison of cross sectional areas at the various vertebral levels between the CS patients and HC subjects. CS subjects presented with significantly lower SC CSA at all levels: this was true both when including and excluding the sites of compression in the patient population. When including sites of compression (**Figure 2.10.B**), the overall two-way ANOVA model was significant ($P<0.0001$) with both the group and level factors having differences at a level of $P<0.0001$. Multiple-comparisons corrected tests between groups at each level were all significant ($P<0.0001$ at all levels, except at C7 where $P=0.0003$, and T1 where $P=0.009$). The percentage difference between the HC and CS spinal cord CSA at various levels was: 18.8% at C2, 24.8% at C3, 28.3% at C4, 26.3% at C5, 23.6% at C6, 21.5% at C7, and 18.6% at T1. Thus, maximal percentage difference in CSA was seen at levels that were more often affected by compression (C3, C4, C5, C6), and the lowest percentage difference was seen at uncompressed levels (C2, C7, T1).

When excluding sites of compression in the analysis (**Figure 2.10.C**), the overall two-way ANOVA model was still significant ($P<0.0001$) with both the group and level factors having differences at a level of $P<0.0001$, though there was a notable increase in CSA at vertebral levels C3-C6 of the CS group when excluding sites of compression. Multiple-comparisons corrected tests between groups at each level were all significant, with C2, C3, and C5 presenting with $P<0.0001$, C4 presenting with $P=0.001$, C6 presenting with $P=0.0002$, and C7 presenting with $P=0.004$. The percentage difference between the HC and CS spinal cord CSA, when excluding sites of compression, at various levels was: 18.8% at C2, 19.4% at C3, 19.1% at C4, 21.4% at C5, 20.5%

at C6, 22.8% at C7, and 18.6% at T1. Thus, though the percentage differences decreased with the exclusion of sites of compression, the spinal cord CSA was still different between the groups.

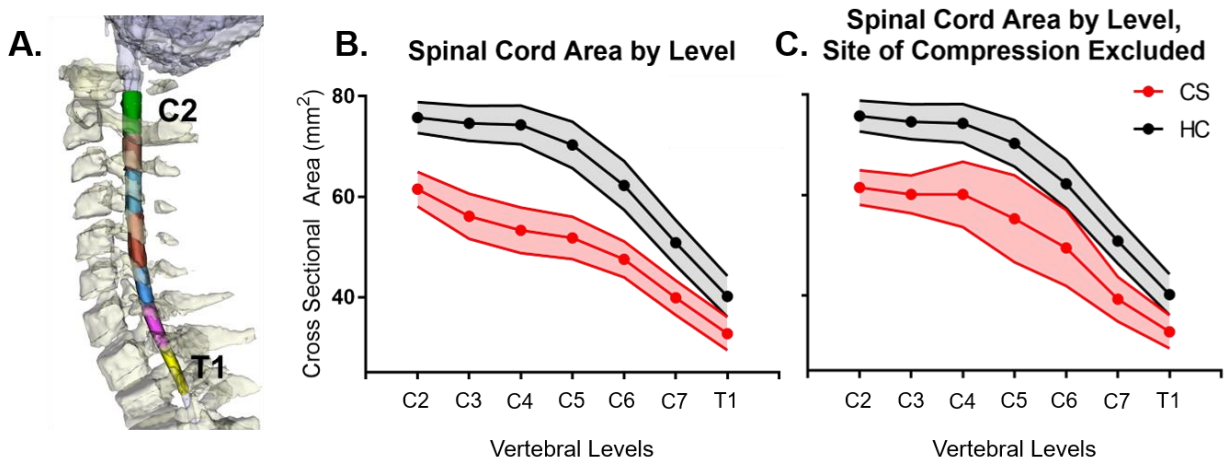

Figure 2.10. Spinal cord cross-sectional area (CSA) by vertebral level (C2-C7 for cervical level, 1 thoracic level, T1). A) Example subject showing the spinal cord segmented by vertebral levels. B) Comparison of spinal cord CSA between HC (black) and CS subjects (red) across all subjects and vertebral levels. C) Comparison of spinal cord CSA between HC and CS subjects across all subjects, but excluding vertebral levels with compression. Dots reflect mean and shaded area reflect 95% confidence intervals. Two-way ANOVAs were significant for both analyses, for the overall models and level and group factors (all $P<0.0001$).

In evaluating the relationship between the site of maximal compression and the spinal cord CSA at the uncompressed most rostral (C2) and most caudal (C7) cervical vertebral levels, the site of maximal compression showed a trend towards a positive Pearson's correlation with the CSA at C2 (r=0.38, P=0.053), while the CSA at C7 showed no correlation (r=-0.07, P=0.8). Thus, the area of the spinal cord at C2 trended towards being lower if the site of compression was more proximal to C2 (*i.e.* more rostral). When comparing the age-related change in the SC CSA, while both C2 and C7 showed a significant group difference when accounting for age (P=0.0005 for C2, P=0.006 for C7), neither showed a significantly different slope of SC CSA with respect to age, though for C2 the result was trending towards significance and may prove significant in a larger cohort (P=0.11 for C2, P=0.85 for C7, **Figure 2.11**).

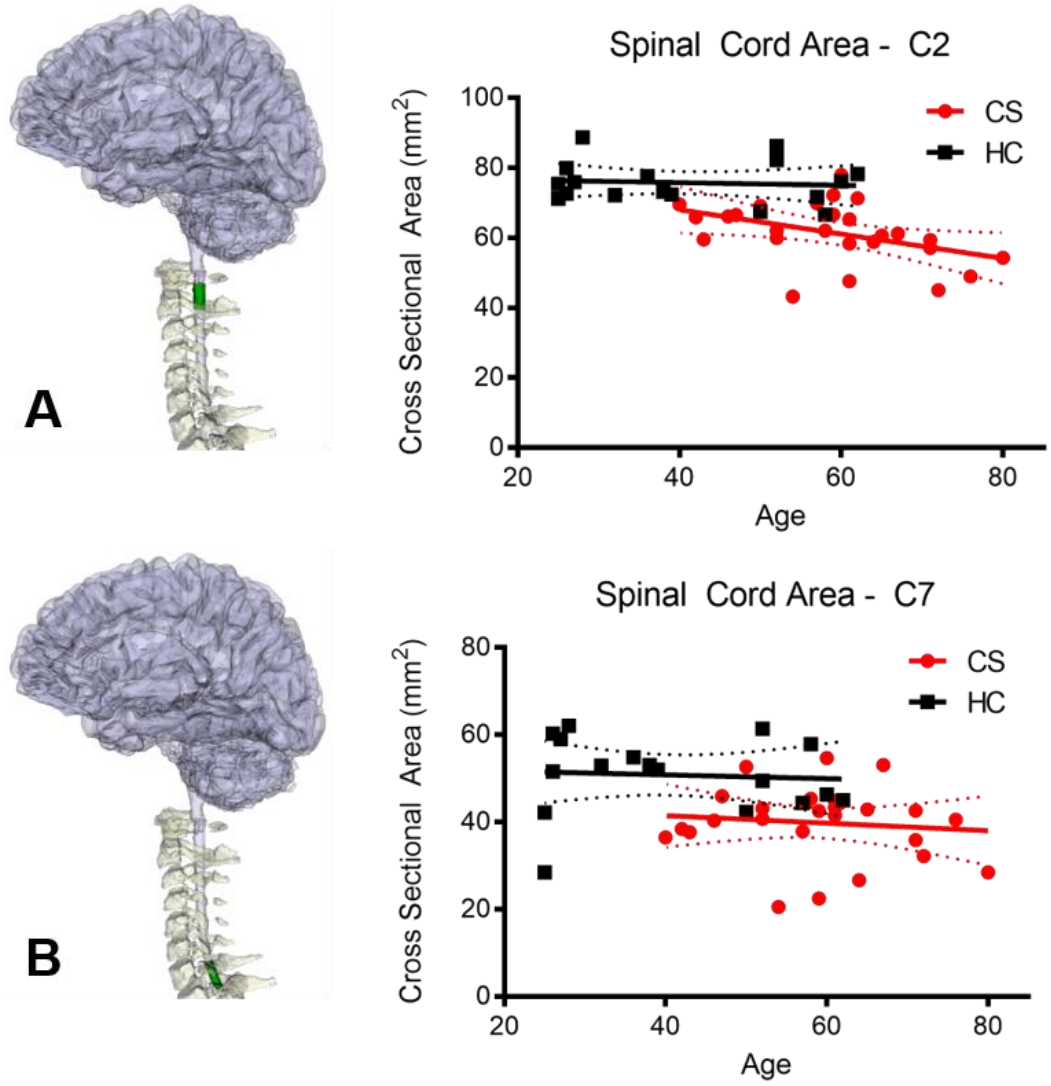

Figure 2.11. Regression of SC CSA with age for CS and HC groups. Spinal cord regions of interest shown on left in green. A) Regression run for CSA at C2 vertebral level, no significant slope difference was found (P=0.11) but a significant mean difference between the groups (P=0.0005) was present. B) Regression run for CSA at C7 vertebral level, no significant slope difference was found (P=0.85) but a significant mean difference between the groups (P=0.006) was present.

Relationship between Conventional MRI Measures and Spinal Cord Cross-Sectional Area

The relationship between the spinal cord structural measures, including conventional MRI measures of compression such as the sagittal spinal cord diameter at the site of maximal compression and the MR-equivalent Torg Ratio, as well as the CSA of the spinal cord at the vertebral level of maximal compression, was evaluated at C2 and at C7. **Figure 2.12** shows a heat-map of the Pearson's correlation coefficients between the various measures, all of which were positively correlated to one another. As expected, the spinal cord diameter at the site of maximal compression and the Torg Ratio had a high Pearson's correlation coefficient (0.91, $P<0.0001$, all reported Pearson's correlation test P-values between spinal cord measures were Bonferroni-corrected), due to fact that the Torg Ratio is the ratio of the spinal cord diameter at the site of maximal compression over the diameter of the vertebral body above. The spinal cord diameter at the site of maximal compression had a correlation of 0.56 with the CSA at the vertebral level of maximal compression ($P=0.03$), a correlation of 0.62 with the CSA at C2 vertebral level ($P=0.01$), and a correlation of 0.42 with the CSA at the C7 vertebral level ($P=0.31$). Similar trends were observed for the Torg Ratio, with the C2 level and site of compression vertebral levels showing the highest correlations (correlation of 0.51, $P=0.08$ for C2, and correlation of 0.60, $P=0.01$ for site of maximal compression), while C7 showed a lower correlation coefficient (0.46, $P=0.19$). As for the relationships between the CSA at the different vertebral levels, CSA at the site of maximal compression showed a strong correlation with the CSA at C2 (0.60, $P=0.01$) and the CSA at C7 (0.65, $P=0.004$), while the CSA at C2 and C7 showed a weaker correlation (0.47, $P=0.16$).

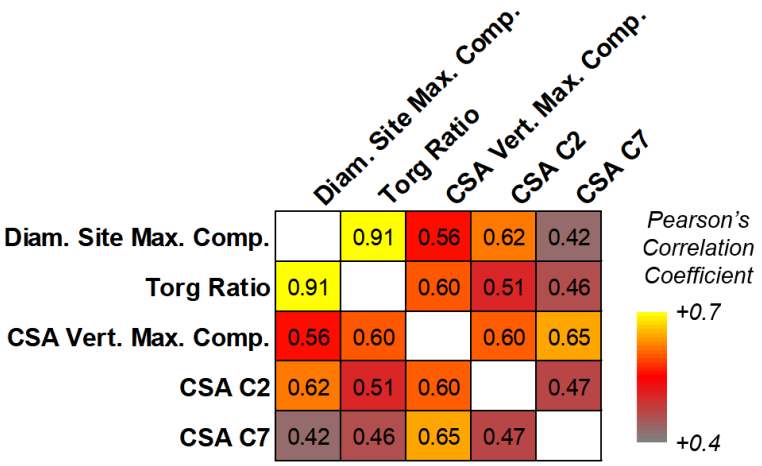

Figure 2.12. Heat map of correlations between spinal cord structural measures, including the sagittal diameter at the site of maximal compression (Diam. Site. Max. Comp.), the MR-equivalent Torg Ratio (Torg Ratio), and the cross-sectional area (CSA) of the spinal cord at the vertebral level of maximal compression (Vert. Max. Comp.), C2, and C7.

Association Between Spinal Cord Cross-Sectional Area and Neurological Function

When evaluating the relationship between the spinal cord structural measures and neurological functional status, none produced a significant relationship with mJOA, neither via Pearson's correlation nor by multiple linear regression against mJOA and age. For correlations, the one that presented with the highest Pearson's correlation coefficient was the diameter of the spinal cord as measured at the site of highest compression (0.30, P=0.13), followed by the Torg Ratio (0.22, P=0.27). For the SC CSA, CSA at the vertebral level of maximal compression and at C7 actually produced slightly negative correlations with mJOA (-0.1, P=0.63, and -0.21, P=0.30, respectively), though neither was significant, while the correlation of CSA at C2 with mJOA was positive but not statistically significant either (0.19, P=0.34). **Figure 2.13** displays the CSA measurements for each patient at each level described, plotted against mJOA.

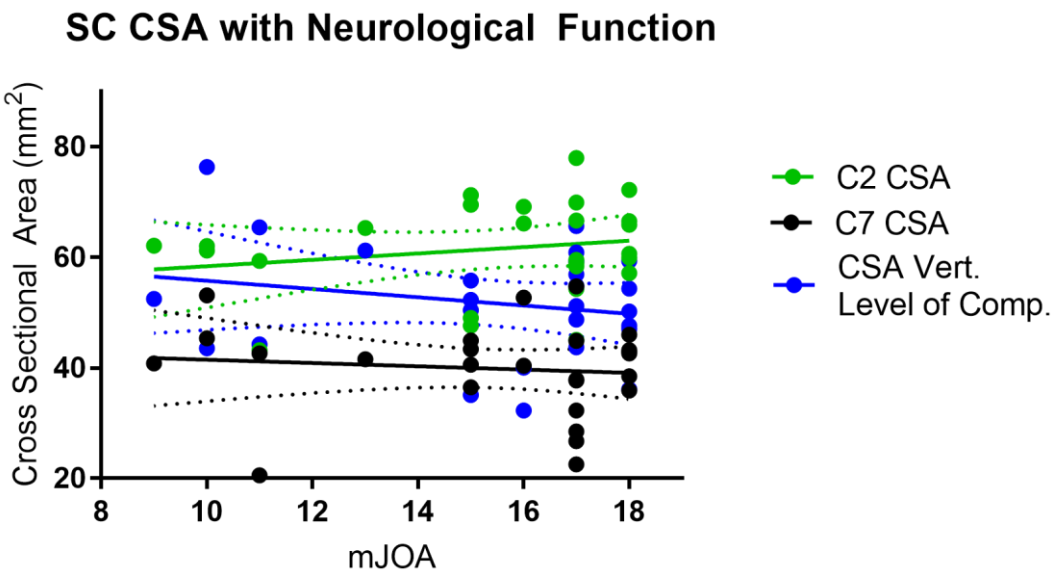

Figure 2.13. Plotting of average CSA at C2 (green), C7 (red), and the level of maximal compression (blue), vertebral levels. No associations were significant, and the C7 and vertebral level of maximal compression correlations were near 0 and slightly negative. The CSA at C2 seems reasonable in its decreasing with worsening mJOA, and may prove to be significant with a different or larger cohort of patients.

iv. Association between Spinal Cord and Brain Structure in CS Patients

When evaluating the associations between cortical thickness and the different spinal cord measures, only the Torg Ratio demonstrated a significantly associated cluster with mJOA, present in the left precentral gyrus (**Figure 2.14**). This region had a positive correlation between cortical thickness and Torg Ratio, so with worsening compression there was a decrease in the cortical thickness in the region. While the region covered a substantial portion of the precentral gyrus, this was mostly located in the lateral-most part of the parcellated region. Since the region was mostly confined to the precentral gyrus, multiple linear regression of the mean cortical thickness with

respect to the Torg Ratio and age for both the left and right precentral gyri was performed, and these values are reported in **Table 2.6.** The mean cortical thickness of the left precentral gyrus had a significant relationship with the Torg Ratio (P=0.02) and with the overall model (R^2=0.35, P=0.008), while the mean cortical thickness of the right precentral gyrus was not significant in the multiple linear regression model, but was trending towards significance (P=0.12) and the overall model was trending towards significance as well (R^2=0.22, P=0.06). To visualize the relationship between Torg Ratio and cortical thickness of the precentral gyri, these were plotted on a graph in **Figure 2.15.**, in which both gyri presented with a positive association between Torg Ratio and cortical thickness. In line with the visual assessment of the graph, simple linear regression of both these regions with the Torg Ratio was significant (P=0.004 for LH, and P=0.04 for RH).

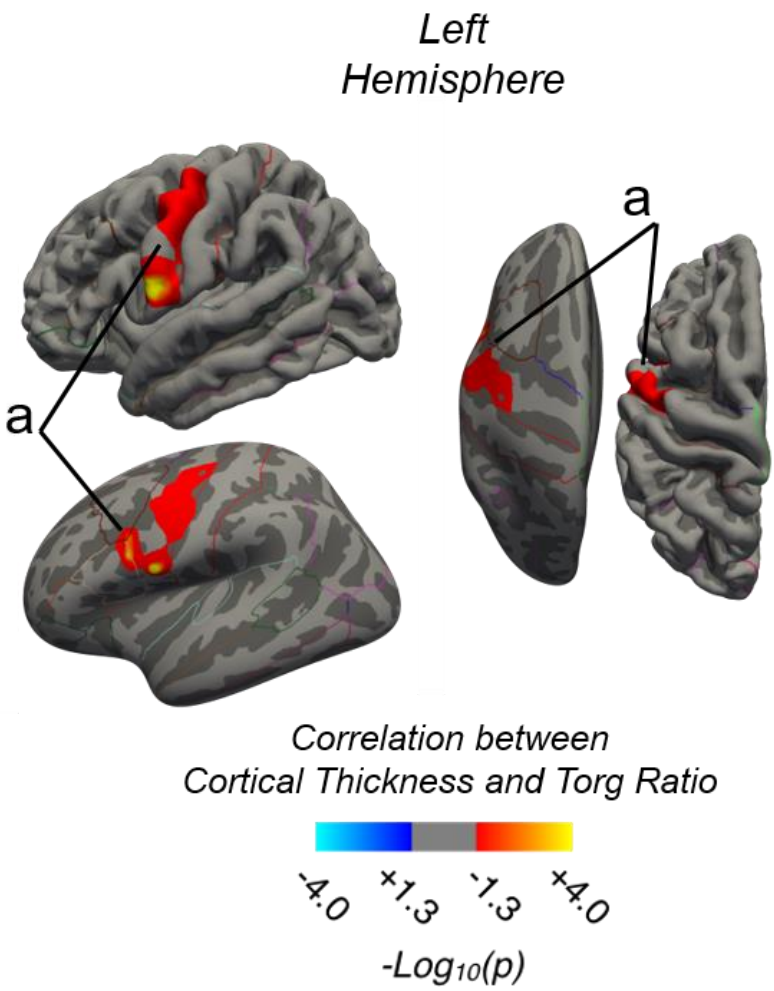

Figure 2.14. Regions demonstrating a strong association between cortical thickness and the MR-equivalent Torg Ratio, in patients with cervical spondylosis (CS). Red-Yellow denotes decreasing cortical thickness with decreasing Torg Ratio (more compression) in CS. A region with significant associations was identified in the left precentral gyrus (a).

Table 2.6. Multiple Linear Regressions of Mean Cortical Thickness with the MR-equivalent Torg Ratio and Age. LH and RH are left and right hemisphere.

Measure	Region	Torg Ratio	Torg P-Val	Age	Age P-Val	R^2	Adj. R^2	Overall Model P-Val
Cortical Thickness	LH Precentral	1.03	0.02	-0.0054	0.19	0.345	0.288	0.008
	RH Precentral	0.74	0.12	-0.0053	0.25	0.2156	0.1474	0.06

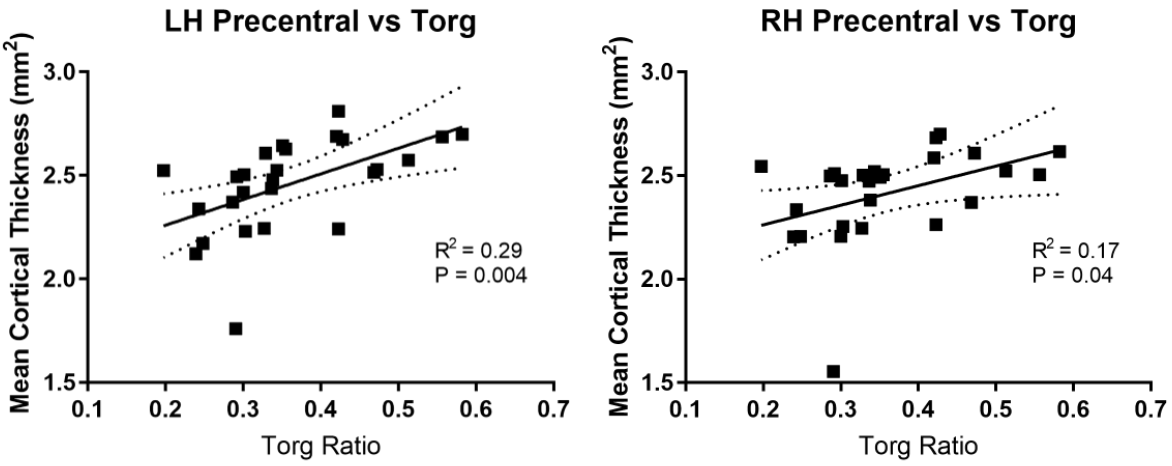

Figure 2.15. Plots of mean cortical thickness of the left and right precentral gyri against the MR-equivalent Torg Ratio. Plotted are the linear regression lines along with the 95% confidence intervals (dashed line).

v. Discussion

Recent studies have demonstrated that spinal cord injury can induce atrophic alterations of the supraspinal neural networks, and that the extent of these changes can correlate with degree of neurological impairment. Hou *et al* [169] found in SCI patients that gray matter volume reduction in

the primary motor cortex significantly correlated with the American Spinal Injury Association (ASIA) motor impairment score. Using voxel based morphometry, Freund *et al* [171] determined that spinal cord atrophy following SCI was significantly correlated with degree of cortical atrophy. Moreover, in a separate study, Freund *et al* [170] established that SCI patients that had lower volume change of the corticospinal tract at the level of the internal capsule had a significantly better neurological outcome than those with a higher volume loss. These investigations highlight some of the upstream adaptations within the sensorimotor network that occur following traumatic SCI and their potential impact on both functional status and recovery.

Results from the current study support the hypothesis that chronic spinal cord injury related to cervical stenosis may result in specific structural changes within the brain compared with neurologically intact healthy volunteers. CS patients displayed a consistent pattern of brain changes with associated clinical symptoms of both neurological function (mJOA) and neck pain (NDI), namely decreased cortical thickness bilaterally within precuneus and superior frontal regions, and decreased volume of the putamen, bilaterally. In addition to these regions, cortical thinning with mJOA and NDI was observed in the anterior cingulate and with NDI in the insula. The results also demonstrate increasing atrophy within BA3a and in primary motor regions with worsening neurological symptom severity. Patients with CS also displayed a faster rate of cortical thinning and atrophy with age compared to HC subjects. These are both critically important findings, and could potentially have an impact on the understanding of the pathogenesis of CSM and recovery following surgical intervention.

Associations Between Structural Brain Measures and Symptoms

Interestingly, the cortical thickness within the precuneus and superior frontal gyrus as well as volume of the putamen appeared strongly correlated with both mJOA and NDI. The precuneus has a wide variety of functions, including a prominent role in the default mode network, and is an area involved in motor planning and imagery, and a key structure in memory retrieval [221]. The putamen also has multiple functions, one of which is the processing of sensorimotor input to the basal ganglia, as the putamen receives the majority of cortical projections from motor, premotor, supplementary motor, and primary sensory cortex, and projects back to these areas via neuronal connections to the globus pallidus and thalamus [222]. Previous studies have suggested both the precuneus and the putamen are involved in motor imagery [223,224] and in motor learning [225], suggesting structural changes may be associated with long-term adaptation of motor function in the presence of impairment.

In the medial prefrontal lobe, multiple regions were significantly associated with neurological function. Brodmann area 8 has been implicated in executive function [226]. More generally, the medial prefrontal cortex appears to be involved in monitoring the performance of motor actions [227], again suggesting structural changes observed in these locations may be related to impairment of motor function. In a study evaluating complex bimanual tasks these were found to involve the precuneus and anterior cingulate more than simple manual tasks [228], and the authors of this study linked the anterior cingulate activity to modulating motor commands, and the precuneus to spatial navigation. This involvement of higher order functional areas of the brain in complex manual tasks may help explain the results in this study: patients with CSM, who have difficulty with complex tasks such as writing, buttoning a shirt, and gait, have decreased cortical thickness in these higher order functional brain regions. Interestingly, the precuneus in primates

has been shown to project to the putamen [229,230], medial Brodmann area 8, and the anterior cingulate [230,231], suggesting these regions may be functionally related.

A strong association was observed between decreased cortical thickness within BA3a and increasing neurological symptom severity, which is consistent with the role of BA3a in receiving afferent information regarding proprioception and motor actions [232] as CS patients with myelopathy are known to have deficits in proprioception [233] relating to both gait [234] and hand function [235]. While cortical thickness in the precentral gyrus, in general, was not associated with neurological impairment, subdivisions of the motor strip (BA4a and BA4p) appeared strongly associated with changes in mJOA. This lack of widespread changes in the precentral gyrus across all patients likely reflects the variability in specific motor deficits across patients (*i.e.* upper or lower extremity deficits) and their relation to reorganization within the motor cortex.

This chapter hypothesized that CS patients would exhibit similar alterations in brain structure to those observed in other chronic pain conditions, namely decreased cortical thickness in sensorimotor regions with increasing neurological symptom severity, and decreased cortical thickness in brain regions implicated in chronic pain with increasing pain severity. To test this hypothesis, the cortical thickness and volumes of subcortical structures involved in sensorimotor processing in CS patients were examined, and these measurements were compared with those of the neurologically intact HCs and clinical symptoms. Results from this study confirmed a decrease in cortical thickness within the cingulate cortex and insular cortex may occur with worsening neck pain, which is consistent with modern theories associated with chronic pain structural reorganization [183,190]. The anterior cingulate cortex (ACC) is known to be a key area in the central sensitization in chronic pain, potentially acting by long-term potentiation [73,74], and a decrease in gray matter within the ACC has been observed in multiple chronic pain studies [236,237]. These

changes suggest neck pain exhibited by some patients with CS may alter neural structures involved in the central sensitization of pain, including the ACC.

Structural Spinal Cord Measures in CS and HC Groups and Relationships to Symptoms

This study continues the line of evidence presented in previous publications in demonstrating the utility of structural MRI for the diagnosis of cervical stenosis [238,239], demonstrating large differences present in SC CSA between CS patients and HC subjects. In this chapter, a semi-automated pipeline was used to obtain the measures of cross-sectional area across multiple vertebral levels, all of which demonstrated group differences between CS and HC. While it is expected that spinal cord levels that are compressed to have a lower CSA in CS compared to HC, this relationship held even at levels that were uncompressed, such as C2 and C7, and even when accounting for age. This was true both when including and excluding the sites where compression was present in CS patients. Previous studies in traumatic SCI have documented decreased structure and atrophy in the rostral unaffected (usually C2 or C3) spinal cord [172,240,241], with cross-sectional area changes between 11% and 30% [241]. Similar to traumatic SCI, studies in CS patients have also found decreases in spinal cord area at rostral uncompressed sites (C2 or C3). A study by Grabher *et al* found a decrease in CSA of the spinal cord of 12.8% in patients with CSM when compared to healthy controls [242], while Martin *et al* found a decrease of 10.2% [243]. While for the present study the difference is somewhat larger (18.8% decrease in CS versus HC), the same trend is present, namely significantly decreased spinal cord area rostral to the site of compression. Also, for the current study exclusion of the sites of compression yielded similar percentage differences between CS and HC for the different vertebral levels (around 20%). These atrophic processes of the spinal cord likely represent neurodegenerative changes [241,244].

The different structural measures of the spinal cord demonstrated internal consistency as assessed by the Pearson's correlation coefficients between the measures. However, similar to previous studies [40,41,239], spinal cord morphological measures assessed on structural MRI did not show strong relationships with neurological symptoms or neck pain. Some of the measures, like the sagittal diameter of the spinal cord at the site of maximal compression, the MR-equivalent Torg Ratio, and the SC CSA at the C2 vertebral level, were trending towards significance and may be significant in a larger cohort, but they were not significant in this study and may potentially only have moderate to low correlations with neurological symptoms in larger cohorts.

While there is currently a dearth of studies using semi-automated spinal cord segmentation for analysis, a recent study by Martin *et al* used the SCT to obtain SC CSA measures (amongst other metrics such as factional anisotropy, magnetization transfer ratio, and T2* white matter to gray matter signal intensity ratio) in patients with cervical spondylosis and healthy controls [243]. This study found relatively high correlations between mJOA and SC CSA (Pearson's correlation of 0.66 between mJOA and CSA at level of maximal compression, 0.44 at site rostral to maximal compression) [243]. However, Martin *et al* included healthy controls in this correlation, which have asymptomatic mJOA scores (18) and have an uncompressed spinal cord. This chapter demonstrated a large difference in SC CSA between CS patients and HC subjects (**Figure 2.9**) and, similar to results from this chapter, Martin *et al* also reported large differences between these two groups especially at the site of maximal compression and at the site rostral to compression. Thus, the correlation between mJOA and SC CSA in the work by Martin *et al* may have been driven by a difference between the HC and CS populations, and would then not accurately reflecting the underlying neurological symptomatology.

The results from this chapter suggest that while structural MRI measures are sensitive biomarkers of cervical stenosis, and thus of diagnostic utility, these are weak predictors of actual neurological deficits or symptomatology. While the spinal cord measures showed large differences between CS and HC groups, the brain structural measures (mean cortical thickness or volume) of several regions showed a stronger relationship with the symptom measures (mJOA and NDI) then the spinal cord structural measures (SC diameter, Torg, SC CSA). Thus, while the spinal cord morphological measures show a greater diagnostic power for determining cervical stenosis, the brain measures may track better with the neurological symptoms and with neck pain. This result makes sense in the context of stenosis being the tightening of the spinal cord; this tightening of the spinal cord, however, is not always associated with neurological symptoms. While the brains of the CS and HC groups are relatively similar (no brain lesions or visibly apparent alterations are present in the CS group), the brains of CS patients appear to reorganize or show degenerative changes in line with the specific neurological deficits.

While the MPRAGE sequence provides sufficient contrast between the spinal cord and surrounding tissue to segment the spinal cord, and it preserves contrast between gray and white matter for the brain, it offers poor difference in contrast between gray and white matter in the spinal cord. As such for this study only the CSA of the spinal cord was used for analysis. However, differences in area of the gray and white matter of the spinal cord, especially at sites of compression because gray matter and white matter have different mechanical and elasticity properties [245]. Thus, future studies should aim to implement sequences that provide gray and white matter contrast in the spinal cord [241], such as using the T2 weighted multiple-echo data image combination (MEDIC) sequence [246].

The results of this chapter reiterate the need for new imaging biomarkers: current structural spinal cord measures do not offer sufficient correlation with neurological status, and upstream nervous system changes are taking place in the brain in association with neurological and pain symptoms. The chapters that follow evaluate advanced functional (fMRI) and microstructural (diffusion MRI) measures in the spinal cord and brain.

Relationship Between Spinal Cord Structure and Brain Structure

When comparing the spinal cord structural measures with the cortical thickness in the brain, while most spinal cord measures did not produce significant results, the MR-equivalent Torg Ratio showed a significant correlation with the cortical thickness in a region of the left precentral gyrus. This relationship held for the mean cortical thickness across the precentral gyrus as a whole and trended towards significance in the right precentral gyrus, as well as both regions showing statistical significance for simple linear regression. This result contrasts with the associations between cortical thickness and the symptom variables in primary sensorimotor areas which, while these appeared significant in some analyses, these were usually more spatially variant and represented either weaker associations or associations in sub-regions, such as along certain portions of the Brodmann sensorimotor strips. The region showing a significant association with Torg Ratio was towards the lateral portion of the precentral gyrus, which on the motor homunculus generally represents the facial muscles, but the ROI may extend up to regions of the hand and arms as well [247,248]. This relationship between Torg Ratio and the region of the precentral gyrus merits further investigation, and further chapters of this dissertation will evaluate functional and microstructural changes in the brain associated with the Torg Ratio.

Chapter III. Functional Connectivity of the Brain and Spinal Cord at Rest in Patients with Cervical Stenosis and Associated Myelopathy

In this chapter the resting state functional connectivity of the brain and spinal cord in patients with cervical stenosis (CS) and healthy controls (HC) was examined. Activation studies of motor tasks using functional magnetic resonance imaging (fMRI) have revealed increased activation of motor regions in patients with CS when compared to healthy controls [203,204]. This chapter aimed to extend this previous work by examining resting state fMRI (rs-fMRI), which leverages low frequency oscillations of blood oxygenation level dependent (BOLD) signal to measure patterns of neural activity at rest. Additionally, this chapter sought to extend the evaluation of rs-fMRI beyond the brain to include the spinal cord as well. This could be accomplished due to technical advances in MRI such as large acceleration factors, and by extending the field of view (FOV) to cover both the brain and cervical spinal cord. In this way, this chapter aimed to probe the functional connectivity (FC) between brain regions, between various gray matter spinal cord structures, and between the spinal cord and the brain.

Altered FC between was expected between brain regions found to be structurally altered with neurological and pain symptoms as described in **Chapter II**, specifically the modified Japanese Orthopedic (mJOA) score, which measures neurological function, and the neck disability index (NDI) which measures neck pain and its adverse effects on the everyday lives of patients. as well as the primary sensory and primary motor brain regions. While rs-fMRI in the spinal cord is not yet a well-established technique, this study aimed to replicate initial findings from a few other studies [134,249], and explore whether the spinal cord FC was altered by stenosis or neurological or pain symptoms.

i. Resting-State fMRI Acquisition and Processing

Patient Population

This chapter used nearly the same cohort of patients as used in **Chapter II**. However, two of the patients from the CS group were excluded from analyses in this chapter: one patient did not undergo an rs-fMRI scan due to interim licensing issues with the sequence on the scanner (43 year old female, mJOA of 17, NDI of 28), and one patient had severe artifacts in their fMRI scan due to excessive motion during acquisition of parallel imaging callibration data and throughout the rest of the scan (54 year old male, mJOA of 11, NDI of 14). Thus, the CS patient cohort that was used for this chapter comprised 24 subjects. The 17 HC subjects that underwent the same T1w scanning as the CS patients (listed in **Chapter II**) also underwent the same rs-fMRI of the brain and spinal cord. The slightly modifed CS cohort and HC cohort demographics are shown in **Table 3.1** (refer to **Table A.1** from **Appendix A** for differences in the cohort used in this chapter). Similar to the results in **Appendix A**, there was a significant difference in age between the groups (t-test, $P<0.001$), but not in body mass index (BMI, t-test, $P=0.3$) or sex (Chi-squared test, $P=0.3$).

Table 3.1. CS patients and HC subjects cohort demographics for rs-fMRI. Differences from Table A.1 are due to the exclusion of two CS patients.

Subject Population	N	Age (mean years +/- SD)	Sex	BMI (mean +/- SD)	mJOA (mean +/- SD)	NDI (mean +/- SD)
CS Patients	24	60 ± 10 years	19M / 5F	27.0 ± 6.2	15.5 ± 2.8	9.6 ± 10.6
HC Subjects	17	41 ± 13 years	11M / 6F	26.2 ± 3.0	18	

Optimizing the rs-fMRI Protocol

A Multi-Band (MB) echo planar imaging (EPI) fMRI protocol supplied by the Center for Magnetic Resonance Research, Department of Radiology (CMRR, https://www.cmrr.umn.edu/multiband/), at the University of Minnesota, via research collaboration with Siemens (*Siemens Healthcare, Erlangen, Germany*) was used to acquire fMRI data of the brain and spinal cord simultaneously. This research sequence used both MB acceleration [250], and parallel imaging via the Controlled Aliasing in Parallel Imaging Results in Higher Acceleration (CAIPIRINHA) technique [250-254]. Voxel sizes were tested with the aim to obtain good signal in the spinal cord where SNR is limited, but still have high enough in-plane resolution for imaging the cervical spinal cord, which has a small cross-sectional area of between 60 and 90 mm^2. Also of consideration in voxel size, this study aimed to match or improve the spatial resolution of standardized brain fMRI protocols, which represent a consensus high-quality acquisition for multisite studies. One example of such a standardized protocols is the set of fMRI sequences recommended by the function biomedical informatics research network (FBIRN, https://na-mic.org/wiki/FBIRN:Aims_and_Goals_of_FBIRN) [211,255], which was used for that study and for other multi-site neuroimaging studies [210]. The spatial resolution of the FBIRN protocol is 3.5mm x 3.5mm in-plane, with 4.5mm slice thickness. Optimal temporal resolution was defined as matching or improving (lowering) the TR of 2000ms used by the aforementioned standardized protocols. Other points of consideration included the geometric distortion in the spinal cord and signal dropout, both of which are ameliorated by the acceleration techniques which were to be implement, particularly parallel imaging, which in this study was achieved via CAIPIRINHA.

Given the considerations for imaging both the brain and spinal cord listed above, the set of parameters used included a voxel size of approximately 1.5mm x 1.5mm x 4mm, and a potential

range for TR from 1500ms to 2000ms. Various combinations of different levels of MB and CAIPIRINHA acceleration that satisfied these constraints were tested. These different protocols were acquired in a single healthy volunteer, and were assessed both visually and by taking the mean signal and temporal signal to noise ratio (TSNR, or the mean signal intensity across time divided by the standard deviation of signal intensity across time) in a manually defined region encompassing the spinal cord at a slice in the C2 vertebral level. **Figure 3.1** displays the results for this analysis. Of interest in **Figure 3.1**, the protocols B) and D) produced good overall image quality, with reduced geometric distortion in the spinal cord, high mean signal intensity in the brain, and high TSNR in the brain. For the image quality in the spinal cord, these acquisitions produced high mean signal intensity, with 214.9 for protocol B, and 181.2 for D, as well as the highest mean TSNR, with 31.4 for protocol B, and 34.6 for protocol D. A second inspection of these images revealed suitable brain image quality (**Figure 3.2**), and the selected protocol was the MB 3, CAIPIRINHA 4, protocol (B) thanks to the reduced TR (1500ms) compared to the other protocol (2000ms), as the increased temporal resolution would help with accounting for respiration artifacts (breathing has a rate of around 0.2 to 0.3 Hz [256]) as well as providing more timepoints for better estimation of functional connectivity measures [213].

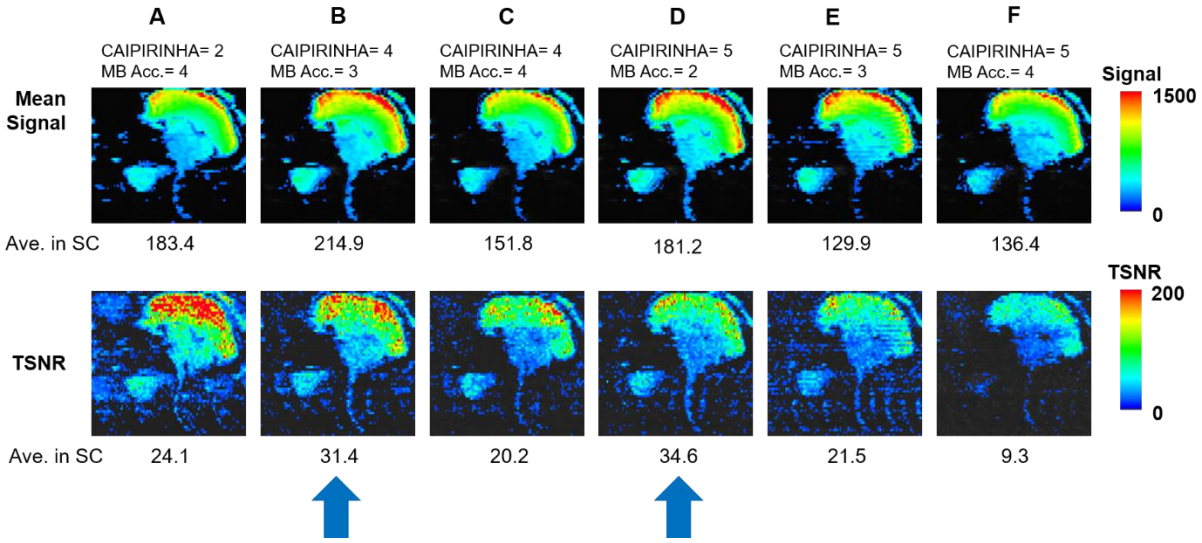

Figure 3.1. Comparison of rs-fMRI protocols with varying acceleration factors for MB and CAIPIRINHA. Top row shows a sagittal mean signal intensity image each rs-fMRI session, and the bottom row displays a sagittal TSNR image at the same slice as the mean signal intensity image. The average value of the signal and TSNR are listed below the respective image for each protocol. The MB and CAIPIRINHA parameters that were tested were as follows: A) CAIPIRINHA=2, MB=3; B) CAIPIRINHA=4, MB=3; C) CAIPIRINHA=4, MB=4, D) CAIPIRINHA=2, MB=5; E) CAIPIRINHA=5, MB=3; F) CAIPIRINHA=5, MB=4. Highlighted with the blue arrows at the bottom are the two protocols selected as optimal, B) and D).

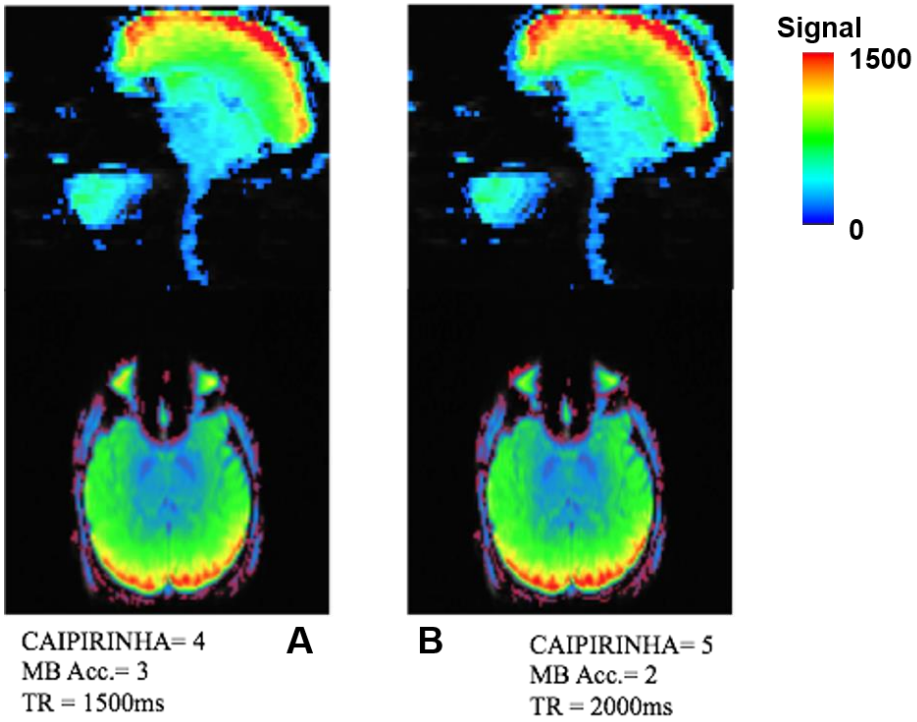

Figure 3.2. Comparison of mean signal rs-fMRI image data on sagittal (top row) and axial (bottom row) slices between selected multiband and parallel imaging acceleration factors. A) CAIPIRINHA=4, MB=3, protocol; B) CAIPIRINHA=5, MB=2, protocol. Given the reduction of distortion preset in the CAIPIRINHA 4, MB 3 image (A), and given the reduced TR (1500ms), the MB acceleration of 3 and a CAIPIRINHA acceleration of 4 protocol was the one selected for this study.

fMRI Acquisition

Acquisition of rs-fMRI was performed in the same scan session as the structural MRI described in **Chapter I**, on the same scanner (*Siemens Prisma 3T; Siemens Healthcare, Erlangen, Germany*). The chosen fMRI protocol parameters were the following: TR of 1500ms; TE of 30ms; slice thickness of 4mm with no interslice gap; FOV of 245mm with an acquisition matrix of

162x81 (50% phase encode sampling) for a voxel size of 1.5mm x 1.5mm x 4mm, and 75 slices to give a coverage of 300mm in the z-direction; interleaved acquisition; flip angle of 90°; parallel imaging via CAIPIRINHA with a factor of 4; multi-band slice acceleration with a factor of 3 (see **Figure 3.2**); FOV shift factor of 2. The slice prescription captured at least the brain and spinal cord down to C7 with 72 slices for most subjects. Slice prescription was given parallel to C4 to try to combat dropout in the posterior regions of the spinal cord brought on by the inhomogeneities caused by the differences in tissue type, from spinous processes to the ligamentum flavum. Additionally, a saturation band was placed anterior to the spinal cord at an angle so as to not affect the brain to help suppress outer volume signal and mitigate respiration artifacts.

Brain rs-fMRI Processing

For the analysis focusing on resting state functional activity within the brain the CONN Toolbox (https://www.nitrc.org/projects/conn) [128] was used, which implements functions from the Statistic Parametric Mapping (SPM, http://www.fil.ion.ucl.ac.uk/spm/) toolbox. Both CONN and SPM run in a MATLAB environment. CONN has a multiplicity of functions, including pre-processing, computation, and evaluation of functional connectivity via general linear models using both ROI-to-ROI (also termed seed-to-seed) connectivity and ROI-to-voxel (also termed seed-to-voxel) connectivity fMRI measures (see **Chapter I**, **Section iv** and **Figure 1.6**). To process the rs-fMRI scans of the brains of both CS and HC subjects, the brains were extracted using the Z-axis slices between the top of the brain and the bottom of the cerebellum. This was done to exclude the spinal cord from the brain analyses, given that CONN can operate with only a limited number of slices, and to improve the brain analyses by providing whole-brain data and avoiding any computations being compromised by the inclusion of excessive neck or spinal cord tissue. The

CONN pipeline was also used for segmentation of tissue types and for registration purposes based on the T1 images of the brain (the acquisition of which is described in **Chapter II**).

Because rs-fMRI is interested in low-frequency oscillations (≤ 0.1Hz, but generally lower than 0.08Hz) and because this study used a relatively fast TR (1500ms, or 1.5s), slice-timing correction was not applied to the fMRI data. This was done based on previous literature suggesting negligible effect of slice timing correction on rs-fMRI analysis [257]. While slice-timing correction is important for task-based fMRI (due to the importance of accurately capturing the BOLD effect from functional activation) for rs-fMRI this processing step is not as crucial, thus this step was excluded from analysis.

The CONN pipeline received as input the structural and functional brain data, and ran functional realignment (motion correction, 12 degrees of freedom) and unwarping, registration of functional data to the structural volume, and registration of the structural volume to the standardized space defined by the Montreal Neurological Institute (MNI) averaged T1 brain (http://nist.mni.mcgill.ca/?p=858) [258], and segmentation of structural volume which included skull stripping and processing of tissue types (GM, WM, and CSF). Artifacts Detection Tool (ART), an SPM package (https://www.nitrc.org/projects/artifact_detect/) that is implemented in the CONN pipeline, was used to remove signal intensity spikes and fMRI volumes with excessive motion from the scan, with thresholds for signal intensity outliers set at 9 standard-deviations above or below the mean. A motion limit of 2mm translation and 2° rotation in any direction was also enforced. Spatial smoothing of the functional data was performed using an 8mm full width at half maximum (FWHM) Gaussian kernel. For denoising, signal from the WM, CSF, and motion parameters were regressed from the functional data, as well as being processed with a band-pass filter of 0.008 – 0.09 Hz. The bandpass filter was used to filter the signals to the range of interest

to resting-state fMRI and reduce noise due to physiological effects, such as respiration and pulsation, and noise due to scanner drift.

Brain Functional Connectivity Analysis

In order to evaluate associations between functional connectivity and neurological and pain symptom variables, both ROI-to-ROI and ROI-to-voxel functional connectivity analyses were performed. ROI-to-ROI analyses implemented general linear models (GLM) of the functional connectivity with respect to the symptom variable of interest, with age included as a covariate, and seed and target ROIs were selected based on *a priori* hypotheses and results from **Chapter II**. The seed regions included: The insular cortex (IC), the superior frontal gyrus (SFG), the middle frontal gyrus (MFG), the pre- and postcentral gyri, the superior parietal lobule (SPL), the supplementary motor area (SMA), the anterior and posterior cingulate (AC and PC, respectively), the precuneus, the cuneus, the thalamus, and the putamen. Associations were evaluated between the functional connectivity and mJOA for all subjects (CS and HC), for mJOA within the CS cohort exclusively, and for NDI in the subset of CS patients with NDI scores. Significance was set at $P<0.05$ (two-sided) for the individual connections, and each seed was further thresholded by a false discovery rate (FDR) < 0.05 based on the number of target regions.

Similar regions of interest were selected for the ROI-to-voxel connectivity analyses, though in these cases some of the regions analyzed changed depending on the clinical variable of interest. For mJOA, the precentral gyrus, postcentral gyrus, the SMA, the AC, the precuneus, the SFG, the cuneus, the thalamus, the putamen, and the cerebellum, were selected as seed regions. For NDI, the pre- and postcentral gyri, the SMA, the SFG, the AC and PC, the IC, the SFG and MFG, the thalamus, and the putamen, were selected as seed regions. For all ROI-to-voxel analyses,

brain structures that were divided into left and right in the atlas were seeded for both sides and the main effect (equal weighting of 0.5 to both structures in the GLM) was used in the experimental design. For the cerebellum, the regions of the Automated Anatomical Labeling (AAL) [259] cerebellar atlas, which is based on parcellations of the cerebellum created by Schmahmann *et al* [260], were used to seed the listed cerebellar regions excluding the vermis (total of 10) for both the left and right hemispheres, to give a total of 20 ROIs and a weighting of 0.05 per ROI for the main effect in the GLM. For all analyses, a P-value threshold of 0.05 was used with two-sided tests. For each analysis there was a total of 10 ROIs, and thus a value of 0.05/10 = 0.005 was used as FDR-corrected P-value threshold for cluster size, wherein permutations of cluster sizes were used to determine the necessary cluster size so that the p-value for the cluster was FDR-corrected at the level of 0.005.

Spinal Cord fMRI Processing

The spinal cord data was processed using the Spinal Cord Toolbox (SCT) [101]. First, in order to enable processing using the SCT tools, the spinal cord portion of the rs-fMRI was selected by including slices from approximately the middle of C1 spinal column level down to the level of the C5 or C6 vertebra. Due to ghosting, shimming, decreasing SNR, and motion-related signal dropout, data from the spinal cord tended to be unusable below the C6 vertebral level, but varied from subject to subject; any slices with visually-assessed usable data were preserved. After the spinal cord portion of the data was extracted, an ROI encompassing the spinal cord was drawn on the mean image in order to capture the spinal cord and indicate the region of interest for the spinal cord fMRI motion correction that followed. Motion correction was performed using the SCT MoCo algorithm within the spinal cord ROI, with a polynomial normalization of 2, a smoothing

kernel of 2mm, mean squares estimation for motion, and linear interpolation of the motion corrected slices registered to the first spinal cord volume. After motion correction, a band-pass (0.09 Hz high-pass and 0.0008 Hz low-pass) filter was applied to the rs-fMRI data using a fast fourier transform (FFT) using the Analysis of Functional Neuroimages (AFNI) software's 3dFourier (https://afni.nimh.nih.gov/pub/dist/doc/program_help/3dFourier.html) command, in order to remove scanner drift artifacts, where over the length of the scan the overall mean intensity of the fMRI volumes tends to increase [125,126], as well as unwanted high frequency oscillations in the data.

In order to perform registration between the structural MRI and the rs-fMRI, the spinal cord was segmented from the temporal signal to noise ratio (TSNR) image (**Figure 3.3.A**), computed from the motion-corrected rs-fMRI data, as follows: i) manual drawing of an ROI around the spinal cord in the mean fMRI image; ii) thresholding of the manually-drawn ROI by the TSNR image at an intensity of 8 (voxels with TSNR $\geq$ 8 were kept); iii) in order to preserve the geometry of the spinal cord across slices with dropout (caused by the susceptibility induced by bony anatomy in the spinal cord) the mask was dilated by 2 voxel-levels and then eroded by 2 voxel-levels using the AFNI 3dmask_tool function (https://afni.nimh.nih.gov/pub/dist/doc/program_help/3dmask_tool.html); this process filled-in any holes in the spinal cord due to signal intensity issues and connected two slices with sufficient TSNR signal even if there was a gap with signal dropout between them. This segmentation of the spinal cord from the TSNR image of the fMRI was then used for registration with the structural MRI of the spinal cord (**Figure 3.3.C**). The registration between the fMRI and the T1 image was done by first performing rigid registration of the mean fMRI and T1 images was performed; then, the spinal cord segmentation from the TSNR described above was registered to the T1 segmentation of the spinal cord (described in **Chapter**

II.ii) using a z-regularized slice-by-slice registration of the center-of-mass for each segmentation, which placed the expected center of the spinal cord as determined by the TSNR images at the center of the segmentation for the T1 image (**Figure 3.3.B**).

Since the targeted neural activity is localized to the gray matter, and based on functional divisions of the spinal cord (**Chapter I**, **Section ii**), the gray matter was divided into quadrants: anterior-posteriorly divided into the ventral (anterior) and dorsal (posterior) portions, and divided by left and right sides. This was done using the spinal cord atlas provided in the SCT, which was created using data from Montreal Neurological Institute (MNI), Polytechnique Montreal (Poly) and Aix-Marseille Université (AMU) [101]. This data (termed the PMU atlas, after the initials of the institutions) includes anatomical templates [103], probabilistic gray and white matter maps [261], and probabilistic labeling of vertebral levels [262]. Masks were created for the quadrants of the spinal cord by first taking the gray matter probability map and thresholding at a level of 0.1 to create a binary mask of the gray matter. Then, the left and right, ventral and dorsal quadrants were extracted from the PMU spinal cord atlas by first splitting the atlas in two across the midsection, and then choosing a position along the y-axis (y = -0.5mm) to split the cord into ventral and dorsal portions. Thus, four gray matter regions were generated for use in analyses: left ventral (LV), left dorsal (LD), right ventral (RV), and right dorsal (RD) quadrants (**Figure 3.3.E**).

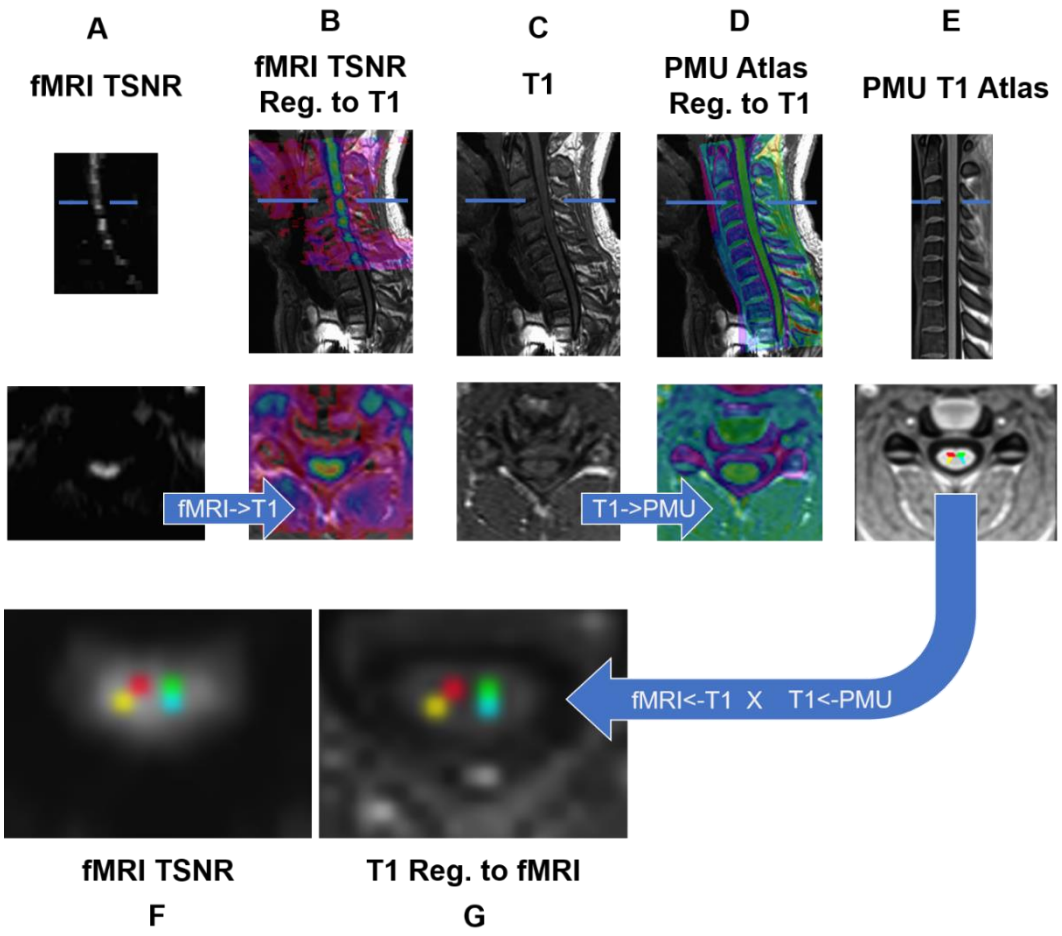

Figure 3.3. Graphical illustration of spinal cord registration procedures. A) through E) display sagittal slices of spinal cord and surrounding anatomy on top, with an axial slice (position indicated by blue lines in the sagittal slice) shown below, while F) and G) show a zoomed-in axial slice of the spinal cord. A) fMRI TSNR was used for registration procedures because it highlighted the spinal cord better than the mean image. B) TSNR image registered to and overlayed on the T1 image. C) T1 image without overlays. E) PMU spinal cord atlas T1w image registered and overlayed on spinal cord T1 image. F) PMU atlas T1w image, with axial image showing the four gray matter quadrants. F) fMRI TSNR and G) T1 registered to fMRI images, with the spinal cord gray matter quadrants from the PMU atlas registered and overlayed.

The PMU atlas spinal cord gray matter quadrants were registered to the T1 space, and from the T1 space to the fMRI space. This was done through several steps using SCT tools. The registration between the T1 image and the PMU spinal cord (**Figure 3.3.D**) atlas was performed using both the segmentations and image data (the acquired T1 image data for the subjects, and the averaged T1 image atlas data for the spinal cord atlas), using the SCT anatomical to atlas registration utility. The inverse of the registration between the T1 space and the PMY atlas was inverted and applied to the spinal cord gray matter quadrant segmentation, with nearest neighbor interpolation, to register the quadrants into the T1 space. The registration warp fields between the fMRI and T1 space (**Figure 3.3.B**) were inverted and used to transform the T1 image, spinal cord segmentation, and spinal cord gray matter quadrants to the fMRI space. **Figure 3.3** provides an outline of this process: registration of fMRI TSNR image (A) to the T1 (C) for the transformation between fMRI space and T1 space (B), and the PMU atlas (E) registration to T1 space (D), both of which were then used to transform the spinal cord gray matter quadrants to the fMRI space (F and G). Once the ROIs from the atlas were registered to the rs-fMRI space, the ROIs were split up by vertebral level to be used for further processing.

Correction of potential physiological confounds that may be present in the spinal cord fMRI data was performed using a simplified version of the component-based correction of physiological noise (CompCorr) [122,263] technique, in which masks of the non-gray matter tissue in the spinal cord and canal were used to extract physiological noise parameters that were then regressed out of the fMRI data. Masks of the WM were created using the segmentation of the spinal cord that was registered to the fMRI space with the gray matter was excluded based on probability maps from the PMU atlas. Masks of the CSF were created by isolating highly varying voxels around the spinal cord using the manually drawn spinal cord ROI, which encompassed both

the spinal cord and the CSF, and excluding the spinal cord mask, then thresholding the remaining mask by the temporal standard deviation fMRI image at a level of 8. These resultant masks of the white matter and CSF in the spinal cord were then used to extract nuisance regressors related to physiological noise.

Previous CompCorr publications reported the number of significant components to use with fMRI data to be around 5 or 6 for the brain [122,263], though similar number of components (3-5) have been used for noise-correction in spinal cord rs-fMRI studies [134]. Thus, staying consistent across brain and spinal cord, the number of components for each region to be used as physiological noise regressors was set to 5. Principle component decomposition of the timeseries was performed in these ROIs using AFNI (3dpc command, https://afni.nimh.nih.gov/pub/dist/doc/program_help/3dpc.html). These 5 principle components form each tissue type (WM and CSF, 10 total) were then regressed out of the motion-corrected data using deconvolution via the AFNI software package (3dDeconvolve command, https://afni.nimh.nih.gov/pub/dist/doc/program_help/3dDeconvolve.html). The residuals from the deconvolutions were used to compare connectivity across the different spinal cord ROIs. Correlations were computed using AFNI (3dNetCorr command, https://afni.nimh.nih.gov/ pub/dist/doc/program_help/3dNetCorr.html).

Spinal Cord rs-fMRI Analysis

The rs-fMRI spinal cord analysis mainly involved two types of measures of interest: connectivity between quadrants within a single vertebral level, and connectivity across the same quadrant but different respective vertebral levels. Previous studies of rs-fMRI connectivity include a study at 7T by Barry *et al* [134], and a recent study at 3T by Eippert et al [249]. Following these studies, FC was calculated across ROIs in the following fashion: lateral connectivity (LV to LD,

and RV to RD), ventral connectivity (LV to RV), dorsal connectivity (LD to RD), and cross connectivity (LV to RD, and LD to RV). These intra-vertebral level connectivities were calculated for vertebral levels C2-C6, and for the mean of the levels C2-C6. The intra-vertebral connectivities were also calculated centered around the site of compression. The mean Pearson's correlation coefficient for each connection of interest was calculated and compared to zero via a one-sample T-test with Bonferroni multiple comparisons correction (resulting uncorrected P-value threshold of 0.0125) to see if these correlations significantly differed from zero. Differences between CS patients and HC subjects were also evaluated at all levels via T-tests with Sidak-Holm multiple comparisons correction to see if any resulted in significance. Pearson's correlations between the spinal cord measures and mJOA and NDI were calculated as well.

Software and Statistical Analyses

The brain-only functional connectivity analysis was performed using the CONN toolbox (Version 16.b, https://www.nitrc.org/projects/conn) in Statistical Parametric Mapping software (Version SPM12, http://www.fil.ion.ucl.ac.uk/spm/), which is based in MATLAB (Version 2014a, https://www.mathworks.com/). Spinal cord segmentation of structural images, and spinal cord registration between fMRI, structural, and atlas spaces (PMU spinal cord T1w atlas and atlas segmentations), as well as motion correction of spinal cord fMRI data, was performed using Spinal Cord Toolbox (SCT Version 3.0.3, https://sourceforge.net/projects/spinalcordtoolbox/). Erosion and dilation of masks for anatomical ROIs, principle component analysis of 4D fMRI data in anatomical ROIs, and calculation of functional connectivity matrices, was performed using the Analysis of Functional Neuroimages software (AFNI Version AFNI_15.3.0, https://afni.nimh.nih.gov/). Statistical analyses were performed using GraphPad Prism (Version

7.0b, La Jolla California USA, www.graphpad.com), and multiple linear regression was performed in Free Statistics Software (Version 1.1.23-r7, http://www.wessa.net/rwasp_multipleregression.wasp/).

ii. Brain Functional Connectivity Results

Association Between Functional Connectivity and Neurological Symptoms

When computing the association between mJOA and FC for ROI-to-ROI results, mJOA presented with both negatively associated (increasing FC with worsening neurological symptoms) and positively associated (decreasing FC with worsening neurological symptoms) connections. For mJOA, the bilateral pre- and postcentral gyri, SMA, and SPL showed decreasing connectivity with the posterior cingulate, while the right putamen displayed increased connectivity with the bilateral thalamus, the left postcentral gyrus, and the left SPL, while the right thalamus had a positive association with the right MFG (**Figure 3.4**, top). When assessing the ROI-to-ROI connectivity within the CS cohort exclusively, similar trends emerged: the putamen displayed positive associations with the thalamus, and left SPL, while the right thalamus showed positive association with the left thalamus and the right MFG, while displaying a negative association with the left and right postcentral gyri (**Figure 3.4**, bottom).

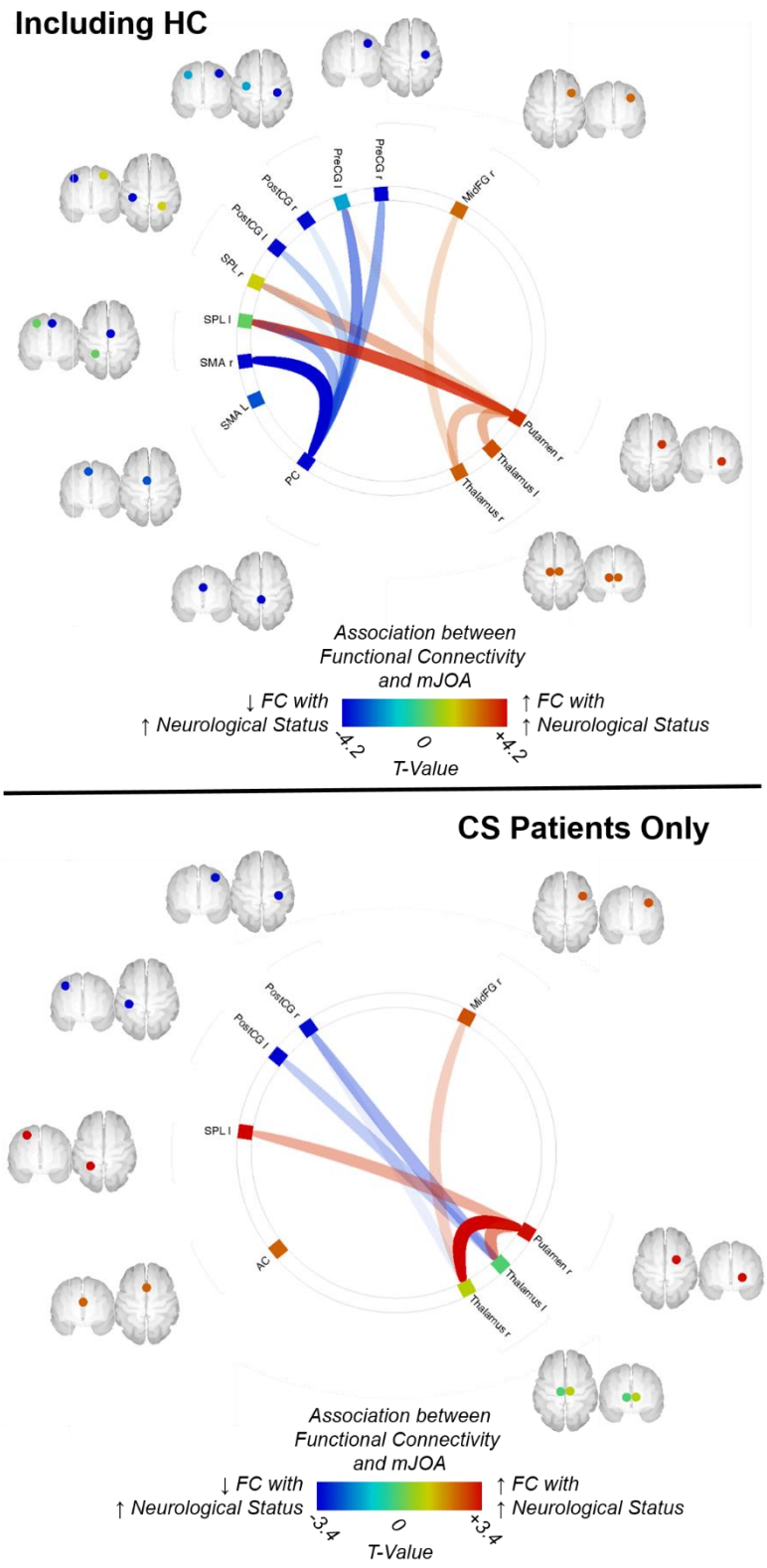

Figure 3.4. Legend presented on next page.

Figure 3.4. Legend: ROI-to-ROI connectivity association with mJOA for group including the HC subjects (top) and group of patients with CS only (bottom). Colors denotes value of the T-statistic, yellow-red denotes positive association (decreasing FC with worsening neurological symptoms), light blue-blue denotes negative association (increasing FC with worsening neurological symptoms). Position of ROIs displayed on midsagittal and mid-axial slices.

For the ROI-to-voxel functional connectivity analysis, multiple seed regions produced clusters where the functional connectivity was significantly associated with mJOA while accounting for age. For mJOA, results where both the overall group, which included HC subjects, and the group of CS patients only demonstrated significant results have been displayed together side-by-side. The results were grouped into sensorimotor cortical regions (precentral gyrus, postcentral gyrus, SMA, **Figure 3.5**), and subcortical regions (thalamus, putamen, cerebellum, **Figure 3.6**). Additionally, regions that showed a significant association with mJOA only in the group that included HC subjects are shown in a separate figure (**Figure 3.7**).

For the sensorimotor regions, both the precentral gyrus and postcentral gyrus displayed a negative association between mJOA and FC (increasing FC with worsening neurological symptoms) with the precuneus and posterior cingulate for the left (**Figure 3.5.A,B,D,E.i**) and the right (**Figure 3.5.A,B,D,E.j**) hemispheres, which was similar across the HC included and CS Only groups. The SMA displayed a larger area of negative association between mJOA and FC in the precuneus and posterior cingulate for left (**Figure 3.5.C,F.i**) and right (**Figure 3.5.C,F.j**) hemispheres in both groups in addition to a regions in the right primary sensorimotor cortex and superior frontal gyrus in both groups (**Figure 3.5.C,F.l**), and a region in the left superior frontal gyrus (**Figure 3.5.F.m**) and left anterior cingulate (**Figure 3.5.F.n**) in the CS Only group.

Additionally, the SMA showed a positive association (increasing FC with increasing mJOA) with the anterior cingulate in the HC Included group (**Figure 3.5.C.k**).

For the subcortical seeds, both the thalamus and cerebellum displayed clusters with a negative association between mJOA and FC (increasing FC with worsening neurological symptoms), particularly with the left (**Figure 3.6.m**) and right (**Figure 3.6.n**) precentral and postcentral gyri in both the HC Included and CS Only groups. The thalamus and cerebellum also presented with a significant positive association (decreasing FC with worsening neurological symptoms) with the anterior cingulate, which was larger for the thalamus (**Figure 3.6.A,D.j** and **A,D.l**,) than for the cerebellum (**Figure 3.6.C,F.j** and **F.l**) for both groups. Additionally, all three structures (the thalamus, cerebellum, and putamen) presented with a significant positive association between mJOA and the bilateral precuneus and posterior cingulate (**Figure 3.6.i,k**) for both groups. The Putamen displayed a large positively associated area around the pre- and postcentral gyri (**Figure 3.6.B,E.o** and **B,E.p**, respectively).

For the additional cortical areas that showed associations only in the HC Included group, the superior frontal gyrus (SFG) displayed a negative association between mJOA and FC (increasing FC with worsening neurological symptoms) with the left anterior cingulate (**Figure 3.7.A.i**) and with the right SMA and precentral gyrus (**Figure 3.7.A.j**). The precuneus displayed a negative association with the left and right precentral and postcentral gyri (**Figure 3.7.B.k** and **B.j**, respectively).

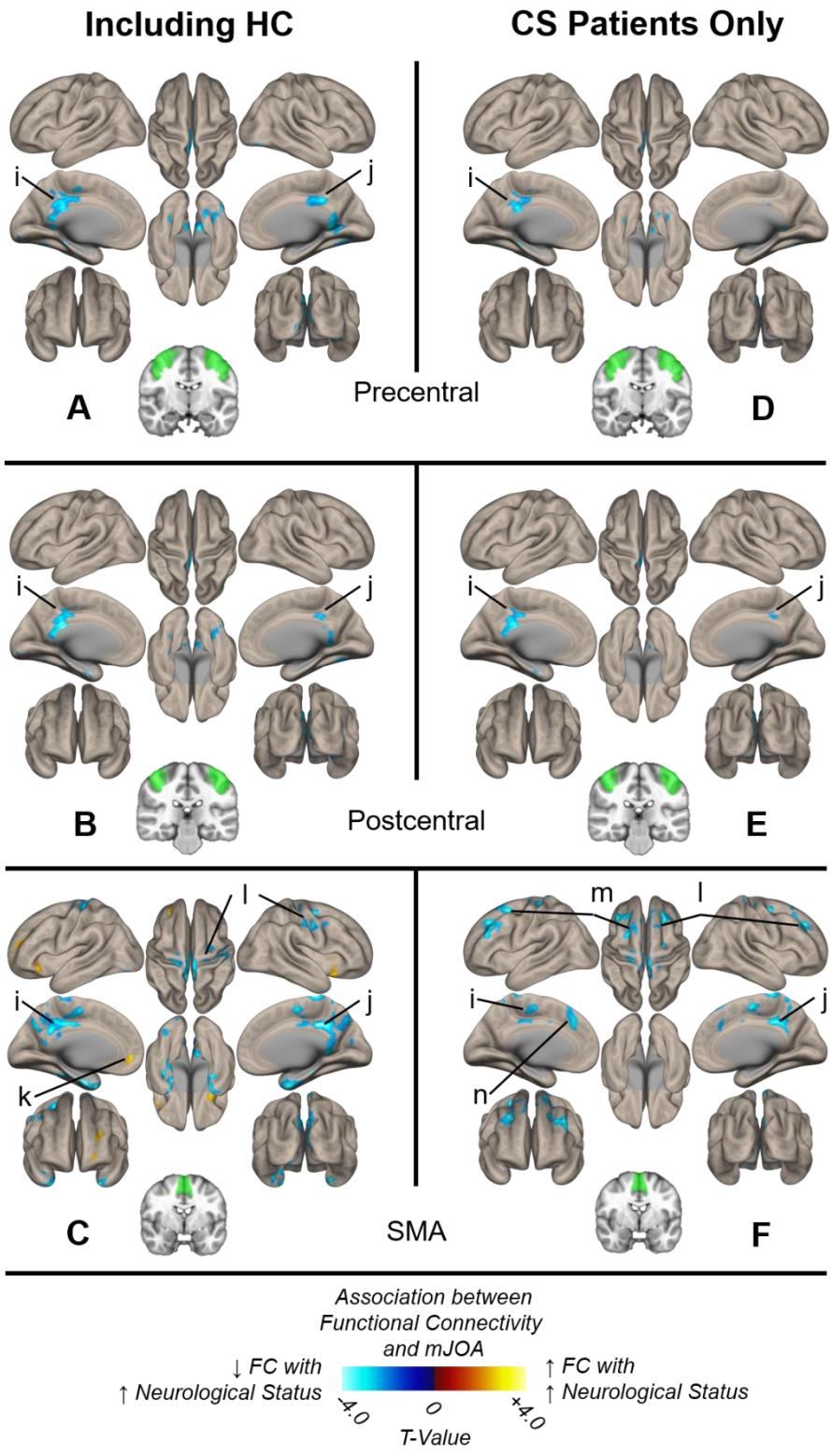

Figure 3.5. Legend Presented on next page.

Figure 3.5. Legend: Brain surface display of associations between functional connectivity (FC) and mJOA based on seeding of sensorimotor cortical regions (displayed on representative MNI brain slices in green) for group including HC subjects (left) and group consisting only of patients with CS (right): A) and D) precentral gyrus, B) and E) postcentral gyrus, C) and F) supplementary motor area (SMA). Blue-light blue denotes negative association between mJOA and FC (increasing FC with worsening neurological symptoms) which occurred in the precuneus and posterior cingulate for the left (i) and the right (j) hemispheres, in regions of the left (l) and right (m) primary sensorimotor cortex, and left superior frontal gyrus (SFG, n). Red-yellow denotes a positive association (increasing FC with increasing mJOA), which was seen in the anterior cingulate (k).

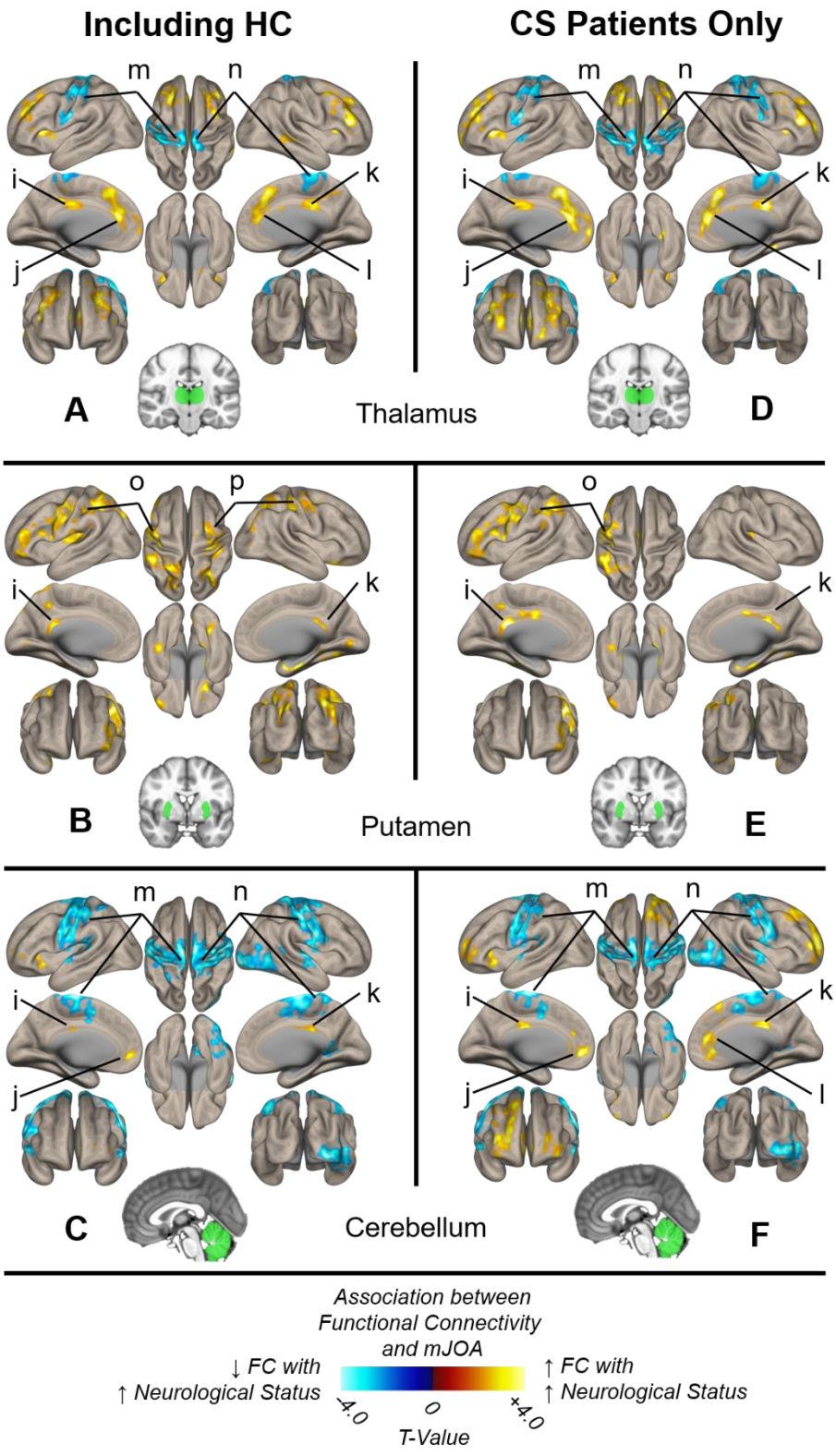

Figure 3.6. Legend presented on next page.

Figure 3.6. Legend: Brain surface display of associations between functional connectivity (FC) and mJOA based on seeding of subcortical regions and cerebellum (displayed on representative MNI brain slices in green) for group including HC subjects (left) and group consisting only of patients with CS (right): A) and D) thalamus, B) and E) putamen, C) and F) cerebellum. Blue-light blue denotes negative association between mJOA and FC (increasing FC with worsening neurological symptoms) which presented in the precentral and postcentral gyri (m and n). Red-yellow denotes a positive association (increasing FC with increasing mJOA), which was seen in the left and right anterior cingulate (j and l, respectively), left and right precuneus and posterior cingulate (i and k, respectively), as well as around the pre- and postcentral gyri (o and p).

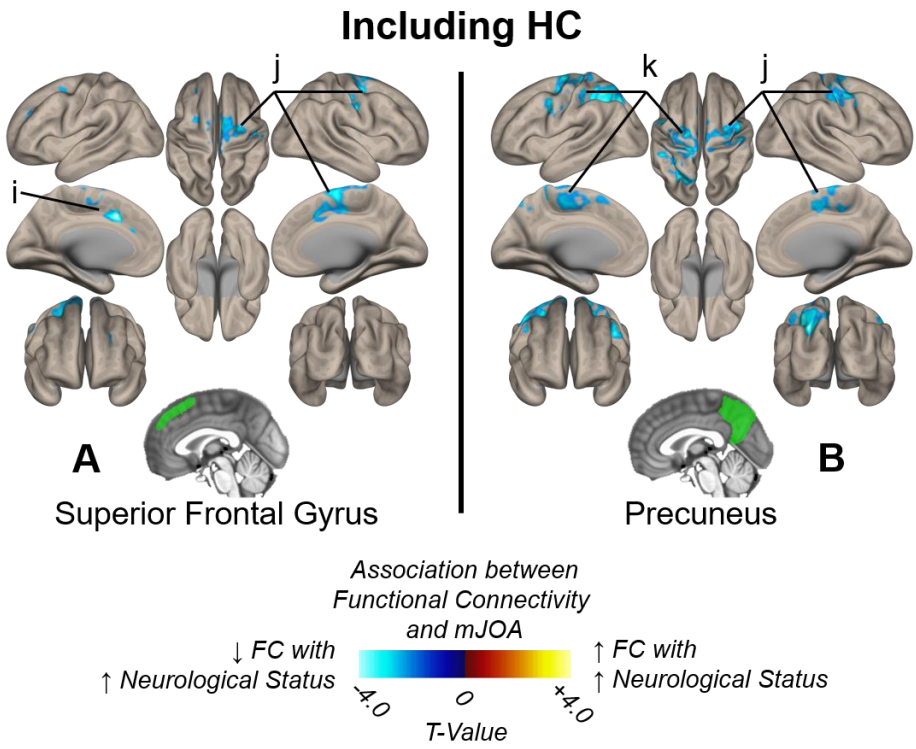

Figure 3.7. Brain surface display of associations between functional connectivity (FC) and mJOA based on seeding of cortical regions (displayed on representative MNI brain slices in green) that only produced significant associations with the overall group that included HC subjects: A) superior frontal gyrus (SFG), B) precuneus. Blue-light blue denotes negative association between mJOA and FC (increasing FC with worsening neurological symptoms) which occurred in the left cingulate (i) and the left and right precentral gyrus and SMA (k and j, respectively).

Table 3.2. Significant clusters from ROI-to-voxel FC analysis association between FC and mJOA for combined group of CS patients and HC subjects, accounting for age.

Seed ROI	Cluster Number	(x,y,z)	Cluster Size (mL)	Cluster P-FDR	Cluster T-Value
PreCG	1	(28, -68, 2)	10.45	0.00003	-6.03
PostCG	1	(6, -82, -32)	10.28	0.00003	-6.77
SMA	1	(-30, -64, -40)	6.29	0.00002	-8.05
	2	(-6, -52, 44)	5.69	0.00002	-4.70
	3	(16, -36, 16)	2.81	0.0006	8.49
SFG	1	(-14, -24, 80)	3.91	0.0004	-4.30
Precuneus	1	(-36, -26, 50)	7.65	0.00003	-4.16
Thalamus	1	(26, -14, 0)	11.30	0.00003	6.65
	2	(4, -24, 60)	4.09	0.00004	-3.74
Putamen	1	(22, -58, -32)	9.38	0.00001	7.52
	2	(-50, 42, 28)	7.82	0.00001	5.32
	3	(24, 0, 76)	3.85	0.00004	4.68
Cerebellum	1	(34, -10, 14)	16.65	0.00002	-4.44
	2	(38, -66, 0)	4.94	0.00003	-5.58
	3	(18, 8, 8)	4.34	0.00005	8.69

Table 3.3. Significant clusters from ROI-to-voxel FC analysis, association between FC and mJOA for group of CS patients only, accounting for age.

Seed ROI	Cluster Number	(x, y, z)	Cluster size (mL)	Cluster p-FDR	Cluster T-Value
PreCG	1	(2, -34, 8)	6.03	0.00005	-6.13
PostCG	1	(-18, -40, 40)	7.36	0.00004	-6.47
SMA	1	(-2, 32, 50)	2.49	0.003	-4.76
	2	(24, -6, 46)	2.38	0.003	-4.18
Thalamus	1	(24, -14, 0)	12.92	0.00002	7.34
	2	(-34, -20, -58)	6.69	0.00002	-4.04
Putamen	1	(-8, -42, 22)	10.38	0.00002	7.80
	2	(-44, -4, 34)	6.04	0.00002	5.30
Cerebellum	1	(18, -18, 74)	14.76	0.00002	-4.67
	2	(18, 8, 8)	8.08	0.00002	5.83

Association Between Functional Connectivity and Neck Pain

When computing the association between NDI and FC for ROI-to-ROI results, NDI presented with both negatively associated (decreasing FC with worsening neck pain) and positively associated (increasing FC with worsening neck pain) connections; in general most of the regions displayed a positive association with FC (**Figure 3.8**). The right thalamus displayed a strong negative relationship with the FC with the anterior cingulate, so with increasing neck pain the FC between thalamus and AC decreased. The bilateral postcentral gyri showed a strong positive association with the bilateral superior frontal gyri, and the bilateral precentral gyri displayed a strong positive association with the bilateral SMA.

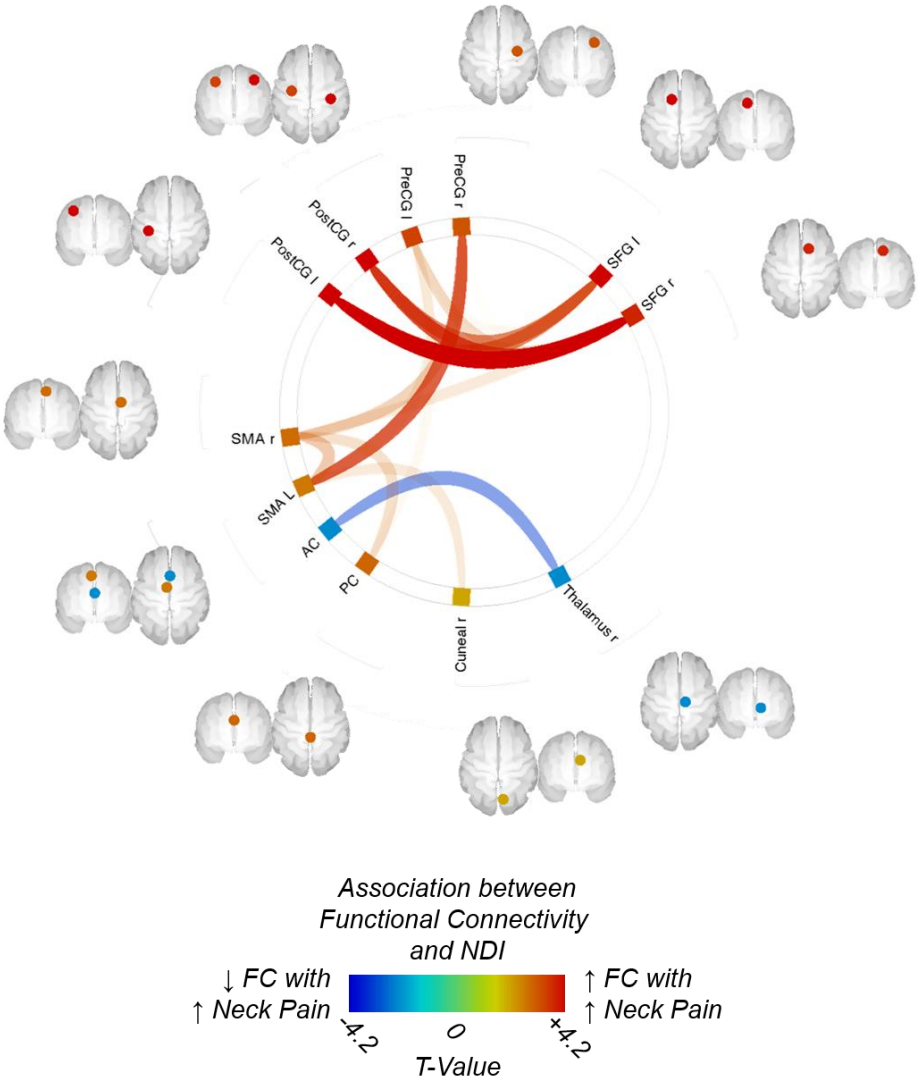

Figure 3.8. ROI-to-ROI connectivity association with NDI. Colors denotes value of the T-statistic, yellow-red denotes positive association (increasing FC with worsening neck pain), light blue-blue denotes negative association (decreasing FC with worsening neck pain). Position of ROIs displayed on midsagittal and mid-axial slices.

For the ROI-to-voxel functional connectivity analysis, several of the seed regions produced clusters where the functional connectivity was significantly associated with NDI while accounting for age. **Figure 3.9** displays the significant associations of the ROI-to-voxel analysis. The most common finding was an increased functional connectivity (increasing FC with worsening neck pain) with the left and right primary sensorimotor cortex (**Figure 3.9.k,l**, respectively). In addition to these predominant associations, the pre- and post-central gyri displayed a positive association of FC to NDI with the left and right superior frontal gyrus (**Figure 3.9.A,B.m,n**, respectively) and the left and right precuneus and posterior cingulate (**Figure 3.9.A,B.i,j**, respectively). The postcentral gyrus also presented with a positive association in the left and right anterior cingulate (**Figure 3.9.B.o,p**, respectively). The thalamus presented with a decreased functional connectivity (decreasing FC with worsening neck pain) in the left and right anterior cingulate (**Figure 3.9.C.q,r**, respectively). The superior frontal and middle frontal gyrus displayed increased FC with the left and right precuneus and posterior cingulate (**Figure 3.9.D,E.i**,**j**, respectively). The posterior cingulate presented with a decreased FC to the right precuneus (**Figure 3.9.F.s**). In addition to these areas, the AC seed also displayed a negative association between NDI and FC, but this region was confined to the subcortical regions, primarily the thalamus, which is seen in the connectome ring in **Figure 3.8**. The clusters produced by the NDI ROI-to-voxel analysis are listed in **Table 3.4**.

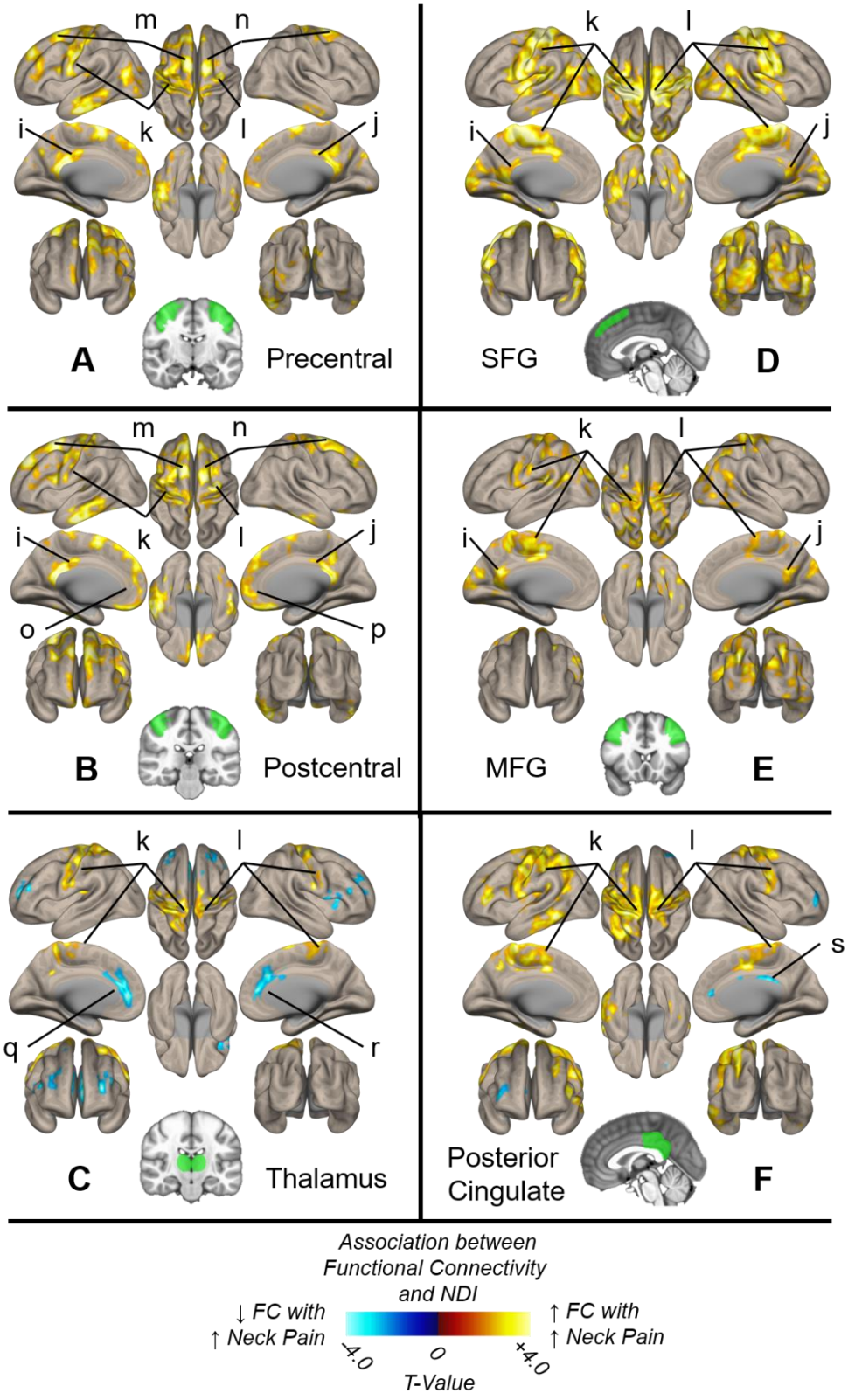

Figure 3.9. Legend presented on next page.

Figure 3.9. Legend: Brain surface display of associations between functional connectivity (FC) and NDI based on seeding of sensorimotor cortical and subcortical regions (displayed on representative MNI brain slices in green): A) precentral, B) postcentral, C) thalamus, D) superior frontal gyrus (SFG), E) middle frontal gyrus (MFG), F) posterior cingulate (PC). Blue-light blue denotes negative association between mJOA and FC (increasing FC with worsening neurological symptoms) which presented in the left and right anterior cingulate (q and r, respectively), as well as the right posterior cingulate (s). Red-yellow denotes a positive association (increasing FC with increasing mJOA), which was seen bilaterally in the posterior cingulate and precuneus (i and j), the pre- and postcentral gyri (k and l), SFG (m and n), and AC (o and p).

Table 3.4. Significant clusters from ROI-to-voxel FC analysis association between FC and NDI for group of CS patients, accounting for age.

NDI	Cluster Number	(x, y, z)	Cluster Size (mL)	Cluster p-FDR	Cluster T-Value
PreCG	1	(-2, -38, 20)	17.56	0.00002	6.16
	2	(-26, -74, -28)	11.44	0.00002	6.22
PostCG	1	(-16, 6, 66)	17.94	0.00002	6.06
	2	(-4, -40, 20)	16.81	0.00002	8.87
Thalamus	1	(68, -6, 22)	9.02	0.00005	5.89
	2	(22, 38, 12)	4.45	0.0001	-6.39
SFG	1	(-34, -12, 2)	54.33	0.00003	5.83
MFG	1	(-36, -40, 20)	16.14	0.00004	4.68
	2	(48, -26, -38)	2.80	0.001	5.02
PC	1	(-30, -58, 62)	23.16	0.00003	5.03
	2	(18, -54, -30)	3.01	0.0007	5.4
	3	(8, -18, 18)	2.32	0.002	-7.76
AC	1	(-10, -10, 8)	3.18	0.003	-9.2

iii. Spinal Cord Functional Connectivity Results

Intra-Vertebral Level Spinal Cord Functional Connectivity

The intra-vertebral level spinal cord connectivity is displayed in **Figure 3.9**, and all levels exhibited a similar pattern: highest correlations for the connectivity across lateral segments, followed by connectivity across ventral segments and connectivity across dorsal segments, followed by connectivity of crossing segments which was close to zero. No visually striking differences seemed to be present between CS patients and HC subjects. **Table 3.5** lists the mean values for Pearson's correlation coefficients across the different levels, which range from 0.17 to 0.39 for lateral connectivity, 0.15 to 0.17 for the ventral connection, 0.05 to 0.19 for dorsal connections, 0.02 to 0.11 for cross-connections. Ventral connections appeared to be stable across levels (small variation, range of only 0.02), while dorsal connections seem to increase in strength further down the cervical cord (C5, C6). Cross-connections were at their highest at C6 (around 0.1), and lateral connections were at their lowest at C6 (around 0.2). At each vertebral level the Bonferroni-corrected significance varied, with the HC dorsal connections not reaching significance at a few levels (C2, C3, and C6) and CS dorsal not reaching significance at C2, while for the cross-correlation multiple levels did not reach a mean correlation coefficient significantly different from zero for both CS (C2, C5, C6) and HC (all individual levels). Only the C2 lateral connection showed a difference for CS vs HC (P=0.01), and no levels or connections showed a significant association with mJOA or NDI scores. When excluding sites where compression in CS patients, either the site of maximal compression or any noted compression, there were still no significant differences between groups or associations with symptom scores.

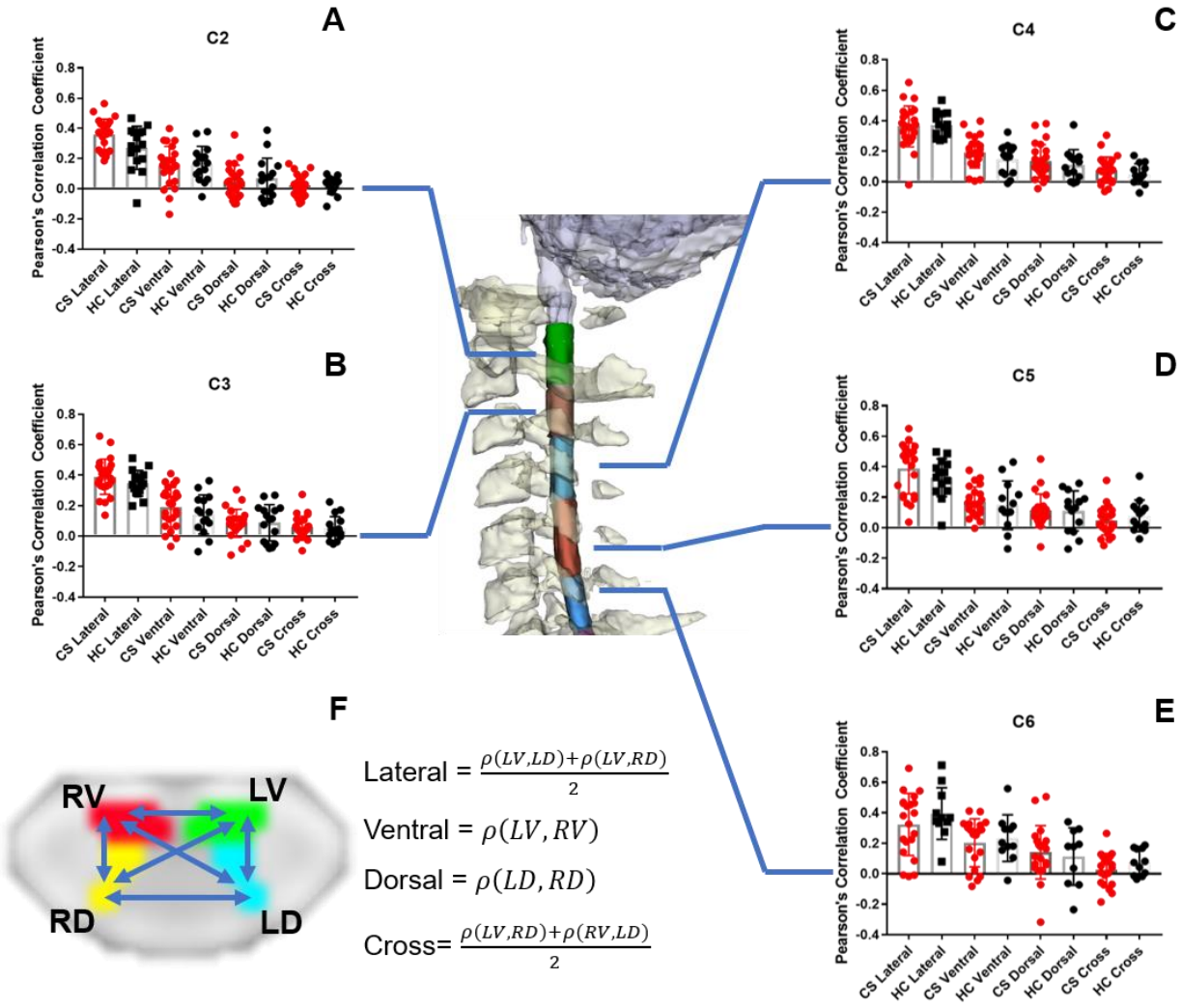

Figure 3.10. Within-level functional connectivity of spinal cord gray matter quadrants. Connectivity is graphed for C2 – C6 (A-E), indicated on the representation of the spinal cord in the center, with the CS patients in red, the HC subjects in black, with mean and standard deviation plotted for each connection. F) displays an illustration of the spinal cord quadrants as well as the labels of the connections between regions that are used for the graphs of the correlations.

The mean values across all vertebral levels were also reported in **Table 3.5**, where the values were, for both CS and HC, lateral connectivity being over 0.3, ventral connectivity being around 0.2, dorsal connectivity being around 0.1, and cross-connectivity being around 0.05. These correlations were found to be significant after Bonferroni multiple comparisons correction. **Figure 3.11.A** displays the mean correlation coefficients averaged across levels C2 - C6, which all show overall positive correlations, but vary in magnitude. No significant differences between intra-level spinal cord connectivity were found between CS patients and HC subjects.

Table 3.5. Intra-level functional connectivity for CS patients (pink shading) and HC subjects (gray shading). Levels C2-C6 are displayed, as well as the mean across C2-C6. Mean, standard deviation (St. Dev.) and Bonferroni-corrected P-value of one-sample T-test (difference from 0) are shown.

Level	Value	CS Lateral	HC Lateral	CS Ventral	HC Ventral	CS Dorsal	HC Dorsal	CS Cross	HC Cross
C2	*Mean*	0.36	0.27	0.15	0.17	0.05	0.07	0.02	0.02
	St. Dev.	0.10	0.14	0.13	0.12	0.11	0.13	0.07	0.06
	P-Value	<0.0001	<0.0001	0.0001	0.0003	0.31	0.48	0.99	0.99
C3	*Mean*	0.39	0.35	0.19	0.14	0.08	0.09	0.06	0.05
	St. Dev.	0.12	0.08	0.13	0.13	0.09	0.12	0.07	0.08
	P-Value	<0.0001	<0.0001	<0.0001	0.006	0.0008	0.08	0.007	0.17
C4	*Mean*	0.36	0.37	0.19	0.15	0.13	0.11	0.08	0.05
	St. Dev.	0.13	0.08	0.10	0.10	0.11	0.10	0.09	0.07
	P-Value	<0.0001	<0.0001	<0.0001	0.0007	<0.0001	0.01	0.001	0.16
C5	*Mean*	0.39	0.33	0.17	0.15	0.11	0.11	0.05	0.08
	St. Dev.	0.17	0.12	0.10	0.16	0.11	0.13	0.09	0.10
	P-Value	<0.0001	<0.0001	<0.0001	0.05	0.0003	0.04	0.17	0.12
C6	*Mean*	0.20	0.17	0.16	0.15	0.18	0.19	0.11	0.09
	St. Dev.	0.04	0.05	0.04	0.05	0.04	0.06	0.02	0.03
	P-Value	<0.0001	0.0001	0.0001	0.004	0.01	0.72	0.99	0.12
Mean C2-C6	*Mean*	0.37	0.33	0.19	0.18	0.10	0.10	0.05	0.05
	St. Dev.	0.07	0.06	0.07	0.09	0.06	0.07	0.05	0.04
	P-Value	<0.0001	<0.0001	<0.0001	<0.0001	<0.0001	0.0003	0.0003	0.0008

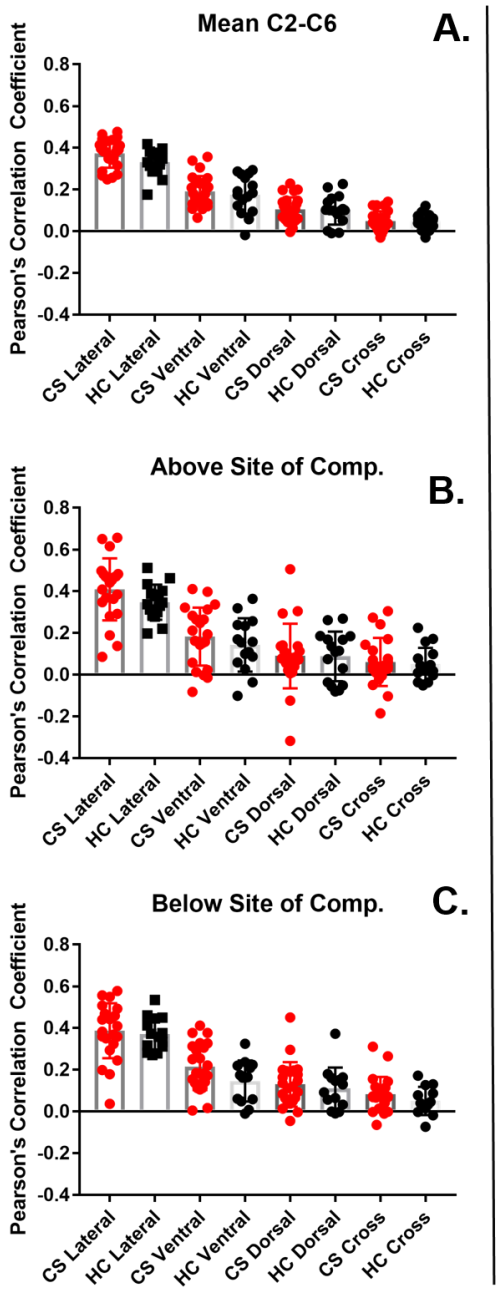

D. mJOA

	Lateral	Ventral	Dorsal
C2	-0.32	0.11	0.28
C3	-0.16	0.14	-0.08
C4	0.27	0.36	-0.17
C5	-0.10	0.23	0.16
C6	-0.10	0.23	0.16
Ave C2-C6	-0.18	0.24	0.21
Site Above Comp.	-0.24	-0.07	-0.07
Site Below Comp.	-0.03	0.08	0.05

Pearson's Correlation Coefficient

+0.3 *-0.3*

0

E. NDI

	Lateral	Ventral	Dorsal
C2	-0.20	0.10	0.31
C3	-0.28	0.01	-0.10
C4	0.11	0.33	-0.03
C5	-0.03	0.17	0.14
C6	-0.06	-0.03	-0.02
Ave C2-C6	-0.22	0.20	0.24
Site Above Comp.	-0.16	0.00	-0.09
Site Below Comp.	0.01	0.33	0.13

Figure 3.11. Pearson's correlation coefficients for intra-level spinal cord connectivity. A) averaged across levels C2-C6 for CS patients (red) and HC subjects (black). B) Above and C) below site of compression for CS, C3 and C4 respectively for HC. Correlations between FC and D) mJOA and E) NDI scores at each vertebral level, averaged across the vertebral levels, and above and below the site of maximal compression.

When evaluating the functional connectivity centered around the site of compression, similar trends emerged as for the individual regions and averaged results: high FC at the lateral connections, followed by ventral and dorsal, and lowest in the cross-connections (**Figure 3.11.B,C**). However, these measures did not differ significantly between the groups and were not found to be associated with symptoms. In order to get some idea of the relationship between symptom measures and the intra-vertebral spinal cord FC, the correlation of each symptom score was computed with respect to the FC at each vertebral level, the average FC across the levels, and the FC at the vertebral level above and below the site of maximal compression (**Figure 3.11.D,E**). While correlation coefficients were low, it appeared that the lateral segment FC was negatively correlated with both mJOA and NDI, the ventral FC was positively associated with mJOA and NDI, and the relationship with the dorsal FC was variable. Additionally, when centering around the site of maximal compression, the correlation coefficients tended to be lower, potentially indicating more unreliable FC measurements around the site of compression.

Inter-Vertebral Level Spinal Cord Functional Connectivity

When examining the functional connectivity between the spinal cord quadrants at different vertebral levels only very weak correlations were seen. The mean FC between any pair of vertebral levels and respective quadrants showed only a maximum of 0.028 for CS subjects and 0.021 for HC, and only a negative maximum (anticorrelation) of -0.053 for both the CS and HC groups. No associations with mJOA or NDI, nor group differences were observed across FC between respective quadrants at any level. No associations or differences were seen when performing tests above and below the site of compression and at C3 for healthy subjects.

iv. Brain Functional Connectivity Results in Relation to Compression

Association Between Brain Functional Connectivity and Torg Ratio

When computing the association between the MR-Equivalent Torg Ratio and FC for ROI-to-ROI results, mJOA presented with only a couple positively associated connections (increasing FC with increasing or worsening compression). The AC showed decreasing connectivity with the right precentral gyrus and the left SMA (**Figure 3.12**). For the ROI-to-voxel functional connectivity analysis, multiple seed regions produced clusters where the functional connectivity was significantly positively associated with Torg Ratio (decreasing connectivity with worsening compression) while accounting for age. Sensorimotor cortical region (precentral, postcentral, SMA) seeds presented with an overall similar pattern, including a positive association between Torg and FC (decreasing FC with greater degree of compression) in clusters in the right precuneus for all seeded regions (**Figure 3.12.k**), and the left precuneus for the precentral gyrus (**Figure 3.12.A.i**). Both the precentral and SMA displayed a positive association with FC in the left and right anterior cingulate (**Figure 3.12.j** and **Figure 3.12.l**, respectively). The anterior cingulate and precuneus presented with a positive association between Torg and FC in clusters in the left and right precentral and postcentral gyri (**Figure 3.14.D.m** and **Figure 3.14.D.n**, respectively). The anterior cingulate also displayed a positive association with the left and right precuneus (**Figure 3.14.D.i** and **Figure 3.14.D.j**, respectively), and the cerebellum displayed a small positively associated cluster spread around postcentral gyrus and insular cortex (**Figure 3.14.F.n**). The clusters produced by the Torg ROI-to-voxel analysis are listed in **Table 3.6**.

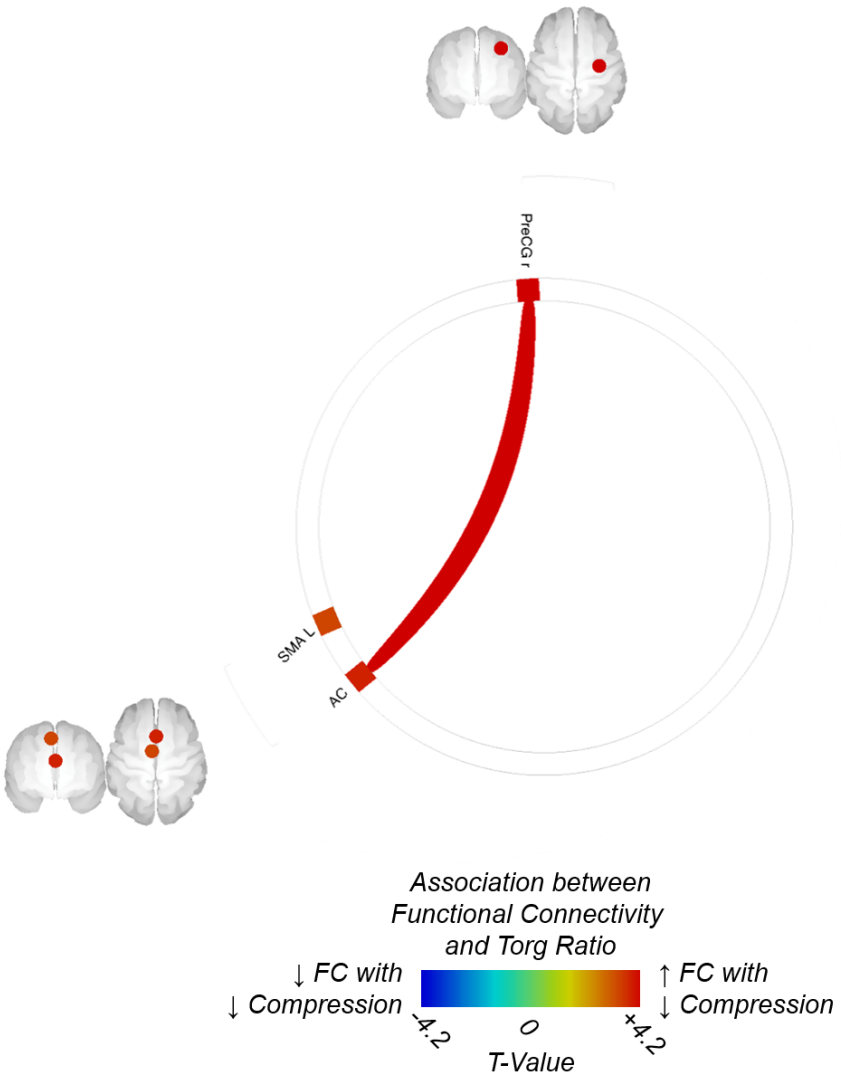

Figure 3.12. Brain ROI-to-ROI connectivity association with MR-Equivalent Torg Ratio. Colors denotes value of the T-statistic, yellow-red denotes positive association (increasing FC with worsening spinal cord compression). Position of ROIs displayed on midsagittal and mid-axial slices.

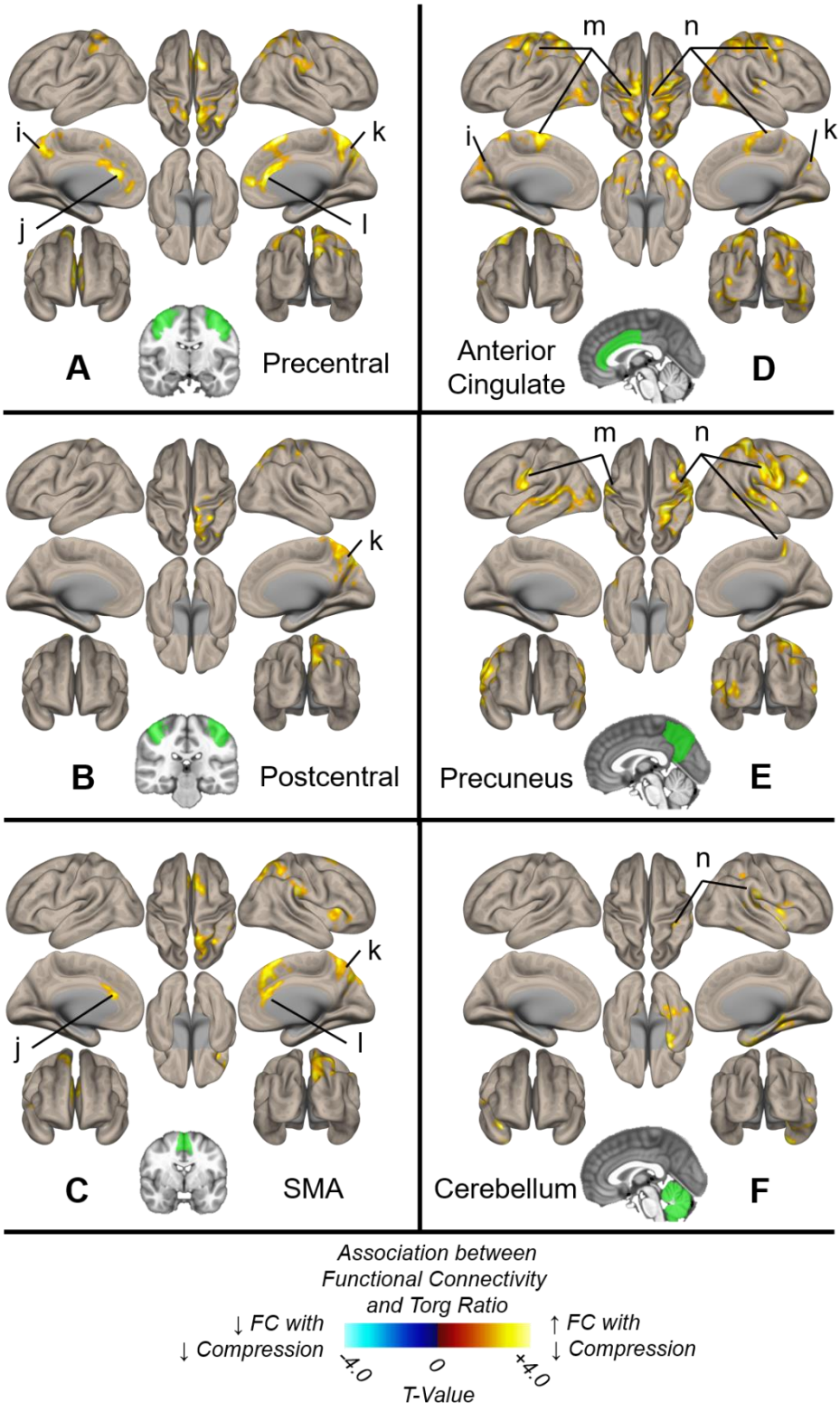

Figure 3.13. Legend presented on next page.

Figure 3.13. Legend: Brain surface display of associations between functional connectivity (FC) and MR-equivalent Torg Ratio based on seeding of sensorimotor cortical regions (displayed on MNI brain slices in green): A) precentral, B) postcentral, C) supplementary motor area (SMA), D) anterior cingulate, E) precuneus, F) cerebellum. Red-yellow denotes a positive association (increasing FC with increasing Torg Ratio or less-severe compression), which was seen in the left and right posterior cingulate and precuneus (i and k, respectively), in the left and right anterior cingulate (j and l, respectively), and in the left and right primary sensorimotor regions (m and n, respectively).

Table 3.6. Significant clusters from ROI-to-voxel FC analysis association between FC and the MR-equivalent Torg Ratio for group of CS patients, accounting for age.

Torg	Cluster Number	(x,y,z)	Cluster Size (mL)	Cluster P-FDR	Cluster T-Value
PreCG	1	(12, -56, 54)	4.64	0.0002	4.79
	2	(8, 14, 62)	2.56	0.003	4.4
PostCG	1	(34, -46, 74)	2.93	0.003	4.99
SMA	1	(50, -28, 30)	3.10	0.001	4.62
	2	(10, -10, 4)	2.38	0.003	5.03
	3	(2, 18, 62)	2.01	0.005	4.18
AC	1	(46, -4, 62)	9.43	0.00002	3.84
	2	(30, -52, -60)	8.95	0.00002	4.65
Precuneus	1	(60, -20, -6)	8.14	0.00004	4.85
	2	(-38, -56, -8)	3.20	0.0005	4.27
Cerebellum	1	(36, -2, -18)	6.86	0.00005	5.68

v. Discussion

Functional activation studies in patients with cervical stenosis (CS) and associated myelopathy have found increased areas of activation in simple motor tasks, such as dorsiflexion of the ankle [203,204]. This increased area of activation decreased in size after surgery and recovery in these patients, returning to levels approximating those of neurologically intact healthy volunteers [203,204]. These increases in functional activation associated with injury to the spinal cord have also been observed in patients with traumatic SCI, where a host of sensorimotor regions have been reported as showing increased activation during functional tasks in fMRI studies [177]. Additionally, resting-state fMRI studies have shown increased functional connectivity between sensorimotor cortical and subcortical regions [175,176]. With the existence of these functional alterations in patients with cervical stenosis, this chapter aimed to evaluate the association between neurological and pain symptoms in patients with CS and the functional connectivity within the brain based on sensorimotor regions of interest and based on the results of altered cortical and subcortical structures presented in **Chapter II**. Additionally, recent studies have been able to identify resting-state functional activity in the spinal cord [134,249,264], and thus one goal of this chapter was to extend the resting-state fMRI to include the spinal cord in addition to the brain. This was possible thanks to technological advancements that enable more rapid acquisition of EPI volumes, namely multi-band (MB) [250,265] and CAIPIRINHA [250,253,254] acceleration techniques. This acceleration enabled the acquisition of both the brain and the spinal cord for analysis.

The results from this chapter indicate an overall increase in functional connectivity with worsening neurological symptoms (mJOA) and with worsening neck pain (NDI) across sensorimotor regions, as well as provide support the involvement of similar supplementary areas, namely the precuneus, superior frontal gyrus, and anterior cingulate, which were assessed as

structurally altered in **Chapter II**. The spinal cord resting state connectivity provided similar results to previous studies, but did not appear to correlate with symptom severity or provide significant differences between patients with CS and HC subjects, potentially indicating that more technical advancements are required before high-enough quality resting-state fMRI data of the spinal cord can detect disease- or symptom-specific changes *in vivo* on clinical MRI scanners.

Associations Between Functional Brain Measures and Symptoms

For the primary sensorimotor structures, increased FC with worsening neurological function (decreasing mJOA score) was seen for the pre- and post-central gyri, and the supplementary motor area (SMA), to the regions of the precuneus and posterior cingulate. Additionally, the thalamus and cerebellum displayed strong increasing FC with worsening neurological symptoms to the pre- and post-central gyri, but displayed increased functional connectivity to areas of the posterior cingulate and precuneus and to areas of the anterior cingulate and superior frontal gyrus. The precuneus showed an increasing FC with worsening neurological symptoms to the pre- and post-central gyri, though this was seen only in the group that included HC as neurologically intact subjects. Only the putamen demonstrated a decreasing relationship of FC to neurological symptoms to the pre- and post-central gyri. The putamen also showed decreased FC to the precuneus and posterior cingulate.

Similar to the hypothesized role of increased area of activation found in functional activation studies in CSM [203,204] and SCI patients [177], the increased functional connectivity with worsening neurological symptoms between primary somatosensory cortex and supplementary areas (precuneus, thalamus, cerebellum, and superior frontal gyrus) may indicate some form of compensatory mechanism for the difficulty to accomplish motor tasks. Additionally, in a study in

CSM patients performed by Hrabalek *et al*, functional activation increases were not limited to primary sensorimotor cortex, but were found in the supplementary motor area, anterior cingulate, thalamus, basal ganglia, and cerebellum [206]. These areas were ostensibly recruited to assist the primary sensorimotor cortex in accomplishing motor tasks. This is reflected in the increased connectivity between these regions in the present study, where all the above regions show increased connectivity with worsening neurological symptoms to regions of the primary sensorimotor cortex, except for the putamen. This may be due to the inhibitory function of the putamen in motor planning and execution [50,56], indicating that the decreased FC with symptom severity exhibited by CS patients indicates decreased inhibition of motor movements, which complements the increased FC seen in other sensorimotor regions. Another relevant study evaluated positron emission tomography (PET) of the resting cerebral metabolic rate of glucose metabolism (CMRGlu) in patients with spinal cord injury and found relatively increased metabolism in the supplementary motor area, the anterior cingulate, and the putamen [266], all of which were shown to be structurally and functionally altered in this and the previous chapter.

Worsening neck pain (increasing NDI score) was associated with increased FC, particularly to the pre- and post-central gyri, the superior frontal gyrus, and the precuneus and posterior cingulate. However, the thalamus did present decreasing FC to the anterior cingulate with increasing neck pain, similar to the relationship presented with the mJOA association (decreasing FC with worsening symptom). While there is variation in the characteristics of functional connectivity findings in chronic pain conditions, the motor cortex is an area that repeatedly appears as altered in chronic pain conditions [267]. In a study of patients with chronic pain from rheumatoid arthritis, there was largely increased functional connectivity across sensorimotor-related regions, such as the primary sensorimotor cortex, the supplementary motor area, and cingulate cortex [268].

Electromyographic recordings of chronic back pain patients have indicated that the organization of the motor cortex was associated with severity of lower back pain [269]. Patients with chronic pelvic pain have demonstrated altered resting state FC of motor regions related to pelvic floor muscle control [270,271]. Thus, a growing area of research is the targeting of motor regions for pain relief. While invasive motor cortex stimulation has been used for cases of intractable pain, research has also been conducted with repetitive transcranial magnetic stimulation (TMS) of the motor cortex over a wide variety of chronic pain conditions [272], and has yielded effects in conditions ranging from fibromyalgia [273], to neuropathic pain [274-276], and chronic back pain [277]. This may be an important factor in patients with chronic neck pain, especially in patients with added myelopathy, as this implicates motor cortex involvement in both neurological symptoms and chronic pain.

Functional Spinal Cord Measures in CS and HC

Results from this chapter follow similar trends to those reported in previous studies of resting-state fMRI in the spinal cord [134], particularly the study by Eippert *et al* which had the most similar methodology [249]. These studies reported functional connectivity between the ventral horns and between the dorsal horns, with the functional connectivity between the ventral horns usually being larger than the dorsal horns, which was also observed in this study. Similarly, the cross-FC (connection between contralateral ventral and dorsal horns) was near zero. In contrast to the study by Eippert *et al*, this study found larger correlations between lateral (left-ventral to left-dorsal, and right-ventral to right-dorsal). This may be due to differences in the sampled anatomic area (Eippert *et al* sampled lower in the spinal cord, going from C6 to T2), or may be due to the fact that the data was analyzed in the subject space and not transformed and resampled to a standardized atlas, where Eippert resampled the data to $1mm^3$ isotropic standard space, introducing additional

smoothing effects. However, in a study in monkeys, Chen *et al* found FC not only between the dorsal and ventral horns, but also laterally across ventral and dorsal horns [164], indicating that our results may better align with this high-resolution study in primates. While patterns of FC were seen within vertebral levels of the cord, little to no associations were seen across intervertebral levels. Chen et al in their study in monkeys found that adjacent slices demonstrated functional connectivity, but as the slices increased in distance from each other the associations became weaker [164]. Since this study was performed across vertebral levels as a whole, the superior-inferior connectivity previously reported by, for example, Kong *et al* [264], may be lost when looking across entire vertebral levels and only present in adjacent segments or in isolated regions throughout the spinal cord.

The spinal cord functional connectivity did not correlate with patient symptoms. This may be due to the presence of excessive noise and large variation in the correlation measures measured from one subject to another, even in the HC population. Thus, more reliable detection and strength of correlation should be established in HC subjects in order to accurately detect deviations of spinal cord functional activity in patient populations.

Associations Between Functional Brain Measures and Spinal Cord Structure

Worsening compression (decreasing Torg Ratio) was associated with decreased FC between all areas, which for the most part included the primary motor, primary sensory, supplementary motor, and anterior cingulate and precuneus regions, along with a small region produced when seeding the cerebellum. The direction of the Torg Ratio associations (decreasing FC with worsening compression) contrasts with the results from mJOA and NDI, where the FC was predominantly increasing with symptom severity and a few select regions displayed the

opposite effect. It is important to bear in mind that the Torg Ratio is generally not reflective of symptom severity, so identical relationships with neuroimaging variables as those presented by mJOA are not expected. However, with greater compression one would expect greater compensation (increased) FC. This discrepancy in Torg Ratio results may be due degenerative processes without accompanying compensatory mechanisms in brain function, or the Torg Ratio may have anatomical correlates that are separate from the disease process but rather more related to aging (such as the change in size of the intervertebral discs) [278], and with age FC tends to decrease in the network of motor regions [279]. While age is accounted for in the model and thus aging itself may not be the cause of these changes, the Torg Ratio may be sensitive to age-related degenerative changes that may be variable from one subject to the next and thus capturing an additional dimension of aging in addition to the physical age of the subject.

Chapter IV. Diffusion MRI and Microstructural Alterations of the Neuraxis in Patients with Cervical Stenosis and Associated Myelopathy

Diffusion magnetic resonance imaging (MRI) of the spinal cord has yielded promising results in the search for imaging biomarkers in patients with cervical stenosis (CS) with neurological symptoms, which is termed cervical spondylotic myelopathy (CSM). Both standard diffusion tensor imaging (DTI) metrics [200,201], as well as diffusion tractography-derived measures such as deterministic tractography and probabilistic tractography track density imaging (TDI) [280], have shown strong correlations with clinical symptom scores, performing better than strictly anatomical measures of the spinal cord such as the Torg Ratio. Additionally, microstructural changes in CSM have also been detected rostral to the site of maximal compression [200], and altered microstructure has been detected in spinal cord injury (SCI) patients even further rostrally, into the cerebral peduncles and internal capsule white matter fibers in the brain [160].

This chapter sought to probe the microstructural changes in patients with cervical stenosis and resulting myelopathy, which extend beyond the spinal cord at the site of compression, and manifest in the white matter pathways in the rostral spinal cord and brain. In order to evaluate these associations, a diffusion MRI sequence was used to acquire both the brain and the spinal cord down to the C3 vertebral level in patients with cervical stenosis (CS) and in healthy control (HC) subjects. A DTI MRI of the spinal cord at the site of compression was also acquired. The relationship between patient symptoms and microstructural characteristics was evaluated via both standard diffusion tensor imaging (DTI) metrics, and advanced diffusion metrics from generalized q-sampling imaging (GQI). These measures were evaluated in *a priori* regions based on atlas-based ROIs in both the brain and spinal cord. Additionally, probabilistic tractography between predefined regions was performed and evaluated with respect to symptom measures.

i. Diffusion MRI Acquisition and Processing

Subject Cohort

The same cohort of CS patients and HC subjects who underwent combined brain and spinal cord imaging was used in this chapter. Patient and HC demographic information is thus listed in **Appendix A** and reflected in **Table A.1**.

Acquisition and of Brain and Upper Cervical Spinal Cord Diffusion MRI Data

Brain and upper cervical spinal cord diffusion MRI data was acquired using a Multi-Band (MB) echo planar imaging (EPI) protocol supplied by the Center for Magnetic Resonance Research, Department of Radiology (CMRR, https://www.cmrr.umn.edu/multiband/), at the University of Minnesota, via research collaboration with Siemens (*Siemens Healthcare, Erlangen, Germany*). The diffusion MRI sequence utilized a q-space diffusion sampling scheme from Siemens, with a q-space factor of 3 and a maximal b-value of 2000 mm^2/s. This resulted in a sequence that acquired 60 different diffusion weighted images, ranging in b-value from 250 to 2000 mm^2/s. **Figure 4.1.A** shows the diffusion sampling scheme.

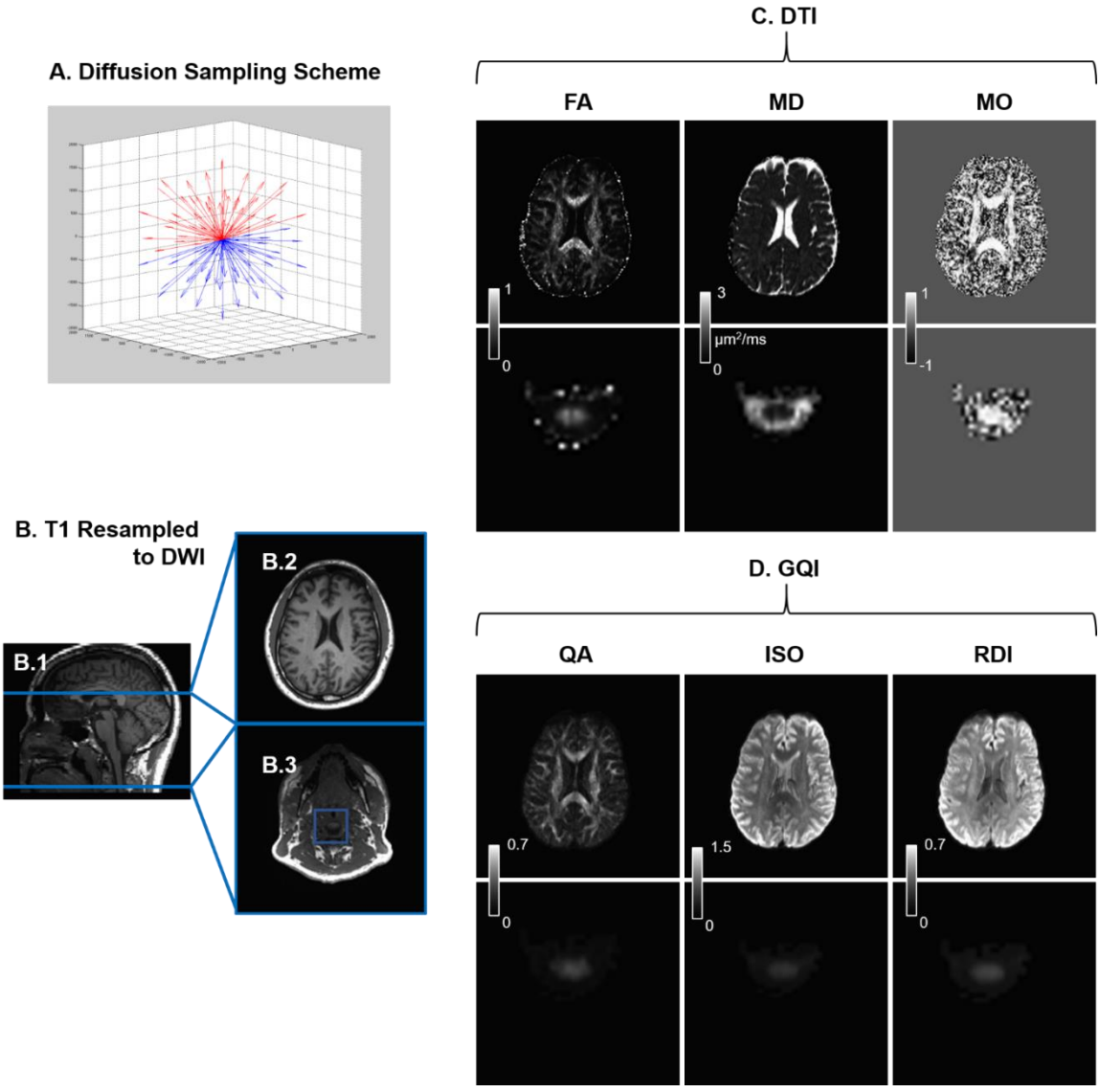

Figure 4.1. Illustration of diffusion MRI metrics used in this chapter. A) diffusion sampling scheme used in this chapter. Red arrows represent acquired diffusion directions with blue arrows filling in the opposite (equivalent) direction to the red arrows. B) T1 image resampled to DWI, displayed on the sagittal slice (B.1) where the axial brain (B.2) and spinal cord (B.3) images were taken from. C) DTI metrics, which included fractional anisotropy (FA), mean diffusivity (MD), and the mode of anisotropy (MO). D) Q-sampling metrics, which include quantitative anisotropy (QA), isotropic component of diffusion (ISO), and the restricted diffusion imaging (RDI).

In order to balance the acquisition for both the brain, which benefits from isotropic voxels, and the spinal cord, which benefits from a large slice thickness and high in-plane resolution due to the elongated and symmetric structure of the cord and the lower signal intensity in the spinal cord, the diffusion MRI scan implemented a field of view (FOV) of 245mm with an acquisition matrix of 160x160, with 2.5mm slices with no inter-slice gap, for a voxel size of 1.5mm x 1.5mm x 2.5mm. A multiband factor of 2 was used along with a generalized autocalibrating partial parallel acquisition (GRAPPA) [281] acceleration factor of 2. Additional diffusion MRI scan parameters included: repetition time (TR) of 6100ms; echo time (TE) of 93ms; slice thickness of 2.5mm, no interslice gap; interleaved acquisition; flip angle of 90°. The slice prescription captured the brain down to at least the C3 level, with a total of 92 slices (230mm). Preliminary visual inspection of this data indicated suitable quality for both basic DTI metrics, such as fractional anisotropy (FA) and mean diffusivity (MD, **Figure 4.1.C**), and for probabilistic tractography (**Figure 4.3**). In addition to the main diffusion MRI sequence listed above, a b0 image with the same scan parameters as the previous scan, but with reversed phase-encode direction (posterior to anterior, or 180° flipped from the previous sequence) was also acquired in order to use reversed-gradient susceptibility distortion techniques to correct for susceptibility artifacts in the diffusion MRI data (**Figure 4.2**).

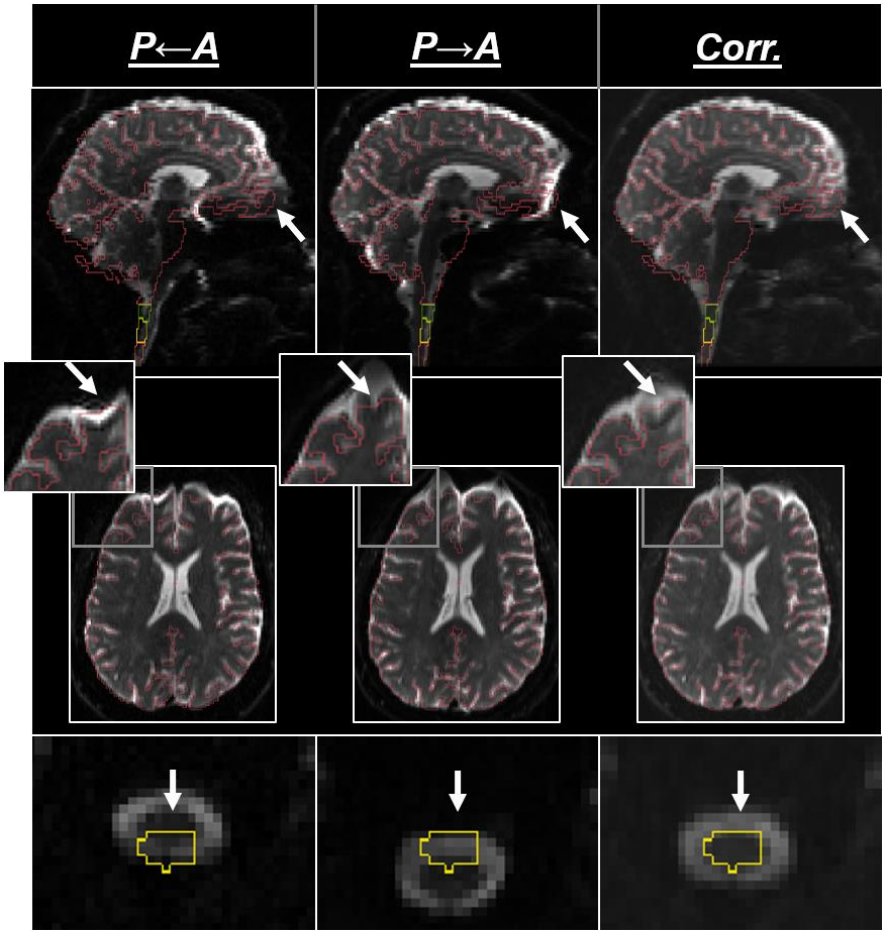

Figure 4.2. Example of susceptibility distortion-correction in a patient with cervical stenosis. Top row shows sagittal, middle row shows brain axial, and bottom row shows spinal cord axial b0 images with brain (red) and spinal cord (green for C1 vertebral level, yellow for C2 vertebral level, and orange for C3 vertebral level) segmentation overlays outlined. Left column shows b0 image with anterior to posterior (*A*→*P*) phase-encoding direction, middle column shows b0 image with posterior to anterior (*A*←*P*) phase-encoding direction, and right column shows distortion-corrected image (*Corr.*). White arrows denote region of distortion that presented with improved anatomical alignment after distortion correction: top row shows the orbitofrontal cortex, middle row shows the frontal lobe, and bottom row shows the C2 vertebral level which was well-aligned with the spinal cord segmentation after distortion correction.

Acquisition of Site of Compression Spinal Cord Diffusion MRI Data

While HC subjects only underwent acquisition of diffusion MRI of the brain and upper cervical spinal cord, CS patients also underwent a clinical spine MRI in which a diffusion MRI sequence was acquired that encompassed the site of compression. This sequence has been used in previous DTI studies [201,280,282-284]. An axial EPI sequence with 2D spatially-selective radiofrequency (RF) excitation pulse was used to acquire a reduced FOV with ramp sampling (ZOOMit) [285]. The FOV was 53 mm × 140 mm in the axial plane, with a matrix size of 48 x 128 and a slice thickness of 4mm with no interslice gap, to give a voxel size of 1.1mm x 1.1mm x 4mm. The TE was set to 73ms and the TR was set to 3000ms. Diffusion weighted images were acquired in 20 non-collinear diffusion sensitizing directions with a b-value of 500 mm^2/s, and a single b= 0 image was acquired. The sequence was acquired four times to use as averages and increase the signal to noise ratio (SNR).

Brain and Upper Cervical Spinal Cord Diffusion MRI Processing

All scans passed quality control assessment, except for the spinal cord portion of the scan for one healthy control subject: for this subject, there was a complete loss of signal below the brainstem, potentially due to acquisition gradients accidentally being turned off prior to acquisition. This being the case, the subject was excluded from the analyses involving the C2 level of the spinal cord.

Susceptibility distortion field maps were created from the b0 of the main diffusion MRI sequence (anterior to posterior phase-encoding gradient direction) and the additional reversed-gradient b0 (posterior to anterior phase-encoding direction) using the FMRIB Software Library (FSL) tool *topup* (https://fsl.fmrib.ox.ac.uk/fsl/fslwiki/topup) [286]. **Figure 4.2** shows an example of

this distortion-correction in a patient. A brain mask was created on the *topup*-corrected b0 image using FSL's brain extraction tool (BET, https://fsl.fmrib.ox.ac.uk/fsl/fslwiki/BET/UserGuide) with a fractional threshold of 0.2, and a spinal cord mask was created by manually selecting the spinal canal and thresholding the manually drawn ROI. The brain and spinal cord masks were joined to create a combined brain and spinal cord mask. The results from *topup* (susceptibility-distortion field map), the raw diffusion MRI data, the b-value and diffusion gradient vector tables, and the combined mask of the brain and spinal cord, were used to process motion-correction and eddy current distortion-correction using the FSL eddy tool (https://fsl.fmrib.ox.ac.uk/fsl/fslwiki/eddy) [287]. Additionally, the eddy tool was used to detect outlier slices (slices with mean signal intensity that were three standard deviations under the mean for that b-value) and replace these slices with Gaussian-normalized slices [288]. The resultant corrected data, along with the mask of the brain and spinal cord, was then used to fit a diffusion tensor model using the FSL diffusion toolkit (FDT, https://fsl.fmrib.ox.ac.uk/fsl/fslwiki/FDT), which produced fractional anisotropy (FA), mean diffusivity (MD), and mode of diffusion (MO) maps (**Figure 4.1.C**).

Generalized q-sampling imaging (GQI) [289] analysis was performed using DSI Studio (http://dsi-studio.labsolver.org/) software. GQI is a model-free reconstruction method for diffusion MRI data, which estiamtes the density of diffusing spins in various orientations. GQI creates a spin distribution function (SDF) by scaling the average propagator from q-space MRI by the density function. The ensemble average propagators is given by:

Equation 4.1. $$S(q) = \int P(R) e^{2\pi i q R} \, dR$$

where S is the diffusion MRI signal, $q = \gamma G\delta/2\pi$ (γ is the gyromagnetic ratio, G is the gradient strength, and δ is the gradient duration), and R is the diffusion displacement. While the propagator can be used to calculate the orientation distribution function (ODF) for diffusion, it can also be further scaled by spin density:

Equation 4.2. $$\Psi(\hat{a}) = Z_0 \sum_s S(\hat{g}, b) H(\sigma\sqrt{6Db} < \hat{g}, \hat{a} >)$$

where $\hat{a}$ is a direction along which the spin distribution is calculated, Z_0 is a scaling constant, S is the diffusion signal, b is the b-value, H is a sinc basis function, σ is the upper diffusion distance limit for which signals are considered, D is the diffusivity, and $\hat{g}$ is the direction of the diffusion-encoding gradient. The density of diffusing spins is then used to represent distinct fiber populations in a voxel. GQI was created as a more flexible framework for fitting varying types of diffusion MRI sampling data, as opposed to the restrictions in acquisition presented by diffusion spectrum imaging (DSI) [290] or Q-ball imaging [291].

GQI was selected because of its flexibility in fitting diffusion MRI data and aims to be a quantitative rather than probabilistic estimation, and because GQI also creates a set of voxelwise measures based on the SDF, which can be directly compared across subjects with the same scan sequence. **Figure 4.3** offers a graphical illustration of some of the DTI and GQI measures used in this study. These measures included quantitative anisotropy (QA) which is a measure of anisotropy for the main fiber orientation determined by each ODF, and is defined by:

Equation 4.3. $$QA_0 = Z_0(\Psi(\hat{a}_0) - ISO(\Psi))$$

where QA_0 is the quantitative anisotropy in the direction of the resolved fiber, Z_0 is a scaling constant, $\Psi(\hat{a}_0)$ is the spin distribution function for the orientation of the resolved fiber, and

$ISO(\Psi)$ is the isotropic component of diffusion (ISO) which measures the minimal or background amount of diffusion taking place based on the SDF. Another voxelwise metric, the component of restricted diffusion (RDI) [152] measures the degree of restricted diffusion as defined at a particular displacement length. Example images of the GQI metrics for the brain and spinal cord can be seen in **Figure 4.1.D**. The displacement length used for the analysis of RDI in this study was based on visual inspection of contrast between different tissue types in the acquired data, particularly contrast between cerebrospinal fluid (CSF), white matter (WM), and gray matter (GM), as seen in the RDI image in **Figure 4.1.D**. The length chosen was 0.2 x *L*, where *L* is the diffusion distance, defined as:

Equation 4.1. $$L = \sqrt{6Dt}$$

where *D* is the diffusivity of free water (taken to be 3.00 μm^2/ms) [292], and *t* is the diffusion time. For this experiment, the effective diffusion time for the equivalent monopolar encoding scheme, with Δ=43.1ms δ=28.0ms, was approximately Δ-δ/3 = 43.1ms/2-23ms/3 = 33.8ms. Thus, the diffusion distance was:

Equation 4.2. $$L = \sqrt{6 * (3.00\ \mu m2/ms) * (33.8ms)} = 24.7\mu m$$

and the sampled diffusion distance for RDI was 0.2 x *L* = 0.2 x 23.6μm = 4.9 μm. Thus, the sampled diffusion distance was approximately 5 μm. GQI fit was performed on the data using the mask of the brain and spinal cord. Calibration of the spin distribution functions with respect to CSF (free water) was performed, with a diffusion sampling length ratio of 1.25 (1.25 times the diffusion distance defined by the measured diffusivity of CSF), an 8-fold ODF tessellation was performed, and the number of fibers resolved per voxel was set to 3.

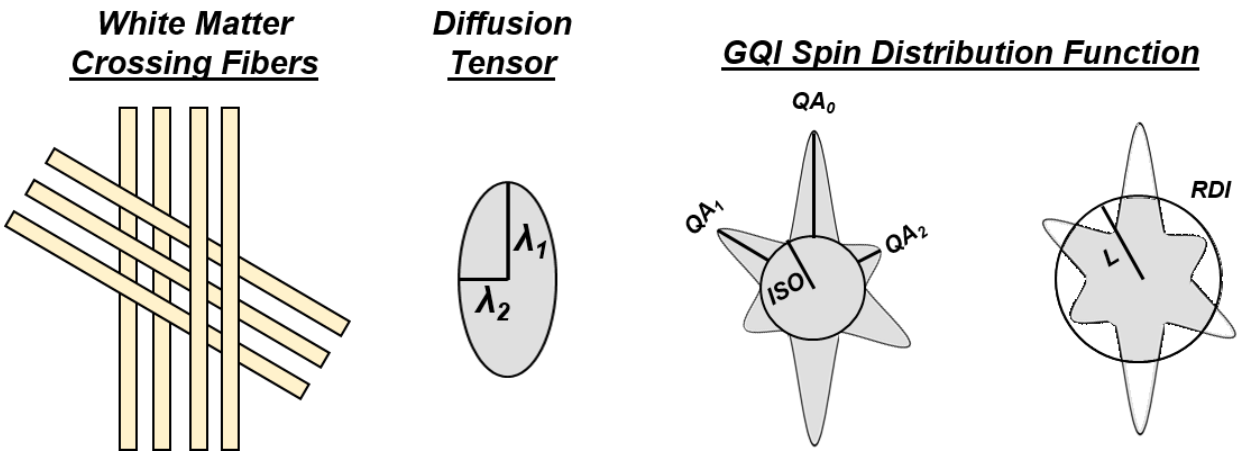

Figure 4.3. Illustration of diffusion tensor imaging (DTI) and generalized q-sampling (GQI) techniques in a region of crossing white matter fibers. Images shown only for in-plane. The diffusion tensor fits an ellipsoid model to the measured diffusion MRI data, and the eigenvalues (λ) can be used to compute the DTI metrics. For the GQI fit, the isotropic component of diffusion (*ISO*) represents the background or minimum diffusion occurring in the voxel, while the quantitative anisotropy (*QA*) can be measured as the deviation from the isotropic diffusion in the resolved fiber directions (0, 1, 2), while the restricted diffusion imaging parameter (*RDI*) defines a particular diffusion length (*L*) and weighs the distribution of spins that remain within that length. GQI measures adapted from Yeh *et al* [293].

After susceptibility distortion correction via *topup*, the spinal cord portion of the scan presented with corrected geometry that was identical to that of the T1w MPRAGE scan (**Figure 4.2**), indicating that the distortion-correction was successful and re-aligned the data to its respective anatomically-correct locations. Given this, only small manual adjustments were performed to align the spinal cord data to the T1w spinal cord data space, which contained segmentations and registered atlas data. This was done using the *tkmedit* tool from FreeSurfer

(https://surfer.nmr.mgh.harvard.edu/fswiki) to align the diffusion data to the T1w spinal cord data, adjusting only translation and rotation as needed. The inverse of the resultant linear transform was then applied to the spinal cord segmentation labeled by vertebral level (see **Chapter II**). Additionally, white matter atlas labels for the gracile and cuneate fasciculi, the corticospinal tract (CST), and the spinal lemniscus tract (which contains the spinothalamic tract) [101,103] were registered to the spinal cord T1 space using the transform between the PMU atlas [101] and the spinal cord T1 image, which is described in **Chapter III**.

For registration of atlas-based ROIs to the individual diffusion space of each subject, the FA maps of each subjects were registered to a standard space defined by the FMRIB FA atlas (https://fsl.fmrib.ox.ac.uk/fsl/fslwiki/FMRIB58_FA), and the inverse of these registrations were used to transform the atlas-based ROIs to each subjects diffusion space. The registration between the FA images was performed in two steps: the first involved linear registration of the subject FA to the FMRIB FA atlas using FMRIB's Linear Image Registration Tool (FLIRT, https://fsl.fmrib.ox.ac.uk/fsl/fslwiki/FLIRT) [294] using 12 degrees of freedom affine registration, correlation ratio weighting, and tri-linear interpolation. The linearly-registered subject FA was then warped to the FMRIB FA atlas using FMRIB's nonlinear registration tool (FNIRT, https://fsl.fmrib.ox.ac.uk/fsl/fslwiki/FNIRT) [295] using default parameters. The inverse warp transform of the nonlinear registration and the inverse of the linear transform between the subject FA and the FMRIB atlas FA were applied to the atlas ROIs to align them to individual subjects space, with nearest neighbor interpolation.

Probabilistic fiber modeling was performed on the distortion- and motion-corrected diffusion data using the Bayesian Estimation of Diffusion Parameters Obtained using Sampling Techniques (BEDPOSTX) algorithm from the FDT program, which uses Markov Chain Monte

Carlo modeling to estimate the number and orientation of fibers in each voxel [296]. A maximum of two fibers were modeled with 1000 iterations per voxel. Probabilistic tractography was run using the ProbtrackX program from FDT, where repetitive sampling of the estimated diffusion directions creates a distribution of fiber tracts [296]. ProbtrackX was run using a curvature threshold of 0.2, a distance threshold of 0 (meaning any tracts connecting two masks are included), a step length of 0.5mm, number of samples of 5000, and 2000 steps per sample.

ROIs for probabilistic tractography analyses used the FreeSurfer parcellations [82,83,89] that were used for the brain analyses in **Chapter II**. To transform these parcellations into each subjects individual diffusion MRI space, first the b0 image was registered to the T1 brain image using FSL's EPI Boundary-Based Registration (BBR, https://fsl.fmrib.ox.ac.uk/fsl/fslwiki/FLIRT_BBR) [297], which leverages contrast between GM and WM to better register EPI scans to anatomical scans. This inverse of this registration was then applied to the FreeSurfer Desikan-Killiany-Tourville (DKT) cortical and subcortical segmentations [216], applying the inverse registration matrices using FSL's Linear Image Registration Tool (FLIRT, https://fsl.fmrib.ox.ac.uk/_fsl/fslwiki/FLIRT) [294,298], with a nearest neighbor interpolation. The regions used for probabilistic tractography analysis included the primary sensorimotor cortex (SM) which consisted of both the precentral and poscentral gyri, the brainstem (B-stem), the anterior cingulate (AC) which comprised both the rostral and dorsal segments of the AC, the superior frontal gyrus (SFG), the precuneus, the thalamus (Thal.), and the putamen (Put.). **Figure 4.4** shows an example of probabilistic tractography between the brainstem and the sensorimotor cortex in a single subject, with the resulting tracts displaying a distribution centered around the corticospinal tract, as expected.

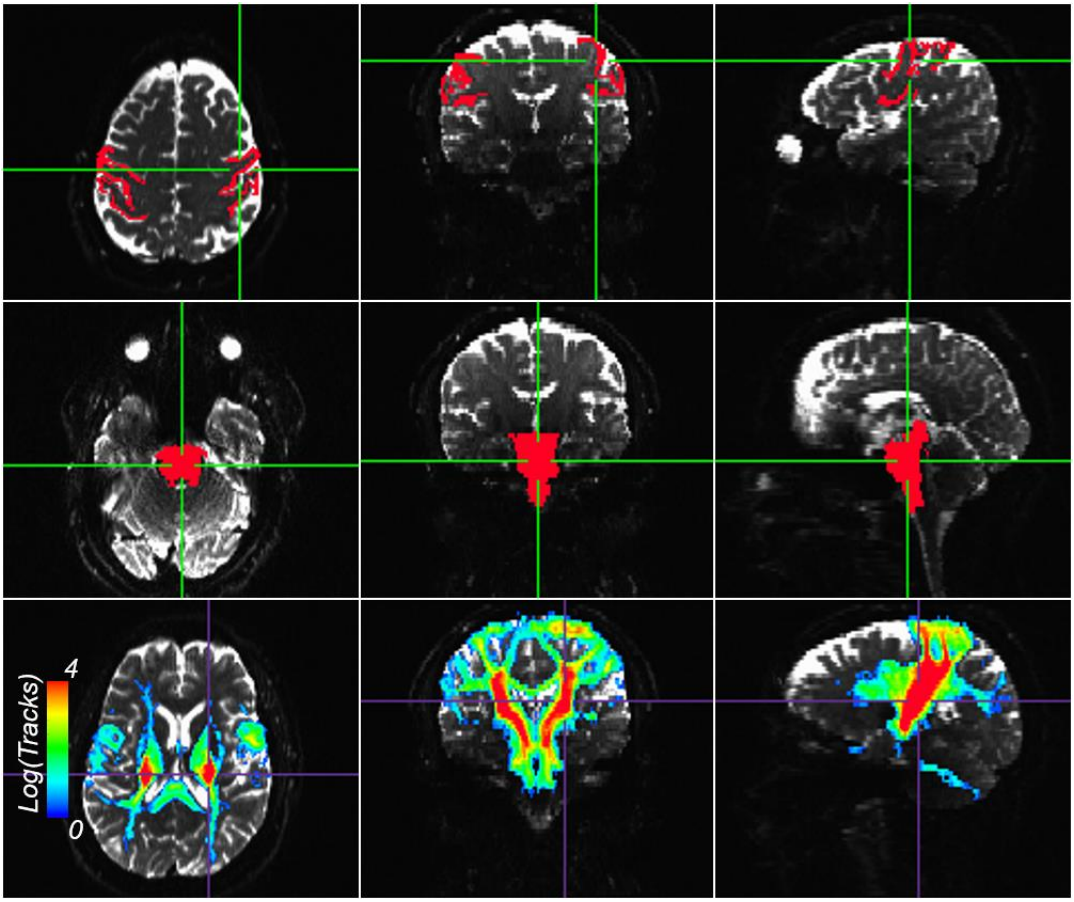

Figure 4.4. Example of seeded probabilistic tractography used for analysis. Axial (left column), coronal (middle column) and sagittal (right column) slices of brain with the susceptibility distortion-corrected b0 image as underlay. Segmentations of the primary sensorimotor cortex (top row) and the brainstem (middle row) used for seeding probabilistic tractography. Log-transformed resultant track counts through voxels after performing probabilistic tractography (bottom row), thresholded at a level of 0.4 log of track count. Cross-hairs show location of respective anatomical planes in each row.

Site of Compression Spinal Cord Diffusion MRI Data Processing

Because of the reduced number of directions (20) and lower b-value (500 mm^2/s), the diffusion MRI data from the site of compression was only analyzed in terms of DTI metrics. The FA and MD values were extracted in two different ways. The first method of measurement involved manual delineation of the spinal cord at the site of highest compression to obtain the mean FA and MD values from the scanner-generated maps. This was done in the Osirix viewer (http://www.osirix-viewer.com/), where a hand-drawn oval ROI was placed so as to cover the greatest extent of the spinal cord in the MD and FA maps, and the slice of the greatest extent of compression was selected in reference to the T2w sagittal MRI scan (described in **Appendix A**). This process is similar to that implemented in previous studies that have shown associations with mJOA scores and temporal stability of DTI measurements using this technique [201,284].

The second method of measurement involved calculating the mean DTI metrics at the site of compression and adjacent vertebral levels using a semi-automated approach. Motion correction of the spinal cord data was processed using the Spinal Cord Toolbox (SCT) [101] with a polynomial normalization of 2, a smoothing kernel of 2mm, mean squares weighting, and linear interpolation of the motion-corrected slices registered to the first spinal cord volume. After motion correction, in order to align the T1w spinal cord segmentations (described in **Chapter II**) with the spinal cord in the diffusion MRI space, manual registration was performed using the *tkmedit* tool between both each of these scans and the T2w axial MRI scan (described in **Appendix A**). The T2w MRI was acquired in the same space and close in time to the diffusion MRI sequence at the site of compression, and as such only minor adjustments between these volumes needed to be made for this registration. The T1w image was also aligned to the T2w MRI, and the appropriate transforms were applied to register the T1w segmentations to the diffusion MRI space (**Figure 4.5**).

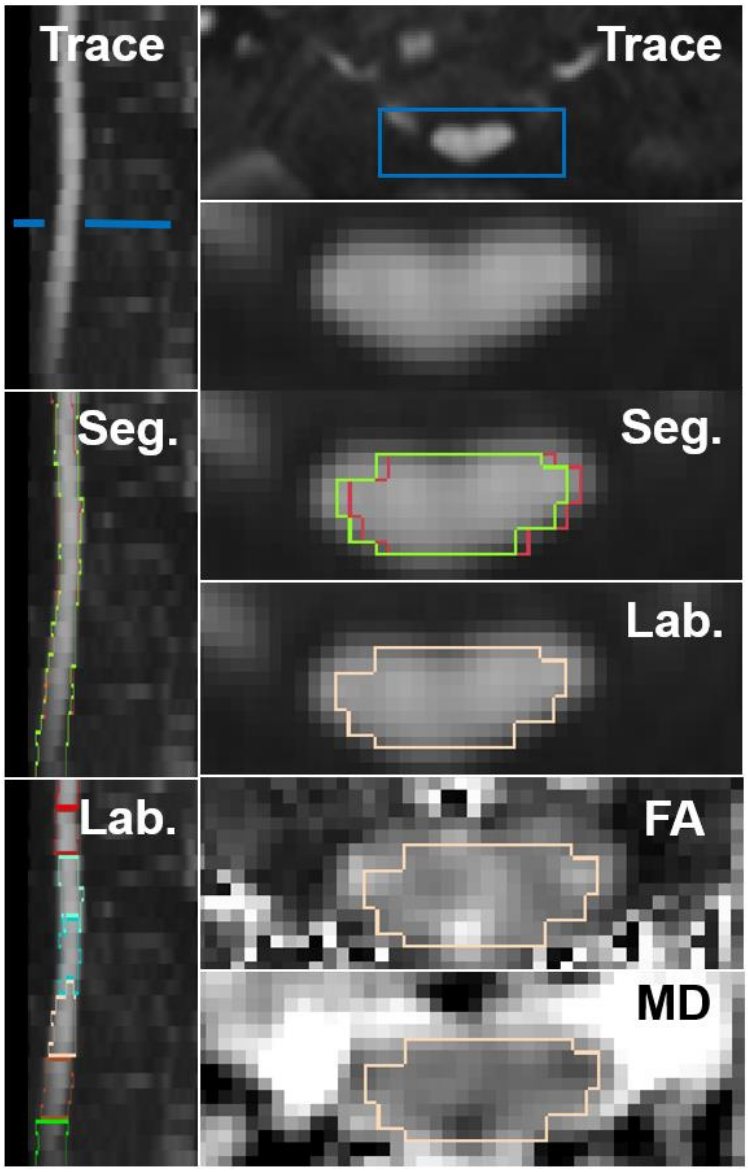

Figure 4.5. Spinal cord diffusion MRI scan and analysis at site of compression. Left side shows sagittal sections of the trace images of the spinal cord, right side shows axial views at reference (blue markers on top sagittal section). Zoomed in section on the segmentations (seg.) shows improved alignment (green) to spinal cord after slice-wise registration compared to 6 DOF registration (red). Vertebral labeling (Lab.) separates different vertebral levels for analysis and used to calculate mean measures from the FA and MD maps at each level.

The spinal cord was segmented from the trace image, which was created by taking the average of all the diffusion weighted volumes. The trace image was thresholded at a level of 100 and separated into clusters using the Analysis of Functional Neuroimages (AFNI) software *3dclust* tool (https://afni.nimh.nih.gov/pub/dist/doc/program_help/3dclust.html), and the cluster pertaining to the spinal cord was selected and used for further processing. This segmentation of the spinal cord from the trace image was then used for the final registration with the T1w structural MRI segmentation of the spinal cord. The T1w segmentation that was registerd to the diffusion MRI space was registered to the spinal cord segmentation using a z-regularized slice-by-slice registration of the center-of-mass for each segmentation through the SCT software. DTI metrics were computed using FDT, and the mean value was extracted for each vertebral level with usable data (**Figure 4.5**).

Analysis of C2 Spinal Cord Diffusion MRI Data

Spinal cord MRI data was analyzed using the segmentation of the C2 vertebral level, produced in **Chapter II**, and registered to the diffusion MRI data as listed above. Linear regression was performed for the mean DTI and GQI variables at the C2 vertebral level with respect to symptom variables, mJOA and NDI, and the Torg Ratio, and significant results were reported. To visualize the general trends of the relationship between the diffusion metrics and the symptom and clinical variables of interest, Pearson's correlations were calculated for the spinal cord white matter regions, namely the gracile and cuneate fasciculi, the lateral corticospinal tract, and the spinothalamic tract. The mean value of the DTI and GQI metrics was calculated for these regions and mapped back onto the spinal cord standard space defined by the PMU spinal cord atlas, color-

coded by strength of correlation (0-0.1 none, 0.1-0.3 weak, 0.3-0.5 moderate, >0.5 strong). for both positive and negative correlations.

Analysis of Brain Diffusion MRI Data

Brain MRI data was analyzed using atlas-based ROIs of white matter and subcortical gray matter. The white matter ROIs were taken from the Johns Hopkins University (JHU) white matter atlas, and the subcortical gray matter ROIs were taken from the Harvard-Oxford subcortical atlas, both of which are distributed with the FSL package (https://fsl.fmrib.ox.ac.uk/fsl/fslwiki/Atlases). White matter ROIs included those along the corticospinal tract, starting at the cerebral peduncles (CP), the anterior and posterior limbs of the internal capsule (ALIC and PLIC, respectively), and the superior and posterior corona radiata (SCR and PCR, respectively). White matter ROIs also included fibers in the frontal lobe and adjacent to cortical regions important for pain, such as the cingulum (connecting to the anterior cingulate and precuneus), the external capsule (EC, connecting to the insula), the anterior corona radiata (ACR, connecting to the superior frontal gyrus). The subcortical structures analyzed included the thalamus, putamen, caudate, and globus pallidus, which were the same structures used for volumetric analysis in **Chapter II**. Linear regression between DTI and GQI variables with respect to symptom variables, the modified Japanese Orthopedic Association (mJOA) score, both for the combined HC and CS and the CS only groups, and the neck disability index (NDI), as well as the MRI-equivalent Torg Ratio, were calculated and significant results were reported. In order to visualize the general trends of the relationship between the diffusion metrics and the symptom and clinical variables of interest, Pearson's correlations were calculated between the mean of the diffusion metrics in the structures and the respective symptom variables and were mapped back onto the regions in standard space,

color coded by strength of correlation (0-0.1 none, 0.1-0.3 weak, 0.3-0.5 moderate, >0.5 strong) for both positive and negative correlations.

Probabilistic tractography was run for each subject and resultant tract counts between ROIs was used for regression analyses with symptom variables. Probabilistic tractography was performed between all regions and the primary sensorimotor cortex. Additionally, probabilistic tractography between the AC and the thalamus, putamen, and precuneus was performed, as well as between the SFG and the thalamus, putamen, and precuneus. These were selected because of the underlying white matter pathways that connect these regions, namely the cingulum bundle connects the precuneus to the AC and SFG, and white matter pathways such as the anterior corona radiata connect the subcortical structures with the AC and SFG. Linear regression of the log-transformed total track counts to symptom variables was performed, and significant results reported.

Analysis of Site of Compression Spinal Cord Diffusion MRI Data

Because of the deformation of the spinal cord caused by compression, and due to the decreased SNR in the lower cervical cord, analysis of the spinal cord at the site of compression and adjacent levels was performed for the whole cord and not within white matter subregions. For the first method of analysis, the mean FA and MD values from the manually placed ROI of the spinal cord at the site of highest compression were compared to mJOA and NDI scores via linear regression. For the second method of analysis, the mean FA, MD, and MO, were computed at the site of compression by using the same slice number from the manual definition of the site of maximal compression, as well as at all available vertebral levels by using the registered T1w label map. Analyses involved looking at vertebral levels individually, or by centering around the site of

maximal compression and using the mean DTI measures from the vertebral levels above and below; these were compared to mJOA and NDI scores via linear regressions. Lastly, the C2 and brain corticospinal regions' mean DTI metrics were evaluated with respect to the DTI metrics at the site of compression and with respect to the level of maximal compression.

Comparison of DTI and GQI Metrics

One last objective of this chapter was to evaluate the relationship between the DTI and GQI metrics in the spinal cord and brain. This was performed using Pearson's correlation matrices with correlation coefficients between the means of every pair of variables. For the spinal cord, this was done at the C2 vertebral level, and for the brain three different regions of interest were selected: the cerebral peduncles (CP, inferior portion of corticospinal tract in the brain), the superior corona radiata (SCR, the superior portion of the corticospinal tract in the brain), and the thalamus (Thal., a subcortical gray matter structure with high degree of myelinated fibers inside). These regions were selected because of their differing properties (location, signal intensity, degree of myelination, degree of single vs multiple crossing fiber populations), which may help elucidate the benefits or drawbacks of either technique across brain regions with differing microstructural features. Specific relationships between metrics were further probed using linear regression and visualization; these included relationships between QA and FA, and between MD and ISO, along with any other variables that showed a strong association in the correlation matrix.

The coefficient of variation was calculated both in the overall and HC group to see how the relative variability of the DTI and GQI measures compared. Lastly, in order to evaluate the utility of combining multiple diffusion MRI metrics to evaluate associations with symptoms and with spinal cord compression, multiple linear regression models were created of the diffusion MRI

metrics with the symptom and compression measures at the C2 vertebral level of the spinal cord, CP, SCR, and thalamus. This was performed for all variables together, for DTI metrics (because of being linearly orthogonal to each other) and based on results from the above correlation matrices (to avoid issues of collinearity).

Software and Statistical Analyses

Susceptibility-distortion, eddy current, and motion-correction of diffusion data, computation of DTI measures, registration of diffusion maps to a standard space, and EPI BBR registration of brain diffusion data to structural brain data, were performed using FMRIB Software Library (FSL Version 5.0, https://fsl.fmrib.ox.ac.uk/fsl/fslwiki). Segmentations of brain regions used to define anatomical ROIs involved the subcortical segmentations and DKT atlas parcellations of cortical structures, and manual registration of the spinal cord diffusion data to the T1w MRI using *tkmedit*, were performed using FreeSurfer (Version 5.3.0, https://surfer.nmr.mgh.harvard.edu/fswiki). Statistical analyses were performed using GraphPad Prism (Version 7.0b, La Jolla California USA, www.graphpad.com), and multiple linear regression was performed in Free Statistics Software (Version 1.1.23-r7, http://www.wessa.net/rwasp_multipleregression.wasp/).

ii. Diffusion MRI Metrics at the C2 Level of Spinal Cord

Diffusion MRI Metrics at the C2 Level

Linear regression analysis of the mean diffusion metrics at the C2 vertebral level of the spinal cord revealed significant associations between the DTI measures and mJOA as well as between DTI measures and the MRI-equivalent Torg Ratio (**Figure 4.6**). mJOA was found to be

significantly associated with FA (R^2=0.11, P=0.03*, decreasing FA with worsening neurological function), and with MD (R^2=0.11, P=0.03*, increasing MD with worsening neurological function) in the combined HC and CS groups. NDI was not found to be associated with any of the DTI measures. The Torg Ratio was associated with all three DTI measures at the C2 level: FA (R^2=0.38, P=0.0008***, decreasing FA with worsening compression), MD (R^2=0.19, P=0.02*, increasing MD with worsening compression), and MO (R^2=0.20, P=0.02*, decreasing MO with worsening compression). The mean GQI measures at the C2 vertebral level of the spinal cord did not produce any significant associations with symptom variables.

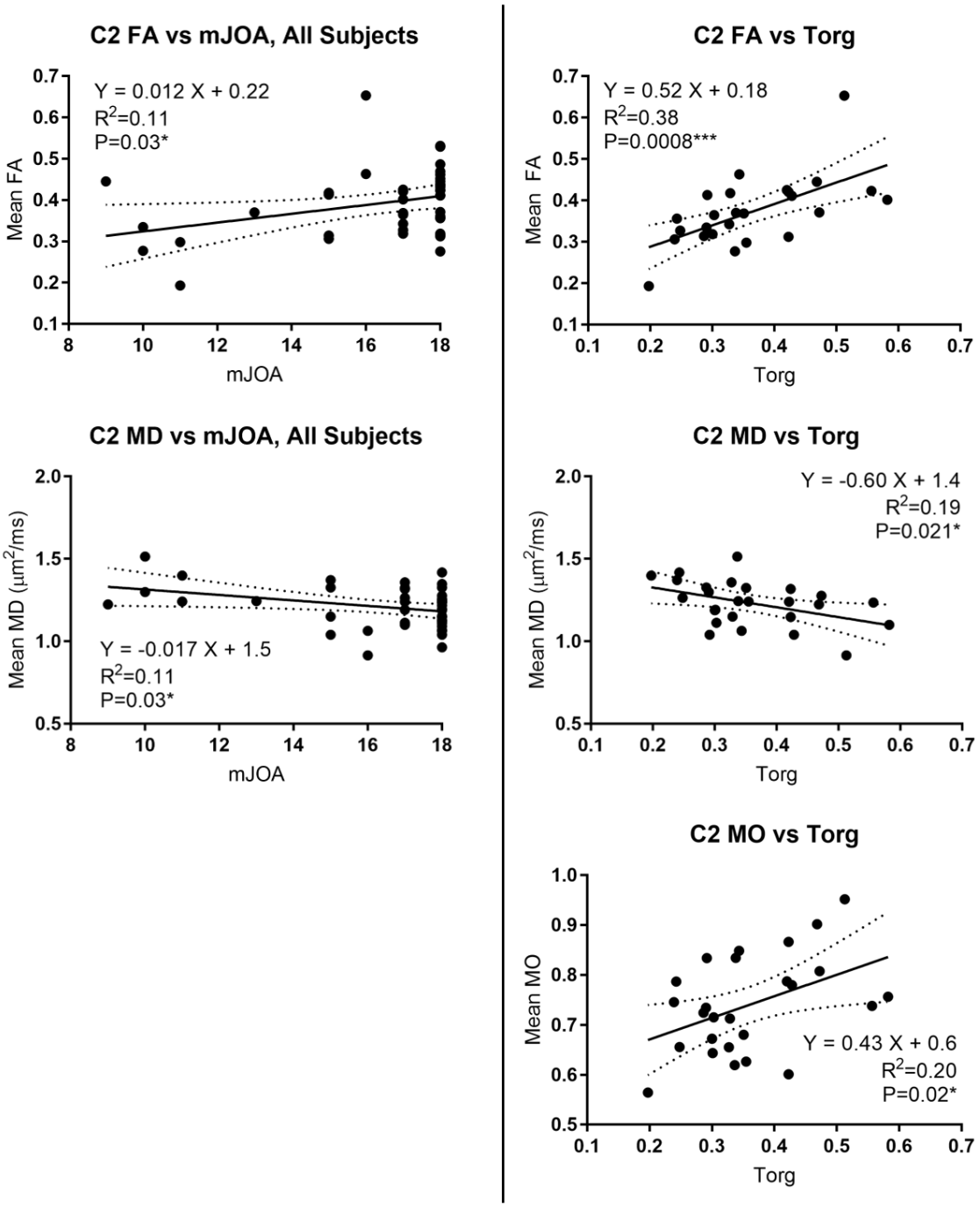

Figure 4.6. Plots of linear regression of diffusion tensor imaging (DTI) metrics, fractional anisotropy (FA), mean diffusivity (MD), and mode of diffusion (MO), vs mJOA score (left) and MR-equivalent Torg Ratio (right). Plotted are the regression line (solid) with 95% confidence intervals (dashed).

In addition to the linear regressions evaluating the relationship between the symptom variables and diffusion measures, visualization of the correlation between specific tracts in the spinal cord revealed similar trends for DTI measures (**Figure 4.7**): increasing FA with increasing mJOA (better neurological status) especially in spinothalamic, corticospinal, and cuneate tracts; decreasing MD with increasing mJOA (better neurological status), especially in the corticospinal and spinothalamic tracts; weak correlations between mJOA and MO; weak correlations with NDI, but increasing FA, decreasing MD, and increasing MO with worsening neck pain; and strong correlations with the Torg Ratio, with increasing FA, decreasing MD, and increasing MO, in most tracts excepting the gracilis. GQI measures presented with weaker correlations overall, and also with a greater degree of spatial heterogeneity: the more posterior gracile tract appeared to display stronger associations with mJOA and NDI (as opposed to the DTI associations), with the opposite occurring for the Torg Ratio (stronger associations in frontal and lateral tracts as opposed to posterior ones).

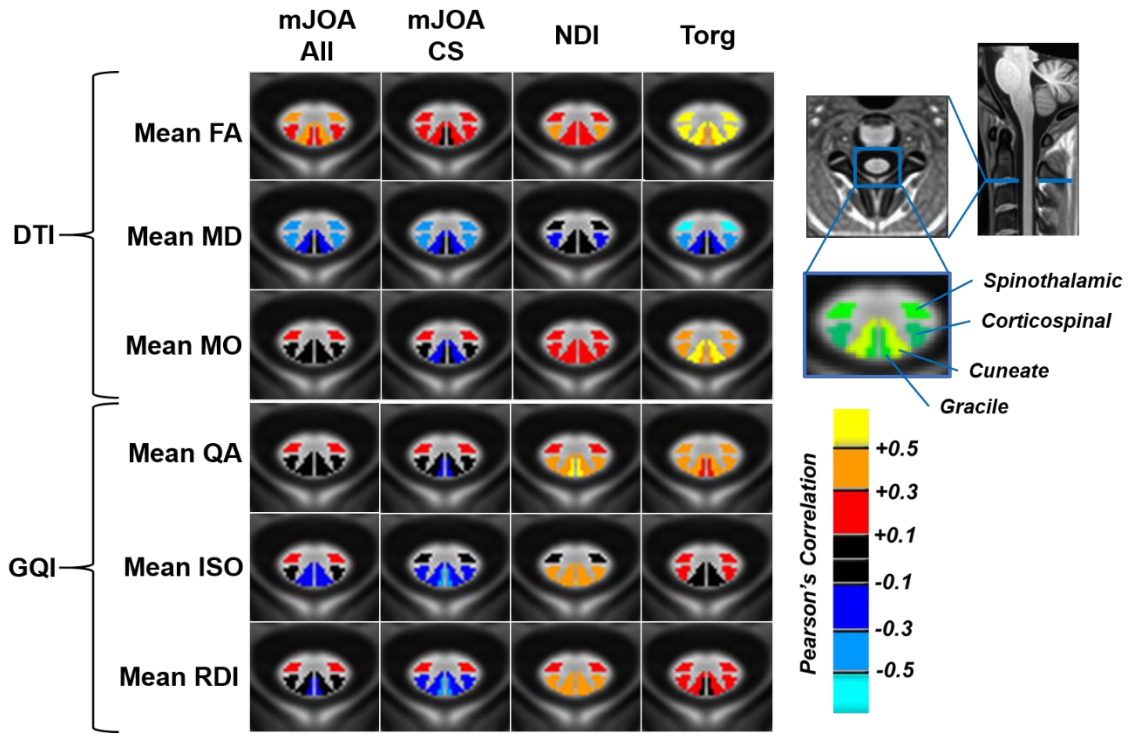

Figure 4.7. Maps of correlations between mean diffusion metrics in several white matter tracts at the C2 vertebral level and clinical variables. Tracts are shown on level of PMU spinal cord atlas displayed at top right. Pearson's correlations between diffusion MRI metrics and clinical variables are color coded by correlation categories: 0 to 0.1 is no correlation (black); 0.1 to 0.3 is minor correlation (red for positive, blue for negative); 0.3 to 0.5 is moderate correlation (orange for positive, light blue for negative); greater than 0.5 is strong correlation (yellow for positive, cyan for negative). Fractional anisotropy (FA), mean diffusivity (MD), and the mode of anisotropy (MO) are shown for diffusion tensor imaging (DTI) metrics, and the isotropic component of diffusion (ISO), quantitative anisotropy (QA), and restricted diffusion imaging component (RDI), are shown for generalized q-sampling imaging (GQI) metrics.

iii. Diffusion MRI Metrics in Brain Regions

DTI Measures

Linear regression analysis of brain WM and subcortical GM regions displayed significant associations between the DTI measures and symptom variables. The general trends for the results included: decreasing FA (**Figure 4.8**, left), increasing MD (**Figure 4.8**, right), and decreasing MO (**Figure 4.9**), with worsening symptoms or compression. The only region that showed a different trend was MO in the superior corona radiata with respect to NDI (**Figure 4.9**, bottom left), which presented an increasing MO with worsening neck pain. A few regions recurred across the associations between DTI measures and symptom variables. These included the cerebral peduncle (CP) was associated with the Torg Ratio for both FA (R^2=0.21, P=0.02*) and MD (R^2=0.11, P=0.03*), as well as for the association between MO and mJOA, both for all subjects (R^2=0.11, P=0.03*) and for the group of CS patients only (R^2=0.23, P=0.01*). The caudate also presented with a significant association with the Torg Ratio for FA (R^2=0.18, P=0.03*) and MD (R^2=0.11, P=0.03*), as well as the association between MO and mJOA for all subjects (R^2=0.11, P=0.03*). In addition to the aforementioned relationship between the mean MO in the SCR and NDI, the SCR was also significantly associated with mJOA in the group with all subjects (R^2=0.11, P=0.03*).

Visualization of the correlation between specific white matter regions in the brain largely revealed similar trends for the DTI measures (**Figure 4.10**). Weak trends for increasing FA with increasing mJOA (better neurological status) was present in the corticospinal tract (CP, ALIC, PLIC, SCR, PCR), thalamus, and caudate, while weakly decreasing FA was found in the putamen. Weak trends for decreasing FA with NDI (worse neck pain) were present in the corticospinal tract, while stronger trends for decreasing FA were present in the anterior corona radiata (ACR) and in

the external capsule (EC). FA was weakly associated with the Torg Ratio in most regions, but was moderately associated in the cerebral peduncles, caudate, and cingulum. MD demonstrated weak negative associations with mJOA (increasing mJOA with worsening neurological symptoms) in most regions, and moderate association with mJOA in all subjects in the SCR and putamen. MD displayed weak negative correlations with NDI (decreasing MD with worsening neck pain) in the CP, ALIC and PLIC, caudate, putamen, and weak positive associations (increasing MD with worsening neck pain) with anterior-posterior tracts such as the SLF, cingulum, and EC, as well as with the SCR. For the associations between MD and the Torg Ratio, MD displayed a strong negative correlation (increasing MD with worsening compression) in the CP, a moderate negative association with the caudate and thalamus, and weak negative correlations in other regions. MO displayed moderate positive associations (increasing MO with better neurological function) with mJOA in the caudate for the group with all subjects, in the ALIC for CS subjects, and in the CP for both. Other regions displayed weak positive associations (the putamen showed a weak negative association in the putamen). For NDI, the CP and internal capsules (ALIC and PLIC) showed a negative association with MO, while the putamen and SCR showed a moderate positive association. For the Torg Ratio, MO showed a moderate positive association (decreasing MO with worsening compression) in the ACR, EC, caudate, and the cingulum.

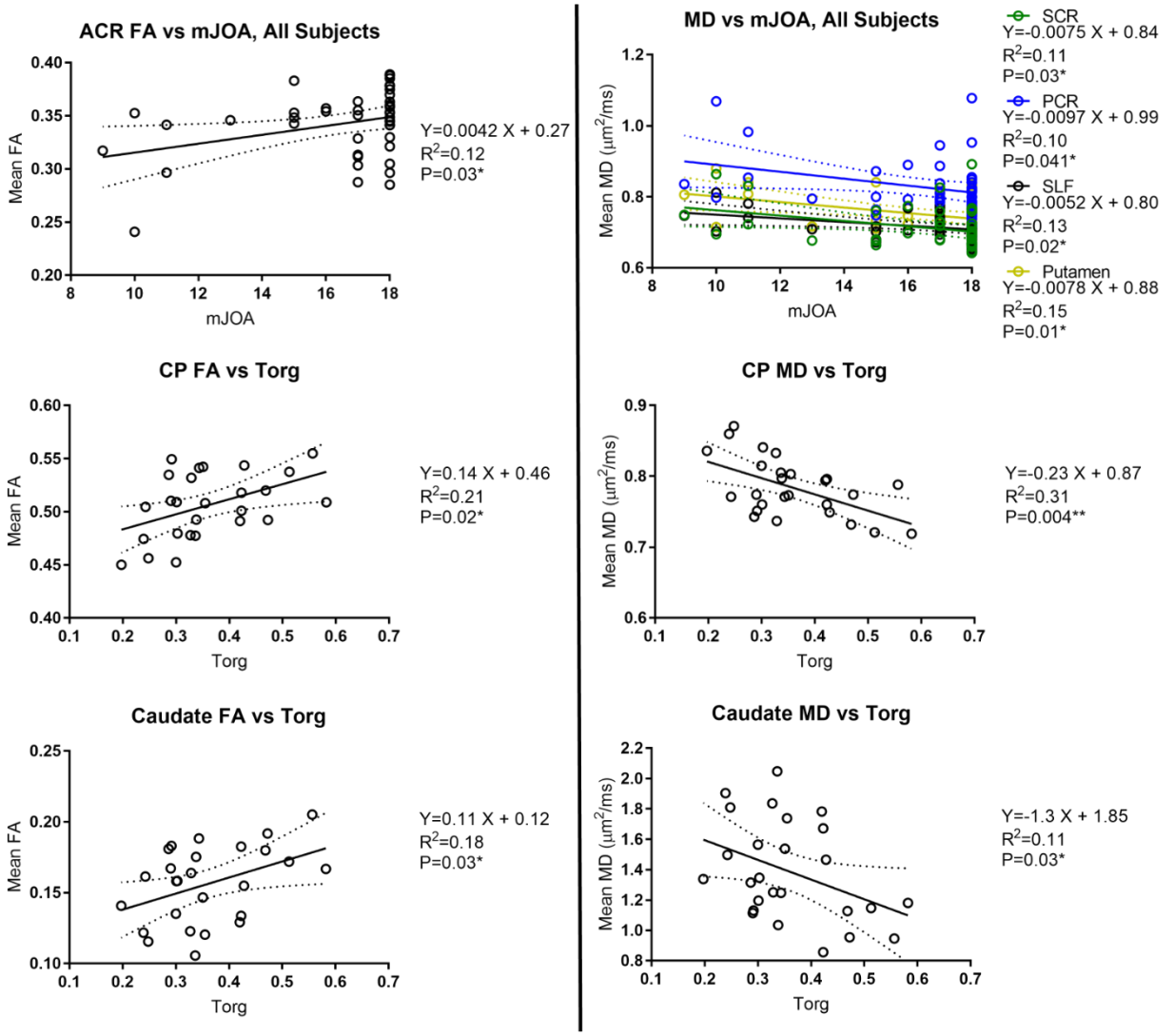

Figure 4.8. Plots of linear regression of fractional anisotropy (FA, left) and mean diffusivity (MD, right) vs mJOA and Torg Ratio. Plotted are the regression line (solid) with 95% confidence intervals (dashed). ACR denotes anterior corona radiata, SCR denotes superior corona radiata, PCR denotes posterior corona radiata, SLF denotes superior longitudinal fasciculus, and CP denotes cerebral peduncles.

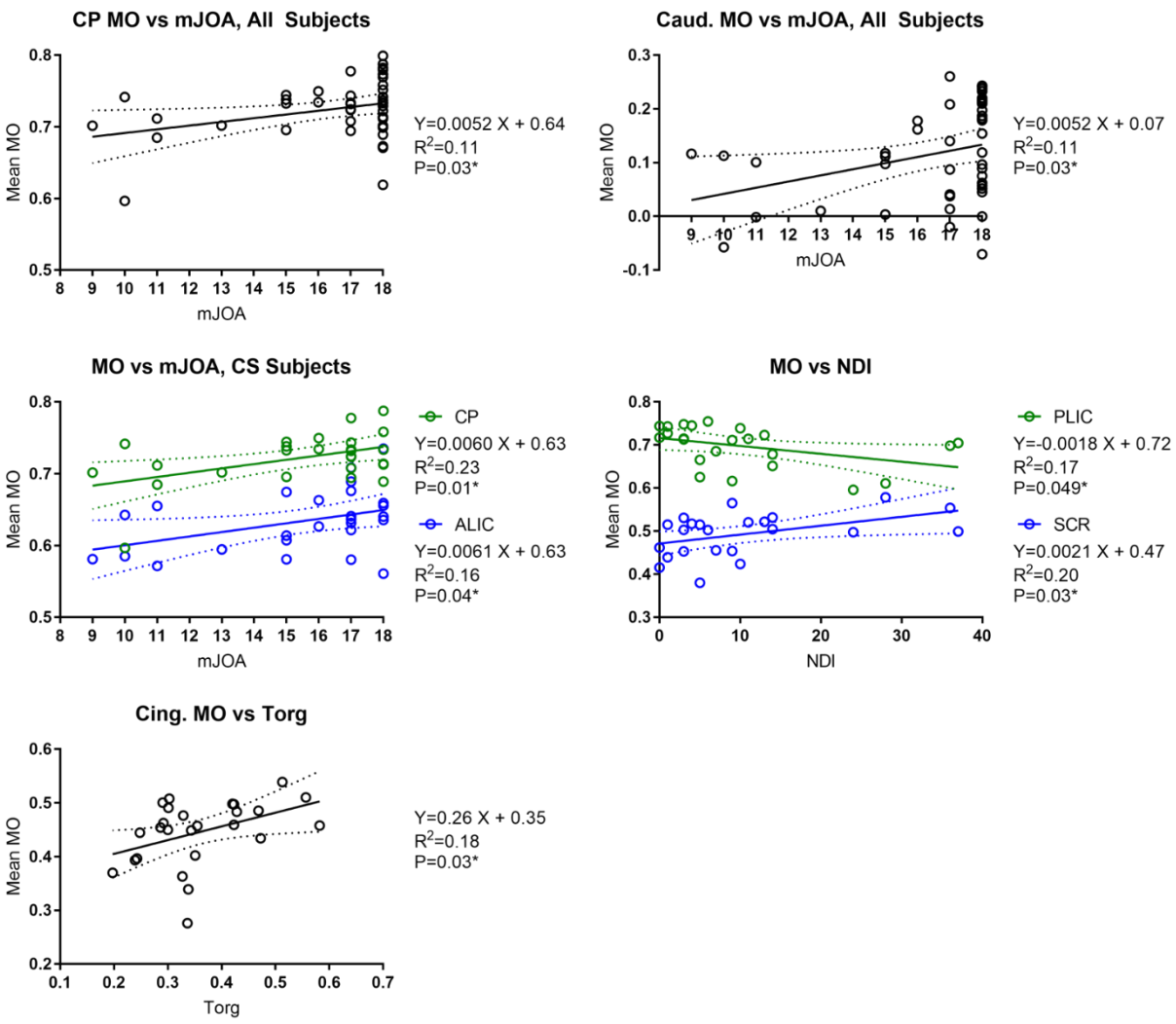

Figure 4.9. Plots of linear regression of the mode of anisotropy (MO) vs mJOA, NDI, and MR-equivalent Torg Ratio. Plotted are the regression line (solid) with 95% confidence intervals (dashed). CP denotes cerebral peduncles, ALIC denotes anterior limb of the internal capsule, PLIC denotes posterior limb of the internal capsule, SCR denotes superior corona radiata, and Cing. denotes cingulum.

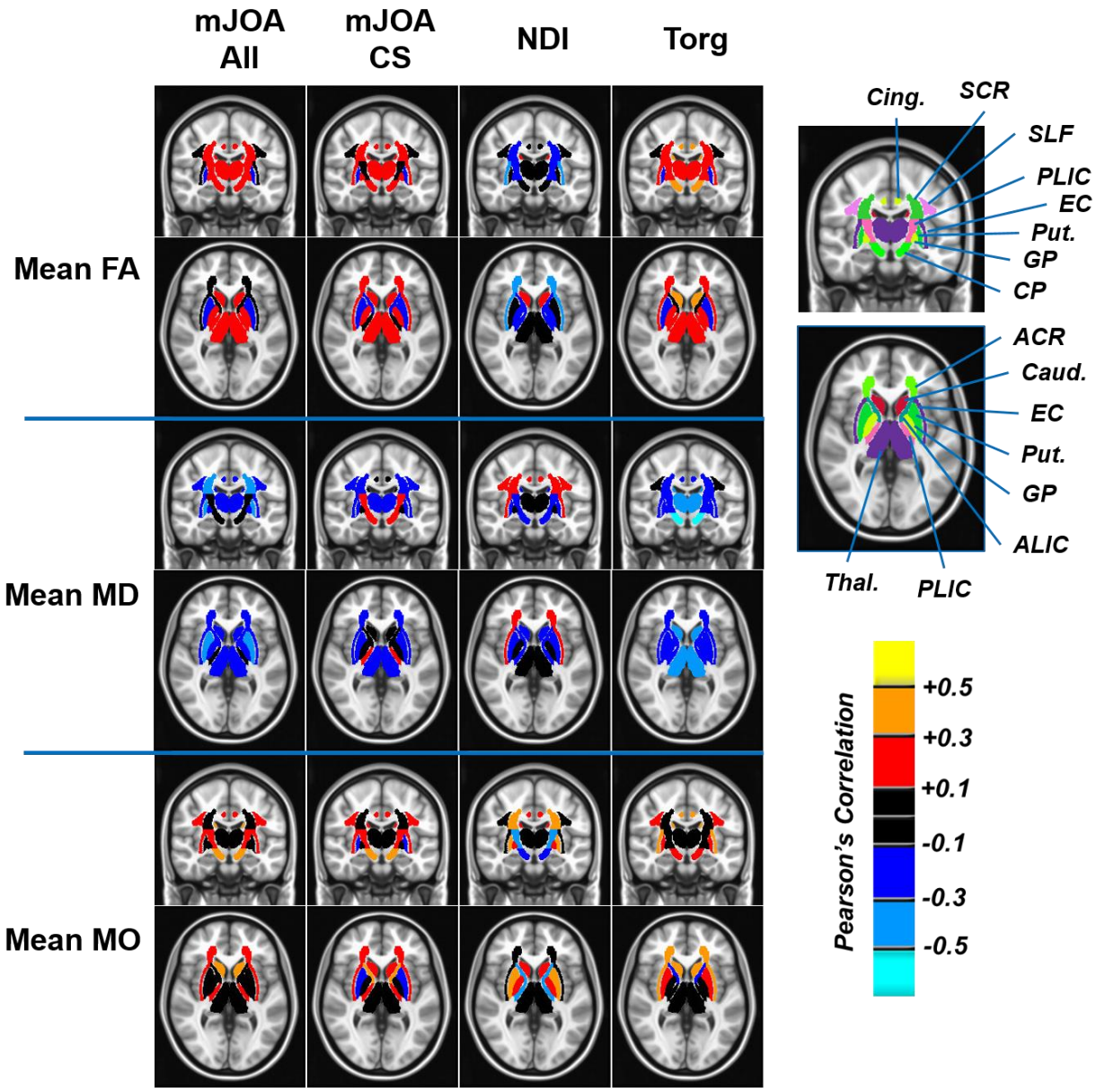

Figure 4.10. Legend presented on next page.

Figure 4.10. Maps of correlations between mean diffusion metrics in several white matter tracts and subcortical gray matter structures in the brain. ROIs are shown on the MNI T1 atlas. Pearson's correlations between metrics and clinical variables are color coded by correlation categories: 0 to 0.1 is no correlation (black); 0.1 to 0.3 is minor correlation (red for positive, blue for negative); 0.3 to 0.5 is moderate correlation (orange for positive, light blue for negative); greater than 0.5 is strong correlation (yellow for positive, cyan for negative). Fractional anisotropy (FA), mean diffusivity (MD), and the mode of anisotropy (MO) are shown for diffusion tensor imaging (DTI) metrics. White matter tracts included the cerebral peduncle (CP), anterior and posterior limbs of the internal capsule (ALIC and PLIC, respectively), anterior and posterior corona radiata (ACR and PCR, respectively), external capsule (EC), and cingulum (Cing.). Subcortical gray matter regions included the thalamus (Thal.), caudate (Caud.), putamen (Put.), and globus pallidus (GP).

GQI Measures

Linear regression analysis of brain WM and subcortical GM regions displayed significant associations between the GQI measures and symptom variables. The general trends for the results included: decreasing QA (**Figure 4.11**), decreasing ISO (**Figure 4.12**), and decreasing RDI (**Figure 4.13**), with worsening symptoms or compression. The only region that showed a different trend was ISO in the caudate with respect to the Torg Ratio (**Figure 4.12**, bottom right), which presented a decreasing ISO with worsening neck pain. Even more so than for the DTI measures, the significant regressions of GQI measures *vs* symptom variables comprised a few select regions, which consisted of the corticospinal tract, from the CP to the anterior and posterior limbs of the interior capsules (ALIC and PLIC, respectively), and the corticospinal tracts nearer to the primary sensorimotor cortex such as the superior and posterior corona radiata (SCR and PCR). In addition

to these the caudate was also significantly associated to various symptom variables for GQI metrics. For mJOA, the SCR displayed a significant association with QA (R^2=0.12, P=0.02* for overall, and R^2=0.26, P=0.008** for CS only), ISO (R^2=0.09, P=0.048* for overall, R^2=0.16, P=0.042* for CS only), and RDI (R^2=0.15, P=0.048* for CS only). Additionally, for mJOA, QA showed a significant positive association in the PCR (R^2=0.11, P=0.03* for overall, R^2=0.25, P=0.009** for CS only) and caudate (R^2=0.10, P=0.04* for CS only). Only QA in the PCR (R^2=0.17, P=0.047*) was associated with NDI. The Torg Ratio was significantly associated with GQI measures across the corticospinal tract, with cerebral peduncles and posterior limb of the internal capsule associated with all three measures, and the ISO and RDI of the anterior limb of the internal capsule (ALIC), superior and posterior corona radiata (SCR and PCR, respectively) associated with the Torg Ratio.

Visualization of the correlation between specific white matter regions in the brain largely revealed similar trends for the GQI measures (**Figure 4.14**), which showed moderate positive correlations in the corticospinal tract for mJOA and Torg Ratio, and low to moderate correlations with NDI in anterior (ACR), superior (SCR) tracts, as well as the external capsule. Particularly, RDI and ISO are notable for their stronger associations along the corticospinal tract as compared to surrounding subcortical structures and other white matter tracts for both mJOA (particulary for the CS only group) and for the Torg Ratio.

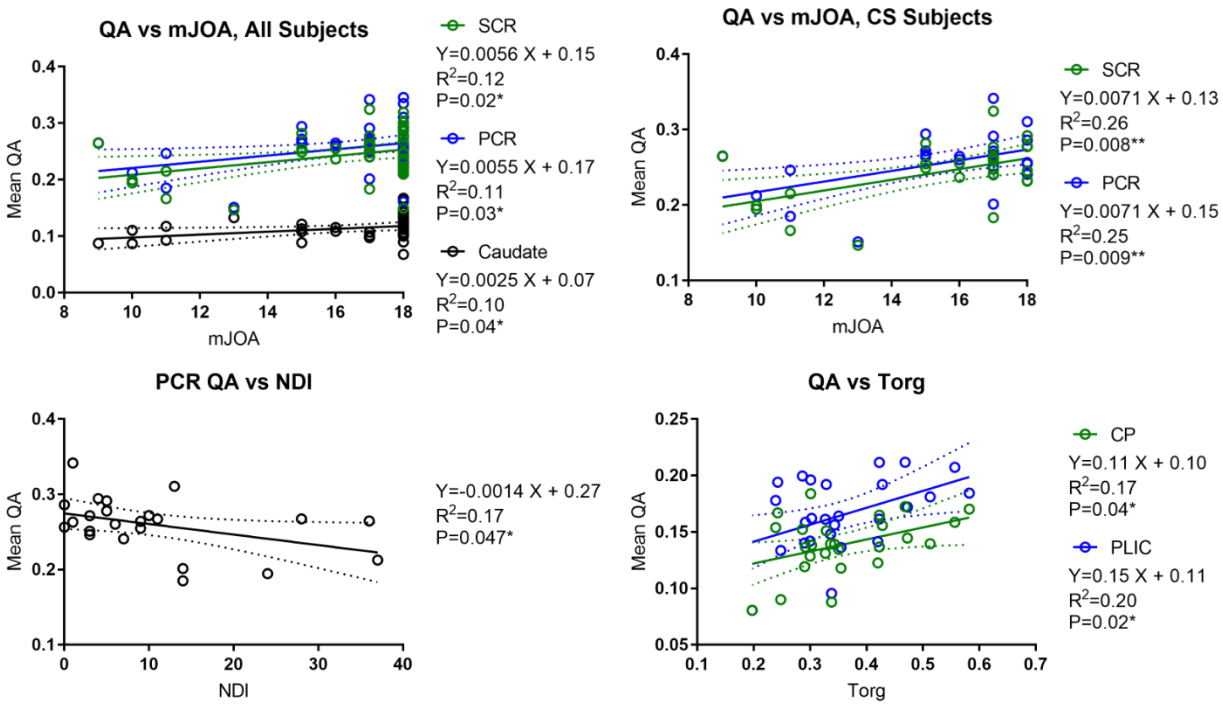

Figure 4.11. Plots of linear regression of the quantitative anisotropy (QA) vs mJOA, NDI, and MR-equivalent Torg Ratio. Plotted are the regression line (solid) with 95% confidence intervals (dashed). SCR denotes superior corona radiata, PCR denotes posterior corona radiata, CP denotes cerebral peduncle, and PLIC denotes posterior limb of the internal capsule.

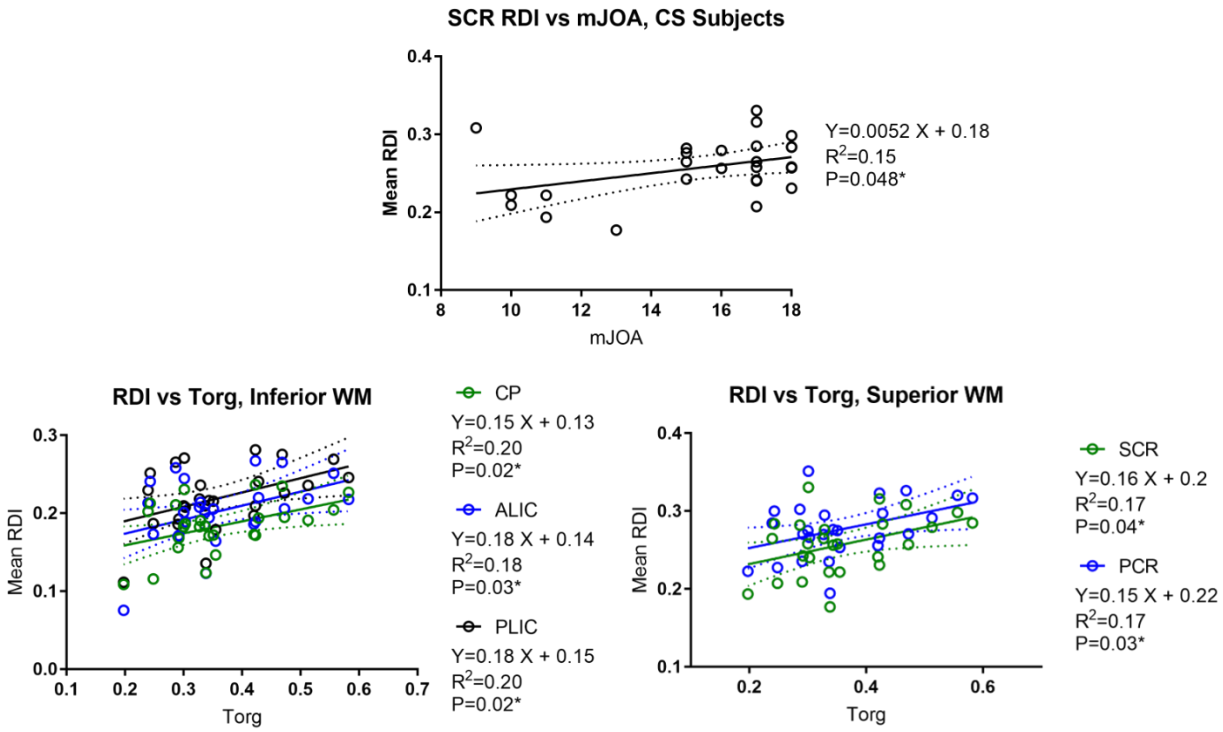

Figure 4.12. Plots of linear regression of the restricted diffusion (RDI) vs mJOA, and MR-equivalent Torg Ratio. Plotted are the regression line (solid) with 95% confidence intervals (dashed). SCR denotes superior corona radiata, CP denotes cerebral peduncle, ALIC denotes anterior limb of the internal capsule, PLIC denotes posterior limb of the internal capsule, PCR denotes posterior corona radiata.

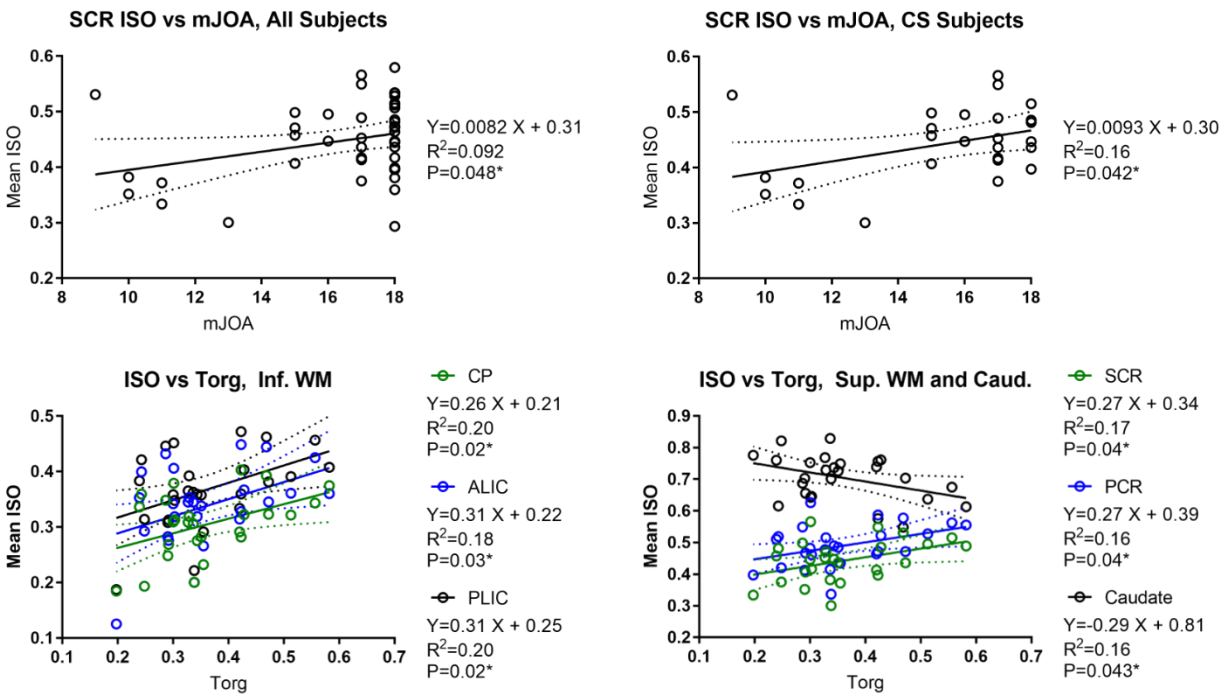

Figure 4.13. Plots of linear regression of the isotropic component of diffusion (ISO) vs mJOA and MR-equivalent Torg Ratio. Plotted are the regression line (solid) with 95% confidence intervals (dashed). SCR denotes superior corona radiata, CP denotes cerebral peduncle, ALIC denotes anterior limb of the internal capsule, PLIC denotes posterior limb of the internal capsule, and PCR denotes posterior corona radiata.

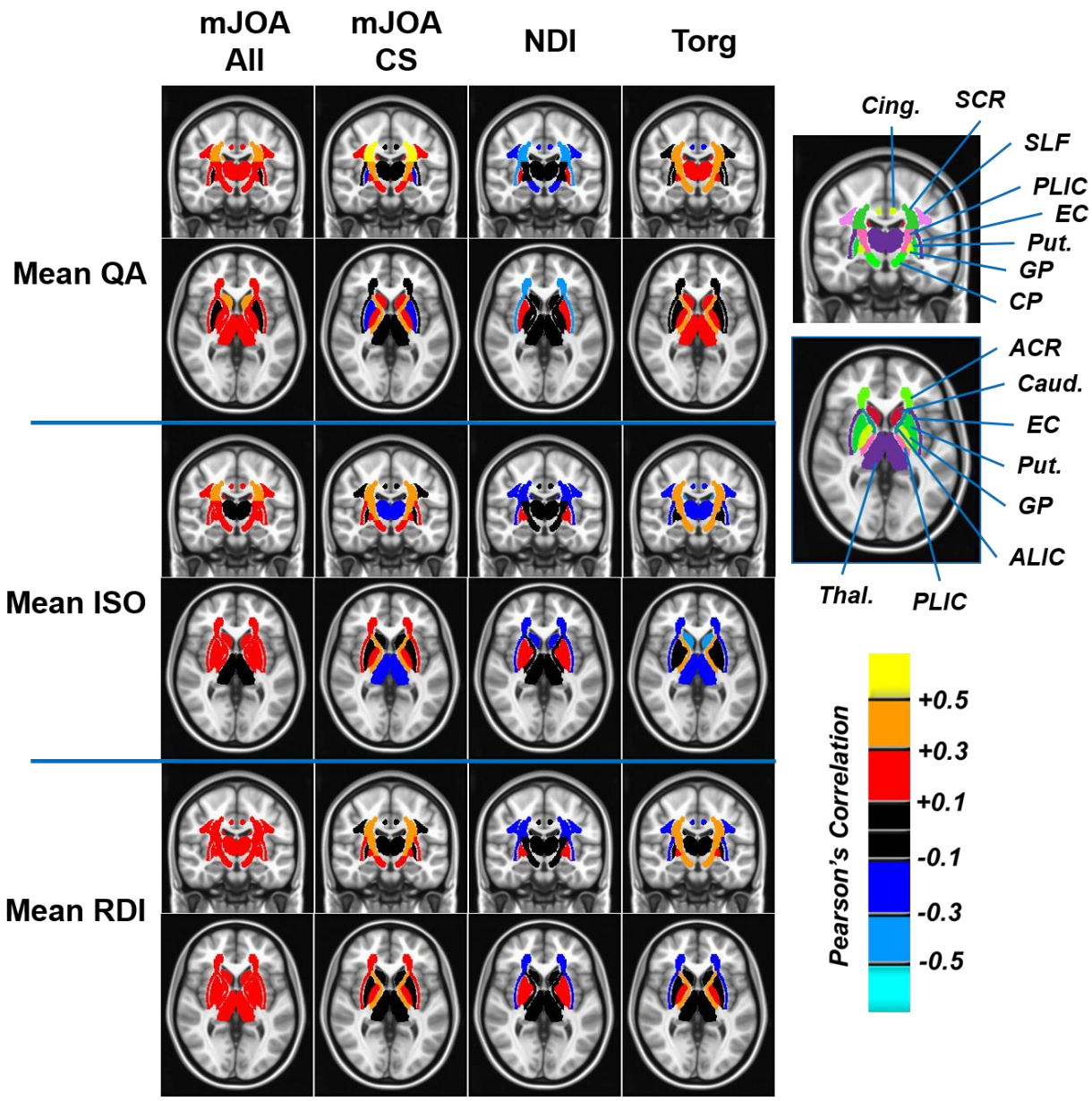

Figure 4.14. Legend presented on next page.

Figure 4.14. Maps of correlations between mean diffusion metrics in several white matter tracts and subcortical gray matter structures in the brain. ROIs are shown on the MNI T1 atlas. Pearson's correlations between metrics and clinical variables are color coded by correlation categories: 0 to 0.1 is no correlation (black); 0.1 to 0.3 is minor correlation (red for positive, blue for negative); 0.3 to 0.5 is moderate correlation (orange for positive, light blue for negative); greater than 0.5 is strong correlation (yellow for positive, cyan for negative). Quantitative anisotropy (QA), the isotropic component of diffusion (ISO), and restricted component of diffusion (RDI), are shown for the generalized q-sampling imaging (GQI) metrics. White matter tracts included the cerebral peduncle (CP), anterior and posterior limbs of the internal capsule (ALIC and PLIC, respectively), anterior and posterior corona radiata (ACR and PCR, respectively), external capsule (EC), and cingulum (Cing.). Subcortical gray matter regions included the thalamus (Thal.), caudate (Caud.), putamen (Put.), and globus pallidus (GP).

Probabilistic Tractography Between Brain Regions

Linear regression analysis of track counts from probabilistic tractography between regions of interest and symptom variables yielded significant results for particular connections (**Figure 4.15**). The tracks between the anterior cingulate (AC) and thalamus (Thal.) were significantly negatively associated (increasing tracks with worsening symptoms) with mJOA for both the whole cohort (R^2=0.20, P=0.003**) and for the CS cohort alone (R^2=0.17, P=0.04*). The track counts between the AC and the putamen (R^2=0.12, P=0.03*) and the AC and the primary sensorimotor cortex (SM, R^2=0.18, P=0.006**) were significantly negatively associated with mJOA in the overall cohort, and the track counts between the brainstem (B-stem) and SM were significant positively associated (decreasing tracks with worsening symptoms) with mJOA in the CS cohort (R^2=0.38, P=0.0008***). NDI was significantly associated with the track counts between the putamen and superior frontal gyrus (SFG, R^2=0.28, P=0.009**) and the track counts between the AC and SM (R^2=0.21, P=0.02*). For the Torg Ratio, associations were present with track counts between the SFG and the Thal. (R^2=0.20, P=0.02*), the AC to Put. (R^2=0.29, P=0.004**), and the AC to Thal. (R^2=0.22, P=0.02*). The average log of the track counts is displayed in standard space in **Figure 4.16**.

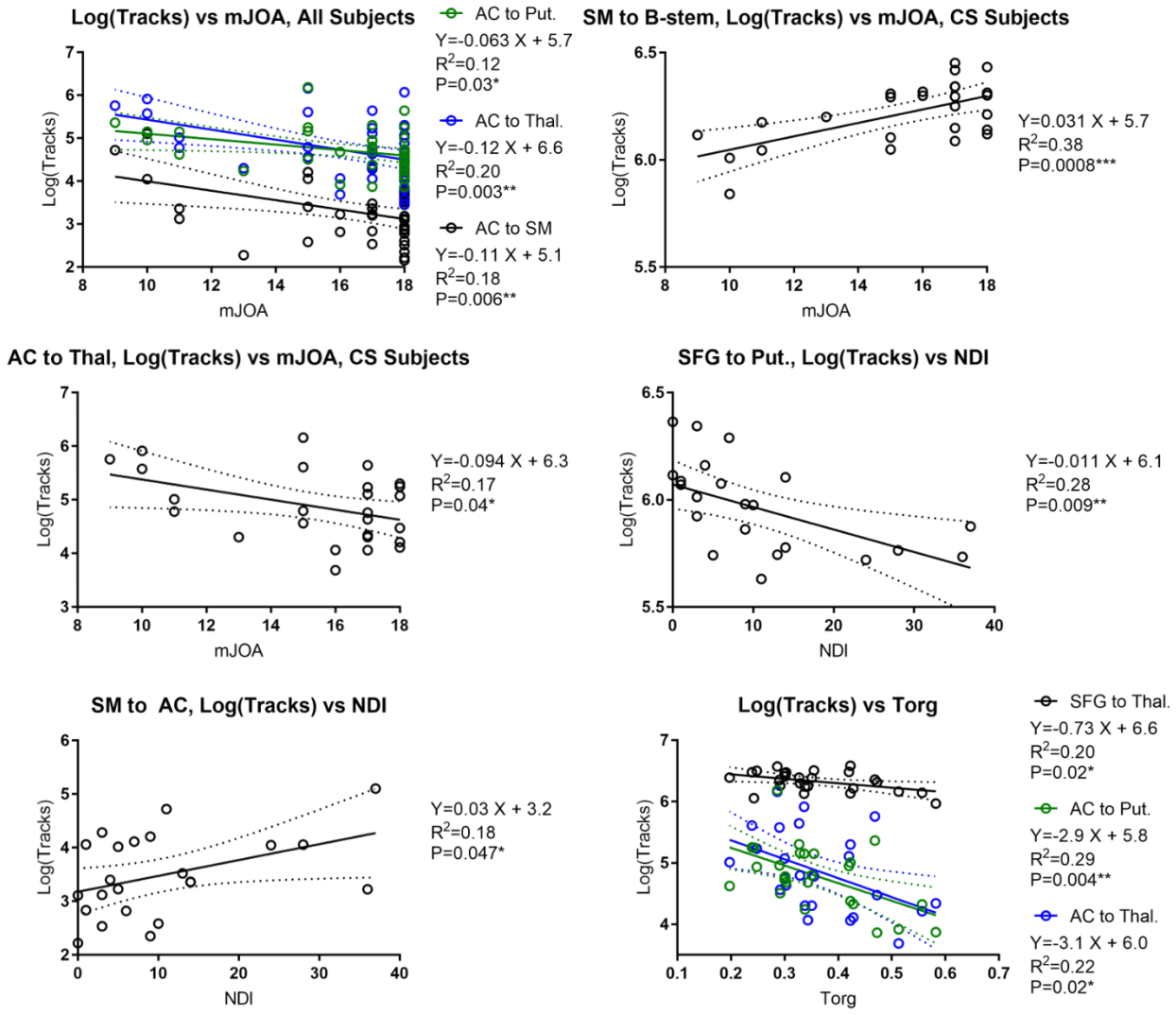

Figure 4.15. Plots of linear regression of log-transformed probabilistic tractography track counts [Log(Tracks)] vs mJOA NDI, and MR-equivalent Torg Ratio. Plotted are the regression line (solid) with 95% confidence intervals (dashed). AC denotes anterior cingulate, Put. denotes putamen, Thal. denotes thalamus, SM denotes primary sensorimotor cortex, B-stem denotes brainstem, and SFG denotes superior frontal gyrus.

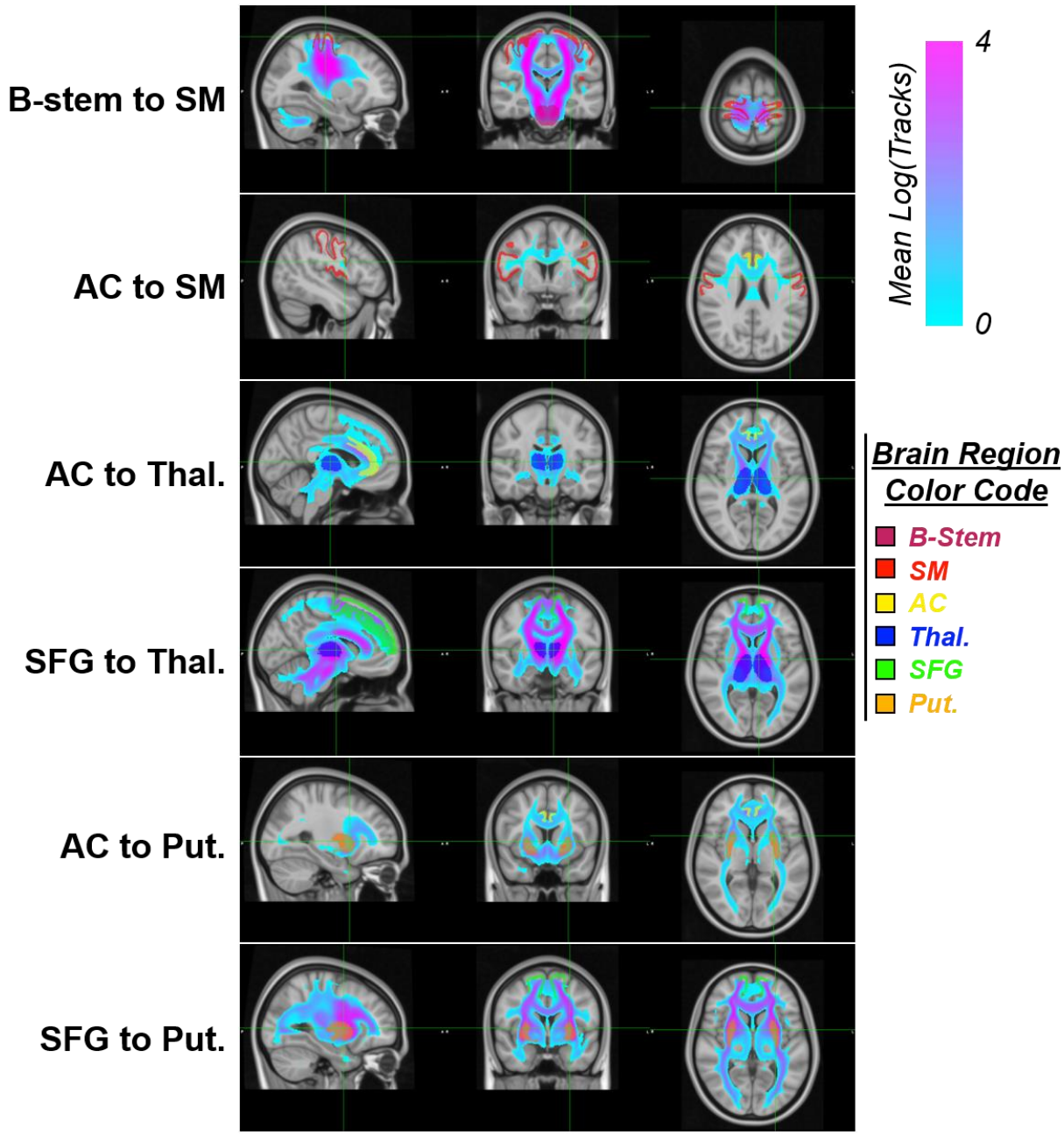

Figure 4.16. Plots of log-transformed voxel-wise track counts [Log(Tracks)] averaged across all subjects. B-stem denotes brainstem, SM denotes primary sensorimotor cortex, AC denotes anterior cingulate, Thal. denotes thalamus, SFG denotes superior frontal gyrus, and Put. denotes putamen.

iv. Diffusion MRI Metrics at the Site of Compression in the Spinal Cord

Diffusion MRI Metrics at the Site of Compression

Linear regression analysis of the mean DTI metrics measured manually at the site of maximal compression in the spinal cord revealed significant associations between FA and mJOA (P=0.03) but not MD (P=0.3, **Figure 4.17.A**) and between Torg and MD (P=0.04) but not FA (P=0.2). When examining the variables based on the vertebral labeling of the spinal cord, neither FA, MD, nor MO showed significant associations with mJOA or NDI for any level evaluated, either centered at the site of compression or across vertebral levels. Generally, mean FA displayed a weak but positive correlation with mJOA (decreasing FA with worsening mJOA) and MD displayed a weak but negative correlation with mJOA (increasing MD with worsening mJOA).

When examining the DTI measures centered around the site of compression (**Figure 4.17.B**) FA displayed slightly larger variation around the site of injury and a slight decrease when moving from more superior to more inferior regions, while MD showed an apparent increase in the vertebral level directly above the site of compression. MO displayed a striking pattern of decreased value at the site of compression that increased the further away from the compression the vertebral levels were (*i.e.* 2nd Above and Below showed a higher value compared to the Above and Below segments, **Figure 4.17.B**). In one-way analysis of variance (ANOVA) for each the DTI measures centered at the site of compression, neither FA nor MD showed significance, but MO did (P<0.0001) and *post hoc* tests showed significant differences between the mean MO at the site of compression and the mean MO at both the 2nd vertebral level above and 2nd vertebral level below (P<0.0001 for both) after Tukey multiple comparisons correction. **Figure 4.17.C** displays the mean FA, MD, and MO values at each vertebral level, with FA decreasing by level, and MD and MO showing higher variance among sites of common compression (C3, C4).

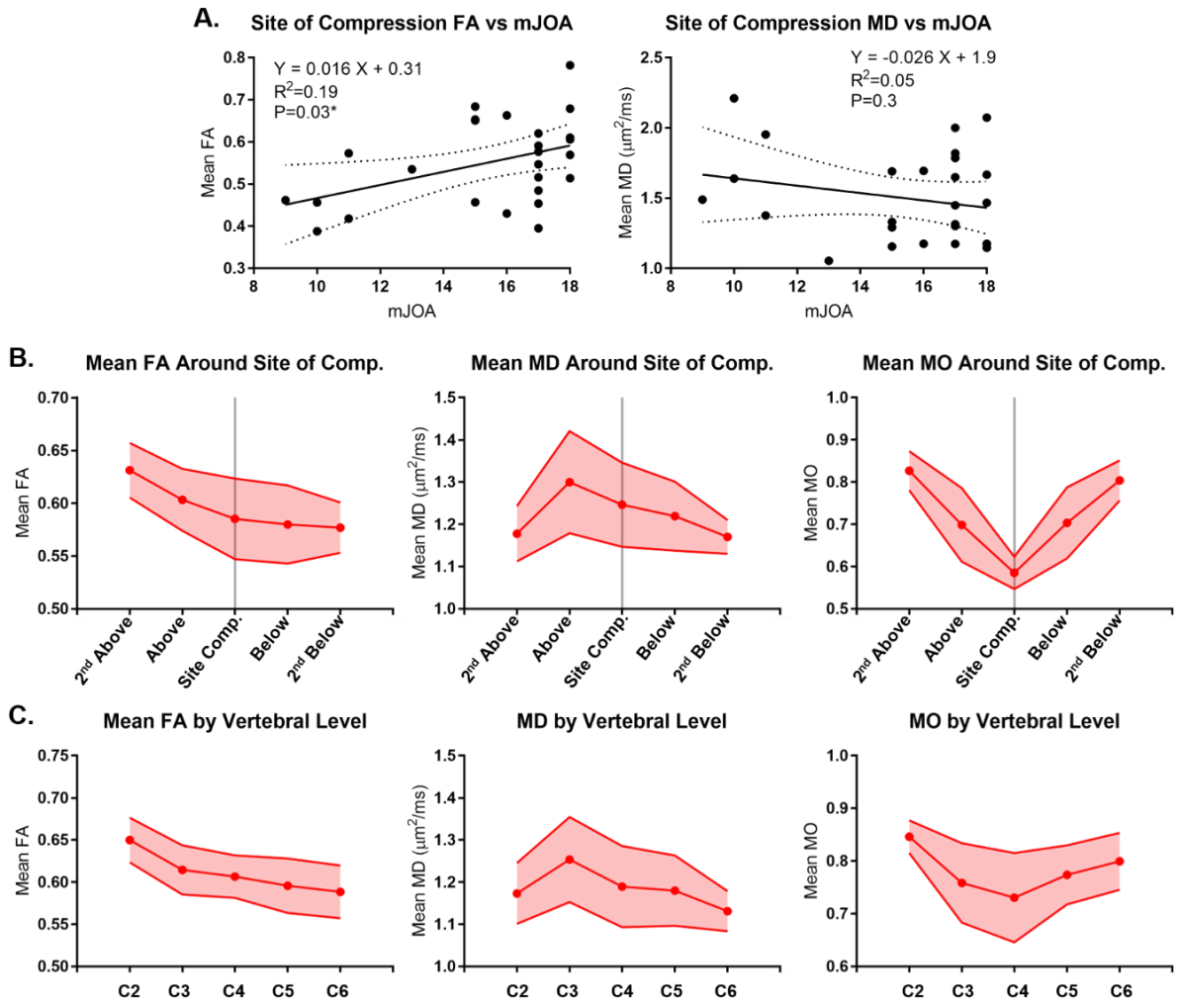

Figure 4.17. Graphs of values from manual measurements and vertebral levels of spinal cord DTI acquired around the site of compression. A) Linear regression of FA and MD from manual measurements of the spinal cord at the site of compression with respect to mJOA. B) DTI measures at site of compression (Site Comp.) and at one (Above, Below) and two (2^{nd} Above, 2^{nd} Below) vertebral levels above and below the lesion, respectively. C) Mean DTI measures per vertebral level in the spinal cord. Points represent mean, and shaded areas are 95% confidence intervals.

Comparison of DTI Metrics at the Site of Compression, C2, and Brain

In order to assess the relationship between the findings in the spinal cord at the site of compression, these were evaluated with respect to the DTI measures at the C2 vertebral level and in the corticospinal tract in the brain (CP, ALIC, PLIC, ACR, SCR, PCR). This was performed for the manually measured FA and MD. Interestingly, mean FA at the site of compression only showed a significant linear relationship with the mean FA in the ACR and PCR (P=0.02 for both), while mean MD at the site of compression showed a significant association with all the regions (lowest P=0.008 for the ALIC) except for the CP and the PLIC (**Figure 4.18.A**).

In relation to the level of the site of maximal compression, or how far away the maximal compression was from the upper cervical spinal cord and brain, only the mean FA at C2 showed a significant relationship, with a strong R^2=0.44, P=0.0002, though the mean FA at the site of compression and the CP did show a trend towards significance (P=0.08 for both, **Figure 4.18.B**). Meanwhile, MD at the C2 level also showed a strong relationship with the level of injury with R^2=0.27, P=0.006, and MD at the site of compression and at the CP were also significantly associated with the level of maximal compression (P=0.03 and 0.02, respectively, **Figure 4.18.B**), as well as the ALIC and ACR (P=0.03 for both).

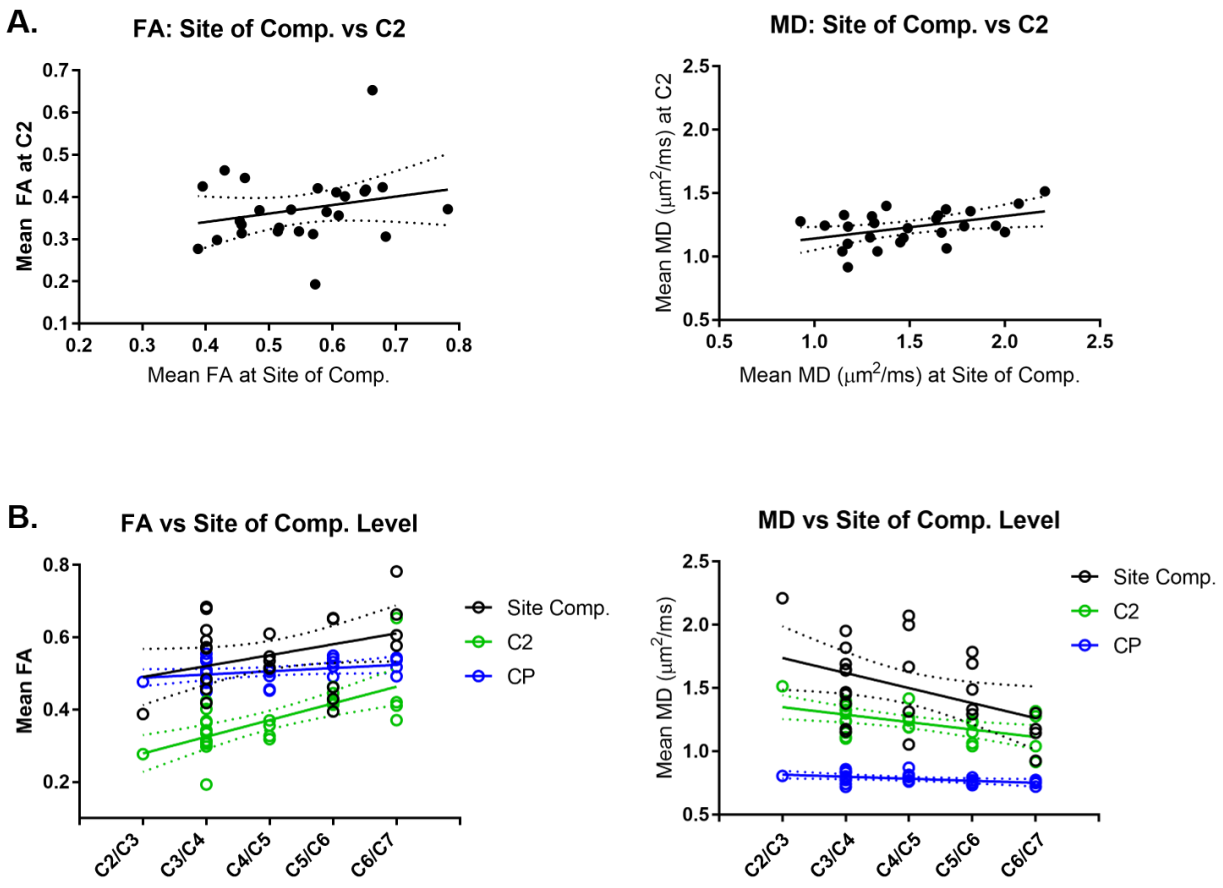

Figure 4.18. Comparison of FA and MD at site of compression with C2 and relationship between FA and MD and level of maximal compression. A) Graphs showing relationship between FA and MD at the site of compression vs at the C2 vertebral level. B) Regression of the mean FA and MD vs the level at which maximal compression was present. Solid lines represent best fit and dashed lines represent 95% confidence intervals.

v. Comparison of DTI and GQI Metrics in the Brain and Spinal Cord

Figure 4.19 shows the correlation matrices between DTI and GQI metrics in the spinal cord and brain regions. Results indicate strong correlations within the DTI metrics and within the GQI metrics in the spinal cord: for DTI, FA was positively associated with MO (0.86) and negatively associated with MD (-0.63), while MD and MO did not demonstrate as strong a relationship (-0.36). Within brain regions, DTI metrics showed similar relationships amongst themselves, with the weakest correlations being present in the SCR, a stronger relationship between variables present in the CP, and the strongest correlations present in the thalamus. GQI metrics displayed very strong correlations between themselves: these correlations were approximately 0.9 and above for all associations in the C2, CP, and SCR (white matter regions), while in the thalamus (subcortical gray matter region) the correlation between QA and ISO was 0.44, but other correlations were 0.89 (QA vs RDI) and 0.78 (ISO vs RDI).

As far as correlations between DTI and GQI measures, the patterns and strengths for these were highly variable across the ROIs. In C2, QA showed a high correlation with FA and MO, while ISO was only slightly correlated with MD and MO (**Figure 4.17**). SCR showed low correlations between most DTI and GQI measures, with only QA being slightly correlated with the DTI metrics, while for CP there were modest correlations throughout, including negative associations between MD and the GQI metrics (**Figure 4.18**). The thalamus, presented as an interesting case, with MD and ISO being modestly positively correlated with each other (0.42) while being negatively correlated with the measure of anisotropy (QA vs MD was -0.52, and FA vs ISO was -0.36), QA presenting a strong correlation with FA (0.62) and a moderate correlation with MO (0.34) (**Figure 4.18**), and RDI presenting with the weakest correlations between DTI and GQI metrics.

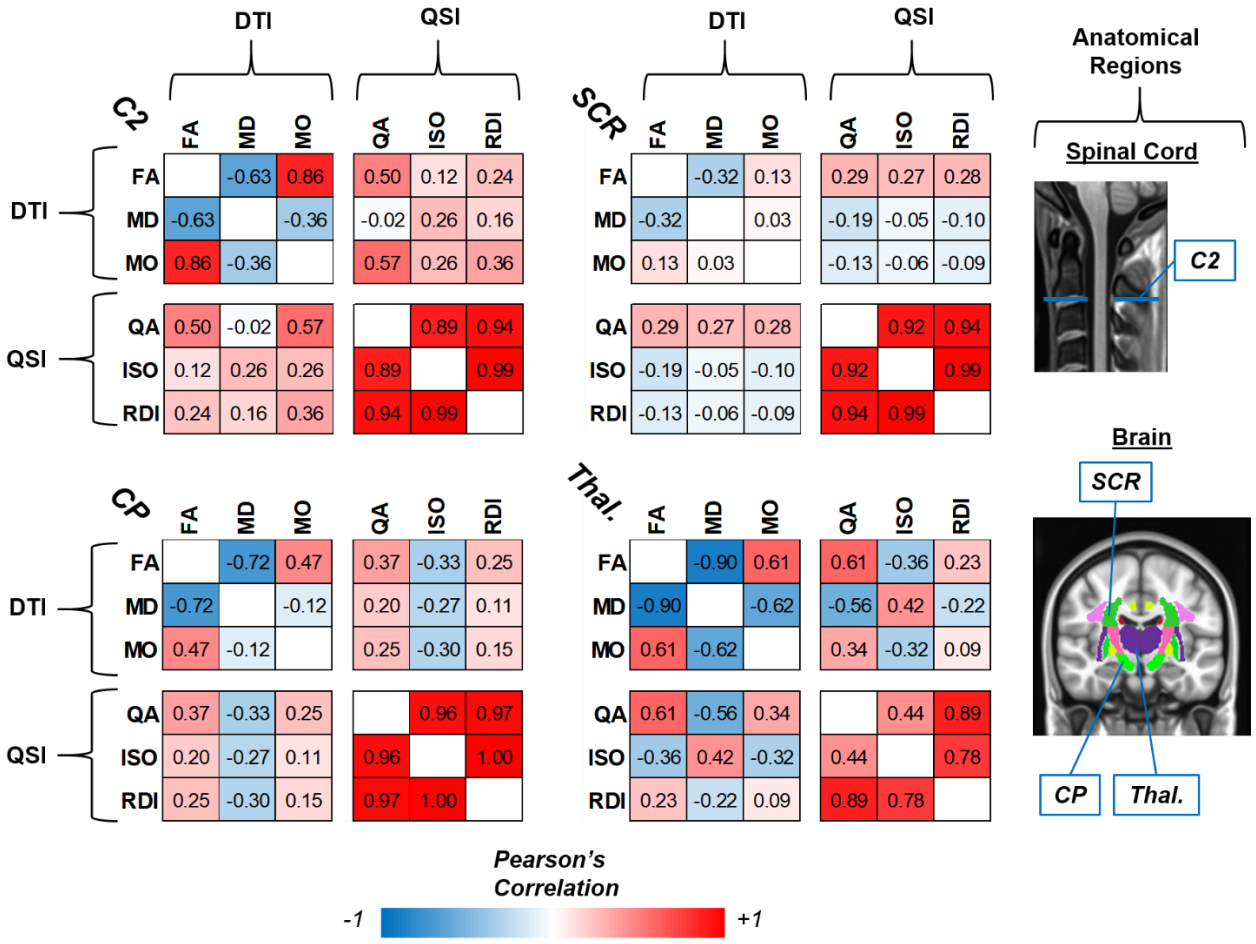

Figure 4.16. Correlations matrix of mean values between diffusion tensor imaging (DTI) metrics fractional anisotropy (FA), mean diffusivity (MD), and mode of diffusion (MO), and generalized q-sampling imaging (GQI) metrics quantitative anisotropy (QA), isotropic component of diffusion (ISO), and restricted diffusion imaging component (RDI). Regions include the C2 vertebral level in the spinal cord, and the cerebral peduncle (CP), superior corona radiata (SCR), and thalamus (Thal.) in the brain.

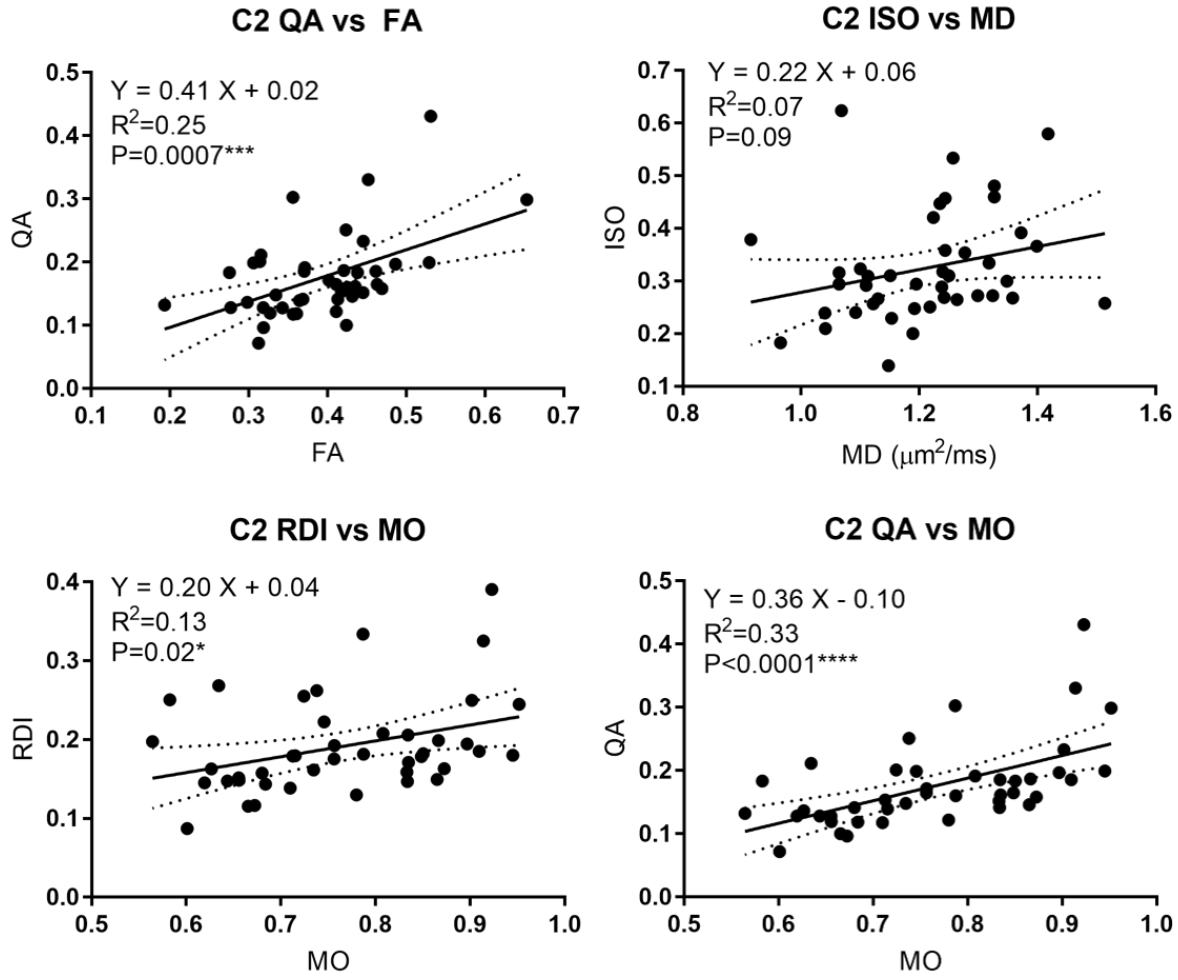

Figure 4.17. Linear regression between diffusion MRI metrics mean values at C2 vertebral level between Diffusion tensor imaging (DTI) and generalized q-sampling imaging (GQI). Quantitative anisotropy (QA) is compared to fractional anisotropy (FA), the isotropic component of diffusion (ISO) is compared to mean diffusivity (MD), and restricted diffusion imaging component (RDI) and QA are compared to the mode of diffusion (MO). Plotted are the regression line (solid) with 95% confidence intervals (dashed).

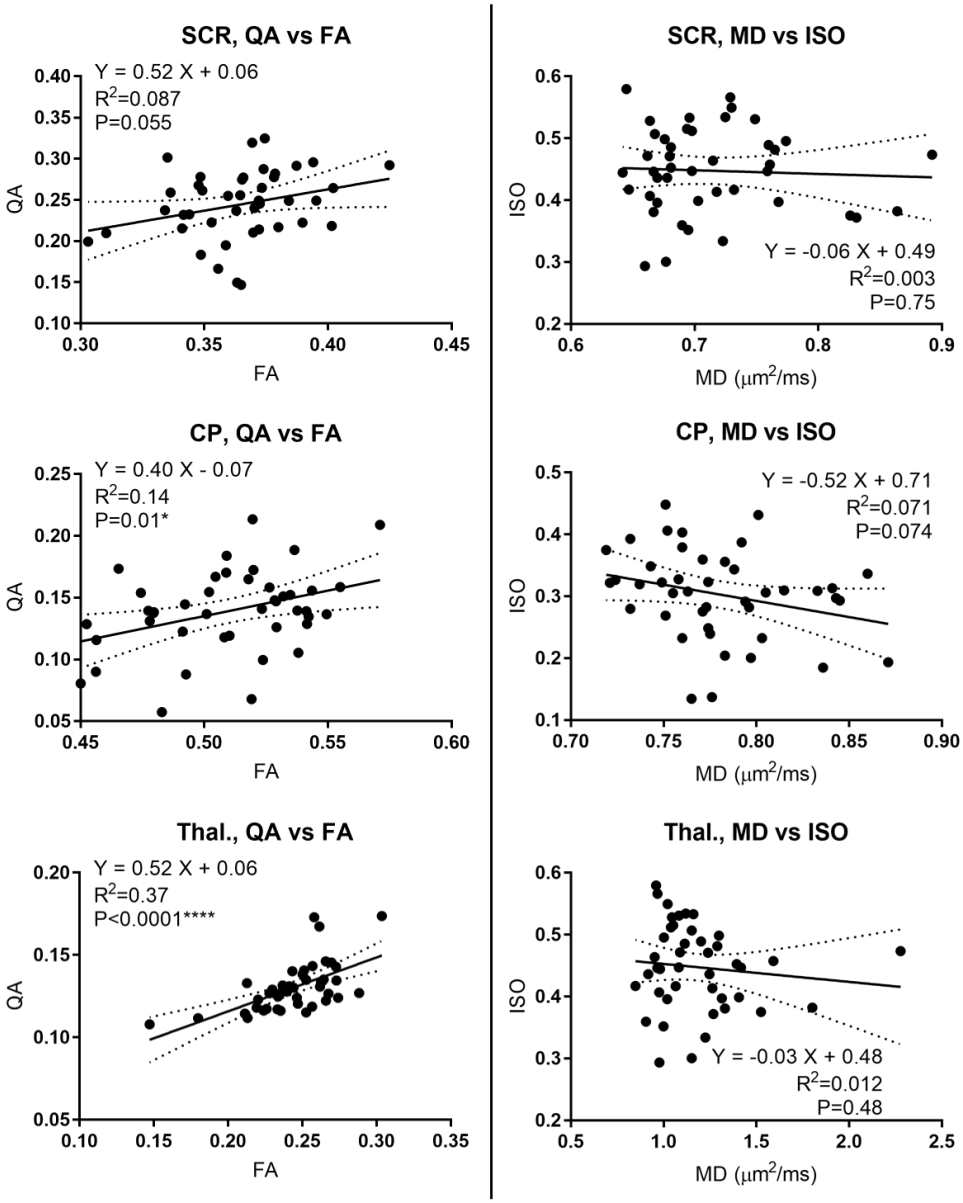

Figure 4.18. Linear regression between diffusion MRI metrics mean values in brain regions between Diffusion tensor imaging (DTI) and generalized q-sampling imaging (GQI). On the left column quantitative anisotropy (QA) is compared to fractional anisotropy (FA), and on the right column isotropic component of diffusion (ISO) is compared to mean diffusivity (MD). SCR denotes superior corona radiata, CP denotes cerebral peduncle, and Thal. denotes thalamus. Plotted are the regression line (solid) with 95% confidence intervals (dashed)

Figure 4.19 shows the coefficient of variation (CoV) of the DTI and GQI metrics across the different ROIs. Trends across the group with all subjects and the group with HC subjects only reveal the same trends. At the C2 level the DTI metrics show mostly low CoV, though for FA is larger (21%), but by comparison GQI measures show a very large CoV (32-38%). For the CP, which is in the brain but shares some characteristics with the C2 spinal cord (compact single orientation fibers) the CoV of the DTI measures were very low (~5%), while they remained high for the GQI metrics (~23%). In the SCR the CoV of the DTI metrics was relatively higher compared to the previous two regions (6-12%), and while it was lower for the GQI measures, these were around 15%. Interestingly, for the thalamus, FA and QA had similar CoV (11.1 and 11.4%, respectively), but the other DTI metrics showed a higher CoV (22.3% for MD and 23.7% for MO) while the other GQI metrics showed a lower CoV (9.7% for ISO and 9.0% for RDI).

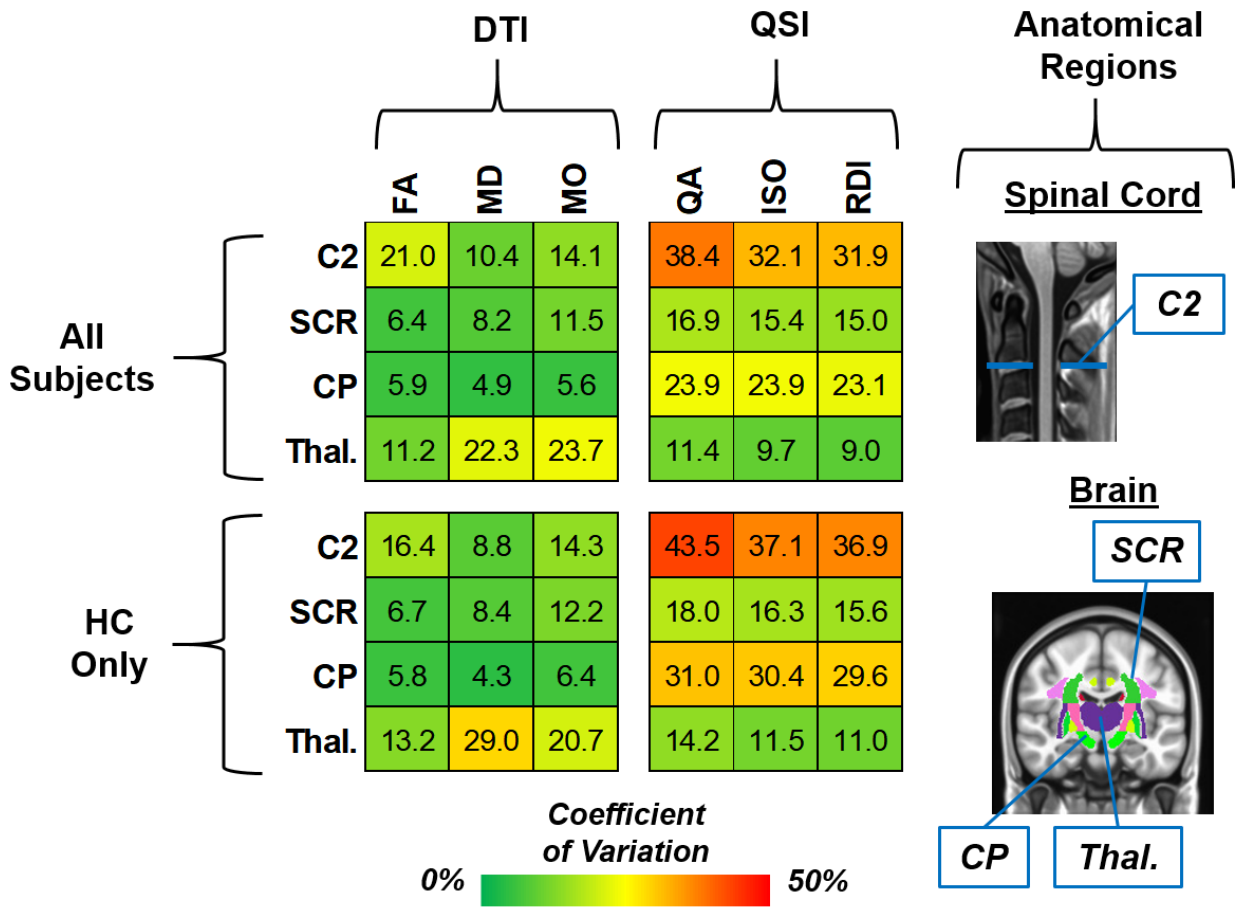

Figure 4.19. Coefficient of variation for diffusion tensor imaging (DTI) measures fractional anisotropy (FA), mean diffusivity (MD), and the mode of diffusion (MO), and generalized q-sampling imaging (GQI) metrics quantitative anisotropy (QA), the isotropic component of diffusion (ISO), and the restricted diffusion imaging component (RDI). Correlations calculated at the C2 vertebral level of the spinal cord, superior corona radiata (SCR), cerebral peduncle (CP), and thalamus (Thal.), computed in both the group with all subjects (top matrices) and in the group of HC subjects (bottom matrices).

Based on the results of the correlation matrices, the models selected for multiple linear regression analysis involved mJOA scores and Torg Ratios (not many significant associations with NDI were present), and the models constituted: all variables, DTI measures, and a model using both FA and QA as representative values of DTI and GQI (given that the GQI metrics were all highly correlated in most regions). In C2, multiple linear regression models of mJOA in all subjects and CS subjects only were not significant for the model with all the variables (P=0.29 for overall, P=0.62 for CS), DTI metrics (P=0.084 for overall, P=0.33 for CS), or for FA and QA (P=0.083 for overall, P=0.36 for CS). For Torg Ratio and metrics at C2, the model with all the metrics was not significant (P=0.85), while with the DTI metrics the model was significant (P=0.01*, R^2=0.39) with FA being a significant independent predictor (P=0.042) while neither MD nor MO were (P=0.92 and P=47, respectively), and the combined FA and QA model was predictive (P=0.004**, R^2=0.38) with FA a significant variable (P=0.003) while QA was not (P=0.76).

In the brain, for CP similar trends to C2 emerged, with the model using all the variables not appearing as significant for mJOA in the whole or CS groups, while Torg was not significant for the model with all variables, but was for the model with DTI variables (P=0.033, R^2=32, though none of the metrics were independently significant), and was significant for the combined FA and QA model (P=0.033, R^2=0.26, though none of the metrics were independently significant). For SCR, significant model with all the metrics were produced for mJOA in the overall (P=0.024, R^2=0.32, with MD, ISO, and RDI as significant independent variables) and CS-only (P=0.015, R^2=0.53, all GQI metrics independently significant) groups, and the FA and QA model produced significant model in the overall (P=0.049, R^2=0.14, no independent significant variables) and CS-only (P=0.028, R^2=0.27, QA significant variable), while this was not the case for the DTI metrics which produced no significant models. No significant models were produced between the SCR

and the Torg Ratio. For the thalamus the only multiple linear regression model that was significant was the model with the DTI variables (P=0.036, R^2=0.32, MD significant independent variable).

vi. Discussion

Recent studies have shown altered microstructure of the spinal cord at the site of compression in patients with cervical stenosis and associated myelopathy, with decreased FA and MD indicative of degenerative changes in the white matter [201,299]. These associations between patient neurological symptoms and the microstructure of the spinal cord are more striking in the context of the degree of compression of the spinal cord: regular measurements of compression on anatomical ROI have shown very limited and weak associations with neurological symptom severity [40-46]. In addition to changes at the site of compression, a recent meta-analysis of DTI patients with cervical stenosis and associated myelopathy indicated that the spinal cord at the C2 vertebral level presents with significantly lower FA and higher MD in patients with CSM compared to healthy controls, though this difference is weaker than at the site of maximal compression [200]. Additionally, studies in traumatic spinal cord injury (SCI) have shown changes that ascend even further rostrally, into the white matter of the brain such as the cerebral peduncle and the internal capsule [160]. While diffusion MRI measures in the spinal cord at the site of compression have shown promise in associations with symptom severity for patients with cervical stenosis, there are likely white matter changes and reorganization happening in the uncompressed rostral spinal cord and brain in addition to those in the spinal cord. This chapter evaluated the association between diffusion MRI changes in the spinal cord at the site of compression, C2 vertebral level, and in the brain in select white matter and subcortical gray matter regions based on *a priori* hypotheses and results from the previous two chapters in this dissertation.

Spinal Cord Diffusion MRI Measures Associated with Clinical Variables

Generally, the spinal cord presented negative associations between mJOA and FA and positive associations between mJOA and MD. Both of these were present significantly at the C2 vertebral level, at the site of compression there was a significant association of mJOA with FA but not with MD. This is in line with previous studies where generally at the site of compression FA has shown a stronger relationship with symptom severity and results with MD have been weaker [201,283,284]. Overall, these results are consistent with previous research both at the site of compression and at uncompressed upper levels. The neck disability index (NDI) did not show significant results of linear regression with mean diffusion MRI metrics of the spinal cord at the C2 level or the site of compression, which may be due to the neck pain being related to a combination of peripheral and central mechanisms instead of being due to injury within the spinal cord itself. Also, the complexity of internal spinal mechanisms for pain regulation [68,179] may render it more difficult to probe using neuroimaging and thus obfuscate any relationships with symptoms.

While the analysis of DTI measures by vertebral level from the spinal cord diffusion MRI data did not yield strong relationships with mJOA, the trends (increasing FA and decreasing MD for worsening neurological symptoms) that were present are expected from previous studies. While FA and MD at vertebral levels centered around the site of compression did not yield striking results, one result of interest was the markedly decreased mode of anisotropy (MO) at the site of compression, which yielded a significant one-way ANOVA and the MO at the vertebral levels that were 2 above or below the site of compression were highly significantly different from the MO at the site of compression. While FA and MD are usually the variables of interest in DTI assessment of spinal cord integrity, one previous study has looked at the axial diffusion anisotropy, ψ, which involves subtracting the mean diffusivity from the axial diffusivity, and found that it was correlated

with mJOA [201]. Thus, not only FA, but additional measures of tensor shape may help better identify sites of compression and assess spinal cord integrity.

Strong associations between the MRI-equivalent Torg Ratio and all three DTI variables (FA, MD, and MO) in the spinal cord at the C2 vertebral level were observed in this chapter. Additionally, MD at the site of compression was also associated with the Torg Ratio. In a previous study that had a similar sample size of CSM patients (n=27), an association between the Torg Ratio and the FA at the site of compression was observed [283]; however, this association, while significant (P=0.02), showed a lower R^2 (0.20) [283] than that observed in the analysis in this chapter (R^2=0.38, P=0.0008***). Another study that analyzed DTI in patients with cervical stenosis found significant associations between FA and the Torg Ratio in the spinal cord, with correlations up to 0.75 (P=0.001) [300]; however, this study evaluated the Torg Ratio at the same vertebral level as the DTI, with the listed correlation being between FA and the Torg Ratio at the C2 vertebral level, with the associations losing strength more inferiorly along the spinal cord. Additionally, in this chapter MD and MO also displayed significant associations with the Torg ratio consistent with degenerative changes. So, while Torg Ratio was not associated with symptoms in this study (R^2=0.050, P=0.3, **Chapter II, Section iii**), it was strongly associated with these rostral degenerative changes as assessed using DTI.

While DTI measures were associated with symptoms and degree of compression, the mean values of the GQI measures were not significantly associated with symptoms or compression. This may be due to several factors. First, imaging of the spinal cord generally presents more challenges than the brain, due to its greater magnetic field inhomogeneity caused by the different tissue types, its smaller cross-sectional area and volume, and increased physiological noise. Because DTI is a model-based method (i.e. a tensor fit of the data is performed based on Gaussian diffusion) these

model constraints may help mitigate some of the signal intensity discrepancies that may reduce the quality of a model-free approach such as GQI, especially when GQI is dependent not only on the orientation distribution of the signal, but is also sensitive to the distribution of spins [152,289]. Additionally, the spinal cord (at the relatively large acquisition voxel-size) can be considered to have a primarily single-fiber orientation organized in the inferior superior direction, and thus a DTI fit of the acquired diffusion data may be sufficient to accurately describe these voxels with mostly a single fiber population. In a previous publication, constrained spherical deconvolution (CSD), which similar to GQI produces an ODF, was used to perform probabilistic tractography of the spinal cord at the site of compression, and the density of track fibers was associated with patient neurological symptoms [280]. However, for this study a response function was created from white matter with an assumed single fiber distribution, and this response function was then used for the deconvolution of the diffusion signal; thus, a model constraint was still being implemented when using the CSD technique, unlike the completely model-free method implemented by GQI.

When examining the regional correlations between white matter tracts in the spinal cord and symptom and compression measures, FA and MD yielded expected patterns: overall positive associations with mJOA for FA and overall negative associations with mJOA for MD. In general, these associations between DTI measures and mJOA were stronger in more lateral tracts (spinothalamic, corticospinal, and cuneate) and less so in the gracile tract. The Torg Ratio presented with strong correlations for all three variables, again more focused on the lateral tracts and less so on the gracilis. The GQI measures showed weak correlations with mJOA, except for ISO and RDI which displayed a moderate correlation with the gracile tract. Correlations between NDI and GQI measures produced moderate-to-strong correlations, though these were not localized to the spinothalamic tract, but were rather present in the corticospinal, cuneate and gracile tracts.

The correlation between the Torg Ratio and the GQI measures yielded moderate correlations with QA and weak correlations with ISO and RDI.

One possible reason for the differences in the relationship between DTI and GQI metrics in the spinal cord at C2, particularly in the gracile fasciculus, is the distribution of stress due to compression and which white matter tracts can be affected. Biomechanical models of spinal cord compression have indicated that while gray matter and posterolateral white matter tracts are frequently affected by higher levels of stress, the gracile fasciculus is relatively spared [245,301]. With the posterolateral tracts being more affected by the compression, DTI may be better suited to detect classical signs of retrograde and anterograde degeneration, while changes occurring in the gracile nucleus may represent more complex reorganization that is better assessed via GQI. This is also in line with the relatively low prevalence of lower limb sensory deficits and paresthesia in patients with CSM, which was 10% in a recent study encompassing 58 patients at UCLA [302].

Brain Diffusion MRI Measures Associated with Clinical Variables

In the brain, there were associations between DTI metrics and mJOA scores and Torg Ratios. Significant regressions with mJOA were present in the corona radiata and in the cerebral peduncles, while for Torg the cerebral peduncle and caudate produced significant results with FA (decreasing FA with worsening symptoms) and MD (increasing MD with worsening symptoms). These are in line with previous studies of the white matter in patients with traumatic spinal cord injury, where degenerative changes appear to be present rostral to the site of injury [160,168,303], and while the exact localization of changes varies from one study to another, these usually involve the corticospinal tract, both superiorly near the motor cortex and inferiorly near the brainstem. NDI was not found to be associated with the mean DTI values in brain regions except for the mode of

diffusion in the cingulum, which may be related to the involvement of the cingulate cortex in chronic pain [304]. The correlation between DTI measures and the brain regions confirmed these results, with global decreases in FA and increases in MD with worsening symptom measures.

For GQI measures, these largely followed similar trends of positive association with mJOA (decreasing metric with worsening neurological symptoms) in the superior and posterior corona radiata for all the symptom and compression measures. Additionally, the Torg Ratio was associated with the mean GQI measures in many regions along the cortical spinal tract, including the cerebral peduncles, the anterior and posterior limbs of the internal capsule, and the corona radiata. Similar to the DTI results, not many significant regressions with NDI were present for GQI metrics, with only the mean QA in the posterior corona radiata showing an association. The map of correlations further solidifies this point: GQI metrics appear highly positively correlated with the corticospinal tract for mJOA and Torg Ratio, with regions outside of these showing lower correlations and sometimes negative correlations.

One of the main advantages of model-free and q-space based diffusion MRI techniques is the representation of more complex fiber populations and microstructural characteristics. However, definition and standardization of appropriate imaging metrics, which is well-established and widely-used for DTI, is not yet well-developed for techniques that evaluate more complex diffusion distributions [305]. This is partially remedied with the development of standard metrics, such as generalized fractional anisotropy (GFA) [291]. and generalized q-sampling imaging (GQI) metrics, such as quantitative anisotropy (QA) [289,293]. Analyses from this chapter indicated that while these measures can be correlated with DTI measures in certain regions, this varies with the different microstructural properties of each region. For example, this chapter found strong associations between the measures in the thalamus, a subcortical gray matter structure with a high

degree of intersecting white matter fibers, while brain white matter regions (cerebral peduncle and superior corona radiata) showed relatively weaker associations. When combining the different measures from DTI and GQI, they seemed to offer the most complimentary information for regions with more complex fiber populations, such as the superior corona radiata (corticospinal tract but with additional fiber populations present) and thalamus (subcortical structure with internal white matter). Additionally, QSI measures tended to show increased coefficient of variation, especially in the spinal cord and cerebral peduncles, indicating the potential need for model constraints in regions susceptible to artifacts and with low signal intensity, while GQI metrics had a lower CoV in the regions with more complex microstructure, namely the SCR and the thalamus.

Probabilistic tractography results indicated increased connectivity between the anterior cingulate and the various cortical and subcortical brain regions with worsening symptoms (decreasing mJOA, increasing NDI, and decreasing Torg Ratio). Specifically, for pain, a previous study in patients with irritable bowel syndrome (IBS) found increased number of connections between the anterior cingulate and the thalamus and between the thalamus and prefrontal cortex when compared to healthy control subjects [196]. In this chapter the anterior cingulate presented with increased connectivity to the primary sensorimotor cortex with increasing neck pain, and the anterior cingulate presented with increased connectivity to the thalamus with worsening neurological symptoms. However, the superior frontal gyrus presented with decreasing connectivity to the putamen with worsening neck pain, indicating that the relationship between the number of tracts and symptoms may not simply be a global increase between subcortical and cortical regions but rather may be more functionally specific.

One result of interest for the probabilistic tractography analysis was the association between mJOA and the brainstem to primary sensorimotor cortex. The corticospinal tract has been

evaluated extensively in other neurological conditions, such as stroke, where altered corticospinal tract integrity was associated with worse motor function and outcome [306,307]. Probabilistic tractography methods have also detected altered corticospinal tract integrity in patients with amyotrophic lateral sclerosis (ALS) [308-310]. Though the mechanism of decreased tract integrity (namely, infarcted tissue for stroke, and upper motor neuron death for ALS) are different for these conditions than that for SCI, corticospinal tract integrity is still shown to be an important marker for motor function and recovery.

Chapter V. Associations and Combined Use of Multimodal MRI Features

The previous three chapters have outlined the acquisition, processing, and analysis of structural, functional, and diffusion MRI data in patients with cervical stenosis. These were evaluated in terms of their association with neurological symptoms and neck pain, and displayed changing brain structure, microstructure, and function, with worsening symptom severity. Across the different MRI modalities, some similar structures appeared related to symptoms, including primary sensorimotor regions such as the primary sensory and motor cortex, the thalamus, and the corticospinal tract, as well as supplemental brain regions involved in motor control or chronic pain such as the putamen, the precuneus, the anterior cingulate, and the superior frontal gyrus.

One goal of this chapter is to qualitatively summarize the results from the previous three chapters by comparing the relationship between symptoms and the involved structures across the different MRI modalities. For example, contrasting results from the anterior cingulate for both structural MRI, which presented decreased cortical thickness, with the functional MRI results, which showed an increased connectivity between regions of the anterior cingulate and the thalamus, and diffusion MRI results which presented with decreased tracts between the anterior cingulate and the thalamus. These results will be presented side-by-side in summary tables and figures. The other goal of this chapter was to use simple machine learning techniques for quantitative comparisons between the different measures. The comparison between, and dimensionality reduction of, the different MRI measures was performed through principal component analysis (PCA) and corresponding correlation matrices. An additional goal of this chapter was to evaluate the association between symptom severity and the computed principal components using multiple linear regression models.

i. Feature Selection and PCA Methods

Subject Data

The data used in this chapter was collected from the analyses of the previous chapters. Subjects used for this chapter included all the patients with cervical stenosis (CS), and the healthy control subjects (HC) that underwent the same imaging protocol (see **Table A.1**). For acquisition and processing of structural MRI data see **Chapter II**; for acquisition and processing of resting-state functional MRI data (rs-fMRI) see **Chapter III**; for acquisition and processing of diffusion MRI data see **Chapter IV**. For analyses using the modified Japanese Orthopedic Association (mJOA) score, the whole cohort of 43 (HC and CS) subjects was used, while for analyses using the Neck Disability Index (NDI) only the 23 CS subjects with NDI scores were used, similar to the analyses performed in the previous chapters.

Qualitative Summary

The results from the previous three chapters are reported in this chapter side-by-side: summaries of structural, functional, and microstructural findings are displayed both in tables and in figures. This was done with respect to the two clinical symptom measures of interest: the mJOA score for neurological symptoms, and the NDI for neck pain. The summaries revolve around *a priori* structures of interest, such as the primary sensorimotor cortex, as well as regions that recurred throughout the results, such as the precuneus. Results are reported with respect to worsening symptom severity, which means that negative changes represent a decrease in the MRI measure with respect to worsening mJOA (lower mJOA) and worsening NDI (higher NDI), which is in contrast to how mJOA was reported in previous chapters. This reversed reporting scheme for

mJOA was done only for the qualitative summary in this chapter to facilitate comparisons across the mJOA and NDI scores.

Feature Selection for Quantitative Analysis

Measures of interest for each MRI modality were selected based on the results from the previous sections, and all variables were calculated from predefined ROIs in respective gray matter and white matter atlases. Briefly, for structural measures, these included the cortical thickness and subcortical volumes of regions defined by the Desikan-Killiany-Tourville (DKT) cortical atlas [216] from FreeSurfer (https://surfer.nmr.mgh.harvard.edu/fswiki) [82,83,89]. For rs-fMRI, these constituted functional connectivity between regions defined by the Harvard-Oxford cortical and subcortical atlases. For diffusion MRI metrics, these included significant DTI, GQI, from the spinal cord at C2 and white matter regions defined by the Johns Hopkins University (JHU) white matter atlas, and subcortical gray matter ROIs taken from the Harvard-Oxford subcortical atlas, both of which are distributed with the FSL package (https://fsl.fmrib.ox.ac.uk/fsl/fslwiki/Atlases). Diffusion MRI metrics also included probabilistic tractography track counts between selected Harvard-Oxford cortical regions. For CS subjects, DTI measures at the site of compression of the spinal cord were also included for a separate CS cohort analysis. For bilateral structures, measures were averaged across hemispheres in order to simplify and reduce the number of variables, as well as to focus on system-wide (*i.e.* overall motor, sensory, pain processes) associations with symptom severity; this averaging across hemispheres also reduced the variance in the measures for most regions, and stabilized the variance in regions where one hemisphere showed markedly increased variance **Figure 5.1** illustrates the case for several measures from the mJOA dataet. Additionally, results from previous chapters indicated mostly bilaterally symmetric findings.

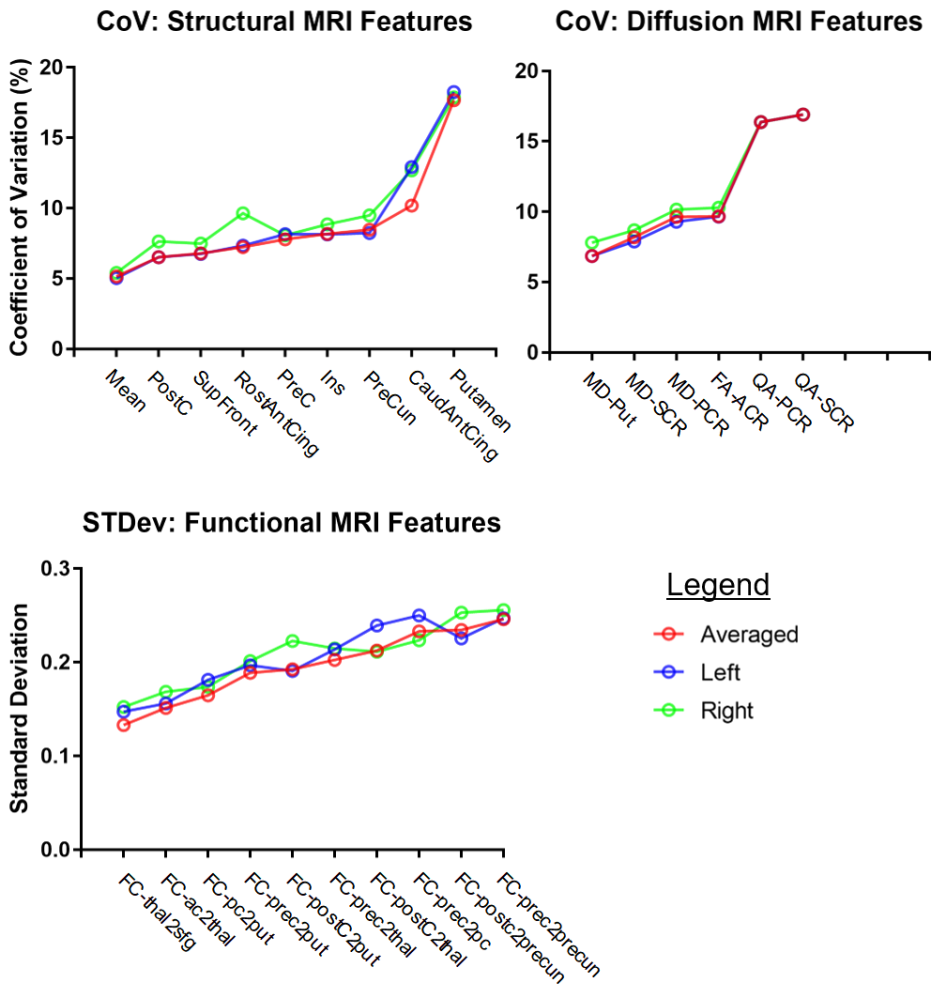

Figure 5.1. Variance in structural, functional, and diffusion MRI features by hemisphere. For Structural and diffusion MRI features, coefficient of variation (CoV) is used because different measures were compared, while for functional MRI features (connectivity) the standard deviation (STDev) is shown instead because these measures were Pearson's correlations and the means are sometimes close to zero, complicating the use of CoV. The averaged (red) measures generally show lower variance, and for cases where one hemisphere showed a larger variance the averaged variance is closer to the lower variance between the two.

Principal Component Analysis

MRI features also needed to pass an additional threshold of a Pearson's correlation coefficient with the symptom measure of interest of 0.2 or higher to be included in the principal component analysis (PCA) [311,312]. In cases where subjects lacked specific values or data for a particular MRI modality these were treated as missing data-points and accounted for using the alternating least squares (ALS) algorithm [313]. PCA was performed in MATLAB (https://www.mathworks.com/) and the different MRI features were standardized using Z-score normalization across subjects for each variable. To determine the number of components to evaluate in further analyses, random matrices were created using the same size as the respective feature vector (mJOA and NDI related features and subjects) and the mean variance explained across each component after 50,000 random permutations was recorded [314]. The principal components ($PC\text{-}MRI_k$) that had a larger explained variance than the respective randomly generated components ($PC\text{-}RAND_k$) were used in further analyses. MATLAB was also used to generate biplots for the respective feature sets for mJOA and NDI, displaying both the observations (subjects) and the coefficients (MRI features) on the first three principal components.

Regression Analyses with respect to Symptom Measures

The final analyses evaluated the relationship between the principal components and the symptom measures mJOA and NDI. These were performed using multiple linear regression in two ways: the first involved evaluating the largest principal component (PC1) of each feature set as the dependent variable in the analysis and age and the symptom measure as the independent variables, similar to the evaluation of single measures from specified regions as performed in previous chapters. The second form of analysis involved creating a multiple linear regression model using

the various principal components, along with age, as independent variables, while having the symptom measure as the dependent variable. The second multiple linear regression model was constructed by pruning the independent variables via a stepwise process of eliminating the variable with the highest individual P-value in the model, re-evaluating the model, and finishing when only variables that significantly contributed individually to the model remained. To ensure the appropriateness of multiple linear regression models, variance inflation factors (VIF) were calculated for the independent variables, Goldfeld-Quandt tests for Heteroskedasticity [315] at type-I error-corrected rate of 0.05, and D'Agostino & Pearson normality tests for the residuals [316].

Software

MATLAB (MATLAB Version 2014a, https://www.mathworks.com/) was used for PCA. Statistical analyses were performed using GraphPad Prism (Version 7.0b, La Jolla California USA, www.graphpad.com), and multiple linear regressions were performed in Free Statistics Software (Version 1.1.23-r7, http://www.wessa.net/rwasp_multipleregression.wasp/).

ii. Qualitative Comparison of Brain and Spinal Cord Multimodal MRI Results

Qualitative Summary of MRI Features Associated with Neurological Score

The results for the association of MRI features with neurological symptoms (as assessed via mJOA scores) are presented in **Table 5.1** and **Figure 5.2**. These results show a decrease in cortical thickness and subcortical volumes in regions involved in motor performance and monitoring, such as the superior frontal gyrus, the precuneus, the anterior cingulate, and the putamen. In addition to these supplemental brain regions for motor function, subdivisions of the primary motor (Brodmann area 4A) and the primary sensory area (Brodmann area 3a) showed

some relationship with neurological function, though these effects were not seen for the entire structure. Functional connectivity (FC) showed both positive and negative association with worsening neurological symptoms (lower mJOA scores). The primary sensorimotor cortex displayed increasing FC to the thalamus and precuneus, while the putamen showed decreasing FC to the precuneus and primary sensorimotor cortex. The thalamus, in contrast to its FC with the primary sensorimotor cortex, displayed a decreasing FC with the anterior cingulate (AC) and the superior frontal gyrus. For diffusion MRI measures, the tractography counts displayed a negative relationship with symptom severity (decreasing connectivity) along the corticospinal tract, and thus between the spinal cord (C2), thalamus, and primary sensorimotor cortex. The AC appears to show increased connectivity with several cortical and subcortical regions, including the thalamus, putamen, and primary sensorimotor cortex. The thalamus and primary sensorimotor cortex were regions where both functional and diffusion connections were present, and these presented with an inverted relationship: increasing functional connectivity with decreasing diffusion connectivity. The thalamus and AC presented with a similar phenomenon: decreasing functional connectivity with increasing diffusion connectivity.

Table 5.1. Tabular qualitative summary of structural, functional, and diffusion MRI analyses with respect to neurological symptoms. All results (i.e. ↓CT) are shown with respect to worsening neurological symptoms (decreasing mJOA score). For measure abbreviations: CT denotes cortical thickness, Vol denotes volume, FC denotes functional connectivity, FA denotes fractional anisotropy, MD denotes mean diffusivity, MO denotes mode of diffusion, GQI denotes generalized q-sampling imaging measures, Trk denotes tracts. For region abbreviations: BA3a denotes Brodmann area 3a, AC denotes anterior cingulate, SFG denotes superior frontal gyrus, SMA denotes supplementary motor area, ACR, SCR, and PCR denote anterior, superior, and posterior corona radiata, respectively, CP denotes cerebral peduncle, and B-stem denotes brainstem.

Region	Structural	Functional	Diffusion
C2 SC	No significant results.	No significant results.	↓**FA** and ↑**MD**.
Primary Motor	Regionally varying ↓**CT**.	↑**FC** to Precuneus, Thalamus, Cerebellum. ↓**FC** to Putamen.	↑**MD**, SCR, PCR. ↓**MO**, CP. ↓**GQI**, SCR. ↓**Trk** to B-stem ↑**Trk** to AC.
Primary Sensory	Regionally varying ↓**CT** in BA3a.	↑**FC** to Precuneus, Thalamus, Cerebellum. ↓**FC** to Putamen.	↑**MD**, SCR, PCR. ↓**MO**, CP. ↓**GQI**, SCR. ↓**Trk** to B-stem ↑**Trk** to AC.
Thalamus	No significant results.	↑**FC** to primary sensorimotor. ↓**FC** to AC, SFG.	↑**Trk** to AC.
Anterior Cingulate	↓**CT**.	↓**FC** to Thalamus, Cerebellum.	↓**FA**, ACR. ↑**Trk** to Primary Sensorimotor, Putamen, Thalamus.
Superior Frontal Gyrus	↓**CT**.	↑**FC** to SMA, ↓**FC** to Thalamus, Cerebellum.	↓**FA**, ACR.
Precuneus	↓**CT**.	↑**FC** to Primary Sensorimotor, SMA. ↓**FC** to Putamen.	↑**MD**, PCR.
Putamen	↓**Vol**.	↓**FC** to Primary Sensorimotor, Precuneus.	↑**MD**. ↑**Trk** to AC.

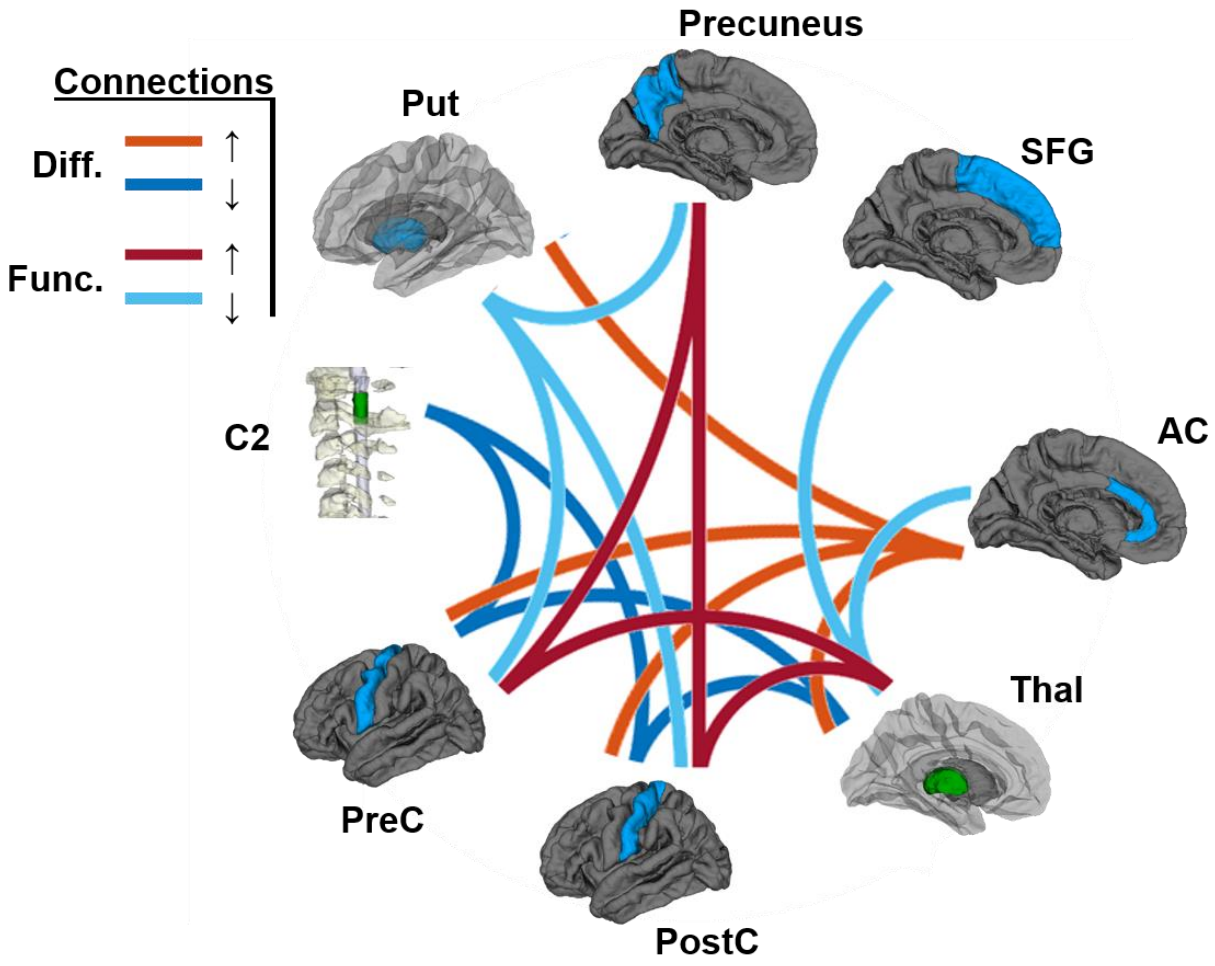

Figure 5.2. Graphic qualitative summary of structural, functional, and diffusion MRI analyses with respect to neurological symptoms. All results are shown with respect to worsening neurological symptoms (decreasing mJOA score). Decreasing structure is shown as blue on the respective brain region, while increasing and decreasing diffusion (Diff.) and functional (Func.) connections are illustrated with colors according to the legend.

Qualitative Summary of MRI Features Associated with Neurological Score

The results for the association with neck pain (as assessed via NDI scores) are presented in **Table 5.2** and **Figure 5.3**. These results show a decrease in cortical thickness and subcortical volumes in regions similar to those seen for neurological symptoms, such as the SFG, the precuneus, the AC, and the putamen. Additionally, decreasing cortical thickness of the insula was associated with neck pain. However, NDI did not show associations with the overall structure or subregions of the primary sensorimotor cortex. Functional connectivity (FC) showed mostly positive associations with worsening neck pain (higher NDI scores), though the FC between the thalamus and the AC presented a negative association with neck pain. The primary sensorimotor cortex displayed increasing FC to the thalamus, precuneus, AC, and SFG, while, similar to neurological symptom severity, the thalamus displayed a decreasing FC with the AC. There were fewer associations between NDI and diffusion connectivity, with only the thalamus and putamen showing a decreasing connectivity, and the primary sensorimotor cortex showing an increasing connectivity with the AC, with respect to NDI. The insula did not appear to display altered functional or diffusion connectivity. Diffusion and functional connectivity only coincided for the AC and primary sensorimotor cortex, which showed an increasing association with NDI for both.

Table 5.2. Qualitative summary of structural, functional, and diffusion MRI analyses with respect to neck pain. All results (i.e. ↓CT) are shown with respect to worsening neck pain (increasing NDI score). For measure abbreviations: CT denotes cortical thickness, Vol denotes volume, FC denotes functional connectivity, FA denotes fractional anisotropy, MD denotes mean diffusivity, MO denotes mode of diffusion, QA denotes quantitative anisotropy, Trk denotes tracks. For region abbreviations: AC denotes anterior cingulate, MFG and SFG denote middle and superior frontal gyri, SMA denotes supplementary motor area, ACR and SCR and PCR denote anterior superior and posterior corona radiata, CP denotes cerebral peduncle, and B-stem denotes brainstem.

Region	Structural	Functional	Diffusion
C2 SC	No significant results.	No significant results.	No significant results.
Primary Motor	No significant results.	↑**FC** to Precuneus, PC, Thalamus, SFG, SMA, AC, MFG.	↓**QA**, PCR. ↑**MO**, PLIC. ↓**MO**, SCR. ↑**Trk** to AC
Primary Sensory	No significant results.	↑**FC** to Precuneus, PC, Thalamus, SFG, SMA, AC, MFG.	↓**QA**, PCR. ↑**MO**, PLIC. ↓**MO**, SCR. ↑**Trk** to AC
Thalamus	No significant results.	↑**FC** to Primary Sensorimotor. ↓**FC** to AC.	No significant results.
Anterior Cingulate	↓**CT**.	↑**FC** to Primary Sensorimotor. ↓**FC** to Thalamus.	↑**Trk** to Primary Sensorimotor.
Insula	↓**CT**.	No significant results.	No significant results.
Superior Frontal Gyrus	↓**CT**.	↑**FC** to Primary Sensorimotor, SMA, PC, Precuneus.	↓**Trk** to Putamen.
Precuneus	↓**CT**.	↑**FC** to Primary Sensorimotor, SFG, MFG.	No significant results.
Putamen	↓**Vol**.	No significant results.	↓**Trk** to SFG.

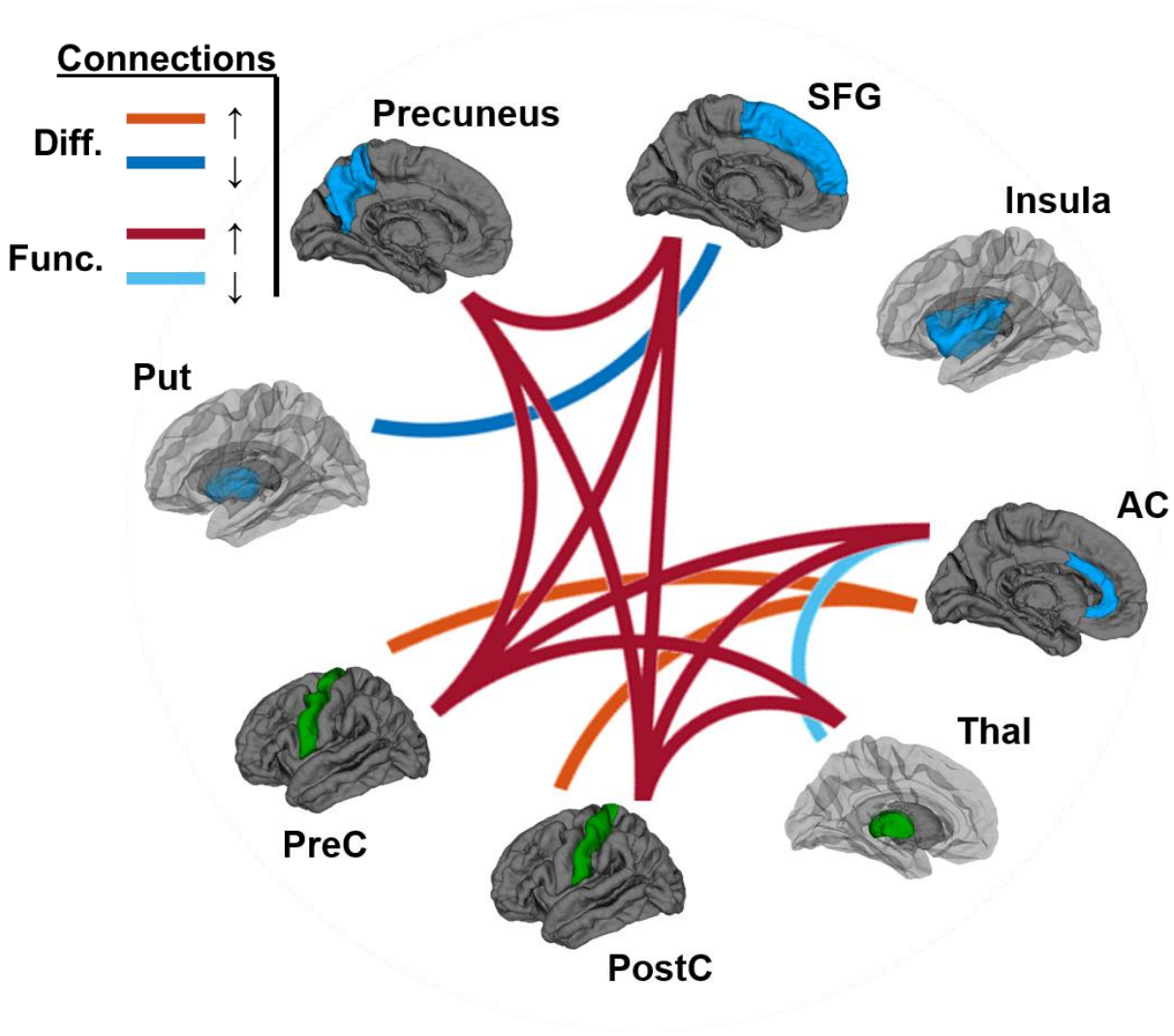

Figure 5.3. Graphic qualitative summary of structural, functional, and diffusion MRI analyses with respect to neck pain severity. All results are shown with respect to worsening neck pain (increasing NDI score). Decreasing structure is shown as blue on the respective brain region, while increasing and decreasing diffusion (Diff.) and functional (Func.) connections are illustrated with colors according to the legend.

iii. Quantitative Comparison of Brain and Spinal Cord Multimodal MRI Results

Evaluation of Trends from Qualitative Assessment

To further investigate the counterintuitive functional and diffusion relationships seen in the features related to neurological symptoms, namely the dichotomy between diffusion/functional increasing and decreasing associations with mJOA, these were evaluated via a correlation matrix. As can be seen in **Figure 5.4.A**, the relationship with mJOA was confirmed: tracks between the AC and the thalamus had a negative correlation with mJOA (-0.41) while the functional connectivity between the AC and the thalamus had a positive correlation (0.47); on the other hand, tracts between the brainstem and the primary sensorimotor cortex (SM) had a positive correlation with mJOA (0.62) while functional connectivity between the thalamus and postcentral gyrus (ostensibly mediated by the corticospinal tract) had a negative association (-0.50). The diffusion and functional measures from the anterior cingulate to thalamus (**Figure 5.4.B**) and the diffusion and functional measures from the corticospinal-related connections (**Figure 5.4.C**) displayed a negative association (-0.38 and -0.25, respectively), though both of these were weaker than the correlation presented with each individual measure and the mJOA score.

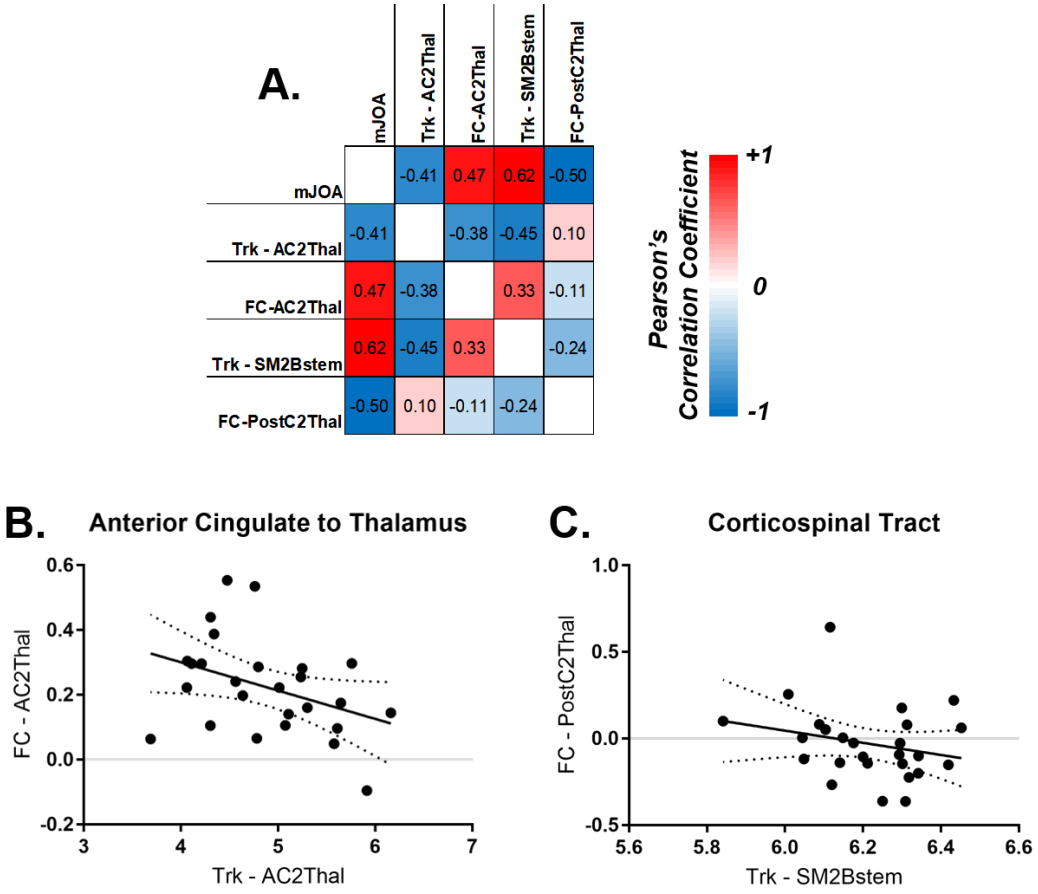

Figure 5.4. Examination of regions with opposite functional and diffusion connectivity trends (anterior cingulate to thalamus and primary sensorimotor to thalamus or brainstem) associated with neurological symptoms in CS cohort. A) Correlation matrix of mJOA and measures between regions. B) Regression between functional and diffusion connectivity of anterior cingulate (AC) to thalamus (Thal). C) Regression between functional connectivity of postcentral gyrus (PostC) to thalamus and primary sensorimotor cortex (SM) to brainstem (Bstem), both mediated by the corticospinal tract. Displayed are regression line (solid) with 95% confidence intervals (dashed).

PCA of MRI Features Associated with Neurological Symptoms: Combined CS and HC Group

A total of 32 features were used in the set of MRI features for neurological symptoms across 43 subjects with mJOA scores. These included: 9 structural MRI features, 13 diffusion MRI features, and 10 functional MRI features (**Figure 5.5.A**). The structural MRI features appeared to all be positively correlated with each other, while positively associated with FA and QA measures, negatively associated with tractography measures, and mostly positively associated with functional connectivity measures, especially the connectivity between primary sensorimotor cortex and the putamen. Diffusion MRI features varied in strength and sign (positive and negative) depending on whether they were measures of fiber coherence, diffusivity, or tractography counts, while showing weaker correlations with functional MRI connectivity. Functional features were mostly weakly positively correlated to each other, with a few similar connections (such as some of those shared by the pre- and post-central gyri) showing stronger correlations (**Figure 5.5.A**). After comparison with the random matrix of 32 features by 43 observations, the first five principal components, which together accounted for 66% of the total variance in the data, were used in subsequent analyses (**Figure 5.5.B**).

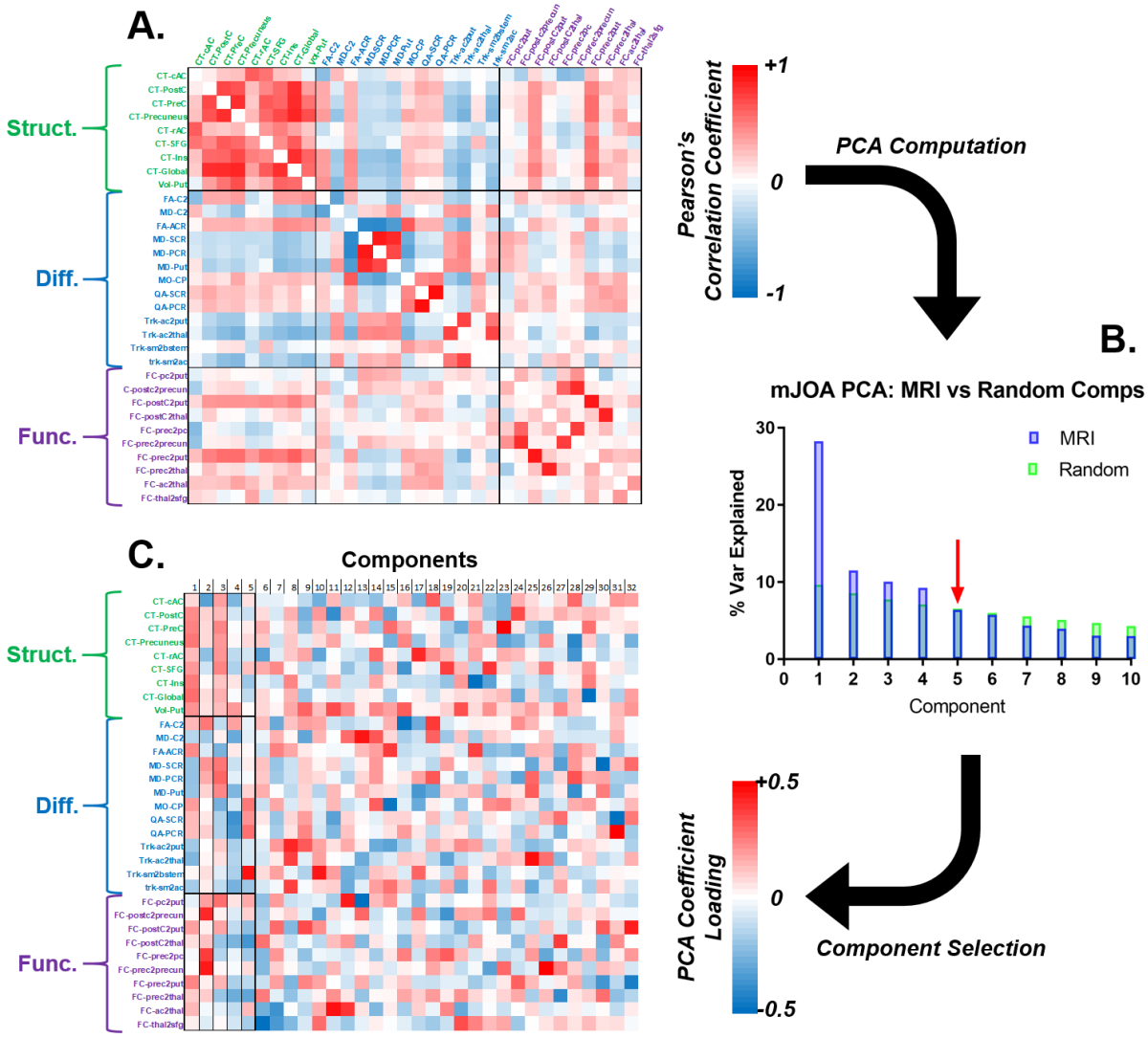

Figure 5.5. Correlation and coefficient plots for principal component analysis of MRI features associated with neurological symptoms in combined CS and HC group. A) correlation matrix of MRI features, color-coded by modality. B) Scree plot of percentage of variance explained by component for mJOA MRI features and randomly created matrices. The last component where variance explained PC-MRI$_k$ > PC-RAND$_k$ was for k=5, so five components were included for further analysis and highlighted in the matrix of coefficients (C).

When evaluating the principal component loadings on the variables (**Figure 5.5.C**), the first component appeared to be positively weighted across the structural features, varying across the diffusion features, and weak across most but not all the functional features. Inspection of the PCA biplot (**Figure 5.6**), revealed similar trends: the first principal component accounted for variance in structural and diffusion features. The second principal component appeared weighted towards a few functional measures, specifically the FC between the precentral gyrus and the precuneus and posterior cingulate (PC), and the FC between the postcentral gyrus and the precuneus (**Figure 5.6.B**). The third principal component also appeared to load evenly across functional and structural features, displayed particularly well when plotted against the first principal component (**Figure 5.6.C**). The fourth principle component appeared weighted more towards diffusion features, while the fifth principle component appeared to be loaded across diffusion and functional features, but presenting with a particularly strong loading on the probabilistic tractography counts between the primary sensorimotor cortex and the brainstem (**Figure 5.5.C**).

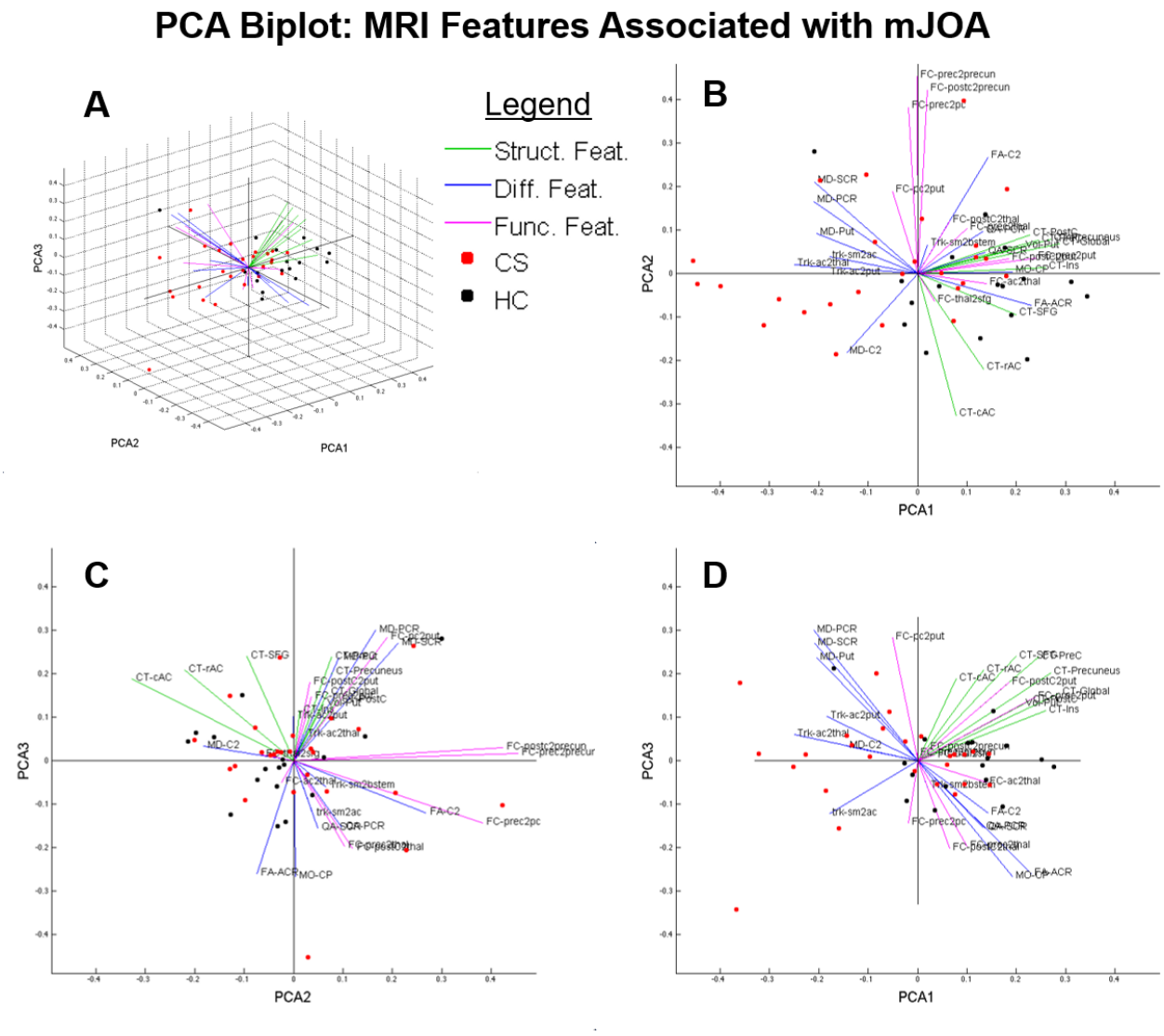

Figure 5.6. Biplot of principal components (axes), subject scores (points), and coefficients of features (lines) for MRI features associated with mJOA in combined CS and HC group. A) 3D biplot with principal components 1,2 and 3. B) 2D biplot with principal components 1 and 2. C) 2D biplot with principal components 2 and 3. D) 2D biplot with principal components 1 and 3.

PCA of MRI Features Associated with Neurological Symptoms: CS Cohort Only

In order to evaluate the dimensionality reduction of MRI features in CS patients alone, and in order to incorporate some of the diffusion metrics (FA and MD) at the site of compression in the spinal cord, an additional PCA analysis was performed using only the 26 CS patients. The spinal cord mean FA and MD were included in this analysis, and the number of components was limited to 26 (same as number of patients) by sequentially eliminating features that had the lowest Pearson's correlation with mJOA. A total of 26 features were used in the set of MRI features for neurological symptoms across 26 subjects with mJOA scores. These included: 5 structural MRI features, 14 diffusion MRI features, and 7 functional MRI features (**Figure 5.7.A**). In comparison to the results for the overall CS and HC analysis of mJOA features described above, there was a higher proportion of diffusion MRI features present in this study (54% for CS only compared to 40% for the overall), though similar trends were seen with respect to the correlation between the different features and modalities. After comparison with the random matrix of 26 features by 26 observations, the first four principal components, which together accounted for 64% of the total variance in the data, were used in subsequent analyses (**Figure 5.7.B**).

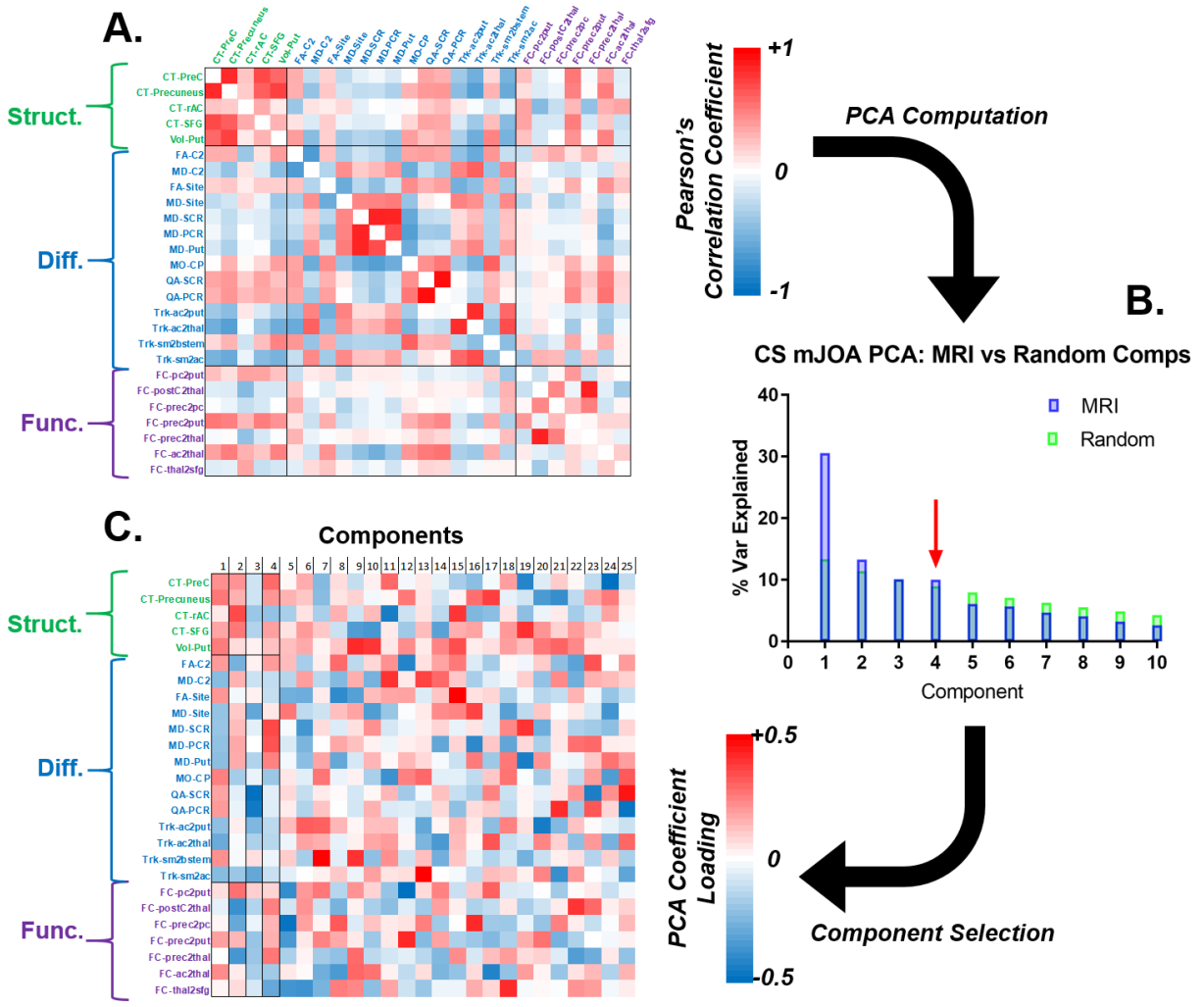

Figure 5.7. Correlation and coefficient plots for principal component analysis of MRI features associated with neurological symptoms exclusively within the CS cohort only. A) correlation matrix of MRI features, color-coded by modality. B) Scree plot of percentage of variance explained by component for mJOA MRI features and randomly created matrices. The last component where variance explained PC-MRI$_k$ > PC-RAND$_k$ was for k=4, so four components were included for further analysis and highlighted in the matrix of coefficients (C).

When evaluating the principal component loadings on the variables (**Figure 5.7.C**) for mJOA within the CS cohort alone, the first component appeared to be positively weighted across the structural features, varying across the diffusion features depending on if they were a measure of diffusivity (negative loaded) or fiber coherence (positively loaded), and weak across most functional features. The second component appeared to also be positively weighted across the structural features, varying across the diffusion features depending on if they were a measure of diffusivity (positively loaded) or fiber coherence (negatively loaded) with opposite loading direction compared to the first compoent, and a few functional features displayed a strong negative loading. The PCA biplot (**Figure 5.8**) showed structural features clustered in the same quadrant across the first and second principal component, while diffusion features, depending on whether they were of fiber coherence or diffusivity, were split across the first two principal components. The third principal component appeared weighted negatively across most features, but especially so for quantitative anisotropy in the upper cerebral white matter regions, the superior and posterior corona radiata (SCR and PCR, respectively, **Figure 5.7.C**), and which is seen well on the biplots with the third principle component (**Figure 5.8.C,D**). The fourth principal component appeared strongly loaded on the mean diffusivity measures in the brain (**Figure 5.7.C**). The functional features were more spread out in this version of the analysis, though the FC of the precentral and postcentral gyri to the thalamus, and the posterior cingulate to the putamen, showed similar loading patterns (**Figure 5.8.**).

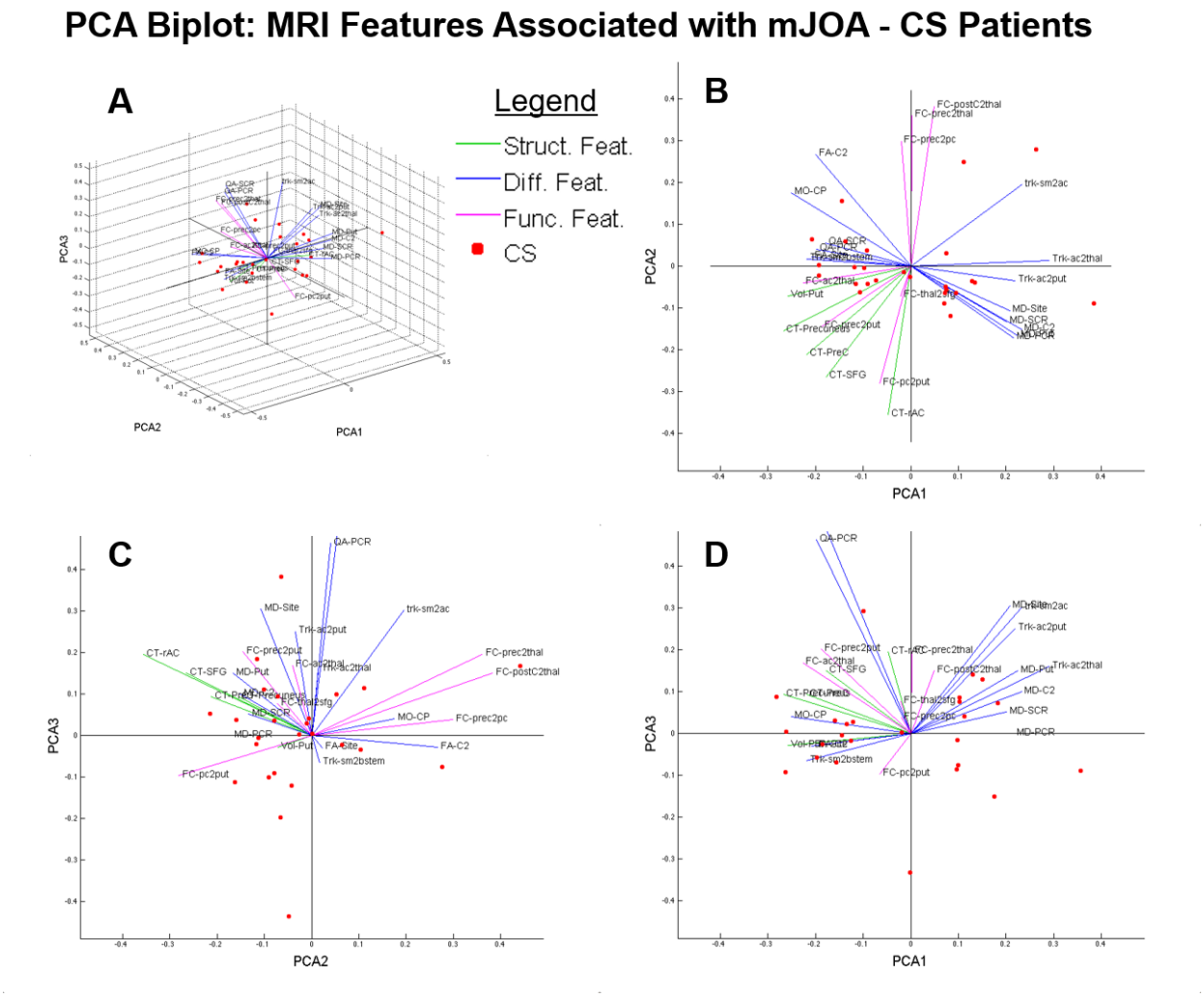

Figure 5.8. Biplot of principal components (axes), subject scores (points), and coefficients of features (lines) for MRI features associated with mJOA within the CS cohort only. A) 3D biplot with principal components 1,2 and 3. B) 2D biplot with principal components 1 and 2. C) 2D biplot with principal components 2 and 3. D) 2D biplot with principal components 1 and 3.

PCA of MRI Features Associated with Neck Pain

A total of 23 features were used in the set of MRI features associated with neck pain across 23 subjects with NDI scores. These included: 6 structural MRI features, 5 diffusion MRI features, and 12 functional MRI features (**Figure 5.9.A**). The within-modality correlations of structural and diffusion features were similar to those presented by the mJOA features, with the structural measures being highly positively correlated, while the diffusion measures were more variable and had positive or negative correlations depending on whether the measures were based on anisotropy or diffusivity. Also, similar to the mJOA features, the structural and diffusion NDI features also displayed weaker and varying relationships to functional connectivity. Functional features presented as highly positively correlated with one another, except for the thalamus to anterior cingulate (final row/column) which appeared negatively associated with the other measures (**Figure 5.9.A**). After comparison with the random matrix of 23 features by 23 observations, only the first two principal components, which together accounted for 55% of the total variance in the data, were used in subsequent analyses (**Figure 5.9.B**).

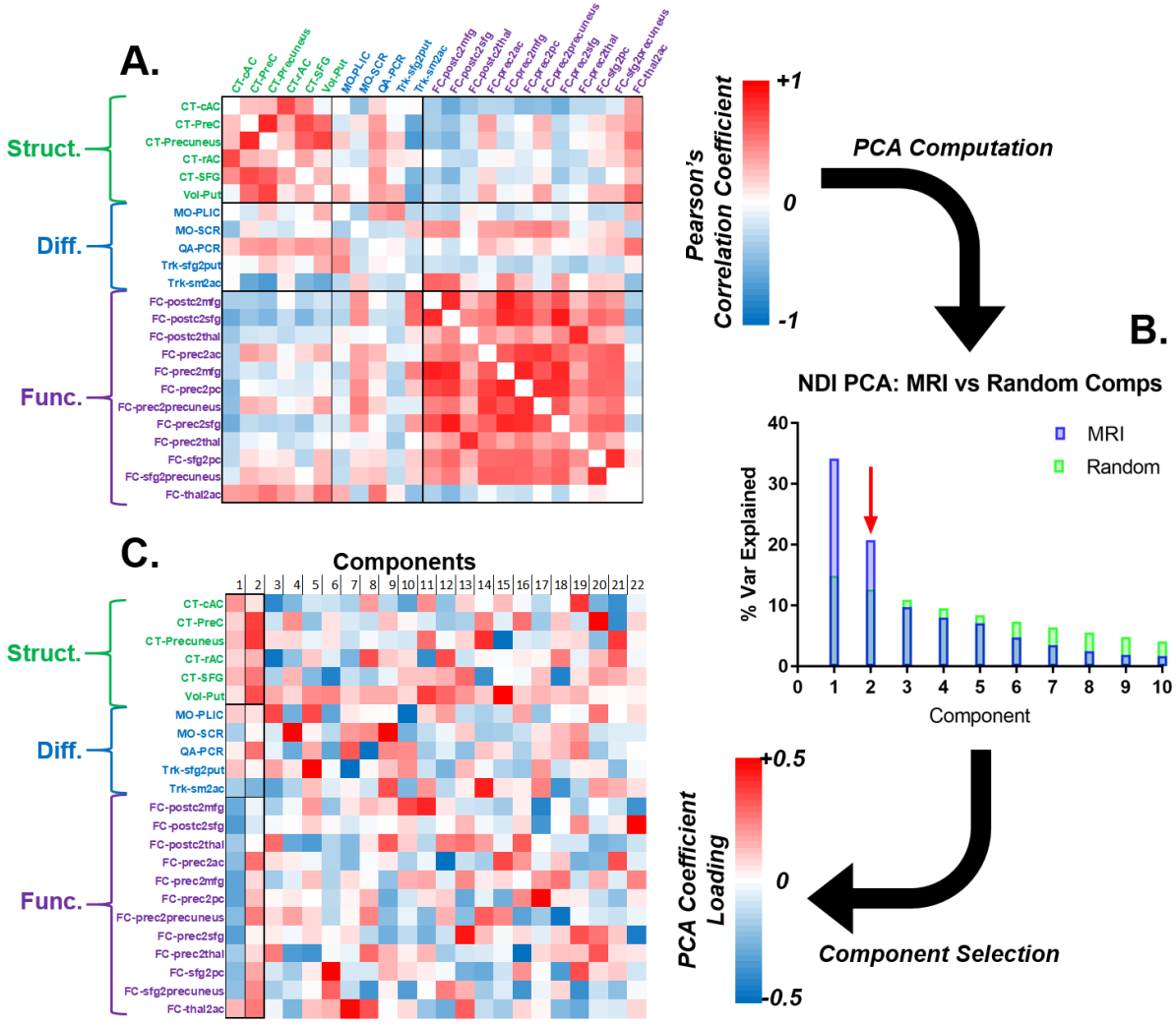

Figure 5.9. Correlation and coefficient plots for principal components of MRI features associated with neck pain. A) correlation matrix of MRI features, color-coded by modality. B) Scree plot of percentage of variance explained by component for NDI MRI features and randomly created matrix. The last component where variance explained $PC\text{-}MRI_k > PC\text{-}RAND_k$ was for k=5, so two components were included for further analysis and highlighted in the matrix of coefficients (C).

When evaluating the principal component loadings on the variables (**Figure 5.10.C**), the first component appeared to be loaded evenly across the variables, presenting a positive loading on the structural features, mixed and weaker loadings on the diffusion features, and a negative loading on the functional features. The second principal component was strongly loaded towards the structural features, and for diffusion features was positively loaded towards the quantitative anisotropy (QA) of the posterior corona radiata (PCR) and negatively loaded on the probabilistic tractography counts from the thalamus to the AC (**Figure 5.10.C**). The second principal component was also mostly moderately positively loaded towards the functional features. The PCA biplot confirmed these associations, with the first principle component splitting across functional and structural features, and the second principal component positively loaded across most features except for notably the probabilistic tractography counts between the primary sensorimotor cortex and the AC (**Figure 5.9.C**).

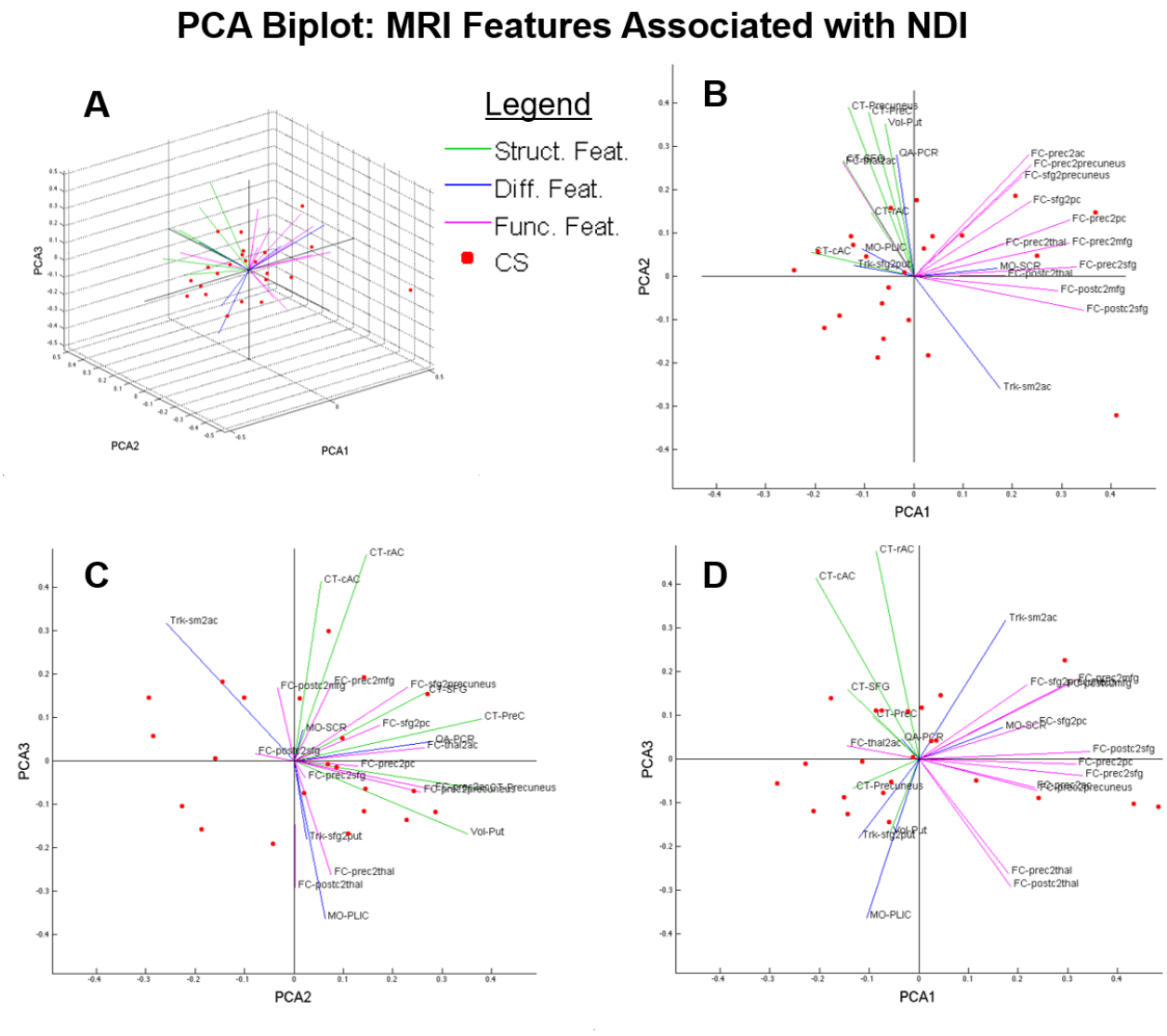

Figure 5.10. Biplot of principal components (axes), subject scores (points), and coefficients of features (lines) for MRI features associated with NDI. A) 3D biplot with principal components 1,2 and 3. B) 2D biplot with principal components 1 and 2. C) 2D biplot with principal components 2 and 3. D) 2D biplot with principal components 1 and 3.

iv. Multiple Linear Regression Analysis of Principal Components

Multiple Linear Regression with Neurological Symptoms: Combined CS and HC Group

When evaluating multiple linear regression of the first principle component as an independent variable with respect to mJOA and age as dependent variables in the combined CS and HC group, this yielded a strong association: the overall model had an R^2=0.58, an adjusted-R^2=0.56, with a significance of P<0.0001; mJOA was a significant independent predictor with a coefficient of +0.42 and P=0.002, while age was also a significant independent predictor with a coefficient of -0.11 and P<0.0001. The VIF for age and mJOA was 1.13, and the model passed tests for heteroskedasticity and normality of residuals. When implementing the principal components as independent variables along with age, and mJOA as a dependent variable in the multiple linear regression model, the non-significant variables were removed in the following order: PC4 (P=0.657), PC3 (P=0.439), Age (P=0.383), and PC2 (P=0.053). This left only PC1 and PC5 as independent predictors in the model, which resulted in n R^2=0.39, and an adjusted-R^2=0.36, with a significance of P<0.0001; PC1 had a coefficient of +0.47 and P<0.0001, while PC5 had a coefficient of +0.54 and P=0.02. The VIF for PC1 and PC5 was 1 (orthogonal measures), thought the model displayed homoscedasticity, likely reflecting the fact that mJOA is a categorical variable and thus less suitable to be a dependent variable in a regression analysis.

Multiple Linear Regression with Neurological Symptoms: CS Cohort Only

When evaluating multiple linear regression of the first principle component as an independent variable with respect to mJOA and age as dependent variables within the CS cohort only, this yielded a very strong association: the overall model had an R^2=0.63, an adjusted-R^2=0.60, with a significance of P<0.0001; mJOA was a significant independent predictor with a

coefficient of +0.56 and P=0.0002, while age was also a significant independent predictor with a coefficient of -0.14 and P=0.0005. The VIF for age and mJOA was 1.00, and the model passed tests for heteroskedasticity and normality of residuals. When implementing the principal components as independent variables along with age, and mJOA as a dependent variable in the multiple linear regression model, the non-significant variables were removed in the following order: PC3 (P=0.587), Age (P=0.324), PC4 (P=0.0.082), and PC2 (P=0.058). This left only PC1 as an independent predictor in the model, which resulted in an R^2=0.37, P=0.001, and PC1 had a coefficient of +0.618. This linear regression is shown in **Figure 5.11**.

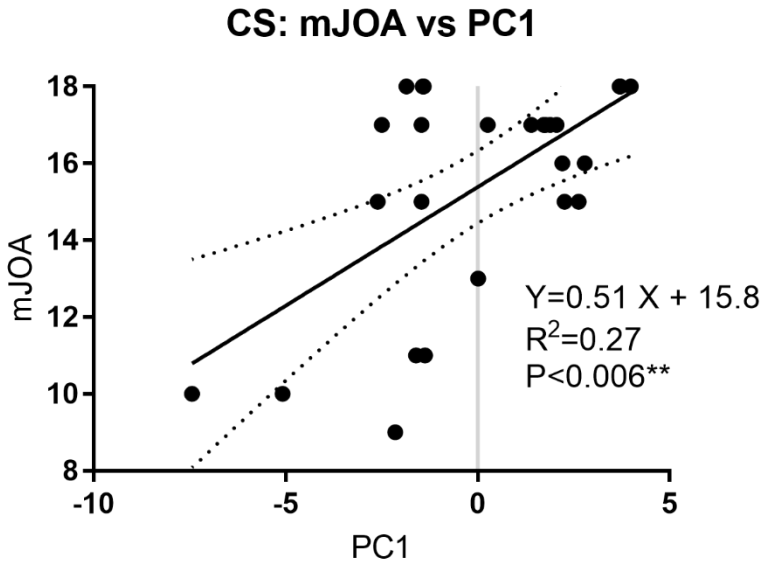

Figure 5.11. Plot of mJOA with respect to the first principal component for patients with CS. Plotted are the linear regression lines along with the 95% confidence intervals (dashed line).

Multiple Linear Regression with Neck Pain

When evaluating multiple linear regression of the first principle component as a dependent variable with respect to NDI and age, this yielded a strong association: the overall model had an R^2=0.50, an adjusted- R^2=0.45, with a significance of P=0.0009; NDI was a significant variable with a coefficient of -0.016 and P=0.0003, while age was also a significant variable with a coefficient of -0.19 and P<0.0001. The VIF for age and mJOA was 1.12, and the model passed tests for heteroskedasticity and normality of residuals. When constructing the multiple linear regression model with NDI as the dependent variable, both PCs and age were significant independent variables, so all were included in the final model, which yielded an R^2=0.74, an adjusted- R^2=0.70, with a significance of P<0.0001; PC1 had a coefficient of -2.38 and P<0.0001, PC2 had a coefficient of -2.63 and P=0.001, and age had a coefficient of -0.50 and P=0.002. The VIFs were 1.05 for PC1, 1.43 for PC2, and 1.48 for age, thought the model displayed homoscedasticity, likely reflecting the fact that NDI is a categorical variable and thus less suitable to be a dependent variable in a regression analysis.

v. Discussion

This chapter summarized the multimodal MRI results from the associations with patient neurological symptoms (mJOA) and neck pain (NDI) measures, from the previous three chapters, and quantitatively evaluated their relationship using principal component analysis (PCA). PCA results were then used for multiple linear regression analysis of the data with respect to the symptom and pain measures. Results indicated that brain structures undergo degenerative changes with worsening neurological symptoms, including region-specific thinning of the primary sensorimotor cortex, and decreased structure in brain regions that supplement motor tasks.

Functional changes included an increased connectivity between the primary sensorimotor cortex and the precuneus and thalamus, and a decreased connectivity between the primary sensorimotor cortex and the putamen. These are accompanied by changes in functional connectivity between the medial prefrontal cortex, the anterior cingulate (AC) and the superior frontal gyrus (SFG), and the subcortical structures of the thalamus and the putamen. Diffusion tractography showed a decreasing connectivity across the corticospinal tract, and an increased connectivity between the AC and the subcortical structures, thalamus and putamen, and with the primary sensorimotor cortex. The decreased diffusion-based connectivity across the corticospinal tract contrasts with the increased functional connectivity between the thalamus and the primary sensorimotor cortex.

For neck pain, the brain presented with decreased thickness in the AC and insula, regions typically associated with pain, as well as in the SFG, precuneus, and decreased putamen volume. These were accompanied by functional changes where the primary sensorimotor cortex displayed greater functional connectivity with the precuneus, thalamus, AC, and SFG with worsening neck pain. The thalamus also displayed a decreasing connectivity with the AC. Only a few diffusion connectivity changes were seen, between the primary sensorimotor cortex and the AC, and between the putamen and SFG. Correlation analyses and PCA results indicated that structural, diffusion, and functional measures appeared mostly strongly correlated within the respective types of measures, but more weakly associated with the findings from other modalities. Loadings of the MRI features on the first principle components appeared to distribute across the different modalities, which may indicate that the different modalities reveal different symptom-related aspects of the disease.

In general, studies have found functional connectivity to be associated with diffusion-derived connectivity. In the advent of the discovery of the default-mode network in resting-state

fMRI, Greicius *et al* later found that functional connectivity at rest of this network largely reflected in structural connections as assessed using DTI [317]. While strong functional connectivity can exist between regions that are not functionally connected, the white matter is nevertheless an anatomical substrate that constrains and influences the presence of functional connectivity [318]. The finding in this study of disparate functional and diffusion connectivity along the corticospinal tract in relation to worsening neurological symptoms appears counterintuitive. However, previous studies in conditions such as amyotrophic lateral sclerosis (ALS), though showing mixed results in terms of functional connectivity [319], several have found decreased white matter connectivity but increased functional connectivity at rest in sensorimotor networks [320,321]. The interpretation for these results in ALS was that there may be a compensatory effect for accomplishing motor function in the presence of white matter degeneration, or that it may be due to a loss of inhibitory circuitry. Thus, the combined data presented in this dissertation may indicate white matter degeneration, which occurs in the spinal cord at the site of injury and rostral to this site, along with increased functional connectivity due to decreased inhibition and seen in functional activation tasks where larger areas are recruited to accomplish the same functional tasks [203,204].

PCA for dimensionality reduction and subsequent classification have been used previously with neuroimaging datasets focused on Alzheimer's disease for both MRI [322] and positron emission tomography (PET) and single photon emission computed tomography (SPECT) [323]. Both of these previous studies (and most studies applying machine learning techniques) generally have larger sample sizes, in the hundreds of subjects, in order to train and test their classification algorithms. Because of the small sample size of this study, PCA was used for dimensionality reduction and to evaluate the general relationships between variables using a simple model (linear regression). PCA techniques have recently been implemented using MRI measures in both cervical [324] and thoracic

[325] acute spinal cord injury, in which grading and structural measurements of the spinal cord were analyzed using PCA and where principal components were found to be useful in predicting neurological scores at discharge. These studies had more similar sample sizes (25 subjects for the thoracic and 95 for the cervical spinal cord injury studies) to that presented in this work, and as such represent a more feasible model for using PCA: extracting principle components and using them for regression analyses with symptom scores, as was done for this work.

The multiple linear regression models for the first principle component *vs* mJOA and age produced strong statistical models, with an R^2=0.58 for the entire group including HC and an R^2=0.58 in the CS-only group. These are larger than the strongest models of structural measures as independent variables from **Chapter II**, namely which presented with $R^2 \sim 0.47$ in the entire cohort, and $R^2 \sim 0.42$ in the CS-only cohort. The results from this chapter also compare favorably to previous results of FA ($R^2 = 0.41$) and MD ($R^2 = 0.26$) in terms of regression with respect to mJOA [201]. This means that the principal component, accounting for the most variance across different multimodal MRI measures, was better represented by neurological symptom severity and age than individual structural MRI measures. For the combined model of mJOA *vs* the principal components and age, the resultant selected principal components were the first and fifth. While the first principal component, which accounts for the most variance in the data, provides an easier interpretation, the significance of the fifth component is harder to interpret, but appears to be strongly linked to the tractography counts from to brainstem to the sensorimotor cortex, to the diffusion measures in the superior and posterior corona radiata, and several functional measures including the connection between the pre- and post-central gyri and the thalamus.

For NDI, the multiple linear regression model of the first principle component vs NDI and age produced a strong R^2=0.50; however, this was similar to the strongest associations seen in the

structural MRI measures in Chapter II, namely several (bilateral Precunues, RH Putamen, LH insula) with $R^2 \sim 0.55$. The multiple linear regression model with NDI as the dependent variable and age and the first two principal components as dependent variables produced an extraordinarily strong association, with an $R^2=0.74$. This means that a model using only these first two principle components and age accounted for almost 75% of the variance in the neck pain scores. Given the small cohort size of CS patients (and smaller still for the patients that also had NDI scores) further data is necessary to validate this finding; however, such a strong model represents significant progress in predicting patient symptoms from imaging biomarkers.

Chapter VI. Conclusion

In the paper "Will imaging biomarkers transform spinal cord injury trials?", Cadotte and Fehlings [326] note that the current system of classification for traumatic spinal cord injury (SCI), the American Spinal Injury Association (ASIA)'s impairment scale (AIS), while easy to administer, does not take advantage of the advancements in understanding about the spinal cord and also fails to account for the heterogeneity of injury and potential development of secondary injuries after the initial trauma, where a significant proportion of patients (30%) will degrade from the lowest symptom severity category (grade A) to worse symptom severity categories (B or C). Cadotte and Fehlings then highlight work performed by Freund *et al* [327] where they tracked symptoms and performed longitudinal brain and spinal cord MRI in patients with SCI, and found that neuroanatomical substrates as assessed by varied MRI methods were altered with injury and tracked with symptom progression. Cadotte and Fehlings conclude: "Through a combination of treatment strategies and adoption of imaging biomarkers, the next generation of clinical trials will have the potential to personalize the care of patients with spinal cord injury."

While the investigation of imaging biomarkers has improved by leaps and bounds in traumatic SCI, less work has been done on patients with chronic compression of the spinal cord, or cervical spondylotic myelopathy (CSM). Arguably, the ability to assess the neuroanatomical substrate is more important in chronic compression cases because the natural history and response to surgery are so variable, and because chronic compression can occur over a long time-span. The work presented in this dissertation presents a step in the direction of further understanding the neurobiological changes in the brain and spinal cord of patients with chronic spinal cord compression through imaging biomarkers and how these neurobiological substrates relate to

patient symptom severity and pain, which are not well represented by traditional MRI or other non-invasive techniques.

The objective of this dissertation was to evaluate the relationship between patient symptom severity and the structure, microstructure, and function of the brain and spinal cord. This work used an MRI protocol that encompassed the brain and extended into all or part of the cervical spinal cord, and scans were acquired in 26 subjects with cervical stenosis (CS), with or without accompanying myelopathy, and in a set of 17 healthy control subjects. Analyses of both the brain and spinal cord data were processed using modality-specific pipelines, and associations were evaluated between the resulting MRI measures and the clinical symptoms and clinical measures of the spinal cord. The modified Japanese Orthopedic Association (mJOA) score was used as measure of neurological function. The neck disability index (NDI) was used as a measure of chronic neck pain. Measures from clinical anatomical MRIs included the Torg Ratio, a measure of the compression of the spinal cord.

Patients with CS demonstrated changes associated with neurological symptom severity, including decreasing cortical thickness in subregions of the primary sensorimotor cortex, as well as motor supplemental brain regions such as the anterior cingulate, superior frontal gyrus, precuneus, and decreasing volume of the putamen. These macrostructural changes in the brain that were associated with symptom severity provide a stark contrast to the macrostructural assessment of the spinal cord in patients with CS, where the degree of spinal cord compression or the cross-sectional area of the spinal cord does not relate strongly to symptom measures. Additionally, this study found that patients with CS and neck pain exhibited a pattern of brain changes that has been well-documented for chronic pain: decreasing cortical thickness in the anterior cingulate and insula, both important regions in the perception and affective assessment of pain. Patients with CS

also displayed decreased cortical thickness in the precuneus and decreasing volume of the putamen with worsening pain. As a group, patients with CS demonstrated a greater decrease in structure with age for particular brain regions when compared to HC subjects, which may indicate that these patients develop chronic brain structural changes that worsen at a greater rate with age compared to the healthy population.

Patients with CS also demonstrated altered connectivity between brain regions at rest that were related to symptom severity. These changes revolved around altered connectivity between the primary sensorimotor cortex and other cortical and subcortical brain regions, where there was an increasing functional connectivity with neurological symptom severity to the precuneus, posterior cingulate, thalamus, and cerebellum, which parallels the previously reported increase in functional activation area of the primary motor cortex exhibited by patients with CS. The putamen instead demonstrated decreasing functional connectivity with the primary sensorimotor cortex. The thalamus and putamen both displayed decreasing functional connectivity to the anterior cingulate and superior frontal gyrus with worsening neurological symptom severity. In relation to neck pain, patients with CS demonstrated generally increasing functional connectivity with worsening neck pain between the precentral and postcentral gyri, superior and middle frontal gyri, and the precuneus. The thalamus also displayed increasing functional connectivity to the primary sensorimotor cortex, but displayed decreasing connectivity to the anterior cingulate. Thus, mostly increasing functional connectivity between sensorimotor brain regions was observed, though the thalamus and putamen demonstrated different patterns of connectivity. These changes may indicate compensatory mechanisms in the brain to accomplish motor tasks in the presence of compromised spinal cord integrity.

Several models of diffusion were used to assess tissue microstructure in white matter and subcortical gray matter in patients with CS. Patients with worsening neurological symptom severity demonstrated decreased fractional anisotropy (FA) and increased mean diffusivity (MD) at the C2 level of the spinal cord, similar to the results previously reported at the site of compression level in previous studies and indicating possible retrograde or anterograde degeneration in the spinal cord rostral to the site of injury. These trends of decreasing white matter integrity were also found in the brain along the corticospinal tract, providing further evidence for rostral changes in white matter. As for subcortical structure results, the putamen presented with increased diffusivity with neurological symptom severity, providing additional evidence to the structural findings that the putamen is altered in association with motor symptoms. Probabilistic tractography results found increasing number of fiber tracts between the anterior cingulate and multiple regions, including the primary sensorimotor cortex, the thalamus, and the putamen, with worsening symptoms, while there was a decreasing number of tracts along the corticospinal tract with worsening symptoms. Fewer associations were found between diffusion measures and neck pain, but the anterior cingulate displayed increased tracts to the primary sensorimotor cortex, and the putamen displayed decreased tracts to the superior frontal gyrus.

The MRI-derived measures proved to be correlated to one another to varying degrees, and even when reduced to a few components via principal component analysis, these components still maintained strong associations with the neurological symptom and pain scores, pointing towards a similar pattern of brain changes across patients with chronic compression of the spinal cord. The multimodal assessment also indicated that various structures showed changes in combinations of structural, functional, and microstructural MRI features, which reinforce the findings of individual MRI modalities.

This dissertation has added to the evaluation of rostral brain and spinal cord changes in patients with chronic compression of the spinal cord, critical work which is needed for spinal cord compression neuroimaging research to catch up to the further-along neuroimaging research which has been conducted for traumatic spinal cord injury. This work also highlights the brain changes occurring in patients with CS and chronic neck pain, an often under-rated patient symptom in the presence of the more blatant neurological symptoms. The current results for brain changes with neck pain are similar to previous research in more well-known and research-intensive chronic pain conditions, and indicate that this is an important disease dimension for physicians to consider and for future research to investigate.

In the paper "Embodied neurology: an integrative framework for neurological disorders", Freund *et al* discuss the need to address the supraspinal, spinal, and peripheral aspects of neurological disorders simultaneously, especially in SCI. Freund *et al* correctly point to the integrative nature of the nervous system and the body, that this proper integration is disrupted by disease, and that treatment should holistically attempt to remedy these deficits. The findings in this dissertation provide targets for future potential brain- or behavior-based therapies, where addressing the whole of the nervous system, from the direct site of injury to the intact spinal cord and the brain, may provide a more holistic treatment that helps patients recover and adapt more fully.

Appendix A. Patient and Healthy Volunteer Demographics and Conventional MRI Findings

Patient and Healthy Volunteer Populations

A total of 26 patients with cervical stenosis with or without myelopathy were prospectively enrolled in a cross sectional study involving observational MRI and evaluation of neurological function. Patients were recruited from an outpatient neurosurgery clinic, and each had at least moderate cervical stenosis on standard cervical MRI, defined as no visible cerebrospinal fluid signal around the spinal cord at the site of maximal compression. All patients signed Institutional Review Board (IRB) approved consent forms, and all analyses were done in compliance with the Health Insurance Portability and Accountability Act (HIPAA). The cohort included 20 males and 6 females, with a mean age of 59 years (range 40 to 80). The modified Japanese Orthopedic Association (mJOA) score was used as a measure of neurological function.[5] The mean mJOA score for the patient cohort was 15 (range 9 to 18). Of the 26 patients, 6 had neck pain only without neurological symptomatology (mJOA=18), 14 presented with mild myelopathy (mJOA between 15 and 17), and 6 presented with moderate to severe myelopathy (mJOA $\leq$ 14). The neck disability index (NDI) was used as a measure of neck pain [20,21]. Of the 26 patients enrolled in this study, 23 had NDI scores: 8 had no disability (NDI between 0 and 4), 10 had mild disability (NDI between 5 and 14), 1 had moderate disability (NDI between 15 and 24), 1 had severe disability (NDI between 25 and 34), and 2 had complete disability (NDI between 35 and 50). There was a significant negative Pearson's correlation ($r=-0.456$, $P=0.03$) between mJOA and NDI scores, which may mean that some of the results may reflect an overlap in the symptoms.

A cohort of 17 neurologically intact, healthy volunteer subjects (11 males and 6 females with average age of 40 years, range 25-62) underwent the same brain and spinal cord research MRI protocol for comparison.

For the structural brain analysis, MRI data from an additional 28 HC subjects (21 males and 7 females) older than age 40 (average age of 49 years, range 40-61) and similar structural MRI scans were extracted from the Pain and Interoception Imaging Network (PAIN) Repository, (http://uclacns.org/programpain-research-program/pain-repository/) maintained by the UCLA Center for the Neurobiology of Stress and Resilience [214]. These subjects had comparable T1 MRI acquisition, but the scan only covered the brain and the top portion of the spinal cord. Thus, this additional cohort of HC subjects was only used for structural brain analyses.

Patients with CS presented with significantly increased age with respect to both the joint HC group and the HC subjects with the research brain and spine MRIs (t-tests, $P<0.001$ for both), but did not present with significantly different body mass index (BMI, t-tests, $P=0.4$ for overall, and $P=0.2$ for brain and spine HC) or sex (Chi-squared tests, $P>0.2$ for both overall and brain and spine HC). Patient and volunteer demographics are summarized in **Table A.1**.

Table A.1. CS patients and HC subjects cohort demographics.

Subject Population	N	Age (mean years +/- SD)	Sex	BMI (mean +/- SD)	mJOA (mean +/- SD)	NDI (mean +/- SD)
CS Patients (Brain + Spine)	26	59 ± 11 years	20M / 6F	27.2 ± 6.7	15.4 ± 2.8	10.6 ± 10
HC Subjects (Brain + Spine)	17	41 ± 13 years	11M / 6F	26.2 ± 3.0	18	
HC Subjects (Brain Only)	28	49 ± 5 years	21M / 7F	26.8 ± 5.5	18	

Conventional Clinical Spine MRI Findings

T2w turbo spin echo (TSE) sagittal and axial MRI scans were acquired in the patient population as part of clinical routine scanning on a 3T scanner, which was the same one used to acquire the research sequences (*Siemens Prisma; Siemens Healthcare, Erlangen, Germany*). The T2w sagittal TSE scan used an echo time (TE) of 105ms, a repetition time (TR) or 4000ms, and a flip angle of 140°; the field of view (FOV) was 220mm x 220mm, with an acquisition matrix of 348 x 348, and a slice thickness of 3mm, to give a voxel size of 0.573mm x 0.573mm x 3mm. The T2w axial TSE used a TE of 84ms, a TR of 9430ms, and a flip angle of 160°; an FOV of 220mm x 220mm with an acquisition matrix of 384 x 384 was obtained, to yield an in-plane resolution of 0.469mm x 0.469mm; a slice thickness of 4mm was acquired with an interslice gap of 1 mm. Both scans covered the entirety of the cervical spinal cord in all patients. Both scans were used to identify sites of compression as well as T2w signal abnormalities in the spinal cord. The T2w TSE sagittal scan was used to compute the MRI-equivalent Torg Ratio.

In the cohort of 26 patients, the distribution of sites of maximal compression was the following: 1 patient had maximal compression at the C2/C3 intervertebral disc, 11 patients had maximal compression at the C3/C4 intervertebral disc, 5 at the C4/C5 disc, 5 at the C5/C6 disc, and 4 at the C6/C7 disc. Compression at multiple intervertebral disc levels was noted for 17 (65%) of the patients. The mean anterior-posterior spinal canal diameter at the site of the largest extent of compression was 6.1mm (±1.6mm standard deviation, range of 3.7mm to 10.3mm), and the mean MRI equivalent of the Torg-Pavlov Ratio was 0.36 (±0.10 standard deviation, range of 0.20 to 0.58) in the cohort of CS patients, which compares well to another study that found a mean Torg Ratio of 0.36 in a cohort of fifty-five patients [284]. Out of the 26 CS patients, 14 (54%) presented with T2 hyperintensity within the cord, 8 of which (30% of total patients, 57% of patients with T2

hyperintensity) presented with "Snake-Eye" Appearance (SEA) [37-39]. Neither spinal canal diameter nor MRI-equivalent Torg-Pavlov Ratio were correlated with neurological function (linear regression with mJOA, R^2=0.092, P=0.1, and R^2=0.050, P=0.3, respectively) or neck pain (linear regression with NDI, R^2<0.0001, P>0.9, and R^2=0.0008, P=0.7, respectively). Subjects with T2 hyperintensity in the spinal cord did not have a significantly different mJOA compared to those without (t-test, P=0.7), but they did present with significantly lower NDI (t-test, P=0.01).

References

1. Kalsi-Ryan S, Karadimas SK, Fehlings MG. Cervical Spondylotic Myelopathy: The Clinical Phenomenon and the Current Pathobiology of an Increasingly Prevalent and Devastating Disorder. The Neuroscientist 2012;19:409-21.

2. Emery SE. Cervical spondylotic myelopathy: diagnosis and treatment. The Journal of the American Academy of Orthopaedic Surgeons 2001;9:376-88.

3. Chang V, Lu DC, Hoffman H, Buchanan C, Holly LT. Clinical results of cervical laminectomy and fusion for the treatment of cervical spondylotic myelopathy in 58 consecutive patients. Surg Neurol Int 2014;5:S133-7.

4. Tracy Ja, Bartleson JD. Cervical spondylotic myelopathy. The neurologist 2010;16:176-87.

5. Yonenobu K, Abumi K, Nagata K, Taketomi E, Ueyama K. Interobserver and intraobserver reliability of the japanese orthopaedic association scoring system for evaluation of cervical compression myelopathy. Spine (Phila Pa 1976) 2001;26:1890-4; discussion 5.

6. Benzel EC, Lancon J, Kesterson L, Hadden T. Cervical laminectomy and dentate ligament section for cervical spondylotic myelopathy. J Spinal Disord 1991;4:286-95.

7. Azimi P, Shahzadi S, Benzel EC, Montazari A. Functional Evaluation Using the Modified Japanese Orthopedic Association Score (mJOA) for Cervical Spondylotic Myelopathy by Age, Gender, and Type of Disease. 2013:1-5.

8. Fukui M, Chiba K, Kawakami M, et al. Japanese Orthopaedic Association Cervical Myelopathy Evaluation Questionnaire (JOACMEQ): part 4. Establishment of equations for severity scores. Subcommittee on low back pain and cervical myelopathy, evaluation of the clinical outcome committee of the Japanese Orthopaedic Association. J Orthop Sci 2008;13:25-31.

9. Fukui M, Chiba K, Kawakami M, et al. Japanese Orthopaedic Association Cervical Myelopathy Evaluation Questionnaire: part 3. Determination of reliability. J Orthop Sci 2007;12:321-6.

10. Fukui M, Chiba K, Kawakami M, et al. Japanese Orthopaedic Association Cervical Myelopathy Evaluation Questionnaire (JOACMEQ): Part 2. Endorsement of the alternative item. J Orthop Sci 2007;12:241-8.

11. Fukui M, Chiba K, Kawakami M, et al. An outcome measure for patients with cervical myelopathy: Japanese Orthopaedic Association Cervical Myelopathy Evaluation Questionnaire (JOACMEQ): Part 1. J Orthop Sci 2007;12:227-40.

12. Tetreault L, Kopjar B, Nouri A, et al. The modified Japanese Orthopaedic Association scale: establishing criteria for mild, moderate and severe impairment in patients with degenerative cervical myelopathy. Eur Spine J 2017;26:78-84.

13. Nurick S. The pathogenesis of the spinal cord disorder associated with cervical spondylosis. Brain 1972;95:87-100.

14. Kalsi-Ryan S, Singh A, Massicotte E, et al. Ancillary Outcome Measures for Assessment of Individuals With Cervical Spondylotic Myelopathy. Spine 2013;38:111-22.

15. Binder AI. Cervical spondylosis and neck pain. Brit Med J 2007;334:527-31.

16. Rao R. Neck pain, cervical radiculopathy, and cervical myelopathy - Pathophysiology, natural history, and clinical evaluation. J Bone Joint Surg Am 2002;84a:1872-81.

17. Nahin RL. Estimates of Pain Prevalence and Severity in Adults: United States, 2012. J Pain 2015;16:769-80.

18. Gaskin DJ, Richard P. The Economic Costs of Pain in the United States. J Pain 2012;13:715-24.

19. Control CfD, Prevention. Severe headache or migraine, low back pain, and neck pain among adults aged 18 and over, by selected characteristics: United States, selected years 1997–2011. Health, United States [http://www cdc gov/nchs/data/hus/2012/047 pdf (Last accessed January 20, 2014) 2013.

20. Vernon H. The Neck Disability Index: state-of-the-art, 1991-2008. J Manipulative Physiol Ther 2008;31:491-502.

21. Vernon H, Mior S. The Neck Disability Index: a study of reliability and validity. J Manipulative Physiol Ther 1991;14:409-15.

22. Al-Tamimi YZ, Guilfoyle M, Seeley H, Laing RJ. Measurement of long-term outcome in patients with cervical spondylotic myelopathy treated surgically. Eur Spine J 2013;22:2552-7.

23. Latimer M, Haden N, Seeley HM, Laing RJ. Measurement of outcome in patients with cervical spondylotic myelopathy treated surgically. Brit J Neurosurg 2002;16:545-9.

24. Matz PG, Anderson PA, Holly LT, et al. The natural history of cervical spondylotic myelopathy. J Neurosurg Spine 2009;11:104-11.

25. Karadimas SK, Erwin WM, Ely CG, Dettori JR, Fehlings MG. Pathophysiology and natural history of cervical spondylotic myelopathy. Spine (Phila Pa 1976) 2013;38:S21-36.

26. Lebl DR, Hughes A, Cammisa FP, Jr., O'Leary PF. Cervical spondylotic myelopathy: pathophysiology, clinical presentation, and treatment. HSS J 2011;7:170-8.

27. Mummaneni PV, Kaiser MG, Matz PG, et al. Cervical surgical techniques for the treatment of cervical spondylotic myelopathy. J Neurosurg Spine 2009;11:130-41.

28. Madhavan K, Chieng LO, Foong H, Wang MY. Surgical outcomes of elderly patients with cervical spondylotic myelopathy: a meta-analysis of studies reporting on 2868 patients. Neurosurg Focus 2016;40:E13.

29. Holly LT, Moftakhar P, Khoo LT, Shamie AN, Wang JC. Surgical outcomes of elderly patients with cervical spondylotic myelopathy. Surg Neurol 2008;69:233-40.

30. Li FN, Li ZH, Huang X, et al. The treatment of mild cervical spondylotic myelopathy with increased signal intensity on T2-weighted magnetic resonance imaging. Spinal Cord 2014;52:348-53.

31. Kadanka Z, Bednarik J, Vohanka S, et al. Conservative treatment versus surgery in spondylotic cervical myelopathy: a prospective randomised study. Eur Spine J 2000;9:538-44.

32. Hachem LD, Ahuja CS, Fehlings MG. Assessment and management of acute spinal cord injury: From point of injury to rehabilitation. J Spinal Cord Med 2017;40:665-75.

33. Yarbrough CK, Murphy RK, Ray WZ, Stewart TJ. The natural history and clinical presentation of cervical spondylotic myelopathy. Adv Orthop 2012;2012:480643.

34. Pavlov H, Torg JS, Robie B, Jahre C. Cervical spinal stenosis: determination with vertebral body ratio method. Radiology 1987;164:771-5.

35. Torg JS, Pavlov H. Cervical spinal stenosis with cord neurapraxia and transient quadriplegia. Clin Sports Med 1987;6:115-33.

36. Nouri A, Martin AR, Mikulis D, Fehlings MG. Magnetic resonance imaging assessment of degenerative cervical myelopathy: a review of structural changes and measurement techniques. Neurosurg Focus 2016;40:E5.

37. Faiss JH, Schroth G, Grodd W, Koenig E, Will B, Thron A. Central Spinal-Cord Lesions in Stenosis of the Cervical Canal. Neuroradiology 1990;32:117-23.

38. Takahashi M, Yamashita Y, Sakamoto Y, Kojima R. Chronic Cervical Cord Compression - Clinical-Significance of Increased Signal Intensity on Mr Images. Radiology 1989;173:219-24.

39. Mizuno J, Nakagawa H, Inoue T, Hashizume Y. Clinicopathological study of "snake-eye appearance" in compressive myelopathy of the cervical spinal cord. Journal of Neurosurgery 2003;99:162-8.

40. Yue WM, Tan SB, Tan MH, Koh DCS, Tan CT. The Torg-Pavlov ratio in cervical spondylotic myelopathy - A comparative study between patients with cervical spondylotic myelopathy and nonspondylotic, nonmyelopathic population. Spine 2001;26:1760-4.

41. Suk KS, Kim KT, Lee JH, Lee SH, Kim JS, Kim JY. Reevaluation of the Pavlov ratio in patients with cervical myelopathy. Clin Orthop Surg 2009;1:6-10.

42. Morio Y, Yamamoto K, Kuranobu K, Murata M, Tuda K. Does Increased Signal Intensity of the Spinal-Cord on Mr-Images Due to Cervical Myelopathy Predict Prognosis. Arch Orthop Traum Su 1994;113:254-9.

43. Puzzilli F, Mastronardi L, Ruggeri A, Lunardi P. Intramedullary increased MR signal intensity and its relation to clinical features in cervical myelopathy. J Neurosurg Sci 1999;43:135-9; discussion 9.

44. Matsumoto M, Toyama Y, Ishikawa M, Chiba K, Suzuki N, Fujimura Y. Increased signal intensity of the spinal cord on magnetic resonance images in cervical compressive myelopathy - Does it predict the outcome of conservative treatment? Spine 2000;25:677-82.

45. de Rota JJF, Meschian S, de Rota AF, Urbano V, Baron M. Cervical spondylotic myelopathy due to chronic compression: the role of signal intensity changes in magnetic resonance images. J Neurosurg-Spine 2007;6:17-22.

46. Mastronardi L, Elsawaf A, Roperto R, et al. Prognostic relevance of the postoperative evolution of intramedullary spinal cord changes in signal intensity on magnetic resonance imaging

after anterior decompression for cervical spondylotic myelopathy. J Neurosurg-Spine 2007;7:615-22.

47. Tetreault LA, Dettori JR, Wilson JR, et al. Systematic Review of Magnetic Resonance Imaging Characteristics That Affect Treatment Decision Making and Predict Clinical Outcome in Patients With Cervical Spondylotic Myelopathy. Spine 2013;38:S89-S110.

48. Bednarik J, Kadanka Z, Dusek L, et al. Presymptomatic spondylotic cervical cord compression. Spine (Phila Pa 1976) 2004;29:2260-9.

49. Cheung WY, Arvinte D, Wong YW, Luk KDK, Cheung KMC. Neurological recovery after surgical decompression in patients with cervical spondylotic myelopathy - a prospective study. Int Orthop 2008;32:273-8.

50. Nolte J. The human brain: an introduction to its functional anatomy: Mosby/Elsevier; 2009.

51. Keller SS, Gerdes JS, Mohammadi S, et al. Volume Estimation of the Thalamus Using Freesurfer and Stereology: Consistency between Methods. Neuroinformatics 2012;10:341-50.

52. Zilles K. 22 - Cortex A2 - Paxinos, George. The Human Nervous System. San Diego: Academic Press; 1990:757-802.

53. Economo C, Parker S. The cytoarchitectonics of the human cerebral cortex. London: Humphrey Milford ; Oxford University Press; 1929.

54. Fischl B, Dale AM. Measuring the thickness of the human cerebral cortex from magnetic resonance images. Proc Natl Acad Sci U S A 2000;97:11050-5.

55. Brodmann K, Gary LJ. Brodmann's localization in the cerebral cortex the principles of comparative localisation in the cerebral cortex based on cytoarchitectonics. New York, NY: Springer,; 2006:xv, 298 p.

56. Grillner S. Chapter 27 - Fundamentals of Motor Systems A2 - Squire, Larry R. In: Berg D, Bloom FE, Lac Sd, Ghosh A, Spitzer NC, eds. Fundamental Neuroscience (Fourth Edition). San Diego: Academic Press; 2013:599-611.

57. Hendry S, Hsiao S. Chapter 24 - The Somatosensory System A2 - Squire, Larry R. In: Berg D, Bloom FE, Lac Sd, Ghosh A, Spitzer NC, eds. Fundamental Neuroscience (Fourth Edition). San Diego: Academic Press; 2013:531-51.

58. Kakei S, Hoffman DS, Strick PL. Muscle and movement representations in the primary motor cortex. Science 1999;285:2136-9.

59. Suppa A, Marsili L, Di Stasio F, et al. Primary Motor Cortex Long-Term Plasticity in Multiple System Atrophy. Movement Disord 2014;29:97-104.

60. Dancause N. Plasticity in the Motor Network Following Primary Motor Cortex Lesion. Adv Exp Med Biol 2013;782:61-86.

61. Sanes JN, Donoghue JP. Plasticity and primary motor cortex. Annu Rev Neurosci 2000;23:393-415.

62. Donoghue JP. Plasticity of adult sensorimotor representations. Curr Opin Neurobiol 1995;5:749-54.

63. Kiernan MC, Vucic S, Cheah BC, et al. Amyotrophic lateral sclerosis. Lancet 2011;377:942-55.

64. Pioro EP, Antel JP, Cashman NR, Arnold DL. Detection of Cortical Neuron Loss in Motor-Neuron Disease by Proton Magnetic-Resonance Spectroscopic Imaging in-Vivo. Neurology 1994;44:1933-8.

65. Rexed B. The cytoarchitectonic organization of the spinal cord in the cat. J Comp Neurol 1952;96:414-95.

66. Ko H-Y, Park JH, Shin YB, Baek SY. Gross quantitative measurements of spinal cord segments in human. Spinal cord : the official journal of the International Medical Society of Paraplegia 2004;42:35-40.

67. McDonald JW, Sadowsky C. Spinal-cord injury. Lancet 2002;359:417-25.

68. Willis W, Coggeshall R. Sensory mechanisms of the spinal cord. Vol 1. Primary afferent neurons and the spinal dorsal horn. New York: Kluwer Academic/Plenum Publishers; 2004.

69. Edgerton VR, Roy RR, DeLeon R, Tillakaratne N, Hodgson JA. Does motor learning occur in the spinal cord? Neuroscientist 1997;3:287-94.

70. Perl ER, Kruger L. Chapier 4 - Nociception and Pain: Evolution of Concepts and Observations. Pain and Touch. San Diego: Academic Press; 1996:179-211.

71. Garland EL. Pain processing in the human nervous system: a selective review of nociceptive and biobehavioral pathways. Prim Care 2012;39:561-71.

72. Dum RP, Levinthal DJ, Strick PL. The spinothalamic system targets motor and sensory areas in the cerebral cortex of monkeys. J Neurosci 2009;29:14223-35.

73. Zhuo M. Long-term potentiation in the anterior cingulate cortex and chronic pain. Philos T R Soc B 2014;369.

74. Bliss TVP, Collingridge GL, Kaang BK, Zhuo M. Synaptic plasticity in the anterior cingulate cortex in acute and chronic pain. Nat Rev Neurosci 2016;17:485-96.

75. Zhuo M. Contribution of Synaptic Plasticity in the Insular Cortex to Chronic Pain. Neuroscience 2016;338:220-9.

76. Zhuo M. Cortical excitation and chronic pain. Trends in Neurosciences 2008;31:199-207.

77. Wansapura JP, Holland SK, Dunn RS, Ball WS. NMR relaxation times in the human brain at 3.0 tesla. Jmri-J Magn Reson Im 1999;9:531-8.

78. Hopkins AL, Yeung HN, Bratton CB. Multiple field strength in vivo T1 and T2 for cerebrospinal fluid protons. Magn Reson Med 1986;3:303-11.

79. Mugler JP, 3rd, Brookeman JR. Three-dimensional magnetization-prepared rapid gradient-echo imaging (3D MP RAGE). Magn Reson Med 1990;15:152-7.

80. Mugler JP, 3rd, Brookeman JR. Rapid three-dimensional T1-weighted MR imaging with the MP-RAGE sequence. J Magn Reson Imaging 1991;1:561-7.

81. Brant-Zawadzki M, Gillan GD, Nitz WR. MP RAGE: a three-dimensional, T1-weighted, gradient-echo sequence--initial experience in the brain. Radiology 1992;182:769-75.

82. Dale AM, Fischl B, Sereno MI. Cortical surface-based analysis - I. Segmentation and surface reconstruction. Neuroimage 1999;9:179-94.

83. Fischl B, Dale AM. Measuring the thickness of the human cerebral cortex from magnetic resonance images. P Natl Acad Sci USA 2000;97:11050-5.

84. Fischl B, Sereno MI, Dale AM. Cortical surface-based analysis - II: Inflation, flattening, and a surface-based coordinate system. Neuroimage 1999;9:195-207.

85. Fischl B, Liu A, Dale AM. Automated manifold surgery: Constructing geometrically accurate and topologically correct models of the human cerebral cortex. Ieee T Med Imaging 2001;20:70-80.

86. Fischl B, van der Kouwe A, Destrieux C, et al. Automatically parcellating the human cerebral cortex. Cereb Cortex 2004;14:11-22.

87. Desikan RS, Segonne F, Fischl B, et al. An automated labeling system for subdividing the human cerebral cortex on MRI scans into gyral based regions of interest. Neuroimage 2006;31:968-80.

88. Lerch JP, Evans AC. Cortical thickness analysis examined through power analysis and a population simulation. Neuroimage 2005;24:163-73.

89. Salat DH, Buckner RL, Snyder AZ, et al. Thinning of the cerebral cortex in aging. Cereb Cortex 2004;14:721-30.

90. Sowell ER, Peterson BS, Kan E, et al. Sex differences in cortical thickness mapped in 176 healthy individuals between 7 and 87 years of age. Cereb Cortex 2007;17:1550-60.

91. Lemaitre H, Goldman AL, Sambataro F, et al. Normal age-related brain morphometric changes: nonuniformity across cortical thickness, surface area and gray matter volume? Neurobiol Aging 2012;33.

92. Lerch JP, Pruessner JC, Zijdenbos A, Hampel H, Teipel SJ, Evans AC. Focal decline of cortical thickness in Alzheimer's disease identified by computational neuroanatomy. Cerebral Cortex 2005;15:995-1001.

93. Lerch JP, Pruessner J, Zijdenbos AP, et al. Automated cortical thickness measurements from MRI can accurately separate Alzheimer's patients from normal elderly controls. Neurobiol Aging 2008;29:23-30.

94. Querbes O, Aubry F, Pariente J, et al. Early diagnosis of Alzheimer's disease using cortical thickness: impact of cognitive reserve. Brain 2009;132:2036-47.

95. Fischl B, Salat DH, Busa E, et al. Whole brain segmentation: automated labeling of neuroanatomical structures in the human brain. Neuron 2002;33:341-55.

96. Fischl B, Salat DH, van der Kouwe AJ, et al. Sequence-independent segmentation of magnetic resonance images. Neuroimage 2004;23 Suppl 1:S69-84.

97. Hennig J, Nauerth A, Friedburg H. Rare Imaging - a Fast Imaging Method for Clinical Mr. Magnet Reson Med 1986;3:823-33.

98. Busse RF, Brau ACS, Vu A, et al. Effects of refocusing flip angle modulation and view ordering in 3D fast spin echo. Magnet Reson Med 2008;60:640-9.

99. Lichy MP, Wietek BM, Mugler JP, et al. Magnetic resonance imaging of the body trunk using a single-slab, 3-dimensional, T2-weighted turbo-spin-echo sequence with high sampling efficiency (SPACE) for high spatial resolution imaging - Initial clinical experiences. Invest Radiol 2005;40:754-60.

100. Fries P, Runge VM, Kirchin MA, Watkins DM, Buecker A, Schneider G. Magnetic resonance imaging of the spine at 3 Tesla. Semin Musculoskel R 2008;12:238-52.

101. De Leener B, Levy S, Dupont SM, et al. SCT: Spinal Cord Toolbox, an open-source software for processing spinal cord MRI data. Neuroimage 2017;145:24-43.

102. De Leener B, Kadoury S, Cohen-Adad J. Robust, accurate and fast automatic segmentation of the spinal cord. Neuroimage 2014;98:528-36.

103. Fonov VS, Le Troter A, Taso M, et al. Framework for integrated MRI average of the spinal cord white and gray matter: The MNI-Poly-AMU template. Neuroimage 2014;102:817-27.

104. Rocca MA, Horsfield MA, Sala S, et al. A multicenter assessment of cervical cord atrophy among MS clinical phenotypes. Neurology 2011;76:2096-102.

105. Bieniek M, Altmann DR, Davies GR, et al. Cord atrophy separates early primary progressive and relapsing remitting multiple sclerosis. J Neurol Neurosur Ps 2006;77:1036-9.

106. Ogawa S, Lee TM, Kay AR, Tank DW. Brain magnetic resonance imaging with contrast dependent on blood oxygenation. Proc Natl Acad Sci U S A 1990;87:9868-72.

107. Ogawa S, Menon RS, Tank DW, et al. Functional brain mapping by blood oxygenation level-dependent contrast magnetic resonance imaging. A comparison of signal characteristics with a biophysical model. Biophys J 1993;64:803-12.

108. Attwell D, Iadecola C. The neural basis of functional brain imaging signals. Trends Neurosci 2002;25:621-5.

109. Biswal B, Yetkin FZ, Haughton VM, Hyde JS. Functional Connectivity in the Motor Cortex of Resting Human Brain Using Echo-Planar Mri. Magnet Reson Med 1995;34:537-41.

110. Damoiseaux JS, Rombouts SARB, Barkhof F, et al. Consistent resting-state networks across healthy subjects. P Natl Acad Sci USA 2006;103:13848-53.

111. Fox MD, Raichle ME. Spontaneous fluctuations in brain activity observed with functional magnetic resonance imaging. Nat Rev Neurosci 2007;8:700-11.

112. Wang L, Zang YF, He Y, et al. Changes in hippocampal connectivity in the early stages of Alzheimer's disease: Evidence from resting state fMRI. Neuroimage 2006;31:496-504.

113. Mohammadi B, Kollewe K, Samii A, Krampfl K, Dengler R, Munte TF. Changes of resting state brain networks in amyotrophic lateral sclerosis. Exp Neurol 2009;217:147-53.

114. Fox MD, Buckner RL, Liu HS, Chakravarty MM, Lozano AM, Pascual-Leone A. Resting-state networks link invasive and noninvasive brain stimulation across diverse psychiatric and neurological diseases. P Natl Acad Sci USA 2014;111:E4367-E75.

115. Greicius MD, Krasnow B, Reiss AL, Menon V. Functional connectivity in the resting brain: A network analysis of the default mode hypothesis. P Natl Acad Sci USA 2003;100:253-8.

116. Lowe MJ, Dzemidzic M, Lurito JT, Mathews VP, Phillips MD. Correlations in low-frequency BOLD fluctuations reflect cortico-cortical connections. Neuroimage 2000;12:582-7.

117. Fox MD, Snyder AZ, Vincent JL, Corbetta M, Van Essen DC, Raichle ME. The human brain is intrinsically organized into dynamic, anticorrelated functional networks. P Natl Acad Sci USA 2005;102:9673-8.

118. Biswal BB, Mennes M, Zuo XN, et al. Toward discovery science of human brain function. P Natl Acad Sci USA 2010;107:4734-9.

119. Shehzad Z, Kelly AMC, Reiss PT, et al. The Resting Brain: Unconstrained yet Reliable. Cerebral Cortex 2009;19:2209-29.

120. Satterthwaite TD, Wolf DH, Loughead J, et al. Impact of in-scanner head motion on multiple measures of functional connectivity: Relevance for studies of neurodevelopment in youth. Neuroimage 2012;60:623-32.

121. Van Dijk KRA, Sabuncu MR, Buckner RL. The influence of head motion on intrinsic functional connectivity MRI. Neuroimage 2012;59:431-8.

122. Behzadi Y, Restom K, Liau J, Liu TT. A component based noise correction method (CompCor) for BOLD and perfusion based fMRI. Neuroimage 2007;37:90-101.

123. Glover GH, Li TQ, Ress D. Image-based method for retrospective correction of physiological motion effects in fMRI: RETROICOR. Magnet Reson Med 2000;44:162-7.

124. Brooks JCW, Faull OK, Pattinson KTS, Jenkinson M. Physiological noise in brainstem fMRI. Front Hum Neurosci 2013;7.

125. Smith AM, Lewis BK, Ruttimann UE, et al. Investigation of low frequency drift in fMRI signal. Neuroimage 1999;9:526-33.

126. Lowe MJ, Russell DP. Treatment of baseline drifts in fMRI time series analysis. J Comput Assist Tomo 1999;23:463-73.

127. Tanabe J, Miller D, Tregellas J, Freedman R, Meyer FG. Comparison of detrending methods for optimal fMRI preprocessing. Neuroimage 2002;15:902-7.

128. Whitfield-Gabrieli S, Nieto-Castanon A. Conn: a functional connectivity toolbox for correlated and anticorrelated brain networks. Brain Connect 2012;2:125-41.

129. Yoshizawa T, Nose T, Moore GJ, Sillerud LO. Functional magnetic resonance imaging of motor activation in the human cervical spinal cord. NeuroImage 1996;4:174-82.

130. Stroman P. Mapping of Neuronal Function in the Healthy and Injured Human Spinal Cord with Spinal fMRI. NeuroImage 2002;17:1854-60.

131. Stroman PW, Ryner LN. Functional MRI of motor and sensory activation in the human spinal cord. Magnetic Resonance Imaging 2001;19:27-32.

132. Stroman PW. Magnetic resonance imaging of neuronal function in the spinal cord: spinal FMRI. Clinical medicine & research 2005;3:146-56.

133. Wei P, Li J, Gao F, Ye D, Zhong Q, Liu S. Resting state networks in human cervical spinal cord observed with fMRI. European Journal of Applied Physiology 2010;108:265-71.

134. Barry RL, Smith Sa, Dula aN, Gore JC. Resting state functional connectivity in the human spinal cord. eLife 2014;3:e02812-e.

135. Brooks JCW, Beckmann CF, Miller KL, et al. Physiological noise modelling for spinal functional magnetic resonance imaging studies. NeuroImage 2008;39:680-92.

136. Kong Y, Jenkinson M, Andersson J, Tracey I, Brooks JCW. Assessment of physiological noise modelling methods for functional imaging of the spinal cord. NeuroImage 2012;60:1538-49.

137. Sprenger C, Bu C. Spinal Cord – Midbrain Functional Connectivity Is Related to Perceived Pain Intensity : A Combined Spino-Cortical fMRI Study. 2015;35:4248-57.

138. Vahdat S, Lungu O, Cohen-Adad J, Marchand-Pauvert V, Benali H, Doyon J. Simultaneous Brain–Cervical Cord fMRI Reveals Intrinsic Spinal Cord Plasticity during Motor Sequence Learning. PLOS Biology 2015;13:e1002186.

139. Einstein A, Fürth R, Cowper AD. Investigations on the theory of the Brownian movement. London: Methuen & Co. ltd.; 1926.

140. Basser PJ. Inferring microstructural features and the physiological state of tissues from diffusion-weighted images. Nmr Biomed 1995;8:333-44.

141. Assaf Y, Freidlin RZ, Rohde GK, Basser PJ. New modeling and experimental framework to characterize hindered and restricted water diffusion in brain white matter. Magnet Reson Med 2004;52:965-78.

142. Beaulieu C. The basis of anisotropic water diffusion in the nervous system - a technical review. Nmr Biomed 2002;15:435-55.

143. Stejskal EO, Tanner JE. Spin Diffusion Measurements: Spin Echoes in the Presence of a Time-Dependent Field Gradient. J Chem Phys 1965;42:288-+.

144. Pipe J. Chapter 2 - Pulse Sequences for Diffusion-Weighted MRI. Diffusion MRI (Second Edition). San Diego: Academic Press; 2014:11-34.

145. Basser PJ, Mattiello J, LeBihan D. Estimation of the effective self-diffusion tensor from the NMR spin echo. J Magn Reson B 1994;103:247-54.

146. Basser PJ, Mattiello J, LeBihan D. MR diffusion tensor spectroscopy and imaging. Biophys J 1994;66:259-67.

147. Ennis DB, Kindlmann G. Orthogonal tensor invariants and the analysis of diffusion tensor magnetic resonance images. Magn Reson Med 2006;55:136-46.

148. Miller KL. Chapter 3 - Diffusion Acquisition: Pushing the Boundaries. Diffusion MRI (Second Edition). San Diego: Academic Press; 2014:35-61.

149. Callaghan PT, Eccles CD, Xia Y. Nmr Microscopy of Dynamic Displacements - K-Space and Q-Space Imaging. J Phys E Sci Instrum 1988;21:820-2.

150. Jensen JH, Helpern JA, Ramani A, Lu HZ, Kaczynski K. Diffusional kurtosis imaging: The quantification of non-Gaussian water diffusion by means of magnetic resonance imaging. Magnet Reson Med 2005;53:1432-40.

151. Bennett KM, Schmainda KM, Bennett R, Rowe DB, Lu HB, Hyde JS. Characterization of continuously distributed cortical water diffusion rates with a stretched-exponential model. Magnet Reson Med 2003;50:727-34.

152. Yeh FC, Liu L, Hitchens TK, Wu YJL. Mapping immune cell infiltration using restricted diffusion MRI. Magnet Reson Med 2017;77:603-12.

153. Seunarine KK, Alexander DC. Chapter 6 - Multiple Fibers: Beyond the Diffusion Tensor. Diffusion MRI (Second Edition). San Diego: Academic Press; 2014:105-23.

154. Alexander DC. Multiple-fiber reconstruction algorithms for diffusion MRI. White Matter in Cognitive Neuroscience: Advances in Diffusion Tensor Imaging and Its Applications 2005;1064:113-+.

155. Tuch DS, Reese TG, Wiegell MR, Makris N, Belliveau JW, Wedeen VJ. High angular resolution diffusion imaging reveals intravoxel white matter fiber heterogeneity. Magnet Reson Med 2002;48:577-82.

156. Alexander DC, Barker GJ. Optimal imaging parameters for fiber-orientation estimation in diffusion MRI. Neuroimage 2005;27:357-67.

157. Tuch DS, Reese TG, Wiegell MR, Wedeen VJ. Diffusion MRI of complex neural architecture. Neuron 2003;40:885-95.

158. Sadowsky C, Volshteyn O, Schultz L, McDonald JW. Spinal cord injury. Disabil Rehabil 2002;24:680-7.

159. Ellingson BM, Ulmer JL, Kurpad SN, Schmit BD. Diffusion tensor MR imaging in chronic spinal cord injury. AJNR American journal of neuroradiology 2008;29:1976-82.

160. Guleria S, Gupta RK, Saksena S, et al. Retrograde Wallerian degeneration of cranial corticospinal tracts in cervical spinal cord injury patients using diffusion tensor imaging. J Neurosci Res 2008;86:2271-80.

161. Tator CH, Fehlings MG. Review of the secondary injury theory of acute spinal cord trauma with emphasis on vascular mechanisms. J Neurosurg 1991;75:15-26.

162. Miyanji F, Furlan JC, Aarabi B, Arnold PM, Fehlings MG. Acute cervical traumatic spinal cord injury: MR imaging findings correlated with neurologic outcome--prospective study with 100 consecutive patients. Radiology 2007;243:820-7.

163. Shimada K, Tokioka T. Sequential MR studies of cervical cord injury: correlation with neurological damage and clinical outcome. Spinal Cord 1999;37:410-5.

164. Chen LM, Mishra A, Yang PF, Wang F, Gore JC. Injury alters intrinsic functional connectivity within the primate spinal cord. P Natl Acad Sci USA 2015;112:5991-6.

165. Hains BC, Black JA, Waxman SG. Primary cortical motor neurons undergo apoptosis after axotomizing spinal cord injury. J Comp Neurol 2003;462:328-41.

166. Barron KD, Dentinger MP, Popp AJ, Mankes R. Neurons of layer Vb of rat sensorimotor cortex atrophy but do not die after thoracic cord transection. J Neuropathol Exp Neurol 1988;47:62-74.

167. Jurkiewicz MT, Crawley AP, Verrier MC, Fehlings MG, Mikulis DJ. Somatosensory cortical atrophy after spinal cord injury: a voxel-based morphometry study. Neurology 2006;66:762-4.

168. Wrigley PJ, Gustin SM, Macey PM, et al. Anatomical changes in human motor cortex and motor pathways following complete thoracic spinal cord injury. Cereb Cortex 2009;19:224-32.

169. Hou JM, Yan RB, Xiang ZM, et al. Brain sensorimotor system atrophy during the early stage of spinal cord injury in humans. Neuroscience 2014;266:208-15.

170. Freund P, Weiskopf N, Ashburner J, et al. MRI investigation of the sensorimotor cortex and the corticospinal tract after acute spinal cord injury: a prospective longitudinal study. Lancet Neurol 2013;12:873-81.

171. Freund P, Weiskopf N, Ward NS, et al. Disability, atrophy and cortical reorganization following spinal cord injury. Brain 2011;134:1610-22.

172. Freund P, Weiskopf N, Ward NS, et al. Disability, atrophy and cortical reorganization following spinal cord injury. Brain 2011;134:1610-22.

173. Grabher P, Callaghan MF, Ashburner J, et al. Tracking sensory system atrophy and outcome prediction in spinal cord injury. Ann Neurol 2015;78:751-61.

174. Oni-Orisan A, Kaushal M, Li WJ, et al. Alterations in Cortical Sensorimotor Connectivity following Complete Cervical Spinal Cord Injury: A Prospective Resting-State fMRI Study. Plos One 2016;11.

175. Hou JM, Sun TS, Xiang ZM, et al. Alterations of Resting-State Regional and Network-Level Neural Function after Acute Spinal Cord Injury. Neuroscience 2014;277:446-54.

176. Min YS, Park JW, Jin SU, et al. Alteration of Resting-State Brain Sensorimotor Connectivity following Spinal Cord Injury: A Resting-State Functional Magnetic Resonance Imaging Study. J Neurotraum 2015;32:1422-7.

177. Kokotilo KJ, Eng JJ, Curt A. Reorganization and Preservation of Motor Control of the Brain in Spinal Cord Injury: A Systematic Review. J Neurotraum 2009;26:2113-26.

178. Wilson PR. Multidisciplinary Management of Chronic Pain. A Practical Guide for Clinicians. Pain Med 2016;17:1376-8.

179. Willis WD, Westlund KN. Neuroanatomy of the pain system and of the pathways that modulate pain. J Clin Neurophysiol 1997;14:2-31.

180. Latremoliere A, Woolf CJ. Central Sensitization: A Generator of Pain Hypersensitivity by Central Neural Plasticity. J Pain 2009;10:895-926.

181. Woolf CJ. Central sensitization: Implications for the diagnosis and treatment of pain. Pain 2011;152:S2-S15.

182. Lee YC, Nassikas NJ, Clauw DJ. The role of the central nervous system in the generation and maintenance of chronic pain in rheumatoid arthritis, osteoarthritis and fibromyalgia. Arthritis Res Ther 2011;13.

183. Apkarian AV, Hashmi JA, Baliki MN. Pain and the brain: Specificity and plasticity of the brain in clinical chronic pain. Pain 2011;152:S49-S64.

184. May A. Chronic pain may change the structure of the brain. Pain 2008;137:7-15.

185. Apkarian AV, Baliki MN, Geha PY. Towards a theory of chronic pain. Prog Neurobiol 2009;87:81-97.

186. Ivo R, Nicklas A, Dargel J, et al. Brain structural and psychometric alterations in chronic low back pain. Eur Spine J 2013;22:1958-64.

187. Davis KD, Pope G, Chen J, Kwan CL, Crawley AP, Diamant NE. Cortical thinning in IBS: Implications for homeostatic, attention, and pain processing. Neurology 2008;70:153-4.

188. Frokjaer JB, Bouwense SAW, Olesen SS, et al. Reduced Cortical Thickness of Brain Areas Involved in Pain Processing in Patients With Chronic Pancreatitis. Clin Gastroenterol H 2012;10:434-U136.

189. Cauda F, Palermo S, Costa T, et al. Gray matter alterations in chronic pain: A network-oriented meta-analytic approach. Neuroimage-Clin 2014;4:676-86.

190. Apkarian AV. The brain adapting with pain : contribution of neuroimaging technology to pain mechanisms2015.

191. Baliki MN, Mansour AR, Baria AT, Apkarian AV. Functional Reorganization of the Default Mode Network across Chronic Pain Conditions. Plos One 2014;9.

192. Tagliazucchi E, Balenzuela P, Fraiman D, Chialvo DR. Brain resting state is disrupted in chronic back pain patients. Neurosci Lett 2010;485:26-31.

193. Fritz HC, McAuley JH, Wittfeld K, et al. Chronic Back Pain Is Associated With Decreased Prefrontal and Anterior Insular Gray Matter: Results From a Population-Based Cohort Study. J Pain 2016;17:111-8.

194. Schmidt-Wilcke T, Leinisch E, Ganssbauer S, et al. Affective components and intensity of pain correlate with structural differences in gray matter in chronic back pain patients. Pain 2006;125:89-97.

195. Woodworth D, Mayer E, Leu K, et al. Unique Microstructural Changes in the Brain Associated with Urological Chronic Pelvic Pain Syndrome (UCPPS) Revealed by Diffusion Tensor MRI, Super-Resolution Track Density Imaging, and Statistical Parameter Mapping: A MAPP Network Neuroimaging Study. PLoS One 2015;10:e0140250.

196. Ellingson BM, Mayer E, Harris RJ, et al. Diffusion tensor imaging detects microstructural reorganization in the brain associated with chronic irritable bowel syndrome. Pain 2013;154:1528-41.

197. Lutz J, Jager L, de Quervain D, et al. White and Gray Matter Abnormalities in the Brain of Patients With Fibromyalgia A Diffusion-Tensor and Volumetric Imaging Study. Arthritis Rheum 2008;58:3960-9.

198. Huang L, Kutch JJ, Ellingson BM, et al. Brain white matter changes associated with urological chronic pelvic pain syndrome: multisite neuroimaging from a MAPP case-control study. Pain 2016;157:2782-91.

199. Jutzeler CR, Huber E, Callaghan MF, et al. Association of pain and CNS structural changes after spinal cord injury. Sci Rep-Uk 2016;6.

200. Guan X, Fan G, Wu X, et al. Diffusion Tensor Imaging Studies of Cervical Spondylotic Myelopathy: A Systemic Review and Meta-Analysis. Plos One 2015;10:e0117707.

201. Ellingson BM, Salamon N, Grinstead JW, Holly LT. Diffusion tensor imaging (DTI) predicts functional impairment in mild to moderate cervical spondylotic myelopathy. The spine journal : official journal of the North American Spine Society 2014;14:2589-97.

202. Wen CY, Cui JL, Mak KC, Luk KDK, Hu Y. Diffusion tensor imaging of somatosensory tract in cervical spondylotic myelopathy and its link with electrophysiological evaluation. Spine Journal 2014;14:1493-500.

203. Dong Y, Holly LT, Albistegui-Dubois R, et al. Compensatory cerebral adaptations before and evolving changes after surgical decompression in cervical spondylotic myelopathy. Journal of neurosurgery Spine 2008;9:538-51.

204. Holly LT, Dong Y, Albistegui-DuBois R, Marehbian J, Dobkin B. Cortical reorganization in patients with cervical spondylotic myelopathy. Journal of neurosurgery Spine 2007;6:544-51.

205. Duggal N, Rabin D, Bartha R, et al. Brain reorganization in patients with spinal cord compression evaluated using fMRI. Neurology 2010;74:1048-54.

206. Hrabalek L, Hlustik P, Hok P, et al. [Effects of spinal cord decompression in patients with cervical spondylotic myelopathy oncortical brain activations]. Rozhl Chir 2014;93:530-5.

207. Bhagavatula ID, Shukla D, Sadashiva N, Saligoudar P, Prasad C, Bhat DI. Functional cortical reorganization in cases of cervical spondylotic myelopathy and changes associated with surgery. Neurosurg Focus 2016;40:E2.

208. Zhu L, Wu G, Zhou X, Li J, Wen Z, Lin F. Altered Spontaneous Brain Activity in Patients with Acute Spinal Cord Injury Revealed by Resting-State Functional MRI. Plos One 2015;10:e0118816.

209. Zhou FQ, Tan YM, Wu L, Zhuang Y, He LC, Gong HH. Intrinsic Functional Plasticity of the Sensory-Motor Network in Patients with Cervical Spondylotic Myelopathy. Sci Rep-Uk 2015;5:9975.

210. Alger JR, Ellingson BM, Ashe-McNalley C, et al. Multisite, multimodal neuroimaging of chronic urological pelvic pain: Methodology of the MAPP Research Network. Neuroimage Clin 2016;12:65-77.

211. Glover GH, Mueller BA, Turner JA, et al. Function biomedical informatics research network recommendations for prospective multicenter functional MRI studies. Journal of Magnetic Resonance Imaging 2012;36:39-54.

212. Cohen-Adad J, Wheeler-Kingshott C. Quantitative MRI of the spinal cord: Academic Press; 2014.

213. Feinberg DA, Moeller S, Smith SM, et al. Multiplexed echo planar imaging for sub-second whole brain FMRI and fast diffusion imaging. PLoS One 2010;5:e15710.

214. Labus JS, Naliboff B, Kilpatrick L, et al. Pain and Interoception Imaging Network (PAIN): A multimodal, multisite, brain-imaging repository for chronic somatic and visceral pain disorders. Neuroimage 2016;124:1232-7.

215. Hagler DJ, Saygin AP, Sereno MI. Smoothing and cluster thresholding for cortical surface-based group analysis of fMRI data. Neuroimage 2006;33:1093-103.

216. Klein A, Tourville J. 101 labeled brain images and a consistent human cortical labeling protocol. Front Neurosci 2012;6:171.

217. Fischl B, Rajendran N, Busa E, et al. Cortical folding patterns and predicting cytoarchitecture. Cerebral Cortex 2008;18:1973-80.

218. Holm S. A Simple Sequentially Rejective Multiple Test Procedure. Scand J Stat 1979;6:65-70.

219. Seaman MA, Levin JR, Serlin RC. New Developments in Pairwise Multiple Comparisons - Some Powerful and Practicable Procedures. Psychol Bull 1991;110:577-86.

220. Fischl B, Salat DH, Busa E, et al. Whole brain segmentation: Automated labeling of neuroanatomical structures in the human brain. Neuron 2002;33:341-55.

221. Cavanna AE, Trimble MR. The precuneus: a review of its functional anatomy and behavioural correlates. Brain 2006;129:564-83.

222. Parent A, Hazrati LN. Functional anatomy of the basal ganglia. I. The cortico-basal ganglia-thalamo-cortical loop. Brain Res Brain Res Rev 1995;20:91-127.

223. Hetu S, Gregoire M, Saimpont A, et al. The neural network of motor imagery: an ALE meta-analysis. Neurosci Biobehav Rev 2013;37:930-49.

224. Bakker M, De Lange FP, Helmich RC, Scheeringa R, Bloem BR, Toni I. Cerebral correlates of motor imagery of normal and precision gait. Neuroimage 2008;41:998-1010.

225. Luft AR, Buitrago MM. Stages of motor skill learning. Mol Neurobiol 2005;32:205-16.

226. Volz KG, Schubotz RI, von Cramon DY. Variants of uncertainty in decision-making and their neural correlates. Brain Res Bull 2005;67:403-12.

227. Ullsperger M, Danielmeier C, Jocham G. Neurophysiology of performance monitoring and adaptive behavior. Physiol Rev 2014;94:35-79.

228. Wenderoth N, Debaere F, Sunaert S, Swinnen SP. The role of anterior cingulate cortex and precuneus in the coordination of motor behaviour. Eur J Neurosci 2005;22:235-46.

229. Yeterian EH, Pandya DN. Corticothalamic connections of the posterior parietal cortex in the rhesus monkey. J Comp Neurol 1985;237:408-26.

230. Leichnetz GR. Connections of the medial posterior parietal cortex (area 7m) in the monkey. Anat Rec 2001;263:215-36.

231. Petrides M, Pandya DN. Projections to the frontal cortex from the posterior parietal region in the rhesus monkey. J Comp Neurol 1984;228:105-16.

232. Patestas MA, Gartner LP. A textbook of neuroanatomy. 2006.

233. Harrop JS, Hanna A, Silva MT, Sharan A. Neurological manifestations of cervical spondylosis: an overview of signs, symptoms, and pathophysiology. Neurosurgery 2007;60:S14-20.

234. Nardone A, Galante M, Grasso M, Schieppati M. Stance ataxia and delayed leg muscle responses to postural perturbations in cervical spondylotic myelopathy. J Rehabil Med 2008;40:539-47.

235. Doita M, Sakai H, Harada T, et al. The influence of proprioceptive impairment on hand function in patients with cervical myelopathy. Spine (Phila Pa 1976) 2006;31:1580-4.

236. Rodriguez-Raecke R, Niemeier A, Ihle K, Ruether W, May A. Brain gray matter decrease in chronic pain is the consequence and not the cause of pain. J Neurosci 2009;29:13746-50.

237. Burgmer M, Gaubitz M, Konrad C, et al. Decreased gray matter volumes in the cingulo-frontal cortex and the amygdala in patients with fibromyalgia. Psychosom Med 2009;71:566-73.

238. Okada Y, Ikata T, Katoh S, Yamada H. Morphologic analysis of the cervical spinal cord, dural tube, and spinal canal by magnetic resonance imaging in normal adults and patients with cervical spondylotic myelopathy. Spine (Phila Pa 1976) 1994;19:2331-5.

239. Morishita Y, Naito M, Hymanson H, Miyazaki M, Wu GZ, Wang JC. The relationship between the cervical spinal canal diameter and the pathological changes in the cervical spine. Eur Spine J 2009;18:877-83.

240. Grabher P, Callaghan MF, Ashburner J, et al. Tracking sensory system atrophy and outcome prediction in spinal cord injury. Ann Neurol 2015;78:751-61.

241. Freund P, Curt A, Friston K, Thompson A. Tracking changes following spinal cord injury: insights from neuroimaging. Neuroscientist 2013;19:116-28.

242. Grabher P, Mohammadi S, Trachsler A, et al. Voxel-based analysis of grey and white matter degeneration in cervical spondylotic myelopathy. Sci Rep 2016;6:24636.

243. Martin AR, De Leener B, Cohen-Adad J, et al. A Novel MRI Biomarker of Spinal Cord White Matter Injury: T2*-Weighted White Matter to Gray Matter Signal Intensity Ratio. AJNR Am J Neuroradiol 2017;38:1266-73.

244. Dusart I, Schwab ME. Secondary cell death and the inflammatory reaction after dorsal hemisection of the rat spinal cord. Eur J Neurosci 1994;6:712-24.

245. Ichihara K, Taguchi T, Sakuramoto I, Kawano S, Kawai S. Mechanism of the spinal cord injury and the cervical spondylotic myelopathy: new approach based on the mechanical features of the spinal cord white and gray matter. J Neurosurg 2003;99:278-85.

246. Schmid MR, Pfirrmann CW, Koch P, Zanetti M, Kuehn B, Hodler J. Imaging of patellar cartilage with a 2D multiple-echo data image combination sequence. AJR Am J Roentgenol 2005;184:1744-8.

247. Metman LV, Bellevich JS, Jones SM, Barber MD, Streletz LJ. Topographic mapping of human motor cortex with transcranial magnetic stimulation: Homunculus revisited. Brain Topogr 1993;6:13-9.

248. Kocak M, Ulmer JL, Ugurel MS, Gaggl W, Prost RW. Motor Homunculus: Passive Mapping in Healthy Volunteers by Using Functional MR Imaging-Initial Results. Radiology 2009;251:485-92.

249. Eippert F, Kong YZ, Winkler AM, et al. Investigating resting-state functional connectivity in the cervical spinal cord at 3 T. Neuroimage 2017;147:589-601.

250. Xu JQ, Moeller S, Auerbach EJ, et al. Evaluation of slice accelerations using multiband echo planar imaging at 3 T. Neuroimage 2013;83:991-1001.

251. Setsompop K, Gagoski BA, Polimeni JR, Witzel T, Wedeen VJ, Wald LL. Blipped-controlled aliasing in parallel imaging for simultaneous multislice echo planar imaging with reduced g-factor penalty. Magnet Reson Med 2012;67:1210-24.

252. Cauley SF, Polimeni JR, Bhat H, Wald LL, Setsompop K. Interslice Leakage Artifact Reduction Technique for Simultaneous Multislice Acquisitions. Magnet Reson Med 2014;72:93-102.

253. Breuer FA, Blaimer M, Heidemann RM, Mueller MF, Griswold MA, Jakob PM. Controlled aliasing in parallel imaging results in higher acceleration (CAIPIRINHA) for multi-slice imaging. Magn Reson Med 2005;53:684-91.

254. Setsompop K, Gagoski BA, Polimeni JR, Witzel T, Wedeen VJ, Wald LL. Blipped-controlled aliasing in parallel imaging for simultaneous multislice echo planar imaging with reduced g-factor penalty. Magn Reson Med 2012;67:1210-24.

255. Friedman L, Glover GH. Report on a multicenter fMRI quality assurance protocol. Journal of Magnetic Resonance Imaging 2006;23:827-39.

256. Ganong WF. Review of medical physiology. 22nd ed. New York: McGraw-Hill Medical; 2005.

257. Wu CW, Chen CL, Liu PY, Chao YP, Biswal BB, Lin CP. Empirical evaluations of slice-timing, smoothing, and normalization effects in seed-based, resting-state functional magnetic resonance imaging analyses. Brain Connect 2011;1:401-10.

258. Grabner G, Janke AL, Budge MM, Smith D, Pruessner J, Collins DL. Symmetric atlasing and model based segmentation: an application to the hippocampus in older adults. Med Image Comput Comput Assist Interv 2006;9:58-66.

259. Tzourio-Mazoyer N, Landeau B, Papathanassiou D, et al. Automated anatomical labeling of activations in SPM using a macroscopic anatomical parcellation of the MNI MRI single-subject brain. Neuroimage 2002;15:273-89.

260. Schmahmann JD, Doyon J, McDonald D, et al. Three-dimensional MRI atlas of the human cerebellum in proportional stereotaxic space. Neuroimage 1999;10:233-60.

261. Taso M, Le Troter A, Sdika M, et al. A reliable spatially normalized template of the human spinal cord - Applications to automated white matter/gray matter segmentation and tensor-based

morphometry (TBM) mapping of gray matter alterations occurring with age. Neuroimage 2015;117:20-8.

262. Cadotte DW, Cadotte A, Cohen-Adad J, et al. Characterizing the Location of Spinal and Vertebral Levels in the Human Cervical Spinal Cord. Am J Neuroradiol 2015;36:803-10.

263. Chai XQJ, Castanon AN, Ongur D, Whitfield-Gabrieli S. Anticorrelations in resting state networks without global signal regression. Neuroimage 2012;59:1420-8.

264. Kong Y, Eippert F, Beckmann CF, et al. Intrinsically organized resting state networks in the human spinal cord. 2014;111.

265. Feinberg Da, Setsompop K. Ultra-fast MRI of the human brain with simultaneous multi-slice imaging. Journal of Magnetic Resonance 2013;229:90-100.

266. Roelcke U, Curt A, Otte A, et al. Influence of spinal cord injury on cerebral sensorimotor systems: a PET study. J Neurol Neurosurg Psychiatry 1997;62:61-5.

267. Martucci KT, Ng P, Mackey S. Neuroimaging chronic pain: what have we learned and where are we going? Future Neurol 2014;9:615-26.

268. Flodin P, Martinsen S, Altawil R, et al. Intrinsic Brain Connectivity in Chronic Pain: A Resting-State fMRI Study in Patients with Rheumatoid Arthritis. Front Hum Neurosci 2016;10:107.

269. Schabrun SM, Elgueta-Cancino EL, Hodges PW. Smudging of the Motor Cortex Is Related to the Severity of Low Back Pain. Spine 2017;42:1172-8.

270. Kilpatrick LA, Kutch JJ, Tillisch K, et al. Alterations in Resting State Oscillations and Connectivity in Sensory and Motor Networks in Women with Interstitial Cystitis/Painful Bladder Syndrome. J Urology 2014;192:947-55.

271. Kutch JJ, Yani MS, Asavasopon S, et al. Altered resting state neuromotor connectivity in men with chronic prostatitis/chronic pelvic pain syndrome: A MAPP Research Network Neuroimaging Study. Neuroimage-Clin 2015;8:493-502.

272. Antal A, Terney D, Kuhnl S, Paulus W. Anodal Transcranial Direct Current Stimulation of the Motor Cortex Ameliorates Chronic Pain and Reduces Short Intracortical Inhibition. J Pain Symptom Manag 2010;39:890-903.

273. Passard A, Attal N, Benadhira R, et al. Effects of unilateral repetitive transcranial magnetic stimulation of the motor cortex on chronic widespread pain in fibromyalgia. Brain 2007;130:2661-70.

274. Leo RJ, Latif T. Repetitive transcranial magnetic stimulation (rTMS) in experimentally induced and chronic neuropathic pain: A review. J Pain 2007;8:453-9.

275. Lefaucheur JP, Drouot X, Menard-Lefaucheur I, Keravel Y, Nguyen JP. Motor cortex rTMS restores defective intracortical inhibition in chronic neuropathic pain. Neurology 2006;67:1568-74.

276. Lefaucheur JP, Drouot X, Keravel Y, Nguyen JP. Pain relief induced by repetitive transcranial magnetic stimulation of precentral cortex. Neuroreport 2001;12:2963-5.

277. Johnson S, Summers J, Pridmore S. Changes to somatosensory detection and pain thresholds following high frequency repetitive TMS of the motor cortex in individuals suffering from chronic pain. Pain 2006;123:187-92.

278. Buckwalter JA. Spine Update - Aging and Degeneration of the Human Intervertebral Disc. Spine 1995;20:1307-14.

279. Wu T, Zang YF, Wang L, et al. Aging influence on functional connectivity of the motor network in the resting state. Neurosci Lett 2007;422:164-8.

280. Ellingson BM, Salamon N, Woodworth DC, Holly LT. Correlation between degree of subvoxel spinal cord compression measured with super-resolution tract density imaging and neurological impairment in cervical spondylotic myelopathy. 2015;22:631-8.

281. Griswold MA, Jakob PM, Heidemann RM, et al. Generalized Autocalibrating Partially Parallel Acquisitions (GRAPPA). Magnet Reson Med 2002;47:1202-10.

282. Holly LT, Ellingson BM, Salamon N. Metabolic Imaging Using Proton Magnetic Spectroscopy as a Predictor of Outcome After Surgery for Cervical Spondylotic Myelopathy. Clin Spine Surg 2017;30:E615-E9.

283. Ellingson BM, Salamon N, Hardy AJ, Holly LT. Prediction of Neurological Impairment in Cervical Spondylotic Myelopathy using a Combination of Diffusion MRI and Proton MR Spectroscopy. Plos One 2015;10.

284. Ellingson BM, Salamon N, Woodworth DC, Yokota H, Holly LT. Reproducibility, temporal stability, and functional correlation of diffusion MR measurements within the spinal cord in patients with asymptomatic cervical stenosis or cervical myelopathy. Journal of Neurosurgery: Spine 2018:1-9.

285. Rosenkrantz AB, Chandarana H, Pfeuffer J, et al. Zoomed echo-planar imaging using parallel transmission: impact on image quality of diffusion-weighted imaging of the prostate at 3T. Abdom Imaging 2015;40:120-6.

286. Andersson JLR, Skare S, Ashburner J. How to correct susceptibility distortions in spin-echo echo-planar images: application to diffusion tensor imaging. Neuroimage 2003;20:870-88.

287. Andersson JLR, Sotiropoulos SN. An integrated approach to correction for off-resonance effects and subject movement in diffusion MR imaging. Neuroimage 2016;125:1063-78.

288. Andersson JLR, Graham MS, Zsoldos E, Sotiropoulos SN. Incorporating outlier detection and replacement into a non-parametric framework for movement and distortion correction of diffusion MR images. Neuroimage 2016;141:556-72.

289. Yeh FC, Wedeen VJ, Tseng WYI. Generalized q-Sampling Imaging. Ieee T Med Imaging 2010;29:1626-35.

290. Wedeen VJ, Hagmann P, Tseng WYI, Reese TG, Weisskoff RM. Mapping complex tissue architecture with diffusion spectrum magnetic resonance imaging. Magnet Reson Med 2005;54:1377-86.

291. Tuch DS. Q-ball imaging. Magn Reson Med 2004;52:1358-72.

292. Le Bihan D. Looking into the functional architecture of the brain with diffusion MRI. Nat Rev Neurosci 2003;4:469-80.

293. Yeh FC, Verstynen TD, Wang Y, Fernandez-Miranda JC, Tseng WY. Deterministic diffusion fiber tracking improved by quantitative anisotropy. PLoS One 2013;8:e80713.

294. Jenkinson M, Bannister P, Brady M, Smith S. Improved optimization for the robust and accurate linear registration and motion correction of brain images. Neuroimage 2002;17:825-41.

295. Jenkinson M, Beckmann CF, Behrens TE, Woolrich MW, Smith SM. Fsl. Neuroimage 2012;62:782-90.

296. Behrens TEJ, Berg HJ, Jbabdi S, Rushworth MFS, Woolrich MW. Probabilistic diffusion tractography with multiple fibre orientations: What can we gain? Neuroimage 2007;34:144-55.

297. Greve DN, Fischl B. Accurate and robust brain image alignment using boundary-based registration. Neuroimage 2009;48:63-72.

298. Jenkinson M, Smith S. A global optimization method for robust affine registration of brain images. Med Image Anal 2001;5:143-56.

299. Ellingson B, Salamon N, Holly L. Advances in MR imaging for cervical spondylotic myelopathy. Eur Spine J 2013;24:1-12.

300. Lindberg PG, Feydy A, Sanchez K, Rannou F, Maier MA. Measures of spinal canal stenosis and relationship to spinal cord structure in patients with cervical spondylosis. J Neuroradiology 2012;39:236-42.

301. Nishida N, Kato Y, Imajo Y, Kawano S, Taguchi T. Biomechanical analysis of cervical spondylotic myelopathy: the influence of dynamic factors and morphometry of the spinal cord. J Spinal Cord Med 2012;35:256-61.

302. Chang V, Lu DC, Hoffman H, Buchanan C, Holly LT. Clinical results of cervical laminectomy and fusion for the treatment of cervical spondylotic myelopathy in 58 consecutive patients. Surgical neurology international 2014;5:S133-7.

303. Koskinen EA, Hakulinen U, Brander AE, Luoto TM, Ylinen A, Ohman JE. Clinical correlates of cerebral diffusion tensor imaging findings in chronic traumatic spinal cord injury. Spinal Cord 2014;52:202-8.

304. Vaccarino AL, Melzack R. Analgesia Produced by Injection of Lidocaine into the Anterior Cingulum Bundle of the Rat. Pain 1989;39:213-9.

305. Van AT, Granziera C, Bammer R. An introduction to model-independent diffusion MRI. Topics in magnetic resonance imaging: TMRI 2010;21:339.

306. Konishi J, Yamada K, Kizu O, et al. MR tractography for the evaluation of functional recovery from lenticulostriate infarcts. Neurology 2005;64:108-13.

307. Cho SH, Kim SH, Choi BY, et al. Motor outcome according to diffusion tensor tractography findings in the early stage of intracerebral hemorrhage. Neurosci Lett 2007;421:142-6.

308. Ciccarelli O, Behrens TE, Altmann DR, et al. Probabilistic diffusion tractography: a potential tool to assess the rate of disease progression in amyotrophic lateral sclerosis. Brain 2006;129:1859-71.

309. Sarica A, Cerasa A, Vasta R, et al. Tractography in amyotrophic lateral sclerosis using a novel probabilistic tool: A study with tract-based reconstruction compared to voxel-based approach. J Neurosci Meth 2014;224:79-87.

310. Bastin ME, Pettit LD, Bak TH, Gillingwater TH, Smith C, Abrahams S. Quantitative Tractography and Tract Shape Modeling in Amyotrophic Lateral Sclerosis. Journal of Magnetic Resonance Imaging 2013;38:1140-5.

311. Hotelling H. Analysis of a complex of statistical variables into principal components. J Educ Psychol 1933;24:417-41.

312. Jolliffe IT. Principal Component Analysis: Springer; 2002.

313. Severson KA, Molaro MC, Braatz RD. Principal Component Analysis of Process Datasets with Missing Values. Processes 2017;5.

314. Kabacoff R. R in Action: Data Analysis and Graphics with R: Manning; 2011.

315. Goldfeld SM, Quandt RE. Some tests for homoscedasticity. Journal of the American statistical Association 1965;60:539-47.

316. D'Agostino RB. Tests for the normal distribution. Goodness-of-fit techniques 1986;68:576.

317. Greicius MD, Supekar K, Menon V, Dougherty RF. Resting-state functional connectivity reflects structural connectivity in the default mode network. Cereb Cortex 2009;19:72-8.

318. Honey CJ, Sporns O, Cammoun L, et al. Predicting human resting-state functional connectivity from structural connectivity. Proc Natl Acad Sci U S A 2009;106:2035-40.

319. Chio A, Pagani M, Agosta F, Calvo A, Cistaro A, Filippi M. Neuroimaging in amyotrophic lateral sclerosis: insights into structural and functional changes. Lancet Neurology 2014;13:1228-40.

320. Douaud G, Filippini N, Knight S, Talbot K, Turner MR. Integration of structural and functional magnetic resonance imaging in amyotrophic lateral sclerosis. Brain 2011;134:3470-9.

321. Agosta F, Valsasina P, Absinta M, et al. Sensorimotor Functional Connectivity Changes in Amyotrophic Lateral Sclerosis. Cerebral Cortex 2011;21:2291-8.

322. Khedher L, Ramírez J, Górriz JM, Brahim A, Segovia F, Initiative AsDN. Early diagnosis of Alzheimer′ s disease based on partial least squares, principal component analysis and support vector machine using segmented MRI images. Neurocomputing 2015;151:139-50.

323. López M, Ramírez J, Górriz JM, et al. Principal component analysis-based techniques and supervised classification schemes for the early detection of Alzheimer's disease. Neurocomputing 2011;74:1260-71.

324. Haefeli J, Mabray MC, Whetstone WD, et al. Multivariate Analysis of MRI Biomarkers for Predicting Neurologic Impairment in Cervical Spinal Cord Injury. AJNR Am J Neuroradiol 2017;38:648-55.

325. Mabray MC, Talbott JF, Whetstone WD, et al. Multidimensional Analysis of Magnetic Resonance Imaging Predicts Early Impairment in Thoracic and Thoracolumbar Spinal Cord Injury. J Neurotrauma 2016;33:954-62.

326. Cadotte DW, Fehlings MG. Will imaging biomarkers transform spinal cord injury trials? Lancet Neurology 2013;12:843-4.

327. Freund P, Weiskopf N, Ashburner J. MRI investigation of the sensorimotor cortex and the corticospinal tract after acute spinal cord injury: a prospective longitudinal study (vol 12, pg 873, 2013). Lancet Neurology 2013;12:846-.